Magnetar-like X-ray Bursts from Anomalous X-ray Pulsars

by

Fotis Panagiotis Gavriil

Department of Physics
McGill University, Montreal
February 2006

A Thesis submitted to McGill University
in partial fulfilment of the requirements of the degree of
Doctor of Philosophy

Your file Votre référence
ISBN: 978-0-494-25153-9
Our file Notre référence
ISBN: 978-0-494-25153-9

Abstract

The leading model for understanding the energetics of anomalous X-ray pulsars (AXPs) is that they are "magnetars" – young, isolated neutron stars powered by the decay of their enormous magnetic fields. The identification of AXPs as magnetars is motivated by the similarity of AXPs to another enigmatic class of sources, the Soft Gamma Repeaters (SGRs). We report on long-term monitoring of AXPs using the *Rossi X-ray Timing Explorer* (*RXTE*). We monitor AXPs with *RXTE* to study their rotational stability, to search for variations in their pulsed flux and pulsed morphology. During our regular monitoring observations we discovered multiple bursts from two AXPs: this was the first time such behavior has been observed from these sources. Prior to our monitoring campaign, the detection of bursts solely from SGRs was the principle difference between AXPs and SGRs. The first detection of AXP bursts came in Fall 2001 when we discovered two SGR-like X-ray bursts from the direction of AXP 1E 1048.1–5937. Due to *RXTE*'s large ($1^\circ \times 1^\circ$) field-of-view we could not unambiguously identify the AXP as the burster. Recently, we detected a third burst from the direction of this source as well as a simultaneous increase in the pulsar's pulsed emission – this clearly identified the AXP as the burster. The most outstanding demonstration of AXP bursting behavior came on 2002 June 18 when AXP 1E 2259+586 underwent a major outburst involving 80 bursts and several changes in the persistent and pulsed emission, including a huge pulsed flux enhancement, a pulse morphology change and a rotational glitch. We also find variations in the persistent emission of AXPs in the absence of an obvious outburst. For example, we discovered two pulsed flux flares from AXP 1E 1048.1–5937. Both flares lasted several months and had well resolved few-week-long rises. The long rise times of the flares is a phenomenon not previously reported for this class of object, but has a clear explanation within the context of the magnetar model. All these results imply a close relationship between AXPs and SGRs, which we now believe are both magnetars, and have posed significant challenges to competing models.

Résumé

Le modèle principal qui explique les propriétés énergiques des pulsars anormaux à rayons X (AXPs) prédit que ces pulsars sont des «magnétoiles» (aussi appelées magnetars) – jeunes étoiles à neutron isolées qui dégagent de l'énergie en raison de l'affaiblissement de leurs champs magnétiques énormes. L'identification des AXPs comme magnétoiles est motivée par les similitudes entre les AXPs et une autre classe mystérieuse de sources, les répéteurs rayons gamma «mous» (SGRs) qui, eux aussi, sont identifiés comme magnétoiles. Ici, nous présenterons les résultats du projet de surveillance à long terme des AXPs, un projet effectué grace au satellite à rayons X «*the Rossi X-ray timing explorer*» ou «*RXTE*». Nous surveillons les AXPs avec ce satellite pour étudier leur stabilité de rotation, et pour chercher des variations dans leur flux pulsé et dans la morphologie de leurs pulsations. Pendant nos observations de surveillance de routine, nous avons découvert des sursauts énergétiques provenant de deux AXPs. C'était la première fois qu'on a observé un tel comportement provenant de ces sources. Avant notre campagne de surveillance, la difference principale entre les AXPs et les SGRs était que seulement les SGRs émettaient des sursauts. La première détection de sursauts provenant des AXPs est arrivée en automne 2001, quand nous avons découvert deux sursauts de rayons X semblables à ceux des SGRs et provenant de la direction du AXP 1E 1048.1–5937. Cependant, en raison du grand champs visuel de *RXTE* ($1°\times1°$), nous ne pouvions pas être absolument certains que ces sursauts provenaient de 1E 1048.1–5937. Récemment, nous avons détecté un troisième sursaut d'énergie provenant de la direction de 1E 1048.1–5937, et simultanément nous avons détecté une augmentation de l'émission pulsée du pulsar – ceci a clairement indiqué que les sursauts provenaient de cet AXP. La démonstration la plus exceptionnelle de AXPs subissant un épisode de sursauts est arrivée le 18 juin 2002, lorsque le AXP 1E 2259+586 a émis 80 sursauts et a manifesté plusieurs changements de son émission persistante et pulsée, y compris une augmentation énorme du flux pulsé, un changement de morphologie des pulsations, et une brusque augmentation de la vitesse de rotation. Il convient de noter ici que des variations de l'émission persistante des AXPs est parfois

observée même quand ces derniers ne sont pas en train de subir un épisode de sursauts. Par exemple, nous avons découvert deux augmentations graduelles à long terme du flux pulsé du AXP 1E 1048.1–5937, suivies par des descentes graduelles. Chacun de ces deux événements a duré plusieurs mois pendant lesquels nous observions clairement l'évolution du flux de semaine en semaine. La longue durée de l'augmentation graduelle du flux pendant ces deux événements, qui constitue un phénomène sans précédent rapporté pour cette classe d'objets, est clairement justifiable par le modèle des magnétoiles. Tous ces résultats indiquent un rapport étroit entre les SGRs et les AXPs, que maintenant nous croyons aussi être des magnétoiles. En conséquence, nos résultats posent des défis de taille aux modèles concurrençant le modèle des magnétoiles.

Preface

This thesis is a collection of five papers accepted for publication in *Nature*, *the Astrophysical Journal* and *the Astrophysical Journal Letters*:

Chapter 6 Gavriil, F. P., Kaspi, V. M., & Woods, P. M. Magnetar-like X-ray Bursts from an Anomalous X-ray Pulsar. Nature, 419, 142–144, 2002.

Chapter 7 Kaspi, V. M., Gavriil, F. P., Woods, P. M., Jensen, J. B., Roberts, M. S. E., & Chakrabarty, D. A Major SGR-like Outburst and Rotation Glitch in the No-Longer-So-Anomalous X-ray Pulsar 1E 2259+586. Astrophysical Journal Letters. 588, L93–L96, 2003.

Chapter 8 Gavriil, F. P., Kaspi, V. M., & Woods, P. M. A Comprehensive Study of the X-ray Bursts from the Magnetar Candidate 1E 2259+586. Astrophysical Journal, 607, 959–969, 2004.

Chapter 9 Gavriil, F. P. & Kaspi, V. M. Anomalous X-ray Pulsar 1E 1048.1–5937: Pulsed Flux Flares and Large Torque Variations. Astrophysical Journal Letters. 609, L67–L70, 2004.

Chapter 10 Gavriil, F. P., Kaspi, V. M., & Woods, P. M. 2006, Astrophysical Journal, in press.

These papers all reported on observations of anomalous X-ray pulsars (AXPs). Each paper reported a new and original result. Before discussing the significance of each result individually, I will give a brief history of the sources in question, AXPs, in order for the reader to have a better understanding of the relevance of each result.

AXPs have been a mystery since the discovery of the first example over twenty years ago. AXPs are rotating isolated neutron stars, and they are slowing down

and therefore losing rotational kinetic energy. But unlike other isolated neutron stars, this loss of rotational kinetic energy is not enough to explain their observed X-ray luminosity. In other words we do not know why we are even able to observe them. The most promising AXP model was that they are magnetars – young, isolated neutron stars powered by the decay of an ultra-high magnetic field. In this scenario it is the decay of the magnetic field rather than rotation that is powering these pulsars. In fact the inferred magnetic field strength of AXPs is in the range of 10^{14}–10^{15} G, thousands of times larger than for typical pulsars. The identification of AXPs with magnetars is further motivated by the similarity of the AXP emission to that of another enigmatic class of objects, the soft gamma-ray repeaters (SGRs). The SGRs share similar properties with the AXPs; the main difference has been that SGRs emit short powerful bursts of gamma rays and X-rays while AXPs do not. The bursts from SGRs can only be explained in the context of the magnetar model.

Statement of Originality

In Gavriil et al. (2002) we discovered two bursts from AXP 1E 1048.1–5937. This was the first example of such behavior from an AXP since the discovery of the source class over a quarter of a century ago. We could not unambiguously identify the AXP as the source of the bursts because the instrument that detected them sees a large area of the sky all at once and cannot distinguish between photons that come from different regions of its field of view. After considering alternate sources for the bursts we concluded that 1E 1048.1–5937 was the most plausible source. In Kaspi et al. (2003) we discovered a major outburst from another AXP, 1E 2259+586. This outburst involved over 80 bursts along with simultaneous changes to every aspect of the pulsar's emission. In this case the AXP was undoubtedly the source of the bursts, thus proving that AXPs and SGRs are the same class of object, as predicted by the magnetar model. In Gavriil et al. (2004) we performed a statistical analysis on these bursts and found that their properties were very similar to those of SGRs, although there were some intriguing

differences.

In Gavriil & Kaspi (2004) we reported the discovery of unusual flux variations in AXP 1E 1048.1–5937. There were past reports of flux variations in AXPs, but the variations we discovered were different from the abrupt and short-lived flux variations in those cases. This time the pulsar had a slow-rising (weeks), long-lasting (months) flux decay. Previous flux decays have been attributed to cooling of the surface after the impulsive injection of heat from bursts. In this case we argued that the flux variation must be attributed to currents in the magnetosphere of the pulsar, which were amplified by internal stresses.

In Gavriil et al. (2005) we discovered another burst from 1E 1048.1–5937 along with a short-term pulsed flux enhancement, identifying 1E 1048.1–5937 as the burster in this case. Given the similarity between this burst and the others from this source, this confirms that 1E 1048.1–5937 emitted all three bursts.

In conclusion, the results that make up this thesis have provided the most plausible solution to the 20-year-old mystery of the AXPs - they are magnetars.

Contribution of Authors

I would like to acknowledge the contributions of my coauthors:

Chapter 6 (Gavriil, Kaspi, & Woods, 2002) Peter M. Woods suggested searching for bursts in the 1E 1048.1–5937 data. He also reanalyzed much of the data using different software and techniques in order to confirm the validity of our findings. He also wrote some of the software used to analyze the bursts and made substantial contributions to the interpretation of the results. Victoria M. Kaspi played the most crucial role in the preparation of the text, the interpretation of the results and made substantial contributions to all aspects of the data analysis.

Chapter 7 (Kaspi, Gavriil, Woods, Jensen, Roberts, & Chakrabarty, 2003) Peter M. Woods performed the spectral and flux analysis of the *RXTE* data of the persistent emission of 1E 2259+586. All of the *Gemini* observations

of this source were acquired and analyzed by Joseph B. Jensen. The *Very Large Area* data on this source were analyzed by Mallory S. E. Roberts. Deepto Chakrabarty was the author of some of the software used in the timing analysis. Victoria M. Kaspi played the most crucial role in the preparation of the text and the interpretation of our results.

Chapter 8 (Gavriil, Kaspi, & Woods, 2004) Peter M. Woods provided useful comments and suggestions on the manuscript. The analysis I performed also used techniques developed by Peter M. Woods, but for different sources. Victoria M. Kaspi played a crucial role in the preparation of the manuscript and in the interpretation of the results.

Chapter 9 (Gavriil & Kaspi, 2004) Victoria M. Kaspi made substantial contributions to the preparation of the text and the interpretation of the results.

Chapter 10 (Gavriil, Kaspi, & Woods, 2005) Peter M. Woods performed all the analysis of the imaging data of the source taken with the *XMM-Newton* and *Chandra* data. Victoria M. Kaspi initiated the Target of opportunity observations of the source and provided substantial comments and suggestions on the manuscript.

Acknowledgments

I am grateful for all the help and advice from my adviser Vicky Kaspi. It was a real honor to have a scientist as exceptional as Vicky for a mentor. Vicky was kind enough to take me on as a graduate student and even offered me a summer job at MIT before I had even officially finished my undergraduate studies. Working on such a popular topic with Vicky awarded me with a lot of exposure in the pulsar world, however the competition was rather fierce, and at times I was under a lot more stress and pressure than the average graduate student. On the other hand, the opportunities and privileges I enjoyed working for Vicky some graduates, and even some post-docs for that matter, would only dream of. I received constant guidance and an infinite amount of help from Vicky, she provided everything I required to get the job done, as well as the travel funding necessary for me to attend many different conferences throughout the world.

Before thanking the rest of the individuals that directly affected this work, I would like to thank individuals which had an important impact in my life. First and foremost I would like to thank the most important person in my life – my wife Claudia. She has been unflinchingly by my side for the past ten years and as well as my wife she is my best friend. She inspires, comforts and fulfills me. Having a husband in grad school is not easy, thus, this thesis is dedicated to Claudia for being so patient and loving during this time. I would also like to thank the rest of my family for always encouraging me in anything I do regardless of whether or not they understood what I was doing.

Coming into the office everyday would not have been as fun were it not for Jason and Cindy. Very few people can say that they share an office with close friends – but I am sure those who do not end up being much more productive than I. I would also like to thank all the other, past and present, members of

the pulsar group for being such cool and friendly people; in alphabetical order they are: René Breton, Rim Dib, Claude-André Giguère, Marjorie Gonzalez, Maggie Livingstone, Maxim Lyutikov, Scott Ransom, Mallory Roberts, as well as honorary member Aaron Berndsen. I would like to thank my good friend Mark Orchard-Webb, who has always been there to listen to me whine. The fact that I remained sane during grad school can be partially attributed to his cynical, yet humorous, view on any issue.

I would like to thank all the individuals listed in the preface as co-authors on the papers which make up this thesis. I would particularly like to thank Pete Woods. I have always admired Pete and I consider him a good friend. This work has benefited from valuable comments, suggestions and useful discussions with many individuals; in alphabetical order they are: K. Hurley, K. Jahoda, C. Kouveliotou, E. Kuulkers, W. Lewin, M. Lyutikov, R. Manchester, M. Muno, D. Psaltis, S. Ransom, M. Roberts, D. Smith, C. Thompson. For the work presented in Chapter 7, we thank F. Nagase and B. Paul for help with the archival *Ginga* data

This work was supported financially throughout the years by: NSERC via Discovery Grant 228738-03 and Steacie Supplement 268264-03; the Canada Foundation for Innovation via a New Opportunities Grant; the Canadian Institute for Advanced Research; SAO grant GO4-5162X; NATEQ; FQRNT Team and Centre Grants; NASA, via a Long-Term Space Astrophysics Grant NAG5-8063 and NASA grant NNG05GA54G; a NSF Career grant. Victoria M. Kaspi is a Canada Research Chair and Steacie Fellow, and was an Alfred P. Sloan Fellow.

This work would not have been possible if it were not for some exceptional instruments and their facilities. We thank J. Swank and the *RXTE* scheduling team. This research has also made use of archival *RXTE* data obtained through the High Energy Astrophysics Science Archive Research Center Online Service[1], provided by the NASA/Goddard Space Flight Center. The *Gemini* Observatory is operated by the Association of Universities for Research in Astronomy, Inc., under a cooperative agreement with the NSF on behalf of the *Gemini* partner-

[1] ftp://legacy.gsfc.nasa.gov

ship: the National Science Foundation (United States), the Particle Physics and Astronomy Research Council (United Kingdom), the National Research Council (Canada), CONICYT (Chile), the Australian Research Council (Australia), CNPq (Brazil), and CONICET (Argentina). We thank F. Jansen for scheduling Target-of-Opportunity observations with *XMM-Newton* and B. Clark for scheduling the Ad Hoc observation with the *Very Large Array*. The National Radio Astronomy Observatory is a facility of the National Science Foundation operated under cooperative agreement by Associated Universities, Inc.

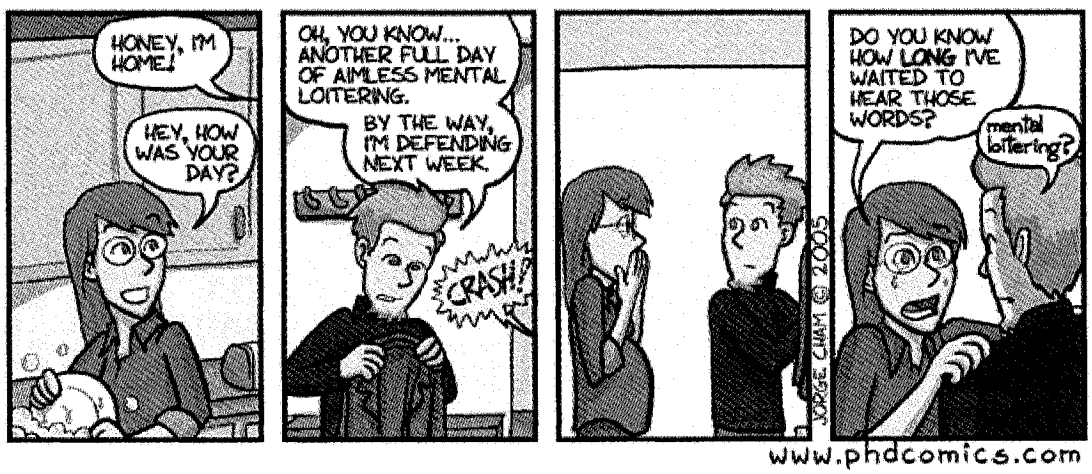

"Piled Higher and Deeper" by Jorge Cham `www.phdcomics.com`

To my wife.

Contents

List of Figures

List of Tables

Chapter 1

Introduction

Just over a year after the discovery of the neutron (Chadwick, 1932), Baade & Zwicky (1934) postulated that the end result of a supernova explosion would be a neutron star. Decades later Hewish et al. (1968) discovered the first rapidly rotating neutron star, or pulsar. The idea that a supernova explosion would result in a neutron star was confirmed when Staelin & Reifenstein (1968) discovered a pulsar in the Crab nebula, the remnant of a supernova explosion discovered by Chinese astronomers in 1054 AD. This thesis is on an unusual class of young neutron stars known as Anomalous X-ray Pulsars (AXPs). Fahlman & Gregory (1981) discovered the first AXP and for many years they remained a mystery. Their properties differ strikingly from other young neutron stars. In order to understand what makes AXPs "anomalous" let us first review the properties of neutron stars in general.

1.1 Neutron Stars

When a massive stars depletes its nuclear fuel it reaches a point where it can no longer support itself against gravity. At this point the star collapses. The stellar core collapses and triggers an explosion which releases an enormous amount of energy – a supernova explosion. Supernova explosions are so bright that they can outshine our galaxy for a brief period of time (Meszaros, 1992). The star subsequently blows off some/most of its outer envelope which expands into the local interstellar medium. Depending on its age, composition and the density of the medium it is expanding into, it might be possible to observe this ejected shell as a supernova remnant (SNR) (Lyne & Smith, 1990). What remains of

the original star is a compact core, whose further collapse cannot be stopped by thermal pressure (Meszaros, 1992).

For a star whose core mass is greater than $M_{\rm Ch} = 1.4 M_\odot$ (Chandrasekhar, 1931), the gravitational pressure is so strong that the inverse beta reaction

$$p + e^- \rightarrow n + \nu_e \tag{1.1}$$

becomes important. If the neutrons provide enough degeneracy pressure to balance gravity, than we are left with a neutron star. If the collapsed core has a mass greater than $\sim$4 $M_\odot$, neutron degeneracy pressure will not suffice to balance gravity and what will be left over is a black hole (Meszaros, 1992).

1.2 Neutron Star Properties

1.2.1 Mass and Radius

We can estimate the mass and radius of the compact cores from first principles. During core collapse, gravity will squeeze the particles together; however, Pauli's exclusion principle sets a limit on how close the particles can get. Following Griffiths (1995) and Meszaros (1992) we can estimate this degeneracy pressure by considering the simple case of particles in a cubical box with sides of length L. Solving Schrödinger's equation for such a system we obtain

$$E = \frac{\pi^2 \hbar^2}{2mL^2} \left(n_x^2 + n_y^2 + n_z^2\right), \tag{1.2}$$

where E is the particle energy, m the particle mass, and n_x, n_y, n_z are the number of quantum states in a given direction. If we plot these states in three dimensions, then the number of particles with energy E or less can be approximated by the volume of an octant of a sphere with radius R, i.e. $(1/8)(4\pi R^3/3) = \pi R^3/6$, where $R^2 = n_x^2 + n_y^2 + n_z^2$. The particles might also have spin; thus, to obtain the total number of particles we must also multiply by their spin degeneracy, $g_s = 2s + 1$, where s is the spin of the particles. For electrons and protons, i.e.

fermions with $s = 1/2$, $g_s = 2$. Thus, the total number of particles that have energy E or less is given by

$$N = g_s \frac{\pi}{6} \left(n_x^2 + n_y^2 + n_z^2\right)^{3/2} \tag{1.3}$$

$$= g_s \frac{\pi}{6} \left(\frac{2mV^{2/3}E}{\pi^2\hbar^2}\right)^{3/2}, \tag{1.4}$$

where we have inserted Equation 1.2 into the above and we have written L in terms of the volume V, i.e $V = L^3$. Simply rearranging the above we find that the energy is given by

$$E = E_F = \frac{\hbar^2}{2m} \left(\frac{6\pi^2}{g_s}\right)^{2/3} \left(\frac{N}{V}\right)^{2/3}. \tag{1.5}$$

The above is known as the Fermi energy. Integrating the above over the number of particles we obtain the total energy of the system

$$U = \int_0^{E_F} E dN \tag{1.6}$$

$$= \frac{3\hbar^2}{10m} \left(\frac{6\pi^2}{g_s}\right)^{2/3} \left(\frac{N}{V}\right)^{5/3} V. \tag{1.7}$$

Now, the pressure is given by the thermodynamic identity $P = -\partial U/\partial V$, hence

$$P = \frac{\hbar^2}{5m} \left(\frac{6\pi^2}{g_s}\right)^{2/3} \left(\frac{N}{V}\right)^{5/3}$$

$$= \frac{\hbar^2}{5m} \left(\frac{6\pi^2}{g_s}\right)^{2/3} n^{5/3}, \tag{1.8}$$

where $n = N/V$ is the number density. The above expression describes the degeneracy pressure for non-relativistic particles. If we write the number density in terms of the mass density, i.e. $\rho = mn$, notice that the above equation describes an adiabatic equation of state

$$P = K\rho^\gamma = K\rho^{1+1/\alpha}, \tag{1.9}$$

where K and γ are constants. Such an equation of state is known as a polytrope where α is the polytropic index. From Eq. 1.8 we see that non-relativistic degenerate matter $\alpha = 3/2$.

We can estimate the mass at which the degeneracy pressure balances gravity by using the equation for hydrostatic equilibrium

$$\nabla P = \frac{GM\rho}{r^2}\hat{\mathbf{r}}, \tag{1.10}$$

which for a spherically symmetric star reduces to

$$\frac{dP}{dr} = -\frac{GM\rho}{r^2}. \tag{1.11}$$

Combining Eq. 1.8 and Eq. 1.11 and solving for the central pressure, P_c, and central density, ρ_c, we find

$$P_c = 0.77\frac{GM^2}{R^4} \tag{1.12}$$

and

$$\rho_c = 1.43\frac{M}{R^3}. \tag{1.13}$$

For a white dwarf the electrons provide the degeneracy pressure. Thus, in this case we must substitute $n = n_e = (Z/A)(\rho/m_p)$ for the number density of particles in Eq. 1.8. We thus obtain the Chandrasekhar mass,

$$M_{\rm Ch} \approx \pi \left(\frac{Z}{A}\right)^2 \left(\frac{\hbar c}{G m_p^2}\right)^{3/2} m_p. \tag{1.14}$$

For $(Z/A) = 0.5$ $M_{\rm Ch} = 1.45$ $M_\odot$. This is the limiting mass for a white dwarf, however it is also important for neutron stars because it is the minimum mass a compact core must have for it to collapse to a neutron star (Meszaros, 1992).

Following Meszaros (1992) we can calculate the limiting mass of a neutron star in a similar fashion as for a white dwarf. Here we must treat the degenerate matter as relativistic. We can follow the same procedure as before but instead of Schrödinger's equation we must use the Klein-Gordon equation, and in so doing

we find that the pressure is given by

$$P = \frac{1}{4}\left(\frac{6\pi^2}{g_s}\right)^{1/3} \hbar c n^{4/3} \tag{1.15}$$

(Meszaros, 1992). The above expression describes the degenerate pressure for relativistic particles. From Eq. 1.15 we see that for a relativistic degenerate gas the polytropic index is $\alpha = 3$, in which case the central density is given by

$$P_c = 11.0\frac{GM^2}{R^4}, \tag{1.16}$$

and the central density by

$$\rho_c = 54.3\left(\frac{3}{4\pi}\right)\left(\frac{M}{R^3}\right). \tag{1.17}$$

In Eq. 1.15 we must replace n by the number density of neutrons $n = n_n = \rho/m_n$. If we equate the degeneracy pressure to the central pressure we obtain

$$M_{\rm lim} \sim \pi\left(\frac{\hbar c}{G m_n^2}\right)^{3/2} m_n, \tag{1.18}$$

which is the limiting mass of a neutron star. Taking Equation 1.18 at face value we find $M \sim 5\ M_\odot$. As pointed out by Meszaros (1992) this is definitely an overestimate because the true neutron star equation of state is unknown (Lattimer & Prakash, 2000) and important effects arising from General Relativity have been neglected. Observations of pulsars in binary systems allow the mass of the neutron star and the companion to be isolated if it is possible to measure relativistic orbital effects. From measurements of 50 radio pulsars in binary systems, Thorsett & Chakrabarty (1999) found that the distribution of neutron star masses was well characterized by a narrow Gaussian with mean $M_{\rm NS} = 1.35 \pm 0.04\ M_\odot$ (however, recent observations are showing that the distribution is much broader, see Nice et al., 2005, for example.). In the rest of this thesis we will take the canonical mass of a neutron star to be $M_{\rm NS} \sim 1.4\ M_\odot$.

We can also use Equations 1.15, 1.16 and 1.17 to estimate the canonical radius

of a neutron star. After some algebra we find

$$R \approx 4.50 \frac{\hbar^2}{G m_p^{8/3}} M^{-1/3}. \tag{1.19}$$

Setting $M = 1.4\ M_\odot$ we obtain a radius of $R = 12$ km. Notice that neutron stars have masses comparable to that of the Sun confined within the diameter (~ 20 km) of a small city.

We can use the canonical mass and radius of a neutron star to estimate the acceleration due to gravity at the surface

$$g \sim \frac{GM}{R^2} \sim 10^{14} \text{ cm s}^{-2}. \tag{1.20}$$

Hence neutron stars have enormous gravitational fields. However as we will see in § 1.3.3 it is in fact the magnetic field which dictates the motion of charged particles.

1.2.2 Magnetic Fields

The measurement of Zeeman splitting in spectral lines of main sequence star spectra provide a direct measure of their magnetic fields (Bowers & Deeming, 1984). Our own Sun has a magnetic field of the order of ~ 10 G. For main sequence stars of type A_p[1] magnetic fields in the range $10^2 - 10^4$ G have been measured (Bowers & Deeming, 1984). Following Meszaros (1992) we can estimate, to order of magnitude, the magnetic field of a neutron star, if we assume that the magnetic field is primordial (left over from the progenitor) and that the magnetic flux is conserved during the collapse

$$\frac{d\Phi}{dt} = \frac{d}{dt} \int_S \mathbf{B} \cdot d\mathbf{a} = 0. \tag{1.21}$$

[1]The A refers to the spectral type and the subscript p refers to chemically peculiar.

If we take a progenitor star with magnetic field strength $B \approx 10^2$ G and radius $R \approx R_\odot = 7 \times 10^{10}$ cm it follows from Equation 1.21 that

$$B_{\rm NS} \sim B \left(\frac{R}{R_{\rm NS}} \right)^2 = 10^{12} \text{ G}, \tag{1.22}$$

where $B_{\rm NS}$ and $R_{\rm NS}$ is the magnetic field and radius of the neutron star. Thus neutron stars are expected to have high magnetic fields. As we will see in § 1.3.1, the period and rate of change of period of a pulsar allows us to infer its dipole magnetic field strength (see Equation 1.39). From Fig. 1.1, neutron star magnetic fields span many orders of magnitude with the majority having magnetic fields of the order $\sim 10^{12}$ G. As discussed later on, the pulsars which are the subject of this thesis have magnetic fields as high as $\sim 10^{15}$ G. How such high magnetic fields are generated is discussed in § 2.1.

Measuring magnetic fields from the spin evolution of a pulsar is an indirect measurement because it is model dependent. Direct measures of neutron star magnetic fields can be made by the observation of lines in their spectra. Following Shapiro & Teukolsky (1983) we can estimate the magnetic field of a neutron star if we assume that lines in their spectra are due to particles making transitions from one energy level to another. In the presence of a magnetic field an electron has its energy quantized in *Landau levels*

$$\epsilon_n = (n + \frac{1}{2})\hbar\omega_B + \frac{p^2}{2m}, \tag{1.23}$$

where p is the momentum of the particle and the frequency ω_B is given by

$$\omega_B = \frac{eB}{mc} \tag{1.24}$$

(Shapiro & Teukolsky, 1983). We can arrive at the above expression for ω_B by considering the classical equation of motion for a particle spiraling around a magnetic field line. Equating the centripetal force to the Lorentz force we find

$$m\omega^2 r = e \left(\frac{\omega r}{c} \right) B. \tag{1.25}$$

Now, if an electron makes a transition from $n = 1$ to the ground state, then the amount of energy it releases is $E = \epsilon_1 - \epsilon_0$. Putting it all together we find that the magnetic field estimated from a line at energy E is given by

$$B = \frac{mc(\hbar\omega_B)}{\hbar e} = \frac{mcE}{\hbar e}. \tag{1.26}$$

There are ~14 neutron stars with features found in their spectra (Heindl et al., 2004). These neutron stars are in binary systems. There are claims of spectral features in isolated neutron stars, but the interpretation of these features is controversial (see discussion by Hailey & Mori, 2002, for an example), and in other cases the absence of these features is puzzling (see Burwitz et al., 2001, for example).

1.2.3 Rotation

Neutron star progenitors (mainly main sequence stars of type B and earlier) are observed to rotate and some are magnetic (Bowers & Deeming, 1984). Following Bowers & Deeming (1984) the angular momentum of the progenitor is approximately given by $J \sim MR^2\Omega$, where Ω and R is the angular frequency and radius of the star. If we assume that angular momentum is conserved during the progenitor's collapse to a neutron star then

$$\Omega_{\rm NS} = \Omega \left(\frac{R}{R_{\rm NS}}\right)^2. \tag{1.27}$$

Here $\Omega_{\rm NS}$ and $R_{\rm NS}$ is the angular frequency and radius of the neutron star. From Equation 1.27 we see that for a main sequence star with a slow rotational frequency of $\Omega \approx 10^{-4}$ rad s^{-1}, we obtain an angular frequency of $\Omega_{\rm NS} \sim 10^4$ rad s^{-1} for the neutron star, where we have used $R_{\rm NS} = 10^6$ cm (see Eq. 1.19) for the radius of the neutron star. Thus just from conservation of angular momentum it follows that neutron stars can be rapid rotators. Observations of pulsars reveal that neutron star rotation periods span many orders of magnitude; see Figure 1.1. The spin frequency of a neutron star is limited by the fact that the centripetal

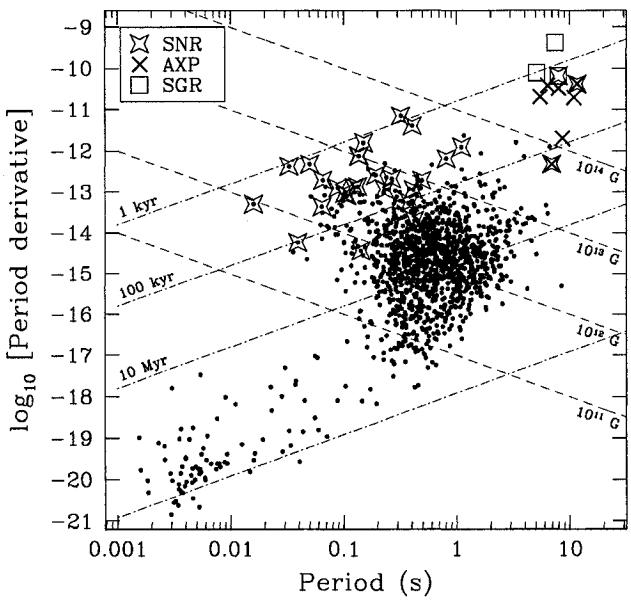

Figure 1.1: Period-Period derivative diagram. A plot of period (P) versus Period-derivative ($\dot{P}$) for all known pulsars for which both these parameters have been measured. The dashed-dot lines represent lines of constant age. The dashed lines represent lines of constant magnetic field. The points encapsulated within a star represent pulsars associated with supernova remnants. The crosses represent the Anomalous X-ray Pulsars, see § 1.5, and the boxes the Soft Gamma repeaters, see § 1.6. The data in this plot were obtained from the Australian Telescope National Facility (ATNF) online pulsar catalog (`http://www.atnf.csiro.au/research/pulsar/psrcat/`).

force ($m\Omega^2 r$) at the equator must be less than the gravitational force (GMm/r^2), otherwise the star will tear itself apart. Thus, we obtain a critical angular frequency of

$$\Omega_{\rm crit} = \sqrt{\frac{GM}{R^3}}. \tag{1.28}$$

For a $M = 1.4\ M_\odot$, $R = 10^6$ cm neutron star this corresponds to a spin period of $P_{\rm crit} = 2\pi/\Omega_{\rm crit} \sim 1$ ms. The actual limit on the spin period of the pulsar depends of course on the neutron star equation of state. To date the fastest known pulsar has a spin period of 1.397 ms (Hessels et al., 2006).

Pulsars are rapidly rotating, magnetized neutron stars. In the following sec-

tions we introduce the two canonical mechanisms for powering pulsars: rotation (§ 1.3) and accretion (§ 1.4).

1.3 Rotation-Powered Pulsars

As their name suggests, rotation-powered pulsars are powered by their loss of rotational kinetic energy (Manchester & Taylor, 1977). All radio pulsars are consistent with being rotation powered pulsars. Most of the radio pulsars known are found within the Galactic plane and some are located in globular clusters. The majority of radio pulsars are isolated; some are in binaries with a regular star; six are in neutron-neutron binaries, and in one case the other neutron star is also a pulsar (Lyne et al., 2004).

1.3.1 Magnetic Dipole Model

We can decipher many properties about rotation-powered pulsars if we model them as rotating magnetic dipoles (Manchester & Taylor, 1977). This magnetic dipole model was developed before pulsars were discovered (Pacini, 1967). Following Longair (1994) and Shapiro & Teukolsky (1983), the rate at which a magnetic dipole dissipates energy in vacuo is given by Larmor's Formula:

$$\frac{dE}{dt} = -\frac{2|\ddot{\boldsymbol{\mu}}|^2}{3c^3}, \tag{1.29}$$

where $\boldsymbol{\mu}$ is the magnetic moment of the neutron star. To first order we can approximate the magnetic field of a pulsar as a perfect dipole

$$\mathbf{B} = \frac{\mu}{r^3}\left(2\cos\theta\hat{\mathbf{r}} + \sin\theta\hat{\boldsymbol{\theta}}\right), \tag{1.30}$$

in which case the magnetic moment is given by

$$\boldsymbol{\mu} = \mu\left(\sin\alpha\cos\phi\hat{\boldsymbol{\imath}} + \sin\alpha\sin\phi\hat{\boldsymbol{\jmath}} + \cos\alpha\hat{\mathbf{k}}\right), \tag{1.31}$$

where α is the angle the rotation axis makes with the magnetic axis. Hence

$$\frac{dE}{dt} = -\frac{2\mu^2 \sin^2 \alpha}{3c^3}\left(\dot{\phi}^4 + \ddot{\phi}^2\right). \tag{1.32}$$

The rotational frequency of the pulsar is $\Omega = \dot{\phi}$, and for all pulsars $\dot{\Omega}^2 \ll \Omega^4$, so we have

$$\frac{dE}{dt} \approx -\frac{2\mu^2 \sin^2 \alpha}{3c^3}\Omega^4. \tag{1.33}$$

As the star is spinning down due to magnetic dipole braking it loses rotation kinetic energy ($E = I\Omega^2/2$, where I is the star's moment of inertia) at a dissipation rate of

$$\frac{dE}{dt} = I\Omega\dot{\Omega}. \tag{1.34}$$

Equating Eq. 1.33 to Eq. 1.34 and using the fact that for a dipole field $\mu = B^2 r^3$, we find

$$\frac{d\Omega}{dt} = -\frac{2\Omega^3 B_S^2 R^6 \sin^2 \alpha}{3Ic^3}, \tag{1.35}$$

where B_S is the magnetic field at the surface $B_S = B(R)$.

1.3.2 Estimating Rotation-Powered Pulsar Parameters

If we can measure a pulsar's spin period ($P \equiv 2\pi/\Omega$) and period-derivative ($\dot{P} = 2\pi\dot{\Omega}/\Omega^2$), then we can use the magnetic dipole model to estimate the star's surface magnetic field strength B_S and spin-down luminosity $\dot{E}$. (Eq. 1.34) The spin-down luminosity is given by (Eq. 1.34

$$\dot{E} = 8\pi^3 I\left(\frac{\dot{P}}{P^3}\right), \tag{1.36}$$

and the magnetic field is found by rearranging Eq. 1.35

$$B_S = \left(\frac{3Ic^3}{8\pi^2 R^6}\right)^{\frac{1}{2}}\left(P\dot{P}\right)^{\frac{1}{2}}. \tag{1.37}$$

Now, the momentum of inertia for a distribution of mass is given by

$$I = \int_V (x^2 + y^2)\rho dV, \tag{1.38}$$

where ρ is the mass density. If we approximate the star as a uniform density sphere then the above reduces to $I = 2MR^2/5$. Using this and the canonical mass and radius of a neutron star ($M \sim 1.4\ M_\odot$ and $R \sim 10^6$ cm; see § 1.2.1), we find

$$B_S \approx 3.2 \times 10^{12} \left(\frac{P}{1\ \mathrm{s}}\right)^{1/2} \left(\frac{\dot{P}}{10^{-14}\ \mathrm{s\ s^{-1}}}\right)^{1/2} \mathrm{G}, \tag{1.39}$$

and

$$\dot{E} \approx -3.9 \times 10^{32} \left(\frac{P}{1\ \mathrm{s}}\right)^{-3} \left(\frac{\dot{P}}{10^{-14}\ \mathrm{s\ s^{-1}}}\right)\ \mathrm{erg\ s^{-1}}. \tag{1.40}$$

We can also use the magnetic dipole model to determine the characteristic age (τ) of the pulsar. From Equation 1.35, we see that

$$\dot{\Omega} = -K\Omega^3, \tag{1.41}$$

where $K = 2R^6 B_S^2 \sin^2\alpha/3Ic^3$ is a constant. Note that we are making the simplification that the magnetic field is constant, even though it would not be unreasonable to assume that the magnetic is evolving; however, as we will show in Chapter 2, for canonical pulsars the timescale for this evolution is much greater than the lifetime of the pulsar (n.b. magnetic field decay is important for the unusual sources which are the the subject of this thesis, in which case the following age estimate should only be considered an upper limit). Integrating Equation 1.41 from $t = 0$ to τ we find

$$\tau = -\frac{1}{2K}\left[\frac{1}{\Omega^2} - \frac{1}{\Omega_0^2}\right], \tag{1.42}$$

where Ω_0 is the neutron star's spin frequency at birth. Substituting Equation 1.41 for K, we obtain.

$$\tau = -\frac{\Omega}{2\dot{\Omega}}\left[1 - \left(\frac{\Omega}{\Omega_0}\right)^2\right]. \tag{1.43}$$

Assuming that the pulsar's initially spin frequency was much higher than its current spin frequency ($\Omega_0 \gg \Omega$) the above simplifies to

$$\tau = -\frac{\Omega}{2\dot{\Omega}} = \frac{P}{2\dot{P}}. \tag{1.44}$$

It is possible that other processes are preventing a pulsar from spinning down as a perfect dipole. In order to understand how much a pulsar is deviating from the perfect magnetic dipole braking model it is useful to parametrize the pulsar's spin-down as

$$\dot{\Omega} = -K\Omega^n, \tag{1.45}$$

where n is known as the braking index. If we differentiate Eq. 1.45 with respect to time we find

$$\ddot{\Omega} = -nK\Omega^{n-1}\dot{\Omega} = n\dot{\Omega}^2\Omega^{-1}. \tag{1.46}$$

Rearranging the above we find

$$n = \frac{\ddot{\Omega}\Omega}{\dot{\Omega}^2}. \tag{1.47}$$

Thus, we wee that if we know the pulsar's frequency and first and second frequency derivative we can measure n. If the pulsar is spinning down like a perfect dipole then $n = 3$.

1.3.3 The Plasma-Filled Magnetosphere

In the previous section we assumed a pulsar is rotating in vacuo. Goldreich & Julian (1969) considered the case of an aligned rotator (i.e. magnetic axis aligned with rotation axis, see Fig. 1.2) and concluded that it is impossible for the magnetosphere of a pulsar to be empty. We can reconstruct this argument following Goldreich & Julian (1969), Meszaros (1992) and Shapiro & Teukolsky (1983). Let us begin by simply writing down Ohm's Law

$$\mathbf{E}' = \frac{\mathbf{J}}{\sigma} - \frac{\mathbf{v}}{c} \times \mathbf{B}', \tag{1.48}$$

where $\mathbf{J}$ is the current density, σ is the conductivity, $\mathbf{v}$ is the velocity of the charged particles and a prime indicates a parameter measured inside the star. Assuming the star to be a perfect conductor $\sigma \to \infty$, Equation 1.48 reduces to

$$\mathbf{E}' = -\frac{\mathbf{v}}{c} \times \mathbf{B}'. \tag{1.49}$$

This is also called the "force-free" equation, since, if the conductivity is infinite, then the Coulomb force $\mathbf{F} = e\mathbf{J}/\sigma$ vanishes (Griffiths, 1999). For a star with angular frequency Ω the above can be written as

$$\mathbf{E}' = -\frac{\mathbf{\Omega}\times\mathbf{r}}{c} \times \mathbf{B}', \tag{1.50}$$

where we have used $\mathbf{v} = \mathbf{\Omega}\times\mathbf{r}$. If we take Ω in the $\hat{\mathbf{z}}$ direction ($\mathbf{\Omega} = \Omega\hat{z}$), and if we assume that the magnetic field is dipolar (Eq. 1.30) everywhere, then at the surface we would measure an electric field

$$\mathbf{E}' = \frac{\Omega\mu}{cR^2}\left(\sin^2\theta\hat{\mathbf{r}} - \sin 2\theta\hat{\boldsymbol{\theta}}\right). \tag{1.51}$$

Now let us assume, as we did in the previous section, that the star is rotating in vacuo, in which case the charge density is $\rho = 0$. From Gauss's law it follows that the external electric field must satisfy

$$\frac{1}{4\pi}\boldsymbol{\nabla}\cdot\mathbf{E} = \rho = 0. \tag{1.52}$$

According to Meszaros (1992) and Shapiro & Teukolsky (1983) the θ-component of the external field must be continuous, in other words $E_\theta = E'_\theta$ at $r = R$. The solution to Eq. 1.52 which satisfies this condition is given by

$$\mathbf{E} = \frac{\Omega\mu R^2}{cr^4}\left(\left(3\cos^2\theta - 1\right)\hat{\mathbf{r}} + \sin 2\theta\hat{\boldsymbol{\theta}}\right). \tag{1.53}$$

The above is a quadrapole electric field. Now, from Eq. 1.49 we see that the internal electric field, $\mathbf{E}'$, is perpendicular to $\mathbf{B}$, thus $\mathbf{E}'\cdot\mathbf{B} = 0$. However from the equation for the exterior electric field (Eq. 1.53) we see that at the surface

$(r = R)$

$$\mathbf{E}\cdot\mathbf{B}|_{r=R} = -\frac{\Omega R}{c} B^2 \cos^3\theta. \tag{1.54}$$

Goldreich & Julian (1969) argued that the electric field at the surface cannot change discontinuously from $\mathbf{E}\cdot\mathbf{B} = 0$ to the above. This implies that almost parallel to the magnetic field the electric field at the surface is given by

$$\begin{aligned} E_{\|} &\approx \frac{\Omega R}{c} B \\ &\approx 6 \times 10^{10} \left(\frac{B}{10^{12}\ \mathrm{G}}\right) \left(\frac{P}{1\ \mathrm{s}}\right)^{-1}\ \mathrm{V\ cm^{-1}} \end{aligned} \tag{1.55}$$

(Meszaros, 1992). This translates to an electric force of $F_e \sim eR\Omega B/c$. If we compare this force to the gravitational force $F_g = GMm/R^2$, we find $F_e/F_g \sim 10^9$ (Shapiro & Teukolsky, 1983). Thus, even if we begin with the assumption that the magnetosphere of a pulsar is empty we see that this cannot be. The electric force, being so much stronger than the gravitational force, will fill the magnetosphere by "pulling" charged particles off the surface (Goldreich & Julian, 1969). This is a remarkable result because it states that even though pulsars have enormous gravitational fields (see § 1.2.1) it is in fact the electrodynamics which dictate the motion of charged particles.

The charged particles in the magnetosphere will corotate with the star. However, because the velocity of the charged particles cannot exceed the speed of light, there is a limit to how far the charged particles can corotate with the star. This limiting distance is given by

$$\begin{aligned} r_{lc} &= \frac{c}{\Omega} = \frac{cP}{2\pi} \\ &\approx 5 \times 10^9 \left(\frac{P}{1\ \mathrm{s}}\right)\ \mathrm{cm}. \end{aligned} \tag{1.56}$$

This is referred to as the light cylinder radius (Meszaros, 1992). Only magnetic field lines within the light cylinder can close , otherwise particles would be forced to move beyond the speed of light. Beyond the light cylinder field lines open, thus allowing charged particles to escape (Meszaros, 1992). Particles escaping

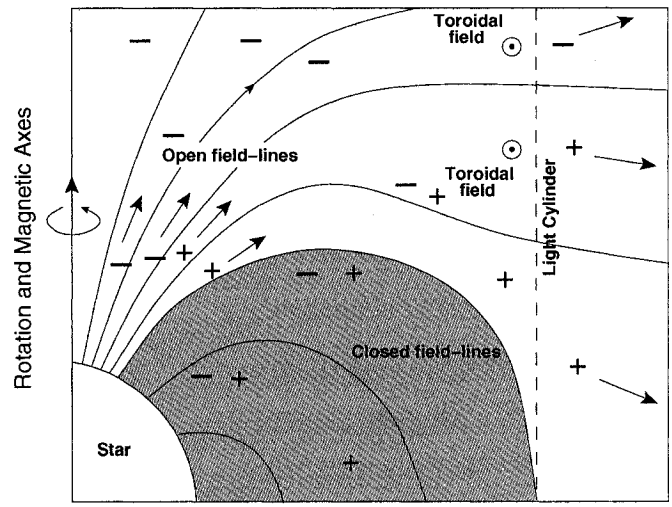

Figure 1.2: The geometry of a pulsar's magnetosphere. Notice that the rotation axis and the magnetic axis point in the same direction. Magnetic field lines can only close within the light cylinder (dashed line). Charged particles within closed magnetic field lines corotate with the star. Beyond the light cylinder magnetic fields become open and charged particles can escape. The escaping charged particles induce a toroidal component to the magnetic field (Meszaros, 1992). The figure is a reproduction of the one found in Manchester & Taylor (1977) and Meszaros (1992).

along open field lines means a current is flowing. These currents induce a toroidal component to the magnetic field (Meszaros, 1992). For the geometry of a pulsar's magnetosphere see Figure 1.2.

Following Goldreich & Julian (1969) and Meszaros (1992) we can estimate the charge density of the plasma-filled magnetosphere. The charge density is given by Gauss's Law

$$\rho = \frac{1}{4\pi}\boldsymbol{\nabla}\cdot\mathbf{E}. \tag{1.57}$$

We saw in the previous section that for a perfect conductor $\mathbf{E} = -(\boldsymbol{\Omega}\times\mathbf{r})\times\mathbf{B}/c$, in which case we obtain

$$\begin{aligned}\rho &= \frac{1}{4\pi c}\boldsymbol{\nabla}\cdot((\boldsymbol{\Omega}\times\mathbf{r})\times\mathbf{B}) \\ &= \frac{1}{4\pi c}\mathbf{B}\cdot(\boldsymbol{\nabla}\times(\boldsymbol{\Omega}\times\mathbf{r})) - \frac{1}{4\pi c}(\boldsymbol{\Omega}\times\mathbf{r})\cdot(\boldsymbol{\nabla}\times\mathbf{B}).\end{aligned} \tag{1.58}$$

Because we took Ω in the $\hat{\mathbf{z}}$ direction we can simplify the first term because $\boldsymbol{\nabla} \times (\boldsymbol{\Omega} \times \mathbf{r}) = 2\Omega\hat{z} = 2\boldsymbol{\Omega}$. So we are left with

$$\rho = -\frac{2}{4\pi c}\mathbf{B}\cdot\boldsymbol{\Omega} + \frac{1}{4\pi c}\mathbf{v}\cdot(\boldsymbol{\nabla} \times \mathbf{B}). \tag{1.59}$$

For a dipolar magnetic field $\boldsymbol{\nabla} \times \mathbf{B} = 0$, so in this case Equation 1.59 reduces to

$$\rho = -\frac{1}{2\pi c}\mathbf{B}\cdot\boldsymbol{\Omega}. \tag{1.60}$$

The above is referred to as the Goldreich-Julian charge density. We can also write the above as a number charge density $n = \rho/e$

$$\begin{aligned} n &= -\frac{1}{2\pi ce}\Omega B_z = -\frac{1}{ce}B_z P^{-1} \\ &\approx 7 \times 10^{10}\left(\frac{B_z}{10^{12}\text{ G}}\right)\left(\frac{P}{1\text{ s}}\right)^{-1}\text{ cm}^{-3}. \end{aligned} \tag{1.61}$$

1.3.4 Pulsar Spin-Down and Glitches

Measurements of pulsar spin periods (P) and spin-down rates ($\dot{P}$) are very important because they tell us a great deal about the pulsar. They allow us to infer the pulsar's spin-down luminosity, magnetic field strength, ages, light cylinder radius location, the density of the plasma in the magnetospheres, etc. Rotation powered pulsars, more specifically radio pulsars, can be highly stable rotators, where by stable we mean that the period is decreasing at a steady spin-down rate (Lyne & Smith, 1990). However, in many cases deviations are observed from a constant spin-down model. Sometimes pulsar exhibit quasi-random deviations which is simply called "timing noise" (Lyne & Smith, 1990). In other cases the pulsar shows discontinuous increases in its spin frequency (Lyne & Smith, 1990). Such deviations are referred to as "glitches" (Lyne & Smith, 1990). A glitch can also be observed in the spin-down rate of the pulsar. Many models have been proposed to explain glitches. Here we will describe a model proposed to explain large glitches in the spin periods of radio pulsars (Anderson & Itoh, 1975). Following Meszaros (1992), a neutron star consists of a $\sim$1 km crust with a superfluid inte-

rior. The angular momentum of this superfluid interior is quantized into vortices (Meszaros, 1992). The number density per area of these vortices is given by

$$n = \frac{2\Omega m_n}{\pi\hbar} \tag{1.62}$$

(Ruderman, 1976). Here m_n is the neutron mass and Ω is the angular spin frequency of the fluid. Now, magnetic dipole braking (see § 1.3.1) forces the crust of the star to slow down. The superfluid interior, in an attempt to make the star behave as a solid body, will try to decrease its angular frequency as well. From Eq. 1.62 we see that the only way to decrease the spin frequency of the superfluid component is for the number of vortices to decrease. Thus, the vortices will move towards the crust where they can annihilate. When at the crust it is possible for some of the vortices to get "pinned" to the nuclei or "deformities" in the crust (Anderson & Itoh, 1975; Alpar et al., 1989, 1993). The crust and the superfluid component are now rotating differentially, because the pinned vortices are not able to annihilate. Glitches are believed to occur when vortices suddenly unpin. When this happens, the vortices, now free to move, will annihilate in an effort to match the angular frequency of the crust. While the superfluid component spins down, all the excess angular momentum it had accrued while the vortices were pinned is transfered to the crust.

1.4 Accretion-Powered Pulsars

Although rotation is capable of powering X-ray emission from neutron stars, a significant fraction of X-ray pulsars are powered by accretion. These systems are in binaries and the compact object is accreting matter from its companion (however, see § 3 for alternative accretion scenarios). From optical observations of the companion and timing of the neutron star, one can sometimes decipher many aspects of the binary including the individual masses of the system (Lyne & Smith, 1990). The neutron star mass measurements span a very narrow range centered about $\sim 1.4 M_\odot$ (however, recently Nice et al., 2005, discovered a 2.1 solar mass pulsar, suggesting that the distribution of neutron star masses is much

broader than previously thought). The companion mass measurements span a much wider range and can be divided into two groups: the high-mass X-ray binaries and the low-mass X-ray binaries.

Currently there are ~130 known high-mass X-ray binaries (HMXBs) (Liu et al., 2000; note that this number also includes black hole systems). HMXBs can be further subdivided into those that have supergiant companions and those that have Be star companions (Liu et al., 2000). The rotation periods of the pulsars in HMXBs span the broad range 0.0338−10008 s. Unlike radio pulsars which always spin down, in these systems the accreted material can transfer angular momentum to the neutron and spin it up (Lyne & Smith, 1990). This torquing of the neutron star results in these systems not being as stable rotators as radio pulsars (Lyne & Smith, 1990). The neutron stars in HMXBs with Be companions usually accrete matter from a wind coming off the companion (Liu et al., 2000). In the supergiant HMXBs systems, the neutron star is either accreting from a wind or from a disk formed when the companion overflowed its Roche lobe (Liu et al., 2000). Roche lobe overflow simply involves the following. If we plot the equipotential gravitational surface of two orbiting gravitating objects, Figure 1.3, then we see this surface takes the form of a figure eight. We can look at this surface as two lobes connected together at the Lagrange point (L1). As the companion star evolves, if it expands to the point where it overflows its Roche lobe, then matter from the star will be funneled through the Lagrange point; but, because this matter has some angular momentum it will settle into a disk around the compact object (Frank et al., 1985).

Currently there are ~150 known low-mass X-ray binaries (LMXBs) (Liu et al., 2001; note that this number also includes black hole systems). The companions in these systems usually have masses $\lesssim 2.5\ M_{\odot}$, and are very faint which limits the amount of information one can extract from these systems (Lyne & Smith, 1990). Most of the X-rays observed from these systems is from a disk which was formed from the companion after it overflowed its Roche lobe. Material accreting onto the neutron star is sometimes collimated to specific spots. As more and more material accretes and the material gets compressed further and further it

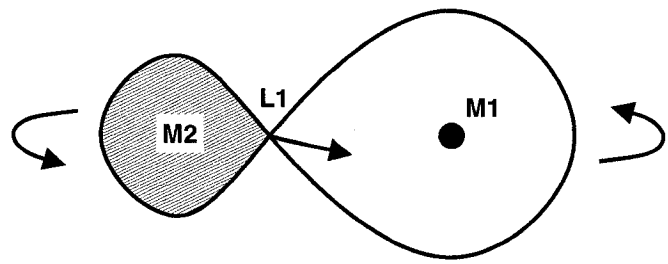

Figure 1.3: A binary system in which a neutron star ($M1$) is accreting matter from a companion ($M2$) that has filled its Roche lobe. Matter is funneled through the Lagrange point ($L1$).

eventually ignites (Muno, 2004). This releases a burst of energy which is referred to as a Type I X-ray burst (see Lewin et al., 1997, for a review). Such bursts have been observed from 70 LMXBs. Some of these bursts show millisecond oscillations (see Strohmayer et al., 1996). We now know that these oscillations correspond to the spin frequency of the star. It was only recently that pulsations from the neutron stars in LMXBs were unambiguously confirmed. The spin periods for LMXBs were expected to lie in the millisecond range because LMXBs are believed to be the progenitors of millisecond radio pulsars. An accreting millisecond pulsar was finally discovered in 1998 (Wijnands & van der Klis, 1998), and four others within the past four years.

1.4.1 Accretion

Accretion is a very efficient way of powering a neutron star (Longair, 1994). Consider a spherically symmetric distribution of gas accreting onto a neutron star. A parcel of gas with mass m accreting onto the neutron star, has gravitation potential energy

$$E = \frac{GMm}{R}, \tag{1.63}$$

where M and R are the mass and radius of the neutron star. This energy will be dissipated at a rate

$$L_{\rm acc} = \frac{GM\dot{m}}{R}, \tag{1.64}$$

where $\dot{m}$ is the mass accretion rate. Notice that the accretion luminosity, $L_{\rm acc}$, depends very strongly on how compact the star is, i.e. the ratio M/R; thus, for neutron stars accretion luminosities can be very high. For example, a neutron star accreting as little as 10^{15} g s^{-1} (or $\sim 1.6 \times 10^{-12}$ solar masses per year; this specific value for the accretion rate will become clear in Chapter 3) will reach a luminosity of

$$L = 1.8 \times 10^{35} \left(\frac{M}{1.4\ M_{\odot}}\right) \left(\frac{R}{10^6\ \text{cm}}\right)^{-1} \left(\frac{\dot{m}}{10^{15}\ \text{g s}^{-1}}\right)\ \text{erg s}^{-1}. \qquad (1.65)$$

Compare this value with the spin-down luminosity (Eq. 1.40) found in § 1.3.2. There is a limit, however, on how high the accretion luminosity can get, which brings us to our next section.

1.4.2 The Eddington Luminosity

The radiation pressure of a neutron star must be less than the gravitational pressure of the accreted material, otherwise the radiative forces will blow the material away and accretion will not be able to occur; this is the so-called Eddington luminosity. We can calculate this luminosity following Longair (1994). If photons are radiated from the surface and there is some material in the magnetosphere made up of electrons and protons, then the photons will Thomson scatter the electrons. Note that the cross section for scattering protons is much smaller, but the protons are still affected by the radiation force because of the electrostatic forces between them and the electrons (Longair, 1994). The energy flux (or energy per unit area per unit time) of the photons is given by

$$f = \frac{1}{\sigma_T} \frac{dE}{dt}, \qquad (1.66)$$

where σ_T is the Thomson cross section and E is the energy lost by the photons in each collision. The energy of a photon is given by $E = pc$, where p is its

momentum. Hence the above can be written as

$$f = \frac{c}{\sigma_T}\frac{dp}{dt}. \tag{1.67}$$

The radiation force is simply $F_{\rm rad} = dp/dt$, inserting this in the above and rearranging we find

$$F_{\rm rad} = \frac{f\sigma_T}{c} = \frac{L\sigma_T}{4\pi r^2 c}. \tag{1.68}$$

Here we have used the relationship between flux and luminosity $L = 4\pi r^2 f$. The radiation force must balance the gravitational force

$$F_{\rm grav} = \frac{GMm_p}{r^2}. \tag{1.69}$$

Notice that both forces scale as $1/r^2$. Equating the two forces and rearranging we obtain the Eddington luminosity

$$\begin{aligned} L_{\rm Edd} &= \frac{4\pi cGm_p}{\sigma_T}M \\ &= 1.5 \times 10^{38}\left(\frac{M}{M_\odot}\right) \text{ ergs s}^{-1}. \end{aligned} \tag{1.70}$$

The Eddington luminosity also sets a limit on the rate at which the neutron star can accrete matter, i.e. $\dot{m}$. Setting the accretion luminosity (Eq. 1.64) equal to the Eddington luminosity (Eq. 1.70) we find that the maximum accretion rate is

$$\begin{aligned} \dot{m}_{\rm Edd} &= \frac{4\pi cm_p R}{\sigma_T} \\ &= 1.5 \times 10^{-8}\left(\frac{R}{10^6 \text{ cm}}\right) M_\odot \text{ yr}^{-1}. \end{aligned} \tag{1.71}$$

From the above we see that a neutron star cannot accrete more than $\sim 10^{-8}$ solar masses per year.

1.4.3 Accretion Disks

So far we have considered spherical accretion; however, in the case of a binary whose companion has filled its Roche lobe, the neutron star will accrete from a disk. The disk is formed from matter that is funneled through the Lagrange point (see Fig. 1.3). The matter that emerges from the Lagrange point has some angular momentum; due to conservation angular momentum the material will settle into a disk. Frank et al. (1985) make the analogy that this is like a spray hose spraying gas onto the compact star. Now, viscous forces will torque the material and allow it to accrete onto the star. The nature of the disk viscosity is not well understood; however, as pointed by Frank et al. (1985) we can still make a reasonable estimate of the disk luminosity regardless. Following Frank et al. (1985); Longair (1994); Shapiro & Teukolsky (1983) we can calculate the luminosity of such an accretion disk. If the viscous force per area is $f = F/A$ then the torque at radius r is given by

$$G = fAr, \tag{1.72}$$

where we have used $G = |\mathbf{F} \times \mathbf{r}|$. Now matter moving at a distance r in the disk has angular momentum

$$J = mv_\phi r = m\Omega r^2, \tag{1.73}$$

where $v_\phi = \Omega r$ is the azimuthal velocity of the matter and Ω is the angular frequency. As matter is accreted angular momentum is removed at a rate

$$\dot{J} = \dot{m}\Omega r^2. \tag{1.74}$$

We can make the assumption that the matter in the disk follows Keplerian orbits, in which case the angular frequency equals the Keplerian angular frequency ($\Omega = \Omega_K$), where

$$\Omega_K = \sqrt{\frac{GM}{r^3}}. \tag{1.75}$$

For Keplerian orbits the rate of change of angular momentum at a distance r is

$$\dot{J}(r) = \dot{m}\sqrt{GMr}. \tag{1.76}$$

The difference in the rate of change of angular momentum from the disk's inner boundary, r_b to a distance r is

$$\Delta\dot{J} = \dot{J}(r) - \dot{J}(r_b). \tag{1.77}$$

Now, conservation of angular momentum dictates that the torque on the disk must be equal to the difference in the rate change of angular momentum ($G = \Delta\dot{J}$). So, writing $r_b = R_* + b$, where R_* is the radius of the star and b is the distance from the star's surface to the disk's inner boundary, after equating Eq. 1.72 to Eq. 1.77, we obtain

$$\begin{aligned} fAr &= \dot{m}\sqrt{GMr} - \dot{m}\sqrt{GMR_* + b} \\ &= \dot{m}\sqrt{GM}\left(r^{1/2} - R_*^{1/2}\left(1 + b/R_*\right)^{1/2}\right). \end{aligned} \tag{1.78}$$

We can make the assumption that $b \ll R_*$, so the above reduces to

$$fAr \approx \dot{m}\sqrt{GM}\left(r^{1/2} - R_*^{1/2}\right). \tag{1.79}$$

Now, the viscous force per area, f, is given by

$$f = \nu\rho r\left(\frac{d\Omega}{dr}\right), \tag{1.80}$$

where ν is the coefficient of kinematic viscosity and ρ is the density of the accreted material (see Frank et al., 1985; Shapiro & Teukolsky, 1983, for a derivation). For a Keplerian disk Ω is given by Eq. 1.75, hence

$$\frac{d\Omega}{dr} = -\frac{3}{2}\sqrt{\frac{GM}{r^5}}. \tag{1.81}$$

Combining Equation 1.79, 1.80 and 1.81 we obtain

$$\nu\rho A = \frac{2}{3}\dot{m}r\left(1-\left(\frac{R_*}{r}\right)^{1/2}\right). \tag{1.82}$$

We can write the above in terms of the surface density. If the disk has a thickness of H, then a ring of the disk at radius r has an area of $A = 2\pi rH$. The surface density of the disk is $\Sigma = \int \rho dz \approx \rho H$, thus Eq. 1.82 can be written as

$$\nu\Sigma = -\frac{\dot{m}}{3\pi}\left(1-\left(\frac{R_*}{r}\right)^{1/2}\right). \tag{1.83}$$

The rate at which energy is dissipated due to viscosity is given by

$$\frac{dE}{dt} = -\nu\Sigma r^2\left(\frac{d\Omega}{dr}\right)^2 \tag{1.84}$$

(see Frank et al., 1985; Shapiro & Teukolsky, 1983, for a derivation). Replacing Equation 1.83 for $\nu\Sigma$ and Equation 1.81 for $d\Omega/dr$ in the above we find

$$\frac{dE}{dt} = \frac{3G\dot{m}M}{4\pi r^3}\left(1-\left(\frac{R_*}{r}\right)^{1/2}\right). \tag{1.85}$$

Notice that the dissipation rate is actually independent of the kinematic viscosity. The total disk luminosity can be obtained by simply integrating the above over the disk area,

$$\begin{aligned} L &= \int_{R_*}^{\infty} -\frac{dE}{dt}2\pi r dr \\ &= \frac{G\dot{m}M}{2R_*} \\ &= 9.2\times10^{34}\left(\frac{M}{1.4\ M_\odot}\right)\left(\frac{R}{10^6\ \mathrm{cm}}\right)^{-1}\left(\frac{\dot{m}}{10^{15}\ \mathrm{g\ s^{-1}}}\right)\ \mathrm{erg\ s^{-1}}. \end{aligned} \tag{1.86}$$

Notice that the disk luminosity only differs from the spherical accretion luminosity (Eq. 1.64) by a factor of two; thus, an accretion disk is also an efficient source of

radiation.

1.4.4 Accretion and Magnetic Fields

As we saw in the previous chapters, neutron stars carry strong magnetic fields. What effect does the magnetic field of a neutron star have on the accretion flow? The magnetic field can in fact prevent material from accreting directly onto the star, and in turn force it to move along the field lines (Carroll & Ostlie, 1996). For a dipolar magnetic field, the material will be forced to accrete at the magnetic poles for instance. We can estimate the characteristic distance where the magnetic field interrupts the accretion flow; this is the so-called Alfvén radius. Following Frank et al. (1985) and Carroll & Ostlie (1996) we can estimate the Alfvén radius, r_A, by balancing the ram pressure by the magnetic pressure

$$\begin{aligned} \rho v^2 &= \frac{B^2}{8\pi} \\ &= B_*^2 \left(\frac{R_*}{r_A}\right)^3. \end{aligned} \tag{1.87}$$

Here ρ is the density of the gas being accreted, v is its velocity, and we have assumed that the magnetic field has a dipolar geometry, i.e. $B = B_* (R_*/r)^3$. We can simplify Expression 1.87 by solving for the density and the velocity of the accreted material. For simplicity we will assume that the neutron star is accreting from a spherically symmetric distribution of gas, in which case the velocity of the accreted material is given approximately by its free-fall velocity from r_A:

$$v = \sqrt{\frac{2GM}{r_A}}. \tag{1.88}$$

Now, the total mass of the gas being accreted is

$$m = \int \rho dV, \tag{1.89}$$

thus the mass accretion rate is given by

$$\dot{m} = \int \frac{\partial \rho}{\partial t} dV. \tag{1.90}$$

Because of mass conservation the accreted material must satisfy the following continuity equation:

$$\frac{\partial \rho}{\partial t} + \boldsymbol{\nabla} \cdot (\rho \mathbf{v}) = 0 \tag{1.91}$$

(see Frank et al., 1985; Shapiro & Teukolsky, 1983, for a derivation). For a spherically symmetric gas the above reduces to

$$\boldsymbol{\nabla} \cdot (\rho \mathbf{v}) = \frac{1}{r^2} \frac{d}{dr} \left(r^2 \rho v_r \right). \tag{1.92}$$

Inserting the above into Eq. 1.90 and integrating we find

$$\dot{m} = 4\pi r^2 \rho v_r. \tag{1.93}$$

Here again we make the assumption that the velocity is given by the free-fall velocity, thus inserting Equation 1.88 onto the above and rearranging, we find that the density at the Alfvén radius is given by

$$\rho = \frac{\dot{m}}{4\pi \sqrt{G M r_A^3}}. \tag{1.94}$$

Combining Equations 1.87, 1.88 and 1.94 we find after a little algebra that the Alfvén radius is given by

$$\begin{aligned} r_A &= \left(\frac{B_*^4 R_*^{12}}{8 G M \dot{m}^2} \right)^{1/7} \qquad (1.95) \\ &\approx 9.45 \times 10^8 \left(\frac{B_*}{10^{12}\ \mathrm{G}} \right)^{4/7} \left(\frac{M}{1.4\ M_\odot} \right)^{-1/7} \left(\frac{R_*}{10^6\ \mathrm{cm}} \right)^{12/7} \left(\frac{\dot{m}}{10^{15}\ \mathrm{g\ s^{-1}}} \right)^{-2/7} \mathrm{cm}. \end{aligned}$$

1.4.5 Spin down Rate and Luminosity

How an accretion disk interacts with the pulsar's magnetosphere really determines the spin evolution of the star. For a neutron star in a binary system accreting

from a thin disk, the accreted material, assuming it travels on Keplerian orbits, transfers angular momentum to the star at a rate $\dot{J} = \dot{m}\Omega_K r^2$, where Ω_K is the Keplerian frequency. Hence in these systems the star is usually spun-up. At the Alfvén radius the accreted matter transfers angular momentum at a rate

$$\dot{J} = \dot{m}\sqrt{GMr_A}, \tag{1.96}$$

thus the star experiences a torque

$$I\dot{\Omega}_* = \dot{m}\sqrt{GMr_A}, \tag{1.97}$$

where I is the moment of inertia of the star, and $\dot{\Omega}_*$ is the rate of change of the star's spin frequency, i.e. $\dot{\Omega}_* = d\Omega_*/dt$. We can replace $\dot{m}$ in the above expression by the disk luminosity (Eq. 1.86) to obtain

$$I\dot{\Omega}_* = L\sqrt{\frac{4Rr_A}{GM}}. \tag{1.98}$$

Writing the Alfvén radius in terms of the disk luminosity,

$$r_A = \left(\frac{GMB^4R^{10}}{32L^2}\right)^{1/7}, \tag{1.99}$$

and inserting it into Equation 1.98 we find

$$I\dot{\Omega}_* = L^{6/7}\left(\frac{16\sqrt{2}B^2R^5}{G^3M^3}\right)^{1/7}. \tag{1.100}$$

So we see in a system in a binary accreting from a accretion disk the spin-up rate is correlated to the luminosity, i.e. $L \propto \dot{\Omega}_*^{7/6}$. This prediction does not hold exactly true for accreting binary systems, but a correlation is generally seen between the luminosity and the torque (Bildsten et al., 1997).

1.5 Anomalous X-ray Pulsars

1.5.1 Observational Properties

Anomalous X-ray Pulsars (AXPs) are labeled as such because they are neither rotation-powered nor accretion-powered X-ray pulsars. There are currently seven confirmed AXPs and one candidate awaiting confirmation.

1E 2259+586 was the first AXP ever discovered (Fahlman & Gregory, 1981). This 7-s pulsar was discovered in the center of the supernova remnant CTB 109 using the *Einstein* X-ray Observatory. Optical/IR observations of the source were able to rule out the presence of a massive companion and this source was initially categorized as a low mass X-ray binary (LMXB). Fahlman & Gregory (1981) realized that there was something unusual about this source, because if it were in fact an accreting system, it would be the first such system inside a supernova remnant.

A few years later Seward et al. (1986) discovered ~6.44 s pulsations from the X-ray source 1E 1048.1–5937. Although reported in 1986, this source was discovered in archival *Einstein* X-ray images of the bright nebula η Carinae taken in 1979. Just as for 1E 2259+586, optical/IR limits ruled out a massive companion for this source. In 1994, using data from the *European X-ray Observatory Satellite* (*EXOSAT*) archive, Israel et al. (1994) discovered 8.7-s pulsations from the puzzling X-ray source 4U 0142+61. The absence of orbital delays in times of arrival suggested that this too was an unusual X-ray source.

The lack of evidence of massive companions and the absence of orbital modulations suggested that if these sources did have companions they would have to be extremely low mass. This led Mereghetti & Stella (1995) to suggest that these three sources (along with two other sources, 4U 1627−67 and RX J1838.4−0301, now recognized to be very different) comprised a new class of LMXB, one in which the neutron star had a very low mass companion. Because of the clear differences between the sources discussed and canonical X-ray pulsars, van Paradijs et al. (1995) coined the term "Anomalous X-ray Pulsar" (AXP) to describe the class.

In 1996 Sugizaki et al. (1997) using the *Advanced Satellite for Cosmology and*

Astrophysics (*ASCA*) discovered 11-s pulsations from the X-ray source 1RXS J170849.0–400910 (hereafter 1RXS J1708–4009) in the Scorpius constellation. This pulsar shared all the properties of the other known AXPs at the time, and thus was added to the class. The same year Vasisht & Gotthelf (1997), using *ASCA*, discovered a similar pulsar (1E 1841–045) with an ~11.8 s spin period at the center of the supernova remnant Kes 73.

A candidate AXP, AX J1845–0258, was serendipitously discovered in *ASCA* data by Gotthelf & Vasisht (1998). Gaensler et al. (1999) determined that the pulsar was at the center of the young supernova remnant G29.6+0.1. This source had a long AXP-like spin period, 7 s, and a soft AXP-like spectrum. Unfortunately, this source faded away after its discovery, making it impossible to determine whether it was undergoing rapid spin down like all other AXPs; thus, this source is pending confirmation before being considered an AXP.

In 2003 Ibrahim et al. (2004) discovered a 5.54 s X-ray pulsar, XTE J1810–197, in the wide field-of-view of *Rossi X-ray Timing Explorer* (*RXTE*) while observing a different source. Its soft spectrum, slow-spin period, rapid spin-down and lack of a binary companion established it as the sixth confirmed member of the class. This source was unusual in that it remained faint for many years and then experienced a two order magnitude increase in flux, which subsequently decayed. This source is colloquially referred to as the transient AXP. The flux behavior exhibited by this source suggests that perhaps the candidate AX J1845–0258 was observed while it underwent an XTE J1810–197-like flux enhancement.

In 2002 Lamb et al. (2002) discovered a possible Anomalous X-ray pulsar in the Small Magellanic Cloud. This source, designated CXOU J0100–7211, had similar spectral properties to those of the other known AXPs. It also had a comparable spin period. In the discovery paper the authors quoted a 5 s pulsation which was aliased[2] at 8 s, however at the time the authors did not have enough information to determine that in fact 5 s was the alias of the true 8 s period. McGarry et al. (2005) measured rapid spin-down from the source, thus establishing CXOU J0100–7211 as a *bona fide* AXP.

[2]see § 5.3.4 for a discussion on the Fourier transform and aliasing.

Table 1.1: Spatial parameters for AXPs.

Source	RA	DEC	Distance† (kpc)	SNR Association	Ref.
4U 0142+61	$01^h\ 46^m\ 22^s.44$	$+61°45'03''.3$	> 2.5	···	1,2
1E 1048.1–5937	$10^h\ 50^m\ 07^s.14$	$-59°53'21''.4$	2.7	···	3,4
1RXS J1708–4009	$17^h\ 08^m\ 46^s.87$	$-40°08'52''.4$	∼8	···	5,6
1E 1841–045	$18^h\ 41^m\ 19^s.34$	$-04°56'11''.2$	∼6.7	Kes 73	7,8,9
1E 2259+586	$23^h\ 01^m\ 08^s.29$	$+58°52'44''.4$	3.0	CTB 109	10,11,12
CXOU J0100–7211	$01^h\ 00^m\ 43^s.14$	$-72°11'33''.8$	57	···	13
XTE J1810–197	$18^h\ 09^m\ 51^s.08$	$-19°43'51''.7$	∼5	···	14,15
AX J1845–0258*	$18^h\ 44^m\ 53^s.$	$-02°56'40''.$	< 20	G29.6+0.1	16,17

(∗) not confirmed; (†) see Özel et al. (2001) for a discussion on distance estimates for the confirmed AXPs; References: (1) Juett et al. (2002); (2) Hulleman et al. (2004); (3) Wang & Chakrabarty (2002); (4) Gaensler et al. (2005); (5) Israel et al. (2003); (6) Özel et al. (2001); (7) Wachter et al. (2004); (8) Sigurdsson & Hernquist (1992); (9) Vasisht & Gotthelf (1997); (10) Hulleman et al. (2001a); (11) Kothes et al. (2002); (12) Fahlman & Gregory (1981); (13) Lamb et al. (2002); (14) Israel et al. (2004); (15) Gotthelf et al. (2004); (16) Vasisht et al. (2000); (17) Gaensler et al. (1999).

Except for CXOU J0100–7211, which is in the Small Magellanic Cloud, all the AXPs are located in the Galactic plane. The equatorial coordinates of AXPs are listed in Table 1.1. AXP distance estimates are also listed in Table 1.1, however, see Özel et al. (2001) for a discussion on AXP distance estimates.

Spin Evolution

AXPs have long spin periods in the very narrow range of 5–12 s. AXPs are all observed to be undergoing rapid spin-down. Their spin periods (P) and their spin-down rates ($\dot{P}$) are listed in Table 1.2 and plotted alongside those of other pulsars in Fig. 1.1 (notice how the AXPs cluster together in the P-$\dot{P}$ diagram). Some AXPs are very rotationally stable, while other AXPs show severe deviations from a constant spin-down model. Two AXPs have been observed to glitch. The first AXP glitch was detected in 1RXS J1708–4009 by Kaspi et al. (2000). The glitch corresponded to an increase frequency of $|\Delta\nu/\nu| \sim 6\times10^{-7}$ and an increase in the spin-down rate of $|\Delta\dot{\nu}/\dot{\nu}| \sim 1 \times 10^{-2}$ (Kaspi et al., 2000). This pulsar

Table 1.2: Spin parameters for AXPs.

Source	P (s)	$\dot{P}$ (10^{-11} s s^{-1})	B_{dp} (10^{14} G)	$\dot{E}_s$ (10^{34} erg s^{-1})	τ_c (kyr)	Ref.
4U 0142+61	8.688	0.196	1.3	0.12	70	1
1E 1048.1–5937	6.452	~2.70	~4.2	~3.9	~3.8	2,3
1RXS J1708–4009	10.999	1.945	4.7	0.57	9.0	1
1E 1841–045	11.775	4.155	7.1	0.99	4.5	4
1E 2259+586	6.979	0.0484	0.59	0.056	230	1
CXOU J0100–7211	8.020	1.88	3.9	1.4	6.8	5
XTE J1810–197	5.539	0.51	1.7	1.2	17	6
AX J1845–0258*	6.971	...	...	...	...	7

(*) not confirmed; References: (1) Gavriil & Kaspi (2002); (2) Kaspi et al. (2001); (3) Gavriil & Kaspi (2004); (4) Gotthelf et al. (2002); (5) McGarry et al. (2005); (6) Halpern & Gotthelf (2005); (7) Torii et al. (1998).

glitched again in 2001 with a similar change in frequency, $|\Delta\nu/\nu| \sim 1 \times 10^{-7}$, but a much larger change in the spin-down rate, $|\Delta\dot{\nu}/\dot{\nu}| \sim 6 \times 10^{-5}$ (Kaspi & Gavriil, 2003; Dall'Osso et al., 2003). The only other AXP ever observed to glitch was 1E 2259+586, however this glitch was related to a major outburst. The glitch and the outburst from 1E 2259+586 are discussed in detail in Chapter 7. Over five years of monitoring AXP 4U 0142+61 with *RXTE* has shown that a constant spin-down model can accurately account for its spin-evolution. However, Morii et al. (2005) analyzed *ASCA* data of 4U 0142+61 and they claim that only a glitch can account for the frequency variations between their *ASCA* data and the overlapping *RXTE* data. We cannot rule out glitches from the other AXPs because we are insensitive to glitches if both the frequency and spacing of the observations is not optimal. In one case, 1E 1048.1–5937, the pulsar is so noisy that it is not clear how to decipher deviations due to noise from intrinsic variability in the pulsar's spin evolution.

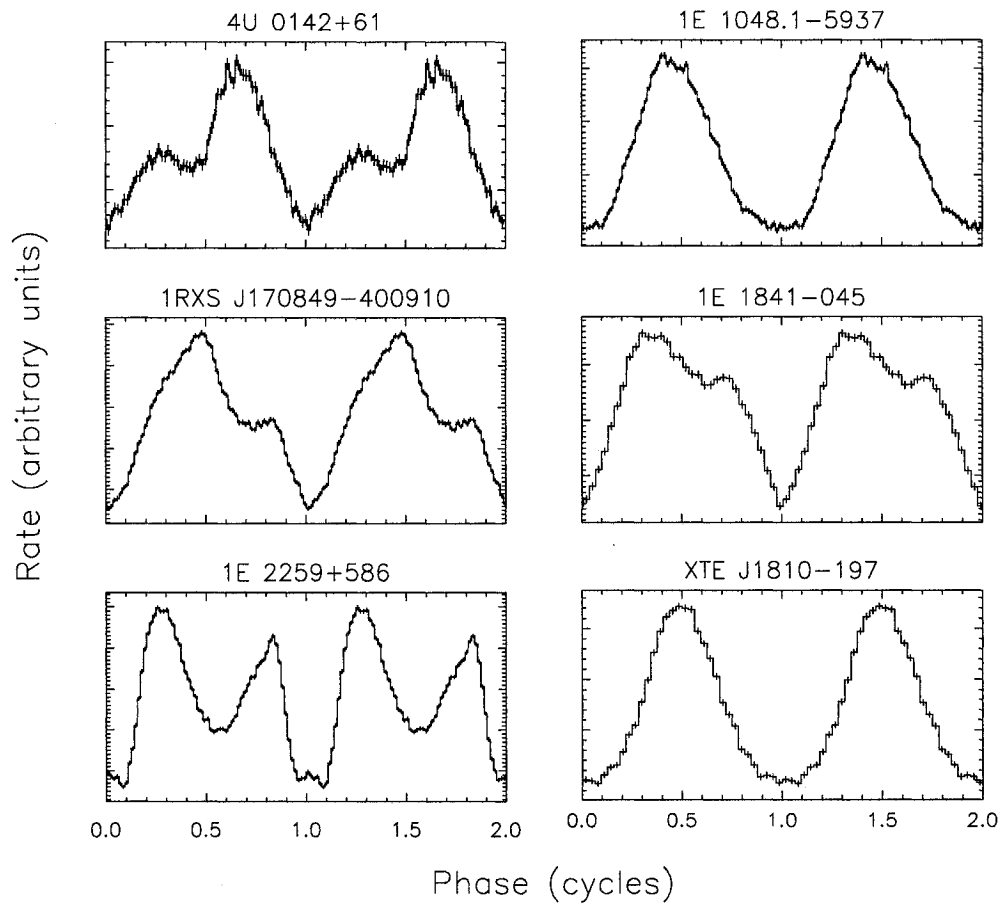

Figure 1.4: AXP pulsed profiles in the 2–10 keV band. Figures prepared by myself for Woods & Thompson (2004).

Pulse Profiles

AXP pulse profiles are broad, with large ($\gtrsim$80%) duty cycles[3], and generally show significant harmonic content. See Figure 1.4 for the long-term phase averaged profiles of all the confirmed AXPs. The profiles show energy dependences that vary from source to source (Gavriil & Kaspi, 2002). A possible trend of greater energy dependence for profiles with higher harmonic content was identified by Gavriil & Kaspi (2002), who also showed that in general, AXP pulse profiles are very stable.

[3]The duty cycle is the fraction of a rotational cycle in which pulsed emission is observed.

Table 1.3: Spectral parameters* for AXPs.

Source	N_H (10^{22} cm^{-2})	Γ	kT (keV)	L_x (10^{35} erg s^{-1})	Ref.
4U 0142+61	0.91	3.62	0.395	>0.53	1
1E 1048.1–5937	0.96	2.9	0.63	0.41	2
1RXS J1708–4009	1.36	2.40	0.44	~5.3	3
1E 1841–045	2.54	2.0	0.44	~1.3	4
1E 2259+586	1.098	4.10	0.411	0.18	5
CXOU J0100–7211	0.91	2.0	0.38	0.35	6
XTE J1810–197	0.96	3.8	0.67	0.51	7
AX J1845–0258*	9.0	4.6	...	<0.77	8

(⋆) The spectral parameters are derived from fits to two-component models (power law + blackbody) whenever possible; (∗) not confirmed; References: (1) Göhler et al. (2005); (2) Mereghetti et al. (2004); (3) Rea et al. (2003); (4) Morii et al. (2003); (5) Woods et al. (2004); (6) McGarry et al. (2005); (7) Rea et al. (2004); (8) Torii et al. (1998).

Spectra

A simple blackbody or power-law model cannot describe AXP spectra. A two component model consisting of both a blackbody with temperature kT ~0.4 – 0.7 keV, and a power-law ($N \sim E^{-\Gamma}$) with photon index Γ ~2 – 4 seems to fit their spectra well (however, see Halpern & Gotthelf, 2005 for a discussion of the deficiencies of this two component model, and see Lyutikov & Gavriil, 2005 for a single component model with the potential to fit AXP spectra). Rotation-powered pulsars also show thermal and non-thermal components, but their non-thermal components are usually harder ($\Gamma \lesssim 2$; Kaspi et al., 2004; Possenti et al., 2002). AXPs were for many years believed to be soft X-ray sources, however recently high energy emission has been discovered from AXPs. The *IBIS/ISGRI* instrument aboard the *Integral* satellite detected hard X-ray/soft γ-ray emission from three AXPs: 4U 0142+61 (den Hartog et al., 2004), 1E 1841–045 (Bassani et al., 2004) and 1RXS J1708–4009 (Revnivtsev et al., 2004). Kuiper et al. (2004) have also detected 1E 1841–045 by averaging together phase aligned pulsed profiles from archival observations from the High Energy X-ray Timing Experiment (*HEXTE*) instrument aboard *RXTE*.

Flux Evolution

Historically, two AXPs have been reported to be highly flux-variable. Oosterbroek et al. (1998) collected all published flux measurements for AXP 1E 1048.1–5937 and concluded that its total flux varies by as much as a factor of 10 between observations spaced by typically 1–2 yr over ~20 yr. Those data were from a diverse set of instruments, including imaging and non-imaging telescopes. Similarly, flux variability by a factor of >4 was reported for AXP 1E 2259+586 by Baykal & Swank (1996), using data also from a variety of instruments.

However, long-term *RXTE* monitoring of the pulsed flux of 1E 1048.1–5937 by Kaspi et al. (2001), 1E 1841–045 by Gotthelf et al. (2002), and of 1E 2259+586, 4U 0142+61 and 1RXS J1708–4009 by Gavriil & Kaspi (2002) using a single instrument and set of analysis software showed no evidence to support such large variability[4]. Also, Tiengo et al. (2002), following a short *XMM-Newton* observation of 1E 1048.1–5937, compared the observed flux with those measured by two other imaging instruments, *ASCA* and *BeppoSAX*. They found that, in the three observations, the total flux was steady to within ~30–50%. They argued that the non-imaging detections included in the Oosterbroek et al. (1998) analysis may have been contaminated by other sources in the instruments' fields-of view; in particular the bright and variable X-ray source Eta Carina lies only 38′ away.

Transient AXPs?

The issue of AXP flux variability is particularly important in light of the recent discovery of a "transient" AXP. XTE J1810–197 is a 5.5-s X-ray pulsar which was discovered when it suddenly brightened by two orders of magnitude (Ibrahim et al., 2004). This discovery established that if AXPs can show such large flux enhancements then there might be many other sources out there which have not been identified as AXPs because they are currently too faint (Ibrahim et al., 2004). Examples of such objects include the 7-s X-ray pulsar AX J1845–0258 which was once bright but then never seen again (Vasisht et al., 2000). Dim

[4]Total flux measurements with *RXTE* were difficult given the large field-of-view of the PCA and the low count rates for the AXPs relative to the background.

isolated neutrons stars could be AXPs which are in a dormant state, i.e. the state XTE J1810–197 was in before it was discovered. Furthermore, empty supernova remnants might not be empty at all, but could appear as such because they contain a dormant AXP. The discovery of a transient AXPs suggests that we really need to rethink our estimates for the number of AXPs in the Galaxy; in fact, it is possible that AXPs could account for a significant percentage of the neutron star population.

1.5.2 The AXP Mystery

Traditionally only two mechanisms were proposed to power pulsars: rotation (§ 1.3) and accretion (§ 1.4). AXPs cannot be rotation-powered pulsars because their observed X-ray luminosities, L_X, are much greater than their spin-down luminosities, $\dot{E}$ (calculated via Eq. 1.40). Could AXPs be accreting X-ray binaries? As already discussed this is improbable because there is no evidence for a companion from which to accrete material. They could all be accreting from very low mass companions in an orbital configuration that makes it difficult to detect the companion. However, the probability of this being the case for all of them is low (Kaspi et al., 2001). Furthermore, if they do have low mass companions then AXPs should be older systems, in order to allow their companions enough time to overflow their Roche lobes, and initiate accretion. But some AXPs are still in supernova remnants (SNR; see Table 1.2 for their SNR associations) which suggests they are young (Brandt & Podsiadlowski, 1995). As already discussed by Kaspi et al. (2001) and Gavriil & Kaspi (2002) the absence of binary companions is not the only evidence against binary accretion. The spin evolution of some AXPs is much more stable than the majority of accreting systems (Gavriil & Kaspi, 2002; Gotthelf et al., 2002). However, one AXP in particular (1E 1048.1–5937) is a very noisy rotator (Kaspi et al., 2001; Gavriil & Kaspi, 2004). No AXP has every been observed to spin-up (i.e. have a positive period derivative for a long-period of time, not to be confused with a glitch), however accreting systems can and do so frequently and for long periods of time (see Bildsten et al., 1997).

1.5.3 AXPs Models

It seems that the most plausible model to explain AXP emission is the so-called "magnetar" model (Thompson & Duncan, 1995). In this model AXPs are powered neither by rotation nor accretion but by the decay of their magnetic fields (Thompson & Duncan, 1996). This model requires that AXPs have magnetic fields many orders of magnitudes greater than conventional pulsars. Even though AXPs are not rotation-powered pulsars we can still use Eq. 1.39 to infer their magnetic fields if their spin-down is primarily due to magnetic dipole radiation. Performing the calculation we find that the AXPs have enormous surface magnetic dipolar fields, in the range $B \sim 10^{14} - 10^{15}$ G. It was also argued that AXPs are magnetars because they are very similar to another class of sources – the Soft Gamma Repeaters (SGRs). Besides rapid spin-down, SGRs emit short energetic bursts which can only be explained within the context of the magnetar model The SGRs are reviewed in the following section, and the magnetar model, including why we believe SGRs are magnetars, is reviewed in greater detail in Chapter 2. The magnetar model's inability to explain the narrow range of spin-periods of AXPs and SGRs, as well as the lack of evidence of bursts from AXPs (however see Chapters 6, 7 and 10) have led to competing models involving unconventional accretion scenarios. A competing model to the magnetar model, the "fall-back" disk model, is discussed in Chapter 3.

1.6 Soft Gamma Repeaters

The following review of SGRs follows the one given by Woods & Thompson (2004). Soft Gamma Repeaters (SGRs) were discovered by their emission of bright ($\sim 10^{41}$ ergs s^{-1}) brief ($\sim$0.1 s) bursts of soft gamma-rays (hard X-rays). The first SGR burst was discovered from the source SGR 1806−20 on 1979 January 7 (Mazets & Golenetskii, 1981). Similar bursts were discovered, however what was causing them was not clear and they were just classified as classical gamma-ray bursts (GRBs). GRBs are cosmological events that are distributed isotropically in the sky. At the time of the discovery of SGR bursts, GRBs were

also a mystery. It is now somewhat accepted that GRBs are due to the collapse of an extremely massive star in a very energetic supernova explosion known as a hypernova (Price et al., 2002; Hjorth et al., 2003). This model for GRBs is known as the "collapsar" model (Woosley, 1993; MacFadyen & Woosley, 1999). It was not very long before SGR bursts began to distinguish themselves from GRBs. Their names alone indicate the main differences: SGR bursts were observed to recur, while no GRB was ever observed to repeat. SGR bursts were also spectrally different, showing predominantly soft gamma-rays, while GRBs had excess high energy emission.

Light was shed (pun intended) on the SGR mystery on March 5, 1979, when SGR 0526−66 emitted the most energetic burst ever detected from an SGR (Mazets et al., 1979). The burst reached a peak luminosity of $\sim 10^{45}$ erg s^{-1} followed by a 3-minute long tail. Furthermore, the burst tail exhibited an ~8 s modulation. The apparent association of SGR 0526−66 with a supernova remnant suggested youth (for supernova remnant associations, positions and distance estimates for all SGRs see Table 1.4). The implied youth along with the long period suggested that the flare was associated with a magnetized neutron star. In this case the peak luminosity of $\sim 10^{45}$ ergs s^{-1} was many orders of magnitude higher than the Eddington luminosity of a neutron star (the Eddington luminosity is defined in § 1.4.2, Eq. 1.70). A second giant flare was observed on August 27 1998, but this time from SGR 1900+14 (Hurley et al., 1999). Very recently a third giant flare was observed from SGR 1806−20 on 27 December 2004. SGR giant flares are so energetic that they can disturb the ionosphere of the Earth! Figure 1.5 depicts how a disturbance to the lower ionosphere was coincident with the August 27 1998 giant flare from SGR 1900+14.

Initial models proposed to understand SGRs as compact objects were unable to accommodate both the giant flares and the more common repeat bursts. The models were also tightly constrained by the lack of persistent emission at other wavelengths. In subsequent years this changed with the detection of persistent X-ray emission from all three SGRs known at the time (Murakami et al., 1994; Rothschild et al., 1994; Vasisht et al., 1994). A major theoretical advance was

Table 1.4: Spatial parameters for SGRs.

Source	RA	DEC	Distance† (kpc)	SNR Association	Ref.
SGR 0526−66	$05^h\ 26^m\ 00^s.89$	$-66°04'36''.3$	50	SNR N49	1,2
SGR 1627−41	$16^h\ 35^m\ 51^s.84$	$-47°35'23''.3$	11	CTB 33	3,4
SGR 1806−20	$18^h\ 08^m\ 39^s.33$	$-20°24'39''.9$	$15.1^{+1.8}_{-1.3}$	···	5,6
SGR 1900+14	$19^h\ 07^m\ 14^s.33$	$+09°19'20''.1$	12–15	···	7,8

References: (1) Klose et al. (2004); (2) Kulkarni et al. (2003); (3) Corbel et al. (1999); (4) Wachter et al. (2004); (5) Corbel & Eikenberry (2004); (6) Kosugi et al. (2005); (7) Vrba et al. (2000); (8) Frail et al. (1999).

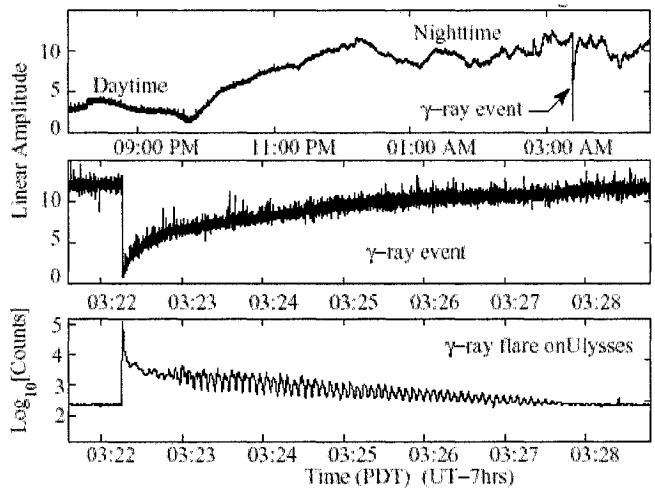

Figure 1.5: A disturbance in the ionosphere by a giant flare from SGR 1900+14 on 1998 August 27. Top: Measurements of the ionosphere. Notice that at the time of the SGR flare the signal descended to day time levels. Middle: Same as above except zoomed in on the time of the flare. Bottom: The lightcurve of the giant flare from SGR 1900+14 on 1998 August 27 as observed by the Ulysses satellite (from Hurley et al., 1999). Figure from Holographic Array for Ionospheric Lighting webpage, `http://www-star.stanford.edu/~vlf/hail/hail.htm`).

made with the proposal of the magnetar model to explain the high-luminosity bursts (Duncan & Thompson, 1992; Paczyński, 1992; Thompson & Duncan, 1995) and the persistent X-ray emission (Thompson & Duncan, 1996). In the magnetar model SGRs are young, ultra-magnetized (2-3 orders of magnitude greater than typical pulsars which have fields $\lesssim 10^{12}$ G) neutron stars powered by the decay of their fields. The magnetar model is explained in detail in § 2. This model

Table 1.5: Spin parameters for SGRs.

Source	P (s)	$\dot{P}$ (10^{-11} s s^{-1})	B_{dp} (10^{14} G)	$\dot{E}_s$ (10^{34} erg s^{-1})	τ_c (kyr)	Ref.
SGR 0526−66	8.05	6.5	7.3	4.9	2.0	1
SGR 1627−41	6.41	...	...	...	...	2
SGR 1806−20	7.49	∼42.2	∼18	∼39	∼0.28	3
SGR 1900+14	5.17	∼7.78	∼6.4	∼22	∼1.1	3

References: (1) Kulkarni et al. (2003); (2) Woods et al. (1999); (3) Woods et al. (2002).

predicted that SGRs should show persistent X-ray pulsations and that the pulsar should be spun-down by magnetic dipole braking.

The magnetar model was given a major boost when Kouveliotou et al. (1998) discovered that the X-ray emission from SGR 106−20 was modulated with a 7.5 s pulsation period. More importantly they determined that the pulsar was rapidly spinning down. A measure of SGR 1806−20's spin-down allowed them to infer that it had an enormous magnetic field $\sim 10^{15}$ G (see Eq. 1.39). Hence, the measurement of rapid spin-down provided evidence independent of the bursts that SGRs had fields orders of magnitudes greater than typical pulsars. To date persistent pulsations have been measured in a total of four SGRs and rapid spin-down has been measured in three (see Table 1.5). The pulse periods fall within the narrow range of those of the AXPs (see Table 1.2, Table 1.5 and Fig. 1.1). SGR spectra are comparable to those of the AXPs yet somewhat harder (see Table 1.3 and Table 1.6). The pulse profiles of the SGRs have very large duty cycles like those of the AXPs (see Fig. 1.6).

1.6.1 SGR Bursts

With the discovery of AXP-like persistent emission from SGRs the only difference between SGRs and AXPs remaining was the fact that SGRs emit bursts and AXPs did not. The next subsection describes the general properties of canonical SGR bursts.

SGR bursts tend to cluster together in periods of activity colloquially referred

Table 1.6: Spectral parameters* for SGRs.

Source	N_H (10^{22} cm^{-2})	Γ	kT (keV)	L_x (10^{35} erg s^{-1})	Ref.
SGR 0526−66	0.55	3.14	0.53	2.0	1
SGR 1627−41	9.0	∼2.95	···	∼0.039	2
SGR 1806−20	6.3	1.95	···	4.4	3
SGR 1900+14	2.7	∼1.98	0.43	1.8–2.8	4

(⋆) The spectral parameters are derived from fits to two-component models (power law + blackbody) whenever possible; References: (1) Kulkarni et al. (2003); (2) Kouveliotou et al. (2003); (3) Mereghetti et al. (2000); (4) Woods et al. (2001).

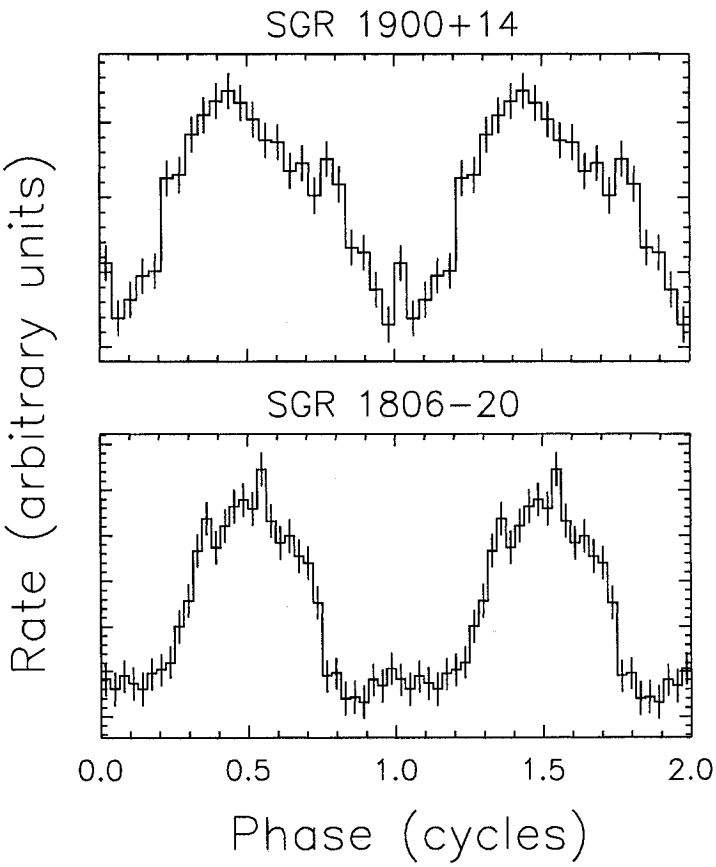

Figure 1.6: SGR pulse profiles in the 2–10 keV band. SGR profiles courtesy of P. M. Woods.

to as "outbursts". The bursts tend to be singled-peaked with shorter rise times than decay times. Some SGR bursts are multi-peaked, however, Göğüş et al. (2001) found that these bursts are consistent with being superpositions of two or more single-peaked bursts (Woods & Thompson, 2004). Burst durations are characterized by their T_{90} parameter which is the time between when 5% and 95% of the total burst counts have been received. The duration of the bursts (T_{90}) are log-normally distributed with means of 162 ms and 94 ms for SGR 1806−20 and SGR 1900+14 respectively (Göğüş et al., 2001). The range of durations observed can span two orders of magnitude. A correlation between burst duration (T_{90}) and burst energy (E) has been seen such that $E \propto T_{90}$. The energy of the bursts (E) follow a power-law distribution such that the number of bursts per energy goes as $dN/dE \propto E^{\alpha}$, with $\alpha \sim -5/3$. The exact value of α varies only slightly between sources. Cheng et al. (1996) noted that this differential energy distribution is very similar to the one found for earthquakes. SGR peak luminosities can obtain values as high as 10^{41} erg s^{-1}. Notice that this is above the Eddington Luminosity (see § 1.4.2) for a neutron star. The distribution of SGR burst luminosities has not been published.

The waiting time (the time between successive bursts) of SGR bursts are log-normally distributed. The mean of the waiting time distribution depends on the intensity of the burst and the sensitivity of the detector (Woods & Thompson, 2004); if one misses bursts because the instrument was not sensitive to them then that will skew the waiting time distribution. Using the same detector (*RXTE*) it was found that the mean waiting time for SGR 1806−20 and SGR 1900+19 was ∼100 s. Cheng et al. (1996) noted that the waiting times for earthquakes are also log-normally distributed. Palmer (2002) found that the time a burst occurs is not correlated with the rotational phase of the pulsar. In other words, SGR bursts do not occur preferentially at particular pulse phases.

The spectrum of the bursts appear to be well modeled by a two-component model consisting of two blackbodies at ∼4 and 10 keV (Olive et al., 2003; Feroci et al., 2004). Only weak (if any) spectral evolution has been noted in SGR bursts. A correlation between energy and hardness ratio (ratio of the number of

high-energy photons to low-energy photons) has been noted such that the more energetic bursts have softer spectra (Göğüş et al., 2001).

1.7 Thesis Outline

This thesis is structured as follows: Chapter 2 reviews the physics of the favored model to explain AXP emission, the so-called magnetar model. We explain how this model can account for the persistent and bursting emission of SGRs and AXPs. Chapter 3 reviews the "fall-back" disk model – the competing model to the magnetar model. Although this model is much more constrained than the magnetar model we discuss how it addresses some properties of AXPs that the magnetar model does not.

Chapter 4 describes the observatory from which we obtained our data, the *Rossi X-ray Timing Explorer* (*RXTE*). Chapter 5 describes the procedures followed to acquire, reduce and analyze our *RXTE* data.

Our results are presented in Chapters 6-10:

In Chapter 6 we report on the discovery of two X-ray bursts from the direction of AXP 1E 1048.1–5937. These bursts were very similar to those observed from SGRs. The large field-of-view of *RXTE* did not allow us to unambiguously identify the AXP as the source of the bursts, however, after considering alternate origins for the bursts we conclude that the AXP is the most likely source.

In Chapter 7 we report on the discovery of a major outburst from another AXP, 1E 2259+586, on 2002 June 18. The outburst consisted of over 80 bursts as well as several changes to the persistent emission. Such outbursts had thus far only been seen in SGRs. In Chapter 6 we could not unambiguously identify AXP 1E 1048.1–5937 as the source of the two bursts discovered in Fall 2001, however the identification of 1E 2259+586 as the burster here is clear. This discovery demonstrated that AXPs and SGRs are the same class of object as uniquely predicted by the magnetar model. A statistical analysis of the bursts from AXP 1E 2259+586's 2002 June 18 outburst is presented in Chapter 8. We show that the temporal, energetic and spectral properties of these bursts uniquely resemble those of the SGRs. On the other hand, we do identify some important differences between AXP and SGR bursts.

In Chapter 9 we report on the discovery of two long-lived pulsed flux enhancements from AXP 1E 1048.1–5937. Thus far, flux enhancements from SGRs

and AXPs had abrupt rises and were associated with major outbursts. The flux enhancements observed here were slow rising and there was no obvious evidence for a major outburst. We show that although such behavior has never before been seen from a magnetar candidate, the magnetar model can account for it.

In Chapter 10 we report on the discovery of a third burst from AXP 1E 1048.1–5937. Contemporaneously with the burst we discovered a short lived pulsed flux enhancement which unambiguously identified 1E 1048.1–5937 as the burst's origin. We argue that the identification of 1E 1048.1–5937 as the burster here confirms that it also emitted the two bursts discovered in Fall 2001.

At the end of each of the chapters comprised of previously published papers I provide a few sentences linking that chapter to the next. The specific conclusions for each paper and the overall conclusions of this thesis are presented in Chapter 11. We also suggest possible avenues for future work in Chapter 11.

Chapter 2

The Magnetar Model

Duncan & Thompson (1992) put forward a model in which SGRs are powered by the decay of their magnetic fields rather than by rotation or accretion. Later on they suggested that a similar mechanism could be powering the AXPs (Thompson & Duncan, 1996). This model requires that these pulsars be highly magnetized $\sim 10^{15}$ G. In order to have an idea of how extreme magnetar fields are let us compare them to the *critical magnetic field.* We saw in § 1.2.2 that if an electron makes the transition from the first energy state to the ground state it releases an amount of energy E. The electron's energy release (E) is related to the magnetic field (B) by

$$B = \frac{m_e c E}{e\hbar}. \tag{2.1}$$

At the *critical field* the electron will move relativistically, and its energy release will be comparable to its rest mass ($E = mc^2$), which yields

$$B_{\rm QED} = \frac{m_e^2 c^3}{e\hbar} \approx 4.4 \times 10^{13} \text{ G}. \tag{2.2}$$

Certain processes can only occur at such high field strengths and the effects of quantum mechanics cannot be neglected.

For pulsars with magnetic fields $B \gtrsim B_{\rm QED}$ the magnetic energy will dominate the spin-down energy at a very early age (Thompson & Duncan, 1996). To estimate this time scale we must first write down the expression for the magnetic energy of the star. The magnetic energy for an arbitrary system is given by

$$E_B = \frac{1}{8\pi} \int |\mathbf{B}|^2 dV. \tag{2.3}$$

For a spherical star with a dipolar field (Eq. 1.30) we obtain

$$E_B = \frac{1}{3}B^2R^3. \tag{2.4}$$

The spin down energy is given by Equation 1.34, $E = I\Omega^2/2 = 2I\pi^2/P^2$. Equating the spin-down energy to the magnetic energy we find

$$\frac{1}{3}B^2R^3 = \frac{2I\pi^2}{P^2}. \tag{2.5}$$

We can express P^2 in terms of the characteristic age and magnetic field using Equations 1.44 and 1.37, respectively. Specifically we have

$$P^2 = 2\tau\dot{P}P = \tau\left(\frac{B^2}{3Mc^3/20\pi^2R^4}\right). \tag{2.6}$$

Plugging the above expression for P^2 back into Equation 2.5 and using canonical values for the neutron star's mass and radius we find

$$t_{\rm mag} \sim 400\left(\frac{B}{10B_{\rm QED}}\right)^{-4} \text{ yr}. \tag{2.7}$$

From the above expression we see that for canonical pulsars with $B \sim 10^{12}$ G, the magnetic energy will not dominate the spin-down energy, for $\sim 10^{13}$ yr, i.e., on a time scale greater than the Hubble time (Thompson & Duncan, 1995)! However for pulsars with $B \sim 10B_{\rm QED}$ the magnetic energy will dominate the spin-down energy in less than a thousand years. Pulsars which are powered by their magnetic fields have been dubbed **magnetars** (Duncan & Thompson, 1992; Thompson & Duncan, 1995; Thompson & Duncan, 1996). Notice that the magnetar model applies to neutron stars that are very young and highly magnetized.

A great review of magnetars is given on the website[1] (hereafter I will refer to this site as RDWP) of one of the "fathers" of the magnetar model Robert C. Duncan.

[1] `http://solomon.as.utexas.edu/ duncan/magnetar.html`

2.1 Magnetic Dynamos and "Fossil" Fields

As discussed in the following sections it is very likely that AXPs and SGRs are young neutron stars with magnetic fields $B \gtrsim B_{\rm QED}$. But how do such high magnetic fields form? We know that the progenitors of neutrons stars are magnetic (see § 1.2.2), therefore either the seed fields are enhanced during the collapse because of magnetic flux conservation or a dynamo process is involved in amplifying the weak initial seed magnetic field. Let us first discuss magnetic dynamos. A basic dynamo equation can be derived by combining Ohm's Law, Faraday's Law and Ampère's Law

$$\frac{\partial \mathbf{B}}{\partial t} = \boldsymbol{\nabla} \times \left(\mathbf{v} \times \mathbf{B} - \frac{c^2}{4\pi\sigma} \boldsymbol{\nabla} \times \mathbf{B} \right). \tag{2.8}$$

For a star that rotates with angular frequency Ω we can write the above as

$$\frac{\partial \mathbf{B}}{\partial t} = \boldsymbol{\nabla} \times \left(\boldsymbol{\Omega} \times \mathbf{r} \times \mathbf{B} - \frac{c^2}{4\pi\sigma} \boldsymbol{\nabla} \times \mathbf{B} \right), \tag{2.9}$$

where we have used $\mathbf{v} = \boldsymbol{\Omega} \times \mathbf{R}$. Now if the star is rotating differentially the poloidal field is wrapped around the star and stretched, see Figure 2.1a. This effect is known as the Ω-effect because it is due to rotation [2]. In this process the poloidal field will serve to build-up the toroidal field. There are two problems with having a dynamo operating on the Ω-effect alone. The first is that the structure of stellar magnetic fields is generally believed to be dipolar, but the Ω-effect will result in a strong toroidal field because there is no mechanism by which to replenish the poloidal field in this process (Tajima & Shibata, 1997). The second and more important objection comes from the fundamental theorem in dynamo theory, called *Cowling's theorem* (Cowling, 1934) which states; *"A steady axisymmetric magnetic field cannot be maintained"*. Hence the field generated by the Ω-effect is not stable enough to survive during the lifetime of a neutron star (Tajima & Shibata, 1997) .

Parker (1955) suggested that convection might be the answer. He suggested that one could have an axisymmetric field if the convective elements have veloci-

ties which are not axisymmetric (Tajima & Shibata, 1997) . As these convective elements move around pressure causes them to rise and expand (Tajima & Shibata, 1997). When this happens, the Coriolis force will twist them, thus twisting the magnetic field lines that moves with them (see Figure 2.1b). Small-scale poloidal fields are thus formed from the toroidal field (Tajima & Shibata, 1997). The small scale poloidal field loops form a large scale field by connecting [2] together (Tajima & Shibata, 1997). The resulting poloidal field is much stronger than the original field because the reservoir by which it was generated, the toroidal field, was "beefed" up by the Ω-effect. This effect is known as the α-effect because the small poloidal loops formed by the process look like the Greek character alpha[3]. Parker (1955) suggested that the α-effect can be modeled by adding a term proportional to B in the dynamo equation

$$\frac{\partial \mathbf{B}}{\partial t} = \boldsymbol{\nabla} \times \left(\boldsymbol{\Omega} \times \mathbf{r} \times \mathbf{B} - \frac{c^2}{4\pi\sigma} \boldsymbol{\nabla} \times \mathbf{B} + \alpha \mathbf{B} \right), \tag{2.10}$$

where α has units of velocity. A dynamo which includes both the α and Ω effect is called an $\alpha\Omega$ dynamo.

Thompson & Duncan (1993) proposed that an $\alpha\Omega$ dynamo operating in newly born neutron stars might be responsible for generating their magnetic fields. In the case of a neutron star born rotating very rapidly, $P \lesssim 1$ ms (near breakup see § 1.2.3), an $\alpha\Omega$ dynamo will generate a magnetar strength field. As explained above, the $\alpha\Omega$ dynamo requires that the star be convective and rotating differentially. Thompson & Duncan (1993) argued that newly born neutron stars satisfy both these properties for a short period of time, but long enough for an $\alpha\Omega$ dynamo to greatly amplify their fields.

Magnetic dynamos have been proposed to explain the magnetic fields of main sequence stars, in particular, magnetic A_p stars (Charbonneau & MacGregor, 2001). Rotation plays an important role in the dynamo process but studies of A_p stars have found no correlation between rotation and magnetic field (Braith-

[2]The small-scale poloidal fields connect by magnetic "reconnection". For a description of reconnection see § 2.3.2.

[3]`http://science.nasa.gov/ssl/pad/solar/dynamo.htm`

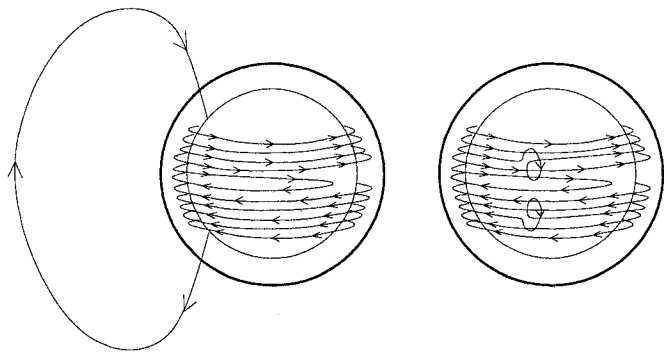

Figure 2.1: The $\alpha\Omega$ dynamo. (a) The Ω-effect. Differential rotation causes the poloidal field to be wrapped around the star and stretched, this builds up the toroidal field. (b) The α-effect. Rising convective elements are rotated because of the Coriolis force, generating small-scale poloidal loops from the toroidal magnetic field (Tajima & Shibata, 1997). These images are reproduction of the ones found on the website of the solar physics division of NASA's Marshall Space Flight Center (`http://science.nasa.gov/ssl/pad/solar/dynamo.htm`).

waite & Spruit, 2004, and references therein). Braithwaite & Spruit (2004) revisited the idea that stellar magnetic fields are remnants of the star's formation or "fossil-fields". The problem with the fossil-field hypothesis has been that analytical studies have provided stable field configurations only on very short times scales, shorter then it takes for a magnetic disturbance to travel across the star. Braithwaite & Spruit (2004) revisited the fossil field idea, but this time using magneto-hydrodynamical numerical simulations. Their model involved an arbitrary initial field configuration inside the star which was allowed to evolve under its own dynamics. Although analytical studies failed to provide long lasting stable configurations, the numerical simulations of Braithwaite & Spruit (2004) were able to generate fields that were stable for billions of years. Not only were Braithwaite & Spruit (2004) able to produce the appropriate time scales, they were also able to reproduce the expected quasi-dipolar structure. The external dipolar field was kept stable by an internal toroidal field which acted like a "ring" around the dipolar lines. Braithwaite & Spruit (2004) claim that the physical reason why they end up with such stable configurations is because the field wants to conserve

magnetic helicity

$$\mathcal{H} = \int \mathbf{A}\cdot\mathbf{B}dV, \tag{2.11}$$

where $\mathbf{A}$ is the vector potential of the magnetic field $\mathbf{B} = \nabla\times\mathbf{A}$. Braithwaite & Spruit (2004) noted that their simulations may apply to the magnetic fields of white dwarfs as well as to those of magnetars. Hence, the simple flux conservation argument of § 1.2.2 might not be so far off.

One important aspect to notice about the stellar magnetic field, whether the external field is generated by a dynamo process or through flux conservation, is that the internal field will always be highly "twisted". Both the dynamo and the fossil-field mechanism require interior fields which are neither purely toroidal nor purely poloidal. Purely toroidal or poloidal interior fields are highly unstable, hence a "twisted" internal field configuration assures the stability of the external quasi-dipolar field. As will be discussed in § 2.6, highly twisted internal magnetic fields play an important role in magnetars.

We saw that both dynamos and flux conservation can produce enormous magnetic fields $B > 10^{14}$ G, but is there a limit to how strong a neutron star's magnetic field can be? The answer is yes, a neutron star cannot support a magnetic field that is strong enough to disrupt the star (Lai, 2001). Following Lai (2001) we can estimate this limit by requiring that the magnetic energy be less than the gravitational binding energy of the star

$$\frac{4\pi R^3}{3}\left(\frac{B^2}{8\pi}\right) \lesssim \frac{GM^2}{R}. \tag{2.12}$$

Rearranging the above we find

$$B \lesssim 10^{18}\left(\frac{M}{1.4\ M_\odot}\right)\left(\frac{R}{10\text{ km}}\right)^{-2}\text{ G}. \tag{2.13}$$

2.2 Burst Emission

What evidence do we have for high magnetic fields in SGRs? First let us consider the first giant flare seen from SGR 0526−66 on 1979 March 5. The energy released

in the tail of the flare was $E_{\rm tail} \approx 3.6 \times 10^{44}$ erg (Mazets et al., 1979). Following Thompson & Duncan (1995) we can calculate the magnetic field strength required to contain this much energy. If energy is released outside the star in a radius ΔR, then the magnetic pressure $P_{\rm mag} = B^2/8\pi$ must exceed the radiation pressure $P_{\rm rad} = U/3$, where the radiation energy density is $U = E_{\rm tail}/V$ and the volume $V \sim \Delta R^3$. Balancing the two pressures we find

$$\frac{[B(R_* + \Delta R)]^2}{8\pi} \gtrsim \frac{E_{\rm tail}}{3\Delta R^3}. \tag{2.14}$$

Rearranging in a more intuitive manner and solving for the magnetic field we find

$$B_* > 4 \times 10^{14} \left(\frac{\Delta R}{10 \text{ km}}\right)^{-3/2} \left(\frac{1 + \Delta R/R_*}{2}\right)^3 \text{ G}. \tag{2.15}$$

Here we have used the fact that for a dipole field $B = B_*(R_*/R)^3$ where B_* and R_* are the magnetic field strength and radius at the surface. From Equation 2.15 we see that even if the energy is contained in a region of the star which is as large as the star itself $\Delta R \sim R \sim 10$ km, we obtain an enormous magnetic field $B \sim 10^{14}$ G (Thompson & Duncan, 1995).

2.3 Burst Triggers

2.3.1 Crustal Fractures

What kind of strain does the magnetic field place on the crust? According to Hooke's law the stress is equal to the strain times the shear modulus

$$\underbrace{P}_{\text{Stress}} = \mu \underbrace{\theta}_{\textit{Strain}}. \tag{2.16}$$

Here P is pressure, μ is the shear modulus, and θ is the dimensionless strain parameter. The pressure the magnetic field imparts is $B^2/8\pi$, so we have

$$\frac{B^2}{8\pi} = \mu\theta, \tag{2.17}$$

where μ is the shear modulus of the crust, and θ is the strain imparted on the crust (Thompson & Duncan, 1995). Baym & Pines (1971) calculated the shear modulus of a neutron star's crust and found it to be of the order $\mu \sim 10^{31}$ erg cm^{-3}. Most materials will fracture at a strain of $\theta \sim 10^{-3}$. So what fields will be required to provide enough magnetic pressure to crack the crust of a neutron star? Rewriting Equation 2.17 in a more convenient form we find

$$B = 2.5 \times 10^{15} \left(\frac{\mu}{10^{31} \text{ erg cm}^{-3}} \right)^{1/2} \left(\frac{\theta}{10^{-3}} \right)^{1/2} \text{G}. \tag{2.18}$$

So we see that the field strengths derived in the earlier sections are strong enough to fracture the crust of a magnetar (Thompson & Duncan, 1995).

2.3.2 Reconnection and Magnetic Instabilities

An important process in the electrodynamics of magnetars is magnetic reconnection (Thompson & Duncan, 1995; Thompson & Duncan, 1996; Thompson et al., 2002; Lyutikov, 2002). Magnetic reconnection can be described as follows: when two plasmas with oppositely oriented magnetic fields are brought together the magnetic field lines will disconnect and reconnect in a lower energy configuration (Tajima & Shibata, 1997). This process can release an enormous amount of energy, and has been used to explain Solar flares (Tajima & Shibata, 1997). The process is shown pictorially in Figure 2.2: a highly twisted magnetic flux loop emerges and comes into contact with an unwound flux loop. The tightly wound flux loop relaxes (unwinds) by reconnecting with the unwound flux loop (Tajima & Shibata, 1997). It might be puzzling how magnetic reconnection is possible in the highly conducting plasmas of neutron star magnetospheres, because according to Alfvén's theorem, the magnetic field lines of a perfectly conducting plasma are *"frozen into the [plasma]"* (Griffiths, 1999). Alfvén's theorem can be demonstrated as follows: magnetic flux is given by

$$\Phi = \int \mathbf{B} \cdot d\mathbf{a}. \tag{2.19}$$

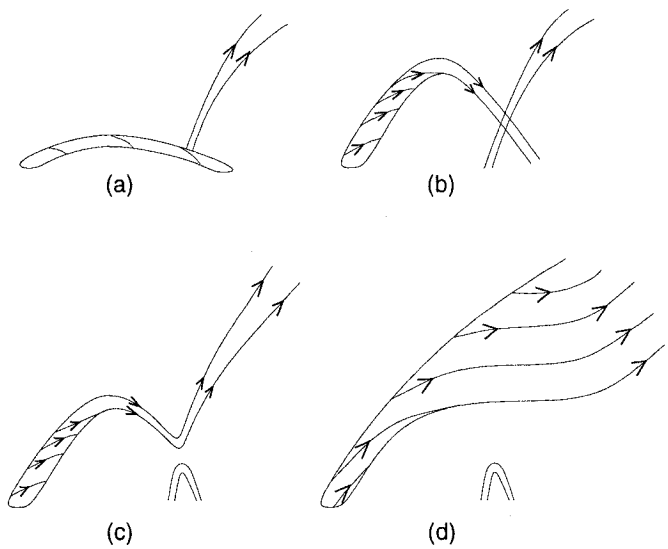

Figure 2.2: An example of magnetic reconnection. The flux tube on the left is highly twisted. It relaxes by reconnecting with an untwisted flux tube, releasing magnetic energy in the process. Figure reproduced from Tajima & Shibata (1997)

The rate of change of the magnetic flux integrated over an area encompassed by a closed loop is

$$\frac{d\Phi}{dt} = \int \left(\frac{\partial \mathbf{B}}{\partial t} - \boldsymbol{\nabla} \times (\mathbf{v} \times \mathbf{B}) \right) \cdot d\mathbf{a}. \tag{2.20}$$

See Griffiths (1999) for a derivation. Using Faraday's law ($\partial \mathbf{B}/\partial t = -c\boldsymbol{\nabla} \times \mathbf{E}$) we can write the above as

$$\frac{d\Phi}{dt} = -\frac{1}{c} \int \left(\boldsymbol{\nabla} \times \left(\mathbf{E} + \frac{\mathbf{v}}{c} \times \mathbf{B} \right) \right) \cdot d\mathbf{a}. \tag{2.21}$$

We saw at the beginning of § 1.3.3 that for a perfect conductor $\mathbf{E} = -(\mathbf{v}/c) \times \mathbf{B}$; thus, according to Eq. 2.21, for a perfect conductor $d\Phi/dt = 0$. However experiments and simulations in plasma physics have shown that when two plasmas carrying oppositely oriented magnetic fields are brought together a current begins to flow between them; this is refereed to as a "current sheet" (Tajima & Shibata, 1997). Even infinitesimal levels of resistivity in these "current sheets" will allow magnetic fields to reconnect (Tajima & Shibata, 1997).

Thompson & Duncan (1995) suggest that more drastic large scale rearrangements or *"interchanges"* of the magnetic field rather than just reconnection are required to explain the giant SGR flares. They explain the small (more frequent) bursts being due to crustal fractures. As the crust cracks it displaces the magnetic field lines a small distance. Such a magnetic disturbance dissipates magnetic energy. The large flares however cannot be explained by small displacements of the magnetic field lines by the crust. Instead Thompson & Duncan (1995) suggest that the giant flares are due to enormous displacements of the magnetic field by the neutron star's core. Being so drastically displaced the magnetic field will rearrange itself into a lower energy configuration, thus releasing an enormous amount of energy in the process. Thompson & Duncan (1995) suggest that some reconnection events might be expected in this global rearrangement scenario. In both the case of the small repeat bursts and the giant flares the energy source is magnetic (Thompson & Duncan, 1995).

Building upon the original magnetar model, Thompson et al. (2002) proposed that the magnetospheres of magnetars are highly twisted; this model is discussed in detail in § 2.6. Lyutikov (2002) suggested that twisted field lines in the magnetosphere could relax by reconnection and release energy which we would observe as SGR bursts. Thus, according to Lyutikov (2002) reconnection in the magnetosphere can also give rise to SGR bursts.

2.4 The Trapped Fireball

What is the effect of a magnetic disturbance on the surface of a magnetar such as a crustal fracture or a large-scale interchange instability? A sudden disturbance would emit magnetic waves into the magnetosphere: such waves are called Alfvén waves, and they travel at the so-called Alfvén speed

$$V_A = \frac{B}{\sqrt{4\pi\rho}}. \tag{2.22}$$

Notice that the definition of the Alfvén speed is analogous to the definition of the speed of sound $v = \sqrt{\gamma P/\rho}$, where the pressure is given by the magnetic pressure

$P = B^2/8\pi$ and γ is a constant of order 1 (Carroll & Ostlie, 1996). Following Thompson & Duncan (1995), the minimum distance in the magnetosphere that the disturbance will travel is given by

$$R_\nu = \frac{V_A}{\nu}, \tag{2.23}$$

where ν is the frequency of the disturbance. If magnetic footpoints move a distance $\Delta\ell$ with velocity V then the frequency is given by

$$\nu \sim \frac{V}{\Delta\ell} \tag{2.24}$$

(Thompson & Duncan, 1995). According to Thompson & Duncan (1995) if the magnetic footpoints are displaced because of a crustal fracture then V is given by

$$V = \sqrt{\frac{\mu}{\rho}}. \tag{2.25}$$

The above is the velocity of a *shear wave* (Thompson & Duncan, 1995). In the magnetosphere Alfvén waves travel virtually at the speed of light, $V_A \sim c$. This together with Equations 2.23, 2.24 and 2.25 gives

$$R = c\sqrt{\frac{\rho}{\mu}}\Delta\ell \tag{2.26}$$

$$= 2\left(\frac{\Delta\ell}{0.1 \text{ km}}\right) \text{ km} \tag{2.27}$$

(Thompson & Duncan, 1995).

What is the immediate consequence of releasing Alfvén waves into the magnetosphere? Thompson & Duncan (1995) argued that this would result in a photon electron-positron pair fireball. In the absence of a magnetic field, electron-positron pairs can be created from the two-photon pair process

$$\gamma + \gamma \rightarrow e^+ + e^-. \tag{2.28}$$

In the presence of a strong magnetic field the field can provide the energy and

momentum for the above reaction to occur with only one photon. Hence we have the one-photon pair creation process

$$\gamma + B \rightarrow e^+ + e^-. \tag{2.29}$$

Furthermore, the above two processes are catalyzed by the fact that in a strong magnetic field we have photon splitting

$$\gamma_1 + B \rightarrow \gamma_2 + \gamma_3, \tag{2.30}$$

thus providing further seed photons for the pair creation processes.

We can summarize the fireball model of Thompson & Duncan (1995) as follows. A magnetic disturbance, which displaces magnetic field lines, will result in the emission of an Alfvén pulse in the magnetosphere. The Alfvén waves will provide the energy and momentum to produce a photon electron-positron fireball. The motions of the electrons and positrons are limited because they can only travel along magnetic field lines, not across them (RDWP). The photons will have a difficult time escaping because they will scatter off the trapped electrons and positrons and/or even produce new electron positron pairs (RDWP). Only photons from the surface can escape freely (RDWP). As photons eventually escape and electrons and positrons annihilate, the trapped fireball is radiated away. The emission from the cooling fireball is what we observe as a burst. Since the fireball is trapped by the closed field lines, it rotates with the star, which is why we see a modulation at the star's spin frequency in giant SGR flares (see Fig. 1.5 for an example). In the giant flares, the magnetic pressure is not enough to contain all of the energy from the fireball; some of it escapes as a wind. The entire process is summarized pictorially in Figure 2.3.

2.5 Persistent Emission

We have seen that the magnetar model can explain the burst emission from SGRs but can it explain their persistent emission? We know that rotational energy of an

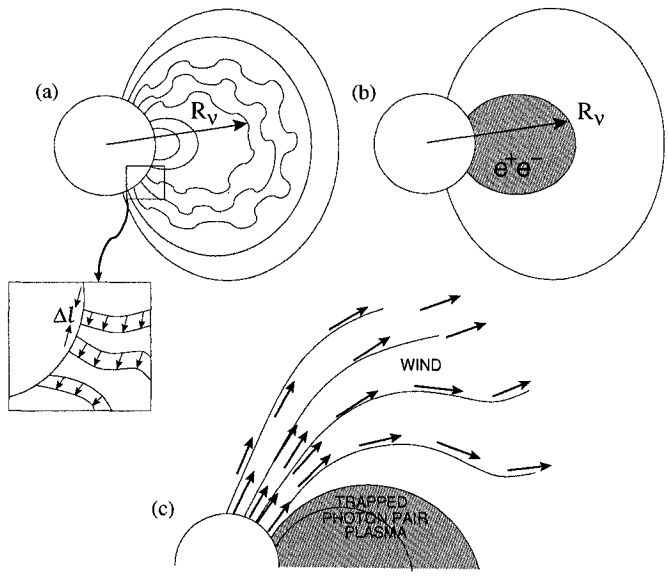

Figure 2.3: The trapped photon electron-positron fireball. (a)First, magnetic field lines are displaced by a distance $\Delta\ell$. This magnetic disturbance is communicated as an Alfvén pulse up to a distance R_ν in the magnetosphere. The Alfvén pulse waves are depicted by the "wiggly" magnetic field lines. (b) The Alfvén waves on the closed field lines induce an electron-positron photon fireball. This fireball is contained by closed field lines. As photons escape and electrons and positrons annihilate, the fireball is radiated away. (c) If the magnetic field lines were displaced by a large distance then the magnetic pressure might not be enough to contain the fireball. In this case some of the energy escapes as a wind. Figure reproduced from Thompson & Duncan (1995).

SGR cannot account for its observed X-ray luminosity, i.e., $L_X t \gg I\Omega^2/2$, where t is the age of the source. Can the magnetic energy of SGRs, however, account for their observed X-ray luminosities? Following Thompson & Duncan (1996) the magnetic energy stored in the crust at depth ΔR is $(B^2_{\rm crust}/8\pi)4\pi R^2\Delta R$. In order for this energy to account for the observed X-ray emission (L_X) it must satisfy

$$\left(\frac{B^2_{\rm crust}}{8\pi}\right) 4\pi R_*^2 \Delta R \gtrsim L_X t. \tag{2.31}$$

Solving for the magnetic field we find

$$B_{\rm crust} \gtrsim 8 \times 10^{14} \left(\frac{L}{10^{35}\ {\rm erg\ s^{-1}}}\right)^{1/2} \left(\frac{t}{10^{4}\ {\rm yr}}\right)^{1/2} \left(\frac{R}{10\ {\rm km}}\right)^{-1} \left(\frac{\Delta R}{1\ {\rm km}}\right)^{-1/2} {\rm G} \tag{2.32}$$

(Thompson & Duncan, 1996). Thus the persistent emission also demands that SGRs have enormous magnetic fields. As stated by Thompson & Duncan (1996), the magnetic field of a magnetar can provide the energy required to power the star. In order for this energy to power the star magnetic fields must be dissipated, i.e. $\partial B/\partial t < 0$. Following Cumming et al. (2004) the magnetic dissipation rate can be written in terms of the electric field via Faraday's law

$$\frac{\partial \mathbf{B}}{\partial t} = -c\boldsymbol{\nabla}\times\mathbf{E}, \tag{2.33}$$

where the electric field is given by writing down Ohm's law for a magnetar

$$\mathbf{E} = \underbrace{\frac{\mathbf{J}}{\sigma}}_{\text{Ohmic Decay}} + \underbrace{\frac{\mathbf{J}\times\mathbf{B}}{n_e e c}}_{\text{Hall Effect}} - \underbrace{\left(\frac{\mathbf{v}_p - \mathbf{v}_e}{c}\right)\times\mathbf{B}}_{\text{Ambipolar Diffusion}} + \underbrace{Q\boldsymbol{\nabla}T}_{\text{Thermoelectric Effect}}, \tag{2.34}$$

and the current density is given by Ampère's law

$$\mathbf{J} = \frac{c}{4\pi}\boldsymbol{\nabla}\times\mathbf{B}. \tag{2.35}$$

As we see from Equation 2.34, Ohm's law for a magnetar contains many terms, each of which has been studied extensively by several different authors. The first term describes ohmic dissipation (§ 2.5.1), the second the Hall effect (§ 2.5.2) and the third ambipolar diffusion (§ 2.5.3). The last term, the thermoelectric effect, involves magnetic dissipation driven by temperature gradients. This term, although promising for magnetars, will not be discussed in the following sections because theoretical work on this effect is still preliminary.

2.5.1 Ohmic Decay

If there is some resistance $\mathcal{R} = 1/\sigma$ in a plasma, then the magnetic field will be subjected to Ohmic losses. From Ohm's law (Eq. 2.34) and Faraday's law (Eq. 2.33) we see that the ohmic dissipation term is

$$\left(\frac{\partial \mathbf{B}}{\partial t}\right)_{\text{ohmic}} = -c\boldsymbol{\nabla}\times\left(\frac{\mathbf{J}}{\sigma}\right). \tag{2.36}$$

Using Ampère's law (Eq. 2.35) we can rewrite the above as

$$\left(\frac{\partial \mathbf{B}}{\partial t}\right)_{\text{ohmic}} = -c^2\boldsymbol{\nabla}\times\left(\frac{\boldsymbol{\nabla}\times\mathbf{B}}{4\pi\sigma}\right). \tag{2.37}$$

Performing dimensional analysis[4] on the above equation we can determine the characteristic time scale τ_{ohmic} for Ohmic dissipation over a length scale ℓ

$$\tau_{\text{ohmic}} \sim \frac{4\pi\sigma\ell^2}{c^2} \tag{2.38}$$

(Goldreich & Reisenegger, 1992). Notice that τ_{ohmic} is independent of the magnetic field and is only a function of the length scale and the conductivity. The conductivity of neutron stars was first studied by Baym et al. (1969) within a year of the discovery of pulsars. We can make an estimate of the conductivity of neutron stars by balancing the electric force by the frictional force of electron collisions

$$eE = m_*\frac{v}{\tau}. \tag{2.39}$$

Here τ is the electron collision rate and m_* is the effective mass of the electron given by $m_* = E_F/c^2$, where E_F is the Fermi energy (Eq. 1.5). The electric field is given by $E = J/\sigma$, where the current density is $J = nev$; hence

$$\sigma = \frac{J}{E} = \frac{nev}{E} = \frac{ne^2\tau}{m_*} = \frac{ne^2c^2}{E_F}\tau. \tag{2.40}$$

[4]We can estimate $\nabla \sim 1/\ell$, where ℓ is a length scale.

Yakovlev & Shalybkov (1990) found that the collision rate of electrons is of the order of $\tau \sim 10^{-17}$ s, so we can rewrite the above as

$$\sigma = 1.52 \times 10^{25} \left(\frac{\tau}{10^{-17}\ \mathrm{s}}\right) \left(\frac{\rho}{10^{12}\ \mathrm{g\ cm^{-3}}}\right)^{2/3} \left(\frac{Y_e}{0.05}\right)^{2/3} \mathrm{s}. \tag{2.41}$$

We can now write the time scale for Ohmic dissipation in a more intuitive format

$$\tau_{\mathrm{ohmic}} = 6.7 \times 10^{9} \left(\frac{\sigma}{1.52 \times 10^{25}\ \mathrm{s}}\right) \left(\frac{\ell}{10\ \mathrm{km}}\right)^{2} \mathrm{yr}. \tag{2.42}$$

From the above we see that for magnetars which have ages of $\tau \sim 10^4$ yr, Ohmic dissipation will not be important throughout the entire star, i.e. for $\ell \sim R_{\mathrm{NS}}$. Ohmic dissipation however can play an important role at small length scales. See Cumming et al. (2004) for a recent and detailed discussion of Ohmic decay in magnetars.

2.5.2 Hall Effect

An electric field will result if a current flows in the presence of a magnetic field; this is the well known Hall effect. This electric field is given by

$$\mathbf{E} = \frac{\mathbf{J} \times \mathbf{B}}{n_e e c} \tag{2.43}$$

(Thompson & Duncan, 1996). Using Faraday's law (Eq. 2.33) we can write the rate of change of the magnetic field due to the Hall effect as

$$\left(\frac{\partial \mathbf{B}}{\partial t}\right)_{\mathrm{Hall}} = -\boldsymbol{\nabla} \times \left(\frac{\mathbf{J} \times \mathbf{B}}{n_e e}\right). \tag{2.44}$$

Using Ampère's law (Eq. 2.35), we can rewrite the above as

$$\left(\frac{\partial \mathbf{B}}{\partial t}\right)_{\mathrm{Hall}} = -c\boldsymbol{\nabla} \times \left(\frac{(\boldsymbol{\nabla} \times \mathbf{B}) \times \mathbf{B}}{4\pi n_e e}\right). \tag{2.45}$$

A property of the Hall effect is that it does not dissipate magnetic energy (Goldreich & Reisenegger, 1992). To demonstrate this we must take the time derivative of the magnetic energy, Equation 2.3, so

$$\frac{dE_B}{dt} = \frac{d}{dt}\left(\frac{1}{8\pi}\int |\mathbf{B}|^2 dV\right). \tag{2.46}$$

Applying Ampère's law (Eq. 2.35) and integrating by parts we obtain

$$\frac{dE_B}{dt} = -\int \mathbf{J}\cdot\mathbf{E} dV. \tag{2.47}$$

Notice that the scalar product of $\mathbf{E}$ and $\mathbf{J}$ vanishes because according to Equation 2.43 the electric field is perpendicular to the current density. Although the Hall effect is non-dissipative it is very important in transporting magnetic fields to regimes where they can be dissipated much more rapidly (Goldreich & Reisenegger, 1992; Jones, 1988). By performing a dimensional analysis on Equation 2.45 we can estimate the characteristic time scale $\tau_{\rm Hall}$ for *hall drift* across a scale length ℓ

$$\tau_{\rm Hall} \sim \frac{4\pi n_e e \ell^2}{cB} \tag{2.48}$$

(Goldreich & Reisenegger, 1992). Thompson & Duncan (1996) claim that in the core, where the length scale $\ell \sim R_{\rm NS}$, even if $B \sim 10^{15}$ G, the time scale is much longer than the age of the star. They suggest that the Hall effect has a much more important effect in the crust where the length scale is small, $\ell \sim 0.2$ km. They propose that oscillations of a strong magnetic field, due to the Hall effect, can stress the crust enough to crack it. More recently, Cumming et al. (2004) revisited the Hall effect using more detailed calculations and determined that it is capable of transporting magnetic fields on much shorter times scales than previously thought in the crust as well as in the core. They suggest the length scale is not of the order of the size of the region but rather its local pressure scale height $\ell \sim H = P/\rho g$ (g is the acceleration due to gravity, and P and ρ are the local pressure and density respectively).

2.5.3 Ambipolar Diffusion

Ambipolar diffusion was studied in great detail by Goldreich & Reisenegger (1992) and Thompson & Duncan (1996). They suggest that as the magnetic field diffuses out, the electron and the protons move with it: this process is known as ambipolar diffusion. As the charged particles migrate they collide with each other and with the neutrons, which make up the majority of the star (Thompson & Duncan, 1996; Reisenegger, 2003). Sometimes the particles will also undergo reactions which will change the relative number of each species. Both these factors (collisions and reactions) delay their migration (Goldreich & Reisenegger, 1992; Thompson & Duncan, 1996). Quantitatively, the equation of motion of the particles can be written down as

$$\underbrace{\frac{m_p \mathbf{v}}{\tau_{\mathrm{pn}}}}_{\text{Interparticle collisions}} + \underbrace{\nabla \Delta\mu}_{\text{Pressure gradient forces}} = \underbrace{\frac{\mathbf{J}\times\mathbf{B}}{n_e c}}_{\text{Magnetic force}} \tag{2.49}$$

(see Goldreich & Reisenegger, 1992; Thompson & Duncan, 1996, for a derivation). The term on the right is the magnetic force, where the current density is given by $\mathbf{J} = n_e(\mathbf{v}_p - \mathbf{v}_e)$ (see Eq. 2.34). The first term on the left is the frictional force due to interparticle collisions, where τ_{pn} is a collision time scale. The second term is due to a pressure gradient force which is due to neutrino-producing reactions which change the relative number of particles, which in turn induces changes in the chemical potential $\Delta\mu$. The most common reactions are beta and inverse-beta decay:

$$n \rightarrow p + e^- + \bar{\nu}_e, \tag{2.50}$$

$$p + e^- \rightarrow n + \nu_e. \tag{2.51}$$

These processes are the so called URCA processes. Apparently the name arises from the fact that the URCA casino in Rio de Janeiro is a great way for one to lose money; similarly, the URCA processes are a great way for a star to lose energy (Shapiro & Teukolsky, 1983). At high nuclear densities, in order for

the URCA processes to conserve both energy and momentum, Chiu & Salpeter (1964) proposed that an extra neutron should be added to both sides of Equations 2.50 and 2.51 (Shapiro & Teukolsky, 1983). These so-called "modified" URCA reactions are given by

$$n + n \rightarrow n + p + e^- + \bar{\nu}_e, \tag{2.52}$$

$$n + p + e^- \rightarrow n + n + \nu_e \tag{2.53}$$

(Chiu & Salpeter, 1964). As we saw in § 1.1, these reactions are important when the star collapses (Shapiro & Teukolsky, 1983). For neutron stars these reactions are important only at high temperatures (Shapiro & Teukolsky, 1983). Thompson & Duncan (1996) suggest that ambipolar diffusion in a highly magnetized neutron star makes it hotter than a canonical neutron star because the dissipation of magnetic energy by ambipolar diffusion heats the star. However, heating the star also increases the dissipation rate (RDWP). According to Thompson & Duncan (1996), if the rate at which magnetic energy is dissipated is balanced by the energy density from the modified URCA reactions, then the temperature is given by

$$T(t) = 4.1 \times 10^8 \left(\frac{t}{10^4 \text{ yr}} \right)^{-1/7} \text{ K}. \tag{2.54}$$

Following Thompson & Duncan (1996), the surface luminosity is given by Stefan's law for blackbody radiation

$$L_X = 4\pi R^2 \sigma_{\text{SB}} T_{\text{eff}}^4, \tag{2.55}$$

where $\sigma_{\text{SB}} = 5.67 \times 10^{-5}$ erg cm^{-2} s^{-1} K^{-4} is Stefan-Boltzmann's constant and T_{eff} is the effective temperature one would measure at the surface. van Riper (1988) studied the atmospheres of magnetized neutron stars and found a core-surface temperature relation for the magnetic field strengths of interest of the form of

$$T_{\text{eff}} = 1.3 \times 10^6 \left(\frac{T_c}{10^8 \text{ K}} \right)^{5/9} \text{ K}, \tag{2.56}$$

where the core temperature (T_c) is given by Equation 2.54. Combining Equations 2.54, 2.55 and 2.56 we obtain the surface X-ray luminosity

$$\begin{aligned} L_X(t) &= 1.2 \times 10^{35} \left(\frac{T_c}{6 \times 10^{38}\ \mathrm{K}}\right)^{20/9} \left(\frac{R}{10^6\ \mathrm{cm}}\right)^2\ \mathrm{erg\ s^{-1}} \\ &= 5 \times 10^{34} \left(\frac{t}{10^4\ \mathrm{yr}}\right)^{-20/63} \left(\frac{R}{10^6\ \mathrm{cm}}\right)^2\ \mathrm{erg\ s^{-1}}. \end{aligned} \tag{2.57}$$

Notice that surface X-ray luminosity L_X given by Equation 2.57 is comparable to the observed X-ray luminosities of SGRs and AXPs which have very young ages (Thompson & Duncan, 1996).

2.6 The "Twisted" Magnetosphere

Thompson et al. (2002) proposed a model in which the magnetosphere of a magnetar is threaded by large-scale currents. These currents arise from stresses imposed on the crust by the highly twisted internal magnetic field (Thompson et al., 2002). As we saw in § 2.1, the magnetic fields of magnetars are believed to be generated by a dynamo process when the star is born which winds up the internal field (Thompson & Duncan, 1993). As we saw in § 1.3.3, it is already believed that there are axisymmetric currents near the light cylinder of a pulsar. The currents discussed here however are non axisymmetric and thread the entire magnetosphere. How large-scale currents such as these are generated is best explained by examining Figure 2.4. In Figure 2.4a we have a purely dipolar field and hence the curl of the magnetic field is zero ($\boldsymbol{\nabla}\times\mathbf{B} = 0$). According to Ampère's law written in integral form,

$$\begin{aligned} I &= \frac{c}{4\pi} \oint_S \boldsymbol{\nabla}\times\mathbf{B}\cdot d\mathbf{a} \\ &= \frac{c}{4\pi} \oint_\ell \mathbf{B}\cdot d\boldsymbol{\ell}, \end{aligned} \tag{2.58}$$

the current is also zero. Now, since the footpoints of these magnetic field lines are well-anchored to the crust, if internal stresses imposed on the crust by the highly

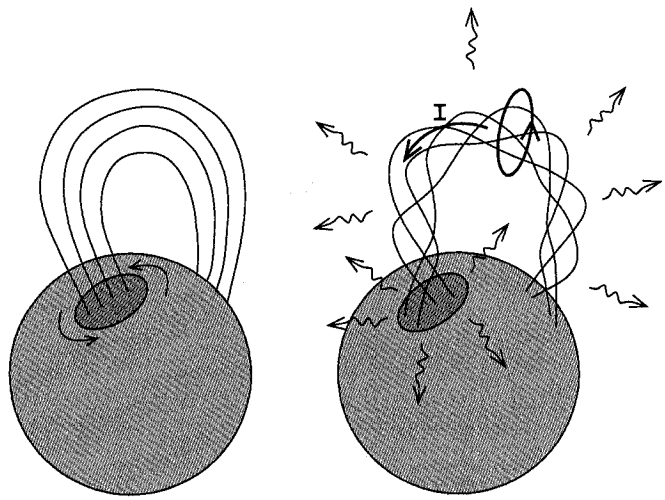

Figure 2.4: A magnetic "twist" in the magnetosphere. (a) A dipolar field with magnetic footpoints anchored in a patch of the crust which is subjected to internal stresses. (b) The internal stresses cause the patch of the crust to twist which in turn twists the external magnetic field. Because the curl of the magnetic field along a closed loop is non-zero a current I can now flow (Eq. 2.59). The currents enhance the X-ray emission (curly arrows). Protons and ions "smash" into the surface and heat it and the electrons are accelerated and radiate. Furthermore, thermal photons from the surface are also Compton up-scattered by the currents. This figure is a reproduction from Robert C. Duncan's webpage at the University of Texas at Austin (`http://solomon.as.utexas.edu/ duncan/magnetar.html`).

wound internal field cause a patch on the surface to twist, then the magnetic field lines will twist with it (Fig. 2.4b). In this case the curl of the magnetic field is non-zero. If we calculate the line integral of the magnetic field along a closed loop (see Fig. 2.4b) we see from Equation 2.59 that a current can flow. As well as small bundles of field lines, Thompson et al. (2002) proposed that the magnetic field of a magnetar is globally twisted. Figure 2.5 shows a globally twisted dipolar field.

What is the effect of these currents? They will enhance the persistent X-ray emission of magnetars and will give rise to a non-thermal component in their energy spectra. The magnetospheric currents will cause the heavier charged par-

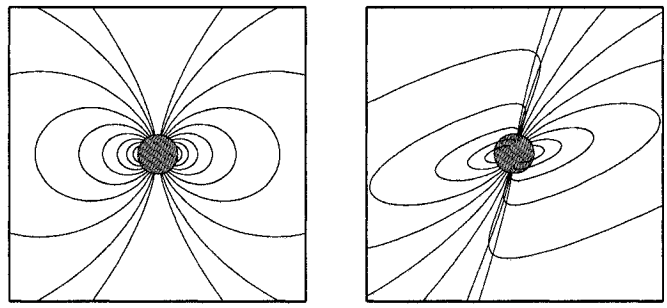

Figure 2.5: An example of a globally twisted magnetosphere. (a) A neutron star with a simple dipolar magnetic field. (b) A neutron star with a globally "twisted" dipolar magnetic field. The twisted fields lines allow large-scale magnetospheric currents to flow. The figure is a reproduction from Thompson et al. (2002)

ticles, the ions, to smash into the surface and thus heat it (RDWP). The lighter charged particles, the electrons, will be easily accelerated by these currents and thus radiate non-thermal emission (RDWP). So we see that one of the effects of the magnetospheric currents is that it enhances the X-ray emission from magnetars. The second effect of these currents is that any thermal photons from the surface (either a result of ions heating the surface or internal dissipative processes) will be up-scattered by the currents which will result in a non-thermal component in the energy spectra of magnetars (Thompson et al., 2002). This second effect is very important because as mentioned in § 1.5 and as is seen from Table 1.3, the energy spectra of AXPs are comprised of two-components: a thermal and a non-thermal component. This model explains that the non-thermal component is just the result of Comptonization of the thermal photons by large-scale currents in the magnetosphere (Thompson et al., 2002). This model then makes the prediction that if AXPs get brighter then their spectra must also get harder, since larger twists enhance X-ray emission and increase the Comptonization of thermal photons.

Following Thompson et al. (2002) we can estimate what persistent X-ray emission is expected from magnetospheric currents. The work done by the electric field (E) to move an ion from the cathode to some maximum height, $R_{\rm max}$, is $W_{\rm ion} = -e\int_{R_{\rm NS}}^{R_{\rm max}} \mathbf{E}\cdot d\mathbf{r}$. Similarly, the work done to move an electron from the

anode to $R_{\rm max}$ is $W_{e^-} = -e\int_{R_{\rm NS}}^{R_{\rm max}} \mathbf{E}\cdot d\mathbf{r}$. Thus, the total work done by the electric field is

$$\begin{aligned} W &= W_{\rm ion} + W_{e^-} \\ &= -2e\int_{R_{\rm NS}}^{R_{\rm max}} \mathbf{E}\cdot d\mathbf{r}. \end{aligned} \tag{2.59}$$

We can estimate the magnitude of the electric field because we know that it must be strong enough to lift the heavy ions, i.e.

$$e\mathbf{E} = m_p \boldsymbol{\nabla}\Phi, \tag{2.60}$$

where Φ is the gravitational potential, $\Phi = GM_{\rm NS}/r$. Inserting Equation 2.60 into Equation 2.59 we find

$$\begin{aligned} W &= -2m_p \int_{R_{\rm NS}}^{R_{\rm max}} \boldsymbol{\nabla}\Phi\cdot d\mathbf{r} \\ &= -2m_p \left(\Phi(R_{\rm max}) - \Phi(R_{\rm NS})\right) \\ &= 2m_p \left(\frac{GM_{\rm NS}}{R_{\rm NS}} - \frac{GM_{\rm NS}}{R_{\rm max}}\right). \end{aligned} \tag{2.61}$$

The above is the work done for a single ion and electron. For N particles the luminosity is $L_X = d(NW)/dt$. The rate can be expressed in terms of the current $dN/dt = I/e$. Now the previous calculation was just for particles at the same spot. For particles smashing over an area da the resulting luminosity will be $dL_X = WdI/e$. The differential of the current can be written in terms of the current density since $dI = \mathbf{J}\cdot d\mathbf{a}$; hence, $dL_X = W(J/e)da$. Using Equation 2.61 we can write

$$dL_X = 2m_p \left(\frac{GM_{\rm NS}}{R_{\rm NS}}\right)\left(1 - \frac{R_{\rm NS}}{R_{\rm max}}\right)\frac{\mathbf{J}}{e}\cdot d\mathbf{a}. \tag{2.62}$$

We can make a rough estimate what this luminosity will be. For $R_{\rm max} > R_{\rm NS}$ we

have $L_X \approx (2m_pGM_{\rm NS}/eR_{\rm NS}) \int \mathbf{J}\cdot d\mathbf{a}$. Using Ampère's law (Eq. 2.35) we have

$$L_X = \frac{2m_pcGM_{\rm NS}}{4\pi eR_{\rm NS}} \int \boldsymbol{\nabla}\times\mathbf{B}\cdot d\mathbf{a} = \frac{2m_pcGM_{\rm NS}}{4\pi eR_{\rm NS}} \int \mathbf{B}\cdot d\mathbf{r} \sim \frac{2m_pcGM_{\rm NS}}{4\pi eR_{\rm NS}} BR_{\rm NS}. \tag{2.63}$$

Writing the above in terms of the appropriate units we find

$$L_X \simeq 3\times 10^{35} \left(\frac{B}{10^{14}\ {\rm G}}\right) \left(\frac{M_{\rm NS}}{1.4\ M_\odot}\right)\ {\rm erg\ s^{-1}}. \tag{2.64}$$

The luminosity obtained from this simple "back of the envelope" calculation is comparable to the luminosity obtained by Thompson et al. (2002) via a detailed calculation using the correct spatial dependence for the magnetic field. Notice from the above equation that if $B \sim 10^{14}$ G the expected X-ray luminosity is comparable to the observed persistent luminosities of AXPs.

Chapter 3

The Fall-Back Disk Model

Despite all the success of the magnetar model in accounting for the persistent and pulsed emission of AXPs and SGRs, as well as the bursting emission of SGRs, there are still some aspects of these sources which it does not explain. In particular, the magnetar model cannot explain the clustering of the AXP and SGR periods in the narrow 5−12 s range. Although it can account for it energetically, the magnetar model makes no predictions for the origin of the optical/IR emission from AXPs. An unconventional accretion model has been proposed in which AXPs are not accreting from a companion but from a disk made up of supernova material which "*fell back*" onto the neutron star after the explosion (Chatterjee et al., 2000; Alpar, 1999; Marsden et al., 2001). This "fall-back" disk model is reviewed in this chapter. Because of its abilities to explain some properties of AXPs that the magnetar model cannot, in particular the period clustering, the fall-back disk model has survived as the only competitor to the magnetar model. However, some serious limitations of this model are discussed at the end of this chapter.

3.1 Fall-Back Disks

A supernova explosion is not a completely symmetric explosion, thus it is possible for some material to fall-back towards the neutron star. Since the progenitor star was initially rotating, conservation of angular momentum will cause the returning material to form a disk around the neutron star. Such a disk is known as a "fall-back" disk (Chatterjee et al., 2000; Alpar, 1999; Marsden et al., 2001). Depending on the location of the disk and the neutron star's magnetosphere it is possible

to observe the neutron star as an X-ray pulsar. Alpar (1999) estimated that even the small amount of the progenitor mass expected to fall back ($\sim$0.15 $M_{\odot}$; Chevalier, 1989) is enough for this mechanism to work.

3.1.1 Mass Accretion Rate

Now, an important difference between a canonical accretion disk and a fall-back disk is that the total disk mass is unavoidably depleted because there is no companion star to provide new material to the disk (Francischelli & Wijers, 2002). Thus, the accretion rate in the fall-back disk is necessarily a time dependent phenomenon (Francischelli & Wijers, 2002). Chatterjee et al. (2000) building upon the work of Cannizzo et al. (1990), suggested the following power-law (self-similar) time dependence for the accretion rate

$$\dot{m} = \dot{m}_0 \left(\frac{t}{t_0}\right)^{-\gamma}, \tag{3.1}$$

where $\dot{m}_0$ is the initial accretion rate. According to Cannizzo et al. (1990), in a system where the neutron star does not have a companion, a power-law dependence for the accretion rate is expected for a disk that evolved under the effects of viscous forces (Chatterjee et al., 2000). The value of the power-law index in Eq. 3.1 depends on the opacity (κ) of the disk. Cannizzo et al. (1990) found that for opacities of the form

$$\kappa = \kappa_0 T^{\alpha} \rho^{\beta}, \tag{3.2}$$

γ is given by

$$\gamma = \frac{38 + 18\alpha - 4\beta}{32 + 17\alpha - 2\beta}. \tag{3.3}$$

If the opacity of the disk is dominated by electron scattering then $\alpha = 0$ and $\beta = 0$, which yields $\gamma = 1.1875$ (Ekşı & Alpar, 2003). See Ekşı & Alpar (2003) and Francischelli & Wijers (2002) for other choices of α and β. In their detailed model Chatterjee et al. (2000) adopted $\gamma = 1.167$ for computational feasibility. The time dependence of the accretion rate leads to different evolutionary phases

for a neutron star with a fall-back disk, which brings us to the next section.

3.1.2 Evolutionary Phases

Chatterjee et al. (2000) suggested that there are specific phases in the life of a neutron star accreting from a fall-back disk. They suggest that all young neutron stars can have such disks and that the observed properties of a young neutron star is determined by the evolutionary phase it is in.

Chatterjee et al. (2000) show that the evolutionary phase is determined by the relative location of three different radii: the light cylinder radius, r_{lc} (Eq. 1.56); the Alfvén radius r_A (Eq. 1.95); and the corotation radius r_{co}. The corotation radius is the radius at which material in the disk is corotating with the star. Setting the angular spin frequency of the star $\Omega_* = \Omega_K$, where the Keplerian angular frequency is given by Eq. 1.75, we find that the corotation radius is given by

$$\begin{aligned} r_{co} &= \left(\frac{GM}{\Omega_*^2}\right)^{1/3} = \left(\frac{GMP_*^2}{4\pi^2}\right)^{1/3} \\ &\approx 1.6 \times 10^8 \left(\frac{M}{1.4\ M_\odot}\right)^{1/3} \left(\frac{P_*}{1\ \mathrm{s}}\right)^{2/3} \ \mathrm{cm}. \end{aligned} \tag{3.4}$$

"Ordinary" Pulsar Phase

If the Alfvén radius, r_A, is located outside the light cylinder, r_{lc}, then the disk is essentially pushed outside the light cylinder; thus, the disk cannot interact with the plasma inside the magnetosphere, so essentially the pulsar and the disk do not know about each other and they both evolve independently (Chatterjee et al., 2000). Since the disk is not affecting the star, the star is behaving as an ordinary rotation-powered pulsar.

The "Propeller" Phase

As the pulsar slows down because of magnetic dipole braking the corotation radius, r_{co}, increases. As the disk evolves, $\dot{m}$ decreases (see Eq. 3.1), so the

Alfvén radius, r_A decreases. Hence, we have the corotation radius r_{co} and the Alfvén radius r_A approaching each other but with $r_A \gg r_{co}$ at all times. The fact that $r_A \gg r_{co}$ corresponds to the spin frequency of the star exceeding the Keplerian frequency of the disk for all disk radii, thus angular momentum is transfered from the star to the disk. Centrifugal forces cause matter to be flung from the disk; the disk is in what is called a "propeller" phase. In this phase the star is being rapidly spun-down and it approaches, but never reaches, an equilibrium spin period. We can estimate this equilibrium spin period by setting the corotation radius (Eq. 3.5) equal to the Alfvén radius (Eq. 1.95), or more exactly:

$$P_{\rm eq} = 21.91 \left(\frac{B_*}{10^{12}\ {\rm G}}\right)^{6/7} \left(\frac{M}{1.4\ M_\odot}\right)^{-5/7} \left(\frac{R_*}{10^6\ {\rm cm}}\right)^{18/7} \left(\frac{\dot{m}}{10^{15}\ {\rm g\ s^{-1}}}\right)^{-3/7} {\rm s}. \tag{3.5}$$

During the propeller phase the system is an X-ray emitter, albeit a faint one.

The "Tracking" Phase

As the spin frequency of the star becomes comparable to the equilibrium spin period, corresponding to $r_A \sim r_{co}$, the star begins accreting much more efficiently and we are in what Chatterjee et al. (2000) call the "tracking" phase. The star is at its brightest in this phase, but since $\dot{m}$ is diminishing the luminosity is also diminishing (see Eq. 1.86).

The ADAF Phase

Narayan & Yi (1995) found that when the luminosity of the disk reaches $\approx 0.01 L_{\rm Edd}$ the disk will overheat and the system will enter an advection-dominated accretion flow (ADAF Narayan & Yi, 1994, 1995) phase. In the ADAF phase, matter will be ejected again (whether as a wind or a jet is not absolutely clear) and hence the source will no longer radiate.

3.1.3 Period Clustering

This model suggests that the reason why AXP spin-periods span such a narrow range is due to the selection effect that fall-back disk accretors are at their brightest during a very short interval in their lives (Chatterjee et al., 2000). More specifically, the tracking phase, when the star's Alfvén radius (Eq. 1.95) is comparable to its corotation radius (Eq. 3.5), corresponds to the AXPs spinning close to their equilibrium spin periods (Eq 3.5). Thus, this model is capable of explaining why AXP spin periods span such a narrow range.

3.1.4 Spin-Down Torque

Spin-down is definitely expected in the fall-back disk model because during the propeller-phase material is flung from the disk, hence angular momentum is transferred from the star to the disk, the opposite of a conventional accretion disk. The exact nature of this spin-down depends of course on the functional form of the torque, which depends on the accretion rate (Eq. 3.1) which in turn depends on the opacity of the disk (Eq. 3.2). How the magnetic field of the star is interacting with the fall-back disk is not obvious, thus the functional form of the rate of change of angular momentum in a fall-back disk is equally as uncertain. Chatterjee et al. (2000) adopted the following prescription for the torque:

$$I\dot{\Omega}_* = 2\dot{m}r_A^2\left(\Omega_K - \Omega_*\right). \tag{3.6}$$

Recall that in the fall-back disk model $\Omega_K(r) \ll \Omega_*$ for all r because $r_A \gg r_{co}$, thus

$$I\dot{\Omega}_* \sim -2\dot{m}r_A^2\Omega_*. \tag{3.7}$$

Conventional accreting sources are known to go through periods of spin-up and spin-down. Notice that $I\dot{\Omega}$ is negative, which implies that the star is spinning down as mentioned in § 3. The inverse, $\Omega_* < \Omega_K$ never happens, or at least very briefly in the beginning of the star's life according to Chatterjee et al. (2000); hence, episodes of spin-up are rare but not entirely unexpected in this model.

However, an episode of spin-up has never been observed from an AXP.

3.1.5 Timing Behavior

Accreting systems exhibit a lot more timing noise than rotation-powered pulsars. Because of the *"turbulent nature"* (Chatterjee et al., 2000) of the fall-back disk, one would also expect such systems to exhibit significant timing noise. One AXP (1E 1048.1–5937) is a very unstable rotator; however, most AXPs have shown long-periods of quiet spin-down. In fact, one AXP has exhibited as much rotational stability as some radio pulsars. Alpar (2001) argues that the current steady spin-down of AXPs could be transient, and he refers to previous reports of deviations from rotational stability in AXPs. Alpar (2001) also notes that the established accreting system 4U 1626-67 has shown periods of extensive rotational stability as well (Chakrabarty et al., 1997). It should be noted however, the rotational stability of this source is still noisier than the most rotationally unstable AXP.

Chatterjee et al. (2000) cautions one to be careful about the conclusions one draws from a pulsar's timing behavior alone. As we saw in § 3.1.2 a fall-back disk accretor's angular spin frequency (Ω_*) asymptotically approaches it Keplerian angular frequency (Ω_K). Following Chatterjee et al. (2000), let us examine the temporal dependence of the star's spin frequency in the asymptotic regime where $\Omega_* \sim \Omega_K$. In this regime, the corotation radius (r_{co}) is comparable to the magnetospheric radius (r_A), thus by setting $r = r_A$ in Eq. 1.75 we can write the Keplerian angular frequency more conveniently as

$$\Omega_K = \Omega_K(r_{A,0}) \left(\frac{r_A}{r_{A,0}} \right)^{-3/2}, \tag{3.8}$$

where $r_{A,0}$ is the value of the magnetospheric radius at $t = t_0$. Using Eq. 1.95 we can write the magnetospheric radius in terms of the accretion rate, in which case the above reduces to

$$\Omega_K = \Omega_K(r_{A,0}) \left(\frac{\dot{M}}{\dot{M}_0} \right)^{3/7}. \tag{3.9}$$

Now, the accretion rate is simply given by Eq. 3.1, hence when $\Omega_* \sim \Omega$, we see that

$$\Omega_* \sim \Omega_K(r_{A,0}) \left(\frac{t}{t_0}\right)^{-3\gamma/7} . \tag{3.10}$$

Now, simply using the definition of characteristic age ($\tau_c = \Omega/2\dot{\Omega}$, see Eq. 1.44) it follows that for the above $\tau_c = (7/6\gamma)t$. Also, using the definition of braking index ($n = \ddot{\Omega}\Omega/\dot{\Omega}^2$, see Eq. 1.47) we find for the above case that $n = 3(7/\gamma + 3)$. Notice that for $\gamma = 7/6$ the characteristic age and braking index we would measure for a fall-back disk accretor would be exactly the same as for a rotation-powered pulsar spinning down via magnetic dipole braking (Chatterjee et al., 2000). Thus, in the asymptotic regime of $\Omega \sim \Omega_K$ (when in fact a fall-back disk accretor is at its brightest) one would not be able to distinguish a fall-back disk accretor from a rotation-powered pulsar via its timing properties alone (Chatterjee et al., 2000).

3.1.6 X-ray Flux

In the fall-back disk model it is accretion which accounts for the X-ray emission of AXPs. Using Eq. 1.64 their observed X-ray luminosities (Table 1.3) can be accounted for if they have accretion rates of $\dot{m} \sim 10^{14} - 10^{16}$ g s^{-1} (however, Eq. 1.64 does not accurately explain the luminosity of an accreting source that is spinning-down, R E. Rutledge personal communication). Furthermore, this model does not require very high (for a pulsar, that is) magnetic fields. This can be demonstrated as follows: if we assume that the AXPs are currently spinning at their equilibrium spin periods, then inserting their inferred mass accretion rates into Equation 3.5 we find $B \sim 10^{10} - 10^{12}$ G. Thus, unlike the magnetar model, this model only requires "ordinary" pulsar strength fields.

Luminosity Torque Relation

Conventional accretors are observed to be flux variable, which can be clearly explained by a variable accretion rate. A variable accretion rate, and thus a variable flux, is not unexpected in this model as well. However, in an accreting system, including an accreting system such as this one, a correlation between

the X-ray luminosity and the torque is expected. This can be demonstrated as follows. Rewriting Eq. 3.7 in terms of the disk luminosity we find

$$I\dot{\Omega}_* = \frac{4LR}{GM} r_A^2 \Omega_*. \tag{3.11}$$

Substituting Eq 1.99 for the Alfvén radius and rearranging we obtain

$$I\dot{\Omega}_* = L^{3/7} \left(\frac{16 B^8 R^{27} \Omega_*^7}{G^5 M^5} \right)^{1/7}. \tag{3.12}$$

So, in the fall-back disk we see that one expects a correlation between the luminosity and the spin-down torque.

3.1.7 Optical/IR emission

Optical/IR emission has been observed from five out of the six AXPs. The origin of this optical/IR emission has a clear explanation within the framework of the fall-back disk model; it is due to X-rays reflected off and reprocessed by the disk. However, this model struggles with the observed ratio of Optical/IR to X-ray flux from AXPs. In some cases the model overpredicts and in others underpredicts the amount of optical/IR emission observed. For one AXP, 4U 0142+61, the optical/IR emission is pulsed, and the fall-back disk cannot account for its high (27%) pulsed fraction[1] (Kern & Martin, 2002). Also, Dhillon et al. (2005) found that the optical/IR pulsations are aligned with the X-ray pulsations. If the optical/IR emission is just reprocessed X-ray emission from the disk, then one might expect a delay between the optical/IR and the X-ray pulsations.

3.2 A Hybrid Model

The fall-back disk model cannot explain the bursts observed from SGRs, thus in this model the similarities between the SGRs and the AXPs are simply coincidental. Furthermore, proponents of the fall-back disk model concedes that is

[1]Ratio of the pulsed flux to the total (pulsed plus unpulsed) flux.

very likely that highly-pulsed optical/IR emission from 4U 0142+61 is magnetospheric (Ekşı & Alpar, 2003). Ekşı & Alpar (2003) proposed a hybrid model in which the magnetic field of AXPs and SGRs is multipolar with a canonical ($\sim 10^{12}$ G) dipolar component, which interacts with a fall-back disk giving rise to the observed spin-periods and spin-down rates, and a stronger ($\sim 10^{15}$ G) higher multipole component, which produces the bursts and the unusual optical/IR emission. However, some would argue that if a strong magnetic field is present then a mechanism is already in place to explain all the properties of these sources except for the narrow range of spin-periods.

Chapter 4

The Rossi X-ray Timing Explorer

All data presented in this thesis were obtained from the *Rossi* X-ray Timing Explorer (*RXTE*), a satellite which provided unprecedented timing resolution to the field. *RXTE* is named after the Italian-born American astrophysicist Bruno B. Rossi, a pioneer of X-ray astronomy. *RXTE* was set into orbit by a Delta II rocket from NASA's Kennedy Space center at Cape Canaveral on December 30, 1995. *RXTE* is at an altitude of ~580 km, and is in a 90 min orbit with an inclination of 23°.1. *RXTE* had a planned lifetime of 2 years, with a goal of 5, but it has persevered for over 9 years and continues to operate even today.

The following description of the *RXTE* spacecraft, scientific and logistic instruments follows the *RXTE* technical appendix (Appendix F)[1]. The reader is referred to this manual for a more detail description of the instruments and their capabilities.

4.1 The Spacecraft

All the scientific instruments aboard *RXTE* are combined in a single sturdy spacecraft. Figure 4.1 is a schematic of the *RXTE* spacecraft which depicts the locations of the various scientific and operational instruments. The *RXTE* spacecraft was built by the engineering directorate of NASA's Goddard Space Flight Center (GSFC) in Greenbelt Maryland. GSFC also serves as the main control room for *RXTE*. *RXTE* is capable of maneuvering by 6° per minute. *RXTE* can point at an any position in the sky, with the viewing constraint

[1] `ftp://legacy.gsfc.nasa.gov/xte/nra/appendix-f/`

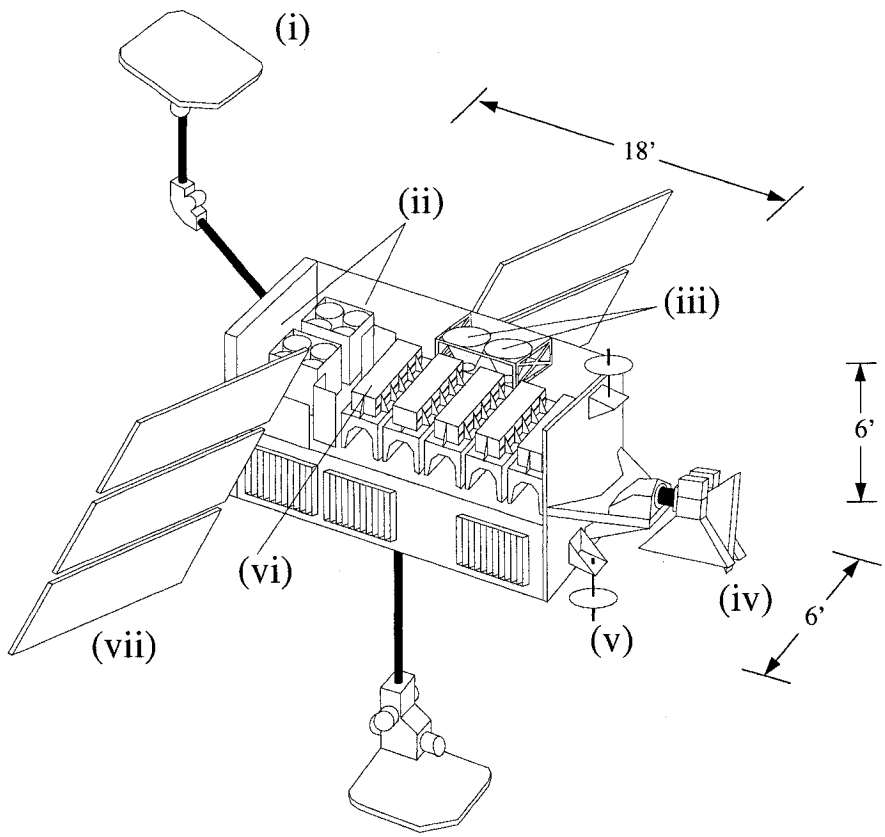

Figure 4.1: The *RXTE* Spacecraft: (i) High-gain antenna; (ii) High-Energy X-ray Timing Experiment (HEXTE); (iii) Star trackers; (iv) All-Sky Monitor (ASM); (v) Low-gain antenna; (vi) Proportional Counter Array (PCA, 1 of 5); (vii) Solar-power array.

that it point no closer than 30° towards the Sun. As well as viewing constraints *RXTE* also suffers from sampling constraints. *RXTE* is regularly shut down when passing through the South Atlantic Anomaly (SAA). The SAA is a region near the South Atlantic which has an anomalously high particle flux. *RXTE* passes through the SAA 6 times a day resulting in a loss of 10–20 mins worth of data during each pass. Data are also lost due to Earth occultations which usually last ~30 min. The attitude of *RXTE* is controlled by the Attitude Control System (ACS), which consists of optical star trackers, gyroscopes, digital fine Sun sensors, coarse Sun sensors, magnetometers, reaction wheels and torque bars.

What makes *RXTE* exceptional is its 1 μs time resolution. The absolute timing of *RXTE* is determined via the User Spacecraft Clock Calibration System (USCCS)[2]. This technique involves sending a pulse from the White Sands Complex to the spacecraft. As soon as the spacecraft receives the signal it returns one to the complex. From the signal's round trip a time offset can be measured. For *RXTE* this technique provides an absolute timing accuracy of 5 μs. Ten such calibrations are performed by the *RXTE* Mission Operations Centers (MOC) a day (Rots et al., 1998).

4.2 The Scientific Instruments

There are three main science instruments aboard *RXTE*: the Proportional Counter Array (PCA), the High Energy X-ray Timing Experiment (HEXTE), and the All Sky Monitor (ASM).

The proportional counter array (PCA) consists of 5 identical proportional counter units (PCUs). Each PCU is a xenon/methane multi-anode proportional counter. The PCA assembly is shown in Figure 4.2. The PCA is sensitive to photons in the 2–60 keV band. It has 256 spectral channels and has an energy resolution ($\Delta E/E$) of 18% at 6 keV. The PCA has a large effective area $\sim$7000 cm^2, and a collimated 1°×1° field-of-view (FOV) at full width half maximum (FWHM). The PCA was built by the Exploring the Universe (EUD, formerly known as the Laboratory for High Energy Astrophysics, LHEA) division of NASA at GSFC.

HEXTE is composed of two independent clusters, each containing four Na(Tl)CsI(Na) phoswich scintillation counters and has a 1°×1° FOV (FWHM). It is sensitive to photons in the 15–250 keV range with an energy resolution ($\Delta E/E$) of 18% at 60 keV. HEXTE was built by the Center for Astrophysics and Space Sciences, the University of California, San Diego.

The ASM monitors $\sim$80% of the sky every 90 minutes. It has a 0.2°×1° FOV (FWHM), with 3' by 15' error boxes at $\gtrsim 5\sigma$. It monitors the $\sim$50 brightest X-ray sources every $\sim$1.5 hours, $\sim$25 transient X-ray sources every $\sim$ day, and is

[2] `http://msp.gsfc.nasa.gov/tdrss/usccs.pdf`

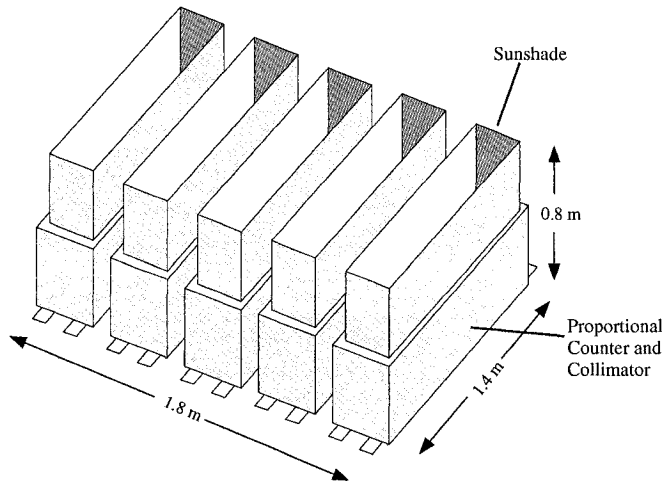

Figure 4.2: The PCA Assembly (5 Units).

constantly on the lookout for new transient X-ray sources. The data from the ASM are made publicly available immediately. The ASM was built by the Center for Space Research (CSR) at the Massachusetts Institute of Technology (MIT).

4.3 Proportional Counter Array (PCA)

Out of the three instruments aboard *RXTE* only the PCA was used in this thesis. The operating principles of proportional counters are outlined in § 4.3.1, and § 4.3.2 provides a physical description of the PCUs which make up the PCA.

4.3.1 Proportional Counters

Proportional counters usually consist of gas-filled multi-anode detectors. When a photon enters the detector, it interacts with the gas. For energies $\lesssim$50 keV the main interaction is the photoelectric effect. The incident photon will create a primary electron-ion pair. A potential difference applied to the gas, thus the electrons will move towards the anode and the ions to the cathode. The heavier ions will hardly interact with the gas, however the lighter electrons will be accelerated

and collide with the gas and thus will produce more electron-ion pairs. These secondary pairs will produce further pairs and so on; such an event is referred to as a Townsend avalanche. When these clusters of electrons reach the electrode they register as a single event. The number of electrons N which reach the anode is proportional to the energy of the incident photon E: $N = E/\Phi$, where Φ is the energy required to release a secondary electron, which is determined by the type of gas used. The PCUs aboard *RXTE* are filled with Xenon, for which $\Phi = 21.5$ eV. Xenon was chosen for the following reason: to allow for the creation of such an avalanche, the gas must not be electronegative and must be inert in order to avoid chemical reactions between the gas and the detector components. Thus Noble gases are usually used because they satisfy both these properties. Hydrocarbons can also be used but they are usually abstained from because they are flammable.

Sometimes the filler gas will be excited and emit a photon, which will in turn cause a Townsend avalanche and be registered as an event. In order to compensate for this effect, usually a hydrocarbon gas, such as methane (CH_4), is used as a quencher gas. The quencher gas will absorb these residual photons without being ionized. It is for this reason the PCUs are filled with a 90%, 10% xenon-methane mixture.

4.3.2 Proportional Counter Units (PCUs)

A schematic of one of the five PCUs is shown in Figure 4.3. The PCUs are independent and identical, so this section applies to all five. As already mentioned, the PCUs are 90% xenon, 10% methane gas-filled detectors. There are three gas filed signal layers, labeled Layer 1, 2 and 3. The top layer (Layer 1) receives the majority of the soft photons, but all three Layers are susceptible to equal amounts of background photons. Thus for soft sources it increases the signal to noise to maintain only events from the top layer. The anodes in each layer are connected in an interleaved fashion, such that the first anode to the left is connected to every second anode, and the first anode on the right is connected to every second anode. The interleaved anodes are labeled left and right, where left

and right does not refer to which side the anodes are on but the direction from which one starts counting. The anodes closest to the sides of the detector and a fourth xenon layer below the last signal layer are designated anti-coincidence layers. Anti-coincidence simply refers to the technique used to discriminate against events produced by high-energy particles. A high energy particle will be able to traverse the detector from any side, so if a photon is detected simultaneously in the detector and in the anti-coincidence layer it will be rejected. A propane veto layer, is located at the top. The propane layer is there to weed out soft electrons and to serve as a front charged particle anti-coincidence layer. The propane layer has some sensitivity to soft photons ($\sim$1–3 keV) but excluding events from this layer greatly reduces the background.

The gain of the detectors is monitored with a radioactive source (americium, Am^{241}), which is used to determine the energy-channel calibration. Photons that are detected simultaneously with an α particle are assumed to be at 59.6 keV, and are flagged as calibration events. The alpha counter, and the Am^{241} calibration source is located inside the gas chamber.

The FOV of the each PCU is collimated by a half-hexagonal collimator located at the top. The collimator is made up of beryllium-copper sheets which are tin coated. A mylar sheet lies between the collimator and the propane layer and between the propane layer and the first xenon signal layer (see Fig. 4.3).

Each PCU is covered by a shield made of tantalum over tin. The shield prevents cosmic X-rays from entering the detector and absorbs residual high energy X-rays emitted from within the spacecraft created by cosmic ray impacts. As well as an X-ray shield, each PCU has a thermal shield, made up of aluminized kapton (a high-performance plastic film insulator). The operational temperature of the PCU is -15 to 35°C. If the system gets down to a temperature of -14 ± 2°C heaters will be turned on. However, the system is only ever expected to get this cold if it is powered down.

If PCUs are not operating smoothly they are turned off. When analyzing *RXTE* it is important to be aware of the number of operational number of PCUs because this obviously affects the count rate.

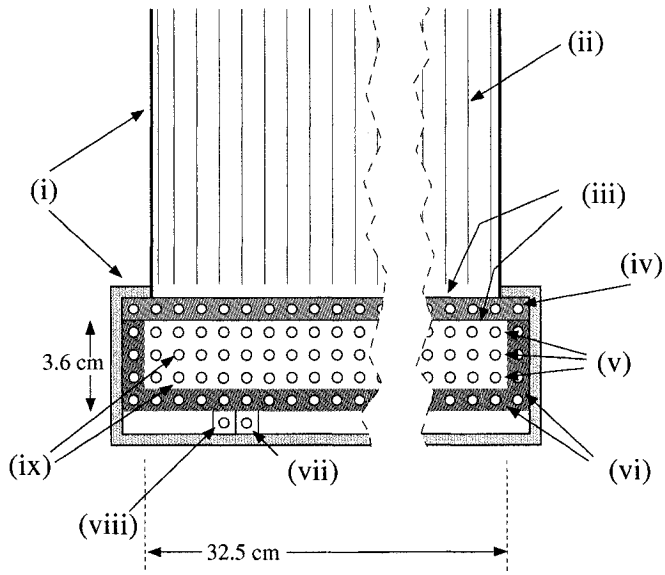

Figure 4.3: One of the five proportional counters: (i) X-ray shielding; (ii) Collimator (hexagonal) 1°×1° FWHM; (iii) Mylar windows (25 μm); (iv) Anticoincidence layer (propane); (v) Three signal layers (xenon/methane); (vi) Anticoincidence chambers (xenon/methane); (vii) Americium source; (viii) Alpha detector; (ix) Anodes.

The PCA is subject to a great deal of cosmic and instrumental background. However, the PCA does not do any filtering; all the events are passed to and evaluated by the on-board electronics.

4.4 Experimental Data System (EDS)

RXTE's large collecting area results in enormous countrates. Because of the large collecting area of the PCA, count rates can get very large. Thus the data are processed and compressed by the on-board electronics before being telemetered to the ground. The Experimental Data System (EDS) is an on board microprocessor used to process data from the PCA and the ASM. The EDS is composed of 8 Event Analyzers (EAs). Six of those are dedicated to the PCA and the other

2 are reserved for the ASM. As well as the EAs the EDS is composed of 2 system managers and 1 power distribution board. The EDS was built by MIT's CSR.

As mentioned in the previous section, the PCA does not do any filtering. All the events are passed directly to the EDS. So, for every X-ray photon that enters the detector the PCU emits an analog pulse, the height of which corresponds to a spectral channel. The PCU electronics amplify these pulses, digitize them and then send them to the EDS which distributes them among the 6 PCA specific EAs. The EDS can time the PCA events to an accuracy of $\sim$1 μs. As well as a timestamp, each event consists of a 3-bit label indicating the PCU it was detected in (5 PCUs yields 3 bits), and 19 bits of other header information, which can be broken down as follows:

- The spectral channel the photon was detected in. 256 channels yield 8 bits.
- The status of the left (L) and right (R) Xenon layer anodes. One bit for each set of anodes (L1, R1, L2, R2, L3, R3), yields 6 bits.
- Whether or not it was a very large event (VLE), 1 bit. A VLE is an event with energy $>$ 75 keV.
- Whether or not it was an event simultaneously detected from the Am^{241} calibration source, 1 bit.
- Whether or not is was detected in the propane layer, 1 bit.
- Whether or not it was detected in the veto layer. Three channels in the veto layer yield 2 bits.

4.4.1 Event Analyzer (EA) Modes and Configurations

There are seven different modes in which the EAs can record PCA data. Each mode has a set of configurable parameters; a mode with a specific set of parameters is called a configuration. There are several configurations available; some of the main ones are described below. For a detailed description of all configurations and the available user parameters for each mode the reader is referred to

the *RXTE* technical appendix[3]. The following EA modes were relevant to the data presented in this thesis:

Event Encoded mode yields a list of event times, thus the user can exploit the 2^{-20} s (~ 1 μs) resolution of *RXTE*. The user is free to filter by spectral channel (256 channel resolution), layer, PCU. Event Encoded mode configurations include:

Good Xenon returns all events from the Xenon layers which were not flagged as background events, which is why this configuration is called "good xenon". `GoodXenon` mode provides the full 256 channels spectral resolution.

Good Xenon with Propane is identical to `GoodXenon` except that it includes all the propane layer events as well.

Transparent more provides all events from the PCA, as well as events that would otherwise be rejected. Because of the indiscriminate nature of this mode it is not useful for astronomical measurements.

Binned Data mode outputs binned time series. The selectable parameters include the time bin width, the spectral channel range and which PCU. Binned Data mode configurations include:

Standard-1 is returned for all observations. It is a binned histogram with a 0.125 s bin width, and is summed over all the 256 channels (no energy resolution). `Standard-1` data only include events which were not flagged as background events.

Standard-2 is returned for all observations. It is a binned histogram with course temporal resolution, 16 seconds. The 256 spectral channels are grouped into 129 channels using the binning scheme given in Table 4.1. Just like `Standard-1` data, `Standard-2` data only comprises events which were not flagged as background events.

[3] `ftp://legacy.gsfc.nasa.gov/xte/nra/appendix-f/`

Channel Boundaries	Grouping	Number of Channels
0–4	combined	1
5–53	unbinned	49
54–135	2	41
136–237	3	34
238–249	4	3
250–255	combined	1
	Total:	129

Table 4.1: Spectral channel binning scheme for `Standard-2` data. The 256 channel spectral resolution of the PCA are grouped together into 129 channels using the above binning scheme.

Burst Catcher mode uses two EAs; one serves as a burst trigger and the other is used to record the burst. The trigger criteria are specified by the user. Burst Catcher mode configurations include:

Event Burst Catcher returns the burst as list of photon events. The user can later filter by spectral channel and PCU.

Binned Burst Catcher returns a binned histogram of the burst in a user specified spectral channel band. In this configurations data from all PCUs are summed.

How these data were acquired and reduced is described in the following chapter.

Chapter 5

Analysis

5.1 The Monitoring Program

In 1996 a program was started at MIT to monitor all five[1] AXPs on a regular basis with *RXTE*. In 2000 I took over this project, which continues to go on, and will hopefully go on until *RXTE* is decommissioned. Our monitoring observations consist of short "snapshots" of all AXPs, with typical exposure times between 1 and 10 ks, depending on the source's signal-to-noise. Figure 5.1 shows the distribution of exposure times of all *RXTE* observations of all AXPs. How often we observe each source depends on the source's variability (variability on all aspects of its emission). Figure 5.2 indicates the coverage of AXPs by *RXTE* throughout its entire mission. *RXTE* observations remain private only for one year, thus we have also incorporated all archival observations of AXPs which were taken before this project's inception.

Our regular monitoring observations of AXPs allow us to measure their rotational stability (§ 5.3.8), and search for variations in their pulse morphology (§ 5.3.7)and pulsed flux (§ 5.3.9). In this chapter I outline the methods used to analyze our *RXTE* observations of AXPs. Further details concerning specific sources or observations is left for their respective chapters. The main result of this thesis was the discovery of bursts from two AXPs. Searching and analyzing bursts in incoming and existing AXP data have become a priority of this project. Details on the burst analysis are left for Chapters 6-8 and 10.

[1]When I took over this project there were only 5 AXPs known. The sixth AXP, XTE J1810–197, was discovered only ~2 years ago (Ibrahim et al., 2004). XTE J1810–197 is not part of the monitoring project, but hopefully data on this source will be incorporated in the future.

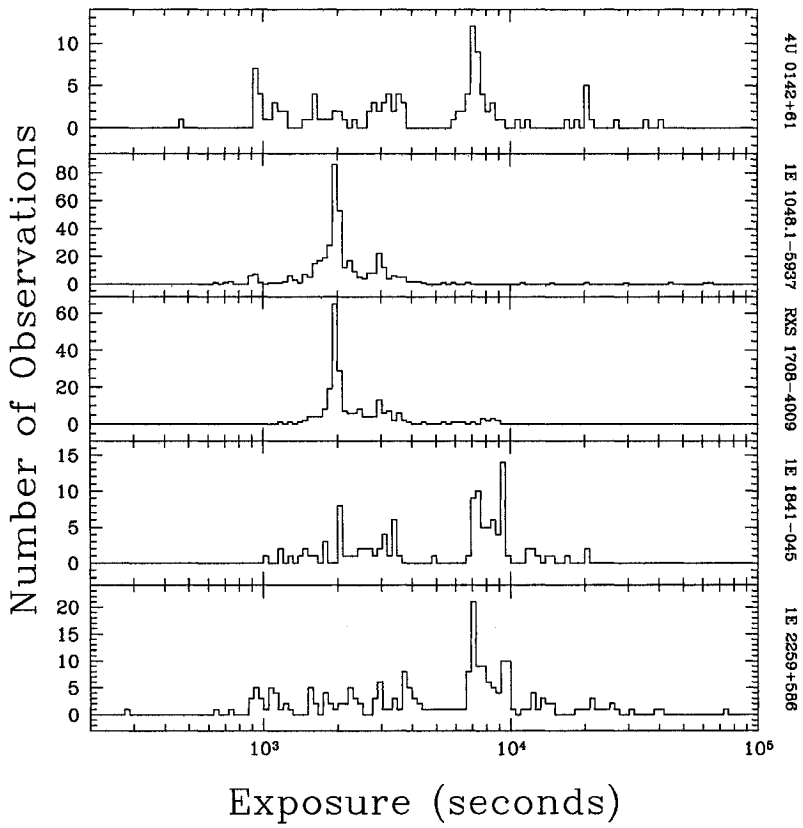

Figure 5.1: Distribution of exposure times of all *RXTE* observations of all AXPs analyzed in this thesis. Note that the exposure times are binned into equi-spaced logarithmic bins.

5.2 Data Format

All data analyzed in this thesis are from the *RXTE*/PCA. With the help of collaborators there were some observations from other instruments as well (see the preface of this thesis). The specific mode used was the `GoodXenonwithPropane` (see § 4.4) mode which returns the time-of-arrival of each photon with 1 μs resolution and maintains the full 256 channel spectral resolution. The data are archived and provided by the High Energy Astrophysics Science Archive Research Center

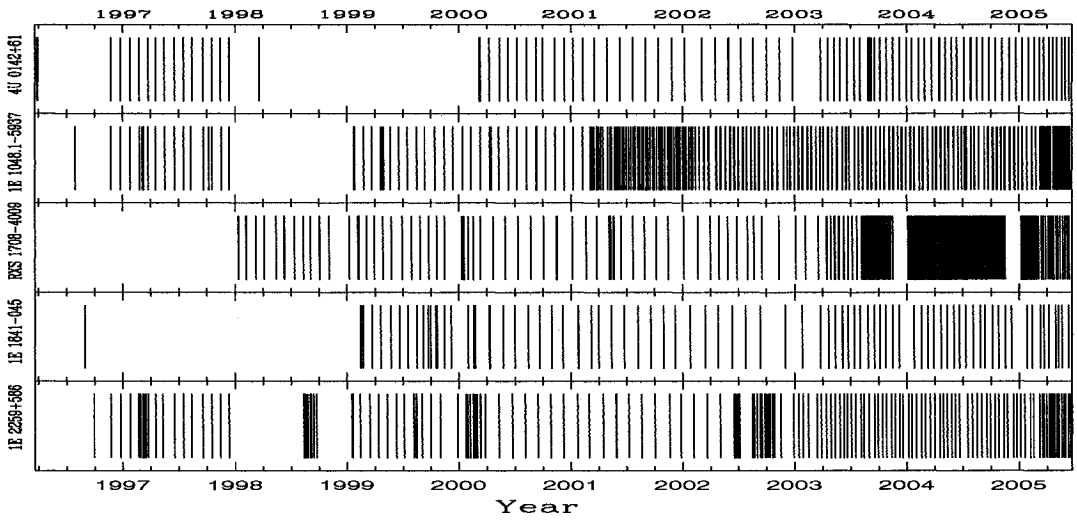

Figure 5.2: Observation frequency of all AXPs with *RXTE*. Each vertical line represents the mid-point of an *RXTE* observation. The large gaps are due to the fact that some sources were added or discovered after our monitoring campaign had begun. Observations to the left of the large gaps were proposed for by other groups. These data were incorporated into this project as soon as they were publicly available.

Online Service[2], provided by the NASA/Goddard Space Flight Center. The data format is in the standard Flexible Image Transport System (`FITS`[3]) format. The CSR at MIT also provides an archive of the data in a binary format commonly referred to as `DS` format. Because the `DS` data become available a lot quicker than the `FITS` format, it was preferentially used since AXPs exhibit transient behavior which may require immediate attention. Software to manipulate `DS` was written by the MIT *RXTE* team and myself.

[2] `ftp://legacy.gsfc.nasa.gov`
[3] `http://fits.gsfc.nasa.gov`

5.3 Timing Analysis

5.3.1 Time Systems

In order to exploit the high temporal resolution capabilities of *RXTE*, one must have an understanding of the time systems relevant to the data. The following time tutorial follows the one given on the *RXTE* mission webpage[4]. International Atomic Time (TAI) is the most precise definition of time, obtained by averaging together various atomic clocks throughout the world. Terrestrial Time (TT) is an artificial time scale which is related to TAI but differs by a constant offset

$$\mathrm{TT} = \mathrm{TAI} + 32.184 \text{ s}. \tag{5.1}$$

The 32.184 s in the above formula is the exact value of the temporal offset between the two systems; it is not a truncated approximation. Universal Time (UT) is defined from 0 hours at midnight to one solar day. Because of variations in the earth's rotation, the solar day is not uniform. To minimize the difference between TAI and UT, Coordinated Universal Time (UTC) was introduced where UTC differs by TAI by an integer (since 1972) number of seconds, or "leap seconds",

$$\mathrm{UTC} = \mathrm{TAI} - (\text{accumulated leap seconds at time TAI}). \tag{5.2}$$

A complete list of the accumulated number of leap seconds from 1972 to the time of the writing of this thesis is given in Table 5.1.

Time Formats

It is common in astronomy to quote time in the format of Modified Julian Date (MJD). The Julian Date (JD) is defined as the number of days since Greenwich mean noon on January 1, 4713 B.C. Modified Julian Date (MJD) is just a truncated JD,

$$\mathrm{MJD} = \mathrm{JD} - 2400000.5 \text{ days}. \tag{5.3}$$

[4] `http://heasarc.gsfc.nasa.gov/docs/xte/abc/time_tutorial.html`

Table 5.1: Number of "leap seconds" from 1972 to present.

Start Date		TAI−UTC
(Date)	(JD)	(s)
1972 JUL 1	2441499.5	11.0
1973 JAN 1	2441683.5	12.0
1974 JAN 1	2442048.5	13.0
1975 JAN 1	2442413.5	14.0
1976 JAN 1	2442778.5	15.0
1977 JAN 1	2443144.5	16.0
1978 JAN 1	2443509.5	17.0
1979 JAN 1	2443874.5	18.0
1980 JAN 1	2444239.5	19.0
1981 JUL 1	2444786.5	20.0
1982 JUL 1	2445151.5	21.0
1983 JUL 1	2445516.5	22.0
1985 JUL 1	2446247.5	23.0
1988 JAN 1	2447161.5	24.0
1990 JAN 1	2447892.5	25.0
1991 JAN 1	2448257.5	26.0
1992 JUL 1	2448804.5	27.0
1993 JUL 1	2449169.5	28.0
1994 JUL 1	2449534.5	29.0
1996 JAN 1	2450083.5	30.0
1997 JUL 1	2450630.5	31.0
1999 JAN 1	2451179.5	32.0
2006 JAN 1	2453736.5	33.0

This table is maintained by the Time Service Department of the US Navy[a]

[a] `ftp://maia.usno.navy.mil/ser7/tai-utc.dat`

When quoting time in JD or MJD it is important to also quote which time system one is using, for example 53000.0000 MJD (UTC) or 53000.0007 MJD (TT). *RXTE* measures time in Mission Elapsed Time (MET), which is the number of seconds elapsed since January 1, 1994 00:00:00 (UTC)[5]. The following are useful

[5] MJD (January 1, 1994 0h UTC) = 49353 MJD (UTC) = 49353 +(28+32.184)/86400 MJD (TT)

formulas for converting MET to MJD (UTC) and MJD (TT).

$$\text{MJD (UTC)} = (\text{MET} + 28 - \delta_{\text{MET}})/86400 + 49353 \text{ days}, \quad (5.4)$$

$$\text{MJD (TT)} = (\text{MET} + 28 + 32.184)/86400 + 49353 \text{ days},, \quad (5.5)$$

where 28 is the number of accumulated leap seconds on January 1, 1994 (see Table 5.1), δ_{MET} is the number of accumulated leap seconds on the specific MET (which can be read off of Table 5.1), and the 32.184 arises from the conversion of UTC to TT (See Eq. 5.1 and 5.2).

5.3.2 Barycentering

RXTE is in a geocentric orbit and the Earth orbits the Sun, therefore from one point in either *RXTE*'s or the Earth's orbit to the next, photons from a celestial source will arrive later or earlier relative to an inertial observer. To avoid these orbital modulations it is useful to measure photon arrival times at some inertial frame of reference. The inertial reference frame used in pulsar astronomy is the Solar System Barycenter (SSB). Following the complete recipe for converting pulsar arrival times to the SSB given on Dr. Craig Markwardt's webpage[6] at GSFC, the barycentric arrival time of a photon is given by

$$t_{\text{b}} = t_{\text{obs}} + t_{\text{clock}} - t_{\text{DM}} + t_{\text{geo}} + t_{\text{E}} - t_{\text{S}}. \quad (5.6)$$

The first term, t_{obs}, is the observed arrival time of the photon. The term t_{clock} is the clock corrections applied to convert the local time, t_{obs}, to TT (see § 5.3.1). This value is instrument-dependent; for *RXTE* the clock correction is ~3.377 s and the fine clock corrections are on the order of tens of microseconds. Both of these values vary with time. Radio photons traveling from a pulsar to an observer are delayed because they are dispersed by the ionized interstellar medium. This

[6] `http://www.lheawww.gsfc.nasa.gov/users/craigm/bary`

dispersion delay is given by

$$t_{\rm DM} = \frac{\rm DM}{2.410 \times 10^{-4}} \left(\frac{\nu}{1 \times 10^6 \ {\rm Hz}} \right)^{-2} \ {\rm s}, \tag{5.7}$$

where ν is the frequency of the bandpass, and DM is the dispersion measure, or the electron density integrated over the distance from the observer to the source. This effect is important for radio waves but for higher frequency emission (optical, IR, X-rays, etc.) this effect is virtually nil (it is only mentioned here for completeness). The most significant effect is $t_{\rm geo}$, which is the time it takes a photon to travel from the observatory to the SSB, given by

$$t_{\rm geo} = \frac{\mathbf{r}_{\rm ob} \cdot \hat{\mathbf{s}}}{c}, \tag{5.8}$$

where $\mathbf{r}_{\rm ob}$ is a vector from the observatory to the SSB, and $\hat{\mathbf{s}}$ is a unit vector from the observatory to the pulsar's position. The unit vector $\hat{\mathbf{s}}$ is determined by the source's right ascension (RA) and declination (DEC). The vector $\mathbf{r}_{\rm ob}$ is obtained by adding the vector from the observatory to the Earth's center ($\mathbf{r}_{\rm o\oplus}$) and the vector from the Earth's center to the SSB ($\mathbf{r}_{\oplus \rm b}$), in other words

$$\mathbf{r}_{\rm ob} = \mathbf{r}_{\rm o\oplus} + \mathbf{r}_{\oplus \rm b}. \tag{5.9}$$

The vector $\mathbf{r}_{\oplus \rm b}$ is provided by the Jet Propulsion Laboratory's planetary ephemeris known as DE200. The vector $\mathbf{r}_{\rm o\oplus}$ for each observation is provided by the *RXTE* team in what are called "orbit files". Because of the motion of the Earth relative to the SSB pulsar, photons are delayed because of the combined effects of Gravitational redshift and time dilation. This is the so-called "Einstein time delay" which is given by

$$t_{\rm E} = 0.001658 \sin(g) + 0.000014 \sin(2g), \tag{5.10}$$

where

$$g = 357.53^\circ + 0.9856003^\circ ({\rm JD} - 2451545.0). \tag{5.11}$$

The "Shapiro delay", t_S, is a relativistic correction due to the bending of a photon's trajectory by the gravitational potential of the Sun. This delay is given by

$$t_S = -\frac{2GM_\odot}{c^3} \log(1 + \cos\varphi), \tag{5.12}$$

where G is the gravitational constant, $M_\odot$ is the Sun's mass, c is the speed of light and φ is the angle between the pulsar-Earth and Earth-Sun vectors. Notice that even at its maximum value $t_S \sim 7$ μs. This of the order of the absolute timing accuracy of *RXTE* so it is negligible for our purposes.

Barycentering is an involved process, but fortunately there are software tools to handle this task which only require as input the RA and DEC of the source and a time series or a list of photon events. For `FITS` data the tool is called `faxbary` which is part of the standard `FTOOLS`[7] package, and for `DS` data the MIT *RXTE* team provides `ds_bary`.

5.3.3 Time series analysis

In its original form each data set is a list of the times of arrivals for each photon as well as header information stating in which channel it was detected, which PCU, etc (see § 4.4). The first step in the analysis is to create a time series. In essence the events are binned into a histogram in a certain spectral channel band that increases the signal to noise. Furthermore, since AXPs have soft spectra we limit the time series to photons from only the top layer of each PCU (see § 4.3.2). The time bins are then barycentered to the solar system barycenter (see § 5.3.2). In what follows, I will outline the several steps followed to reduce the data. I will often use an observation (observation ID 70094-01-10-00) of the source 1E 2259+586 as an example. A time series of this observation binned with 1/32 s time resolution is shown in Figure 5.3. The gaps are earth occultations.

[7] "A general package of software to manipulate FITS files."
(`http://heasarc.gsfc.nasa.gov/docs/software/ftools/`)

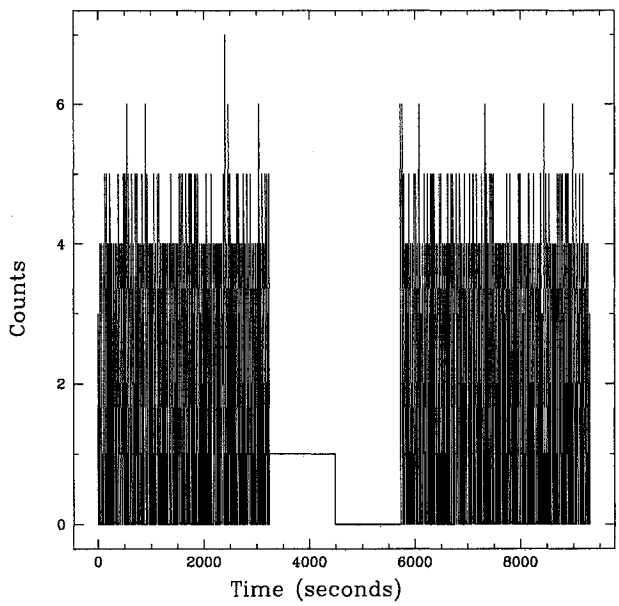

Figure 5.3: A time series of an *RXTE* observation of AXP 1E 2259+586 binned with 1/32 s.

5.3.4 Fourier Analysis

In order to search for a periodic signal with unknown pulse period P, the first step is to perform a Fourier transform (FT). For example if the signal in the time domain is $c(t)$, then its Fourier transform is given by

$$H(\nu) = \int_{-\infty}^{\infty} c(t) e^{i2\pi\nu t} dt, \tag{5.13}$$

where $i^2 = -1$ and $\nu = 1/P$ is the pulse frequency. The signal $c(t)$ can be retrieved by performing the inverse Fourier transform

$$c(t) = \int_{-\infty}^{\infty} H(\nu) e^{-i2\pi\nu t} d\nu. \tag{5.14}$$

Now, the Fourier transform assumes the signal is spread over infinite time and continuous, but real data are neither. Physical data have some finite duration T and are not continuous but discretely sampled at some sampling rate $\nu_{\rm samp} =$

$1/\Delta t$, where Δt is a time bin width. Due to these limitations of real data the Fourier transform becomes the discrete Fourier transform (DFT)

$$H_k = \frac{1}{N}\sum_{n=0}^{N-1} c_n e^{i2k\pi\nu nT/N}, \tag{5.15}$$

where N is the total number of time bins, $N = T/\Delta t$, and the notation c_n refers to the counts in the n^{th} time bin. Notice that for $k = 0$, the complex coefficient H_0 corresponds to the average of the signal,

$$H_0 = \langle c \rangle . \tag{5.16}$$

Here again, the signal can be retrieved by performing the inverse DFT,

$$c_n = \sum_{k=0}^{N-1} H_k e^{-i2k\pi\nu nT/N}. \tag{5.17}$$

The minimum frequency resolution, for a time series with a total integration time T is given by

$$\Delta\nu = \frac{\nu_{\text{samp}}}{N} = \frac{1}{N\Delta t} = \frac{1}{T}. \tag{5.18}$$

Thus, the finite duration of the time series limits the frequency resolution. Now, an important point is that a signal with frequency ν can be completely reconstructed as long as it is sampled at a rate not less than $\nu_{\text{samp}} = 1/\Delta t$ which is half the Nyquist frequency

$$\nu_{\text{Nyquist}} = \frac{\nu_{\text{samp}}}{2} = \frac{1}{2\Delta t}. \tag{5.19}$$

Thus the discrete nature of the data limits the maximum frequency that we can detect $\nu_{\text{max}} = \nu_{\text{Nyq}} = (2\Delta t)^{-1}$. Another effect of the discrete sampling is that the Fourier transform is mirrored about the Nyquist frequency. The Fourier coefficients are divided into "positive" and "negative" frequencies. For example if a time series has N time bins, then the complex Fourier coefficients, H_k from $k = 0...N/2$ correspond to frequencies $\nu = 0...\nu_{\text{Nyq}}$ in steps of $\Delta\nu = T^{-1}$, and from

$k = N/2...N-1$, the Fourier coefficients correspond to frequencies $\nu = -\nu_{\rm Nyq}...0$ in steps of T^{-1}. This effect is known as aliasing. The alias of coefficient H_k corresponds to its complex conjugate $H_{-k} = H_k^*$.

To compute the DFT of a time series by brute force is computationally expensive, especially for time series with long exposure times and/or high time resolution. However there is an efficient algorithm to calculate the above in fractions of the time it would take to calculate the coefficients directly. This algorithm is known as the Fast Fourier Transform (FFT). The easiest FFT algorithm to code requires the data to be a power of 2. If the number of data points is not a power of 2, data points with zero counts are added until the number of data points is a power of two. This is usually referred to "zero padding", and it is equivalent to interpolating in the Fourier domain.

Once an FT of a data set is obtained, it is useful to know how the relative power of the signal is distributed over frequency. The power is given by

$$P_k = H_k^* H_k = |H_k|^2 , \tag{5.20}$$

where the H_k are given by Eq. 5.15 and $*$ denotes complex conjugation. A plot of power versus frequency is referred to as a power spectrum. A "Fourier power spectrum" is shown in Figure 5.4. Figure 5.4 is actually the Fourier Transform of the time series shown if Fig. 5.3. Notice how the $\sim$1/7 Hz signal is now obvious.

5.3.5 Epoch Folding

Notice that the time series in Fig. 5.3 has an exposure of $\sim$9000 s, and from Fig. 5.4 we saw that it contains a $\sim$7 s signal, which means that there are over 1200 individual pulsations in Fig. 5.3. In order to increase the signal-to-noise of the underlying periodic signal we could add all the individual pulsations. This requires transforming the time of each time-bin into a pulse phase (relative to some reference epoch) and making a histogram in pulse phase. This process is commonly refereed to as "folding" the data and the resulting histogram is referred

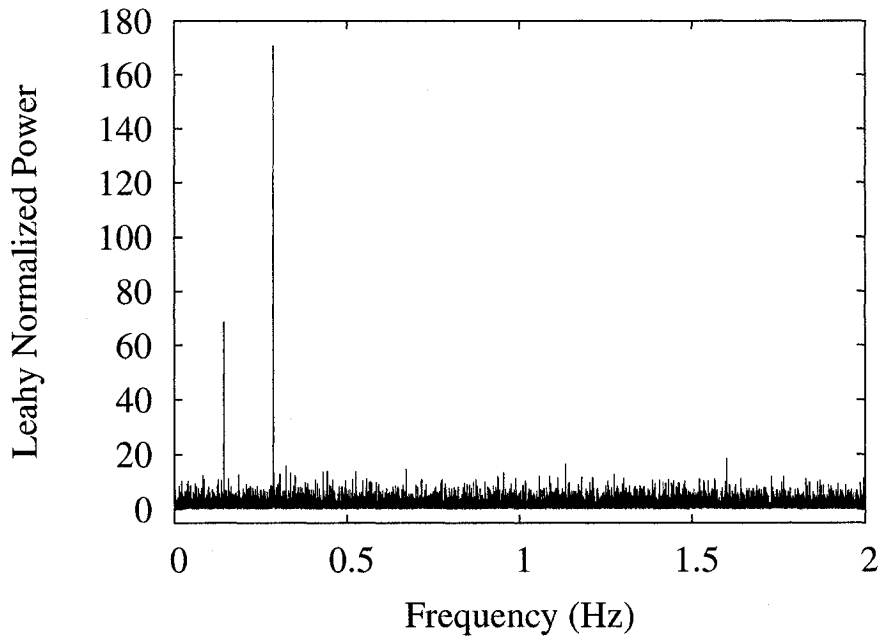

Figure 5.4: An FFT of an *RXTE* observation of AXP 1E 2259+586. Notice the fundamental at ~1/7 Hz and the even stronger harmonic.

to as a pulse profile. Now, the frequency can be Taylor expanded about some reference epoch t_0:

$$\nu(t) = \nu_0 + \dot{\nu}_0(t - t_0) + \frac{1}{2}\ddot{\nu}_0(t - t_0)^2 + \cdots , \tag{5.21}$$

where $\dot{\nu} \equiv d\nu/dt$, etc., and subscript '0' denotes a parameter evaluated at the reference epoch $t = t_0$. Note that even though $(t - t_0)^n$ gets larger with increasing n the above series converges because the term $\frac{d^n\nu}{dt^n}\big|_{t=t_0}(t - t_0)^n$ diminishes with increasing n (i.e. over a certain stretch of time the contribution of the higher order derivatives gets smaller and smaller). The pulse phase is related to the frequency by

$$\frac{d\phi}{dt} = \nu, \tag{5.22}$$

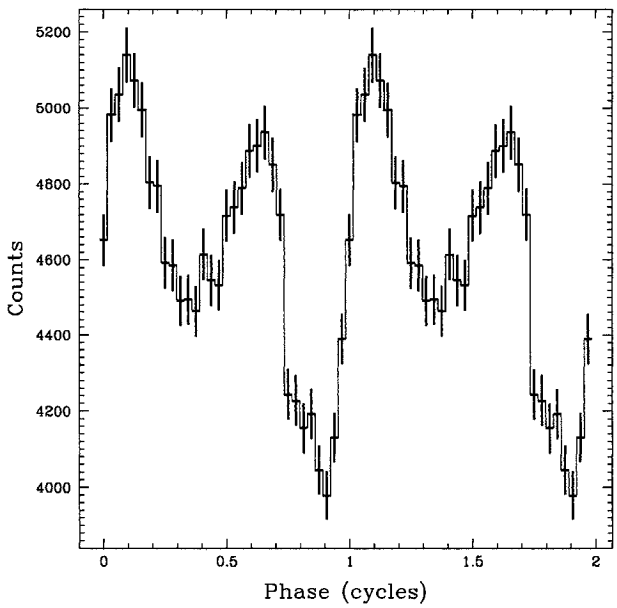

Figure 5.5: A pulse profile of an *RXTE* observation of AXP 1E 2259+586, obtained by folding the time series presented in Figure 5.3.

hence, by integrating Eq. 5.21 the pulse phase ϕ at any time t can be expressed as a Taylor series as well,

$$\phi(t) = \phi(t_0) + \nu_0(t - t_0) + \frac{1}{2}\dot{\nu}_0(t - t_0)^2 + \frac{1}{6}\ddot{\nu}_0(t - t_0)^3 + \cdots . \tag{5.23}$$

How the frequency and its time derivatives (ν, $\dot{\nu}$, $\ddot{\nu}$, $\cdots$) are determined with high-precision is discussed in § 5.3.8.

Figure 5.5 displays a pulse profile made by folding the time series presented in Figure 5.3 with 64 phase bins. Two pulse cycles have been plotted for clarity. Notice that the two-component structure of the profile was evident by the strong second harmonic in its Fourier transform (Fig. 5.4). The error bars are just Poisson errors bars, in other words the error on the counts, c_n, in the n^{th} phase bin is $\sigma_{c_n} = \sqrt{c_n}$.

5.3.6 Period Searching Through Epoch Folding

Another way of searching for a pulsed signal in the case where we have a rough idea of where the frequency should lie, is through epoch folding at different trial frequencies. If there is no signal at a certain trial frequency, then the total number of counts should be equally distributed in pulse phase. In other words, if we fold a time series with N phase bins, if the number of counts p_j in phase bin, j are equally distributed in pulse phase, then $p_j = \langle p \rangle$, where $\langle p \rangle = \frac{1}{N}\sum_{j=0}^{N-1} p_j$. For each trial frequency, we can compare how consistent each resulting pulse profile is with being uniformly distributed in pulse phase by calculating a χ^2 statistic,

$$\chi^2_d = \frac{1}{d}\sum_{j=0}^{N-1}\left(\frac{p_j - < p >}{\sigma_{p_j}}\right)^2, \tag{5.24}$$

where d is the number of degrees of freedom, $d = N - 1$ (1 degree for the frequency), σ_{p_j} is the error on p_j. If one assumes Poisson errors, $\sigma_{p_j} = \sqrt{p_j}$. Equation 5.24 is just the usual χ^2 statistic with the model parameter in the numerator replaced by the average. In the field of statistics this specific variant of the χ^2 test is known as Pearson's χ^2. If at a specific trial frequency the reduced $\chi^2_d \gg 1$, then the pulse profile is inconsistent with being uniformly distributed in pulse phase, indicating a significant pulsation. The true frequency is the one that maximizes Eq. 5.24. A plot of χ^2_d versus period is commonly referred to as a periodogram. A periodogram made by folding the time series in Figure 5.3 through a frequency range centered around the frequency found in the previous section is shown in Fig. 5.6.

5.3.7 Fourier Decomposition of the Pulse Profile

If we have a pulse profile then we can decompose it into its Fourier components by expressing it as a Fourier series

$$p_n = \sum_{k=1}^{N-1} H_k e^{i2\pi kn/N}, \tag{5.25}$$

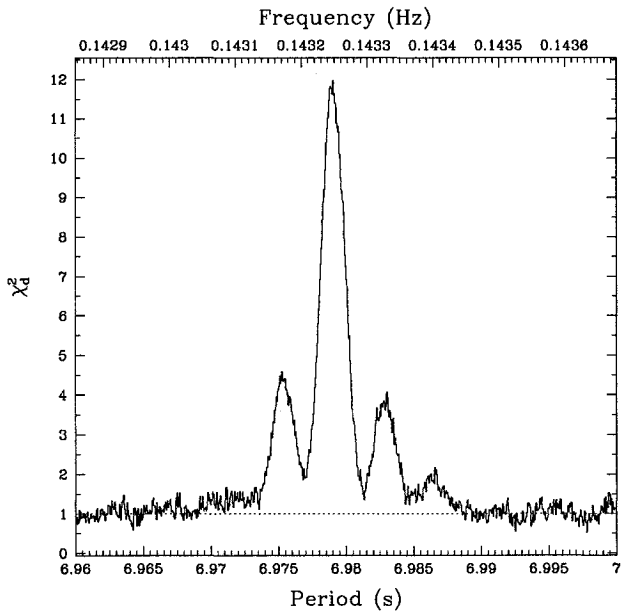

Figure 5.6: A periodogram of an *RXTE* observation of AXP 1E 2259+586.

where p_n is the count rate in the n^{th} phase bin, N is the number of phase bins, and

$$H_k = \frac{1}{N}\sum_{n=0}^{N-1} p_n e^{i2\pi kn/N}. \tag{5.26}$$

We can also write the Fourier coefficients in terms of sine and cosine functions

$$\alpha_k = \frac{1}{N}\sum_{n=0}^{N-1} p_n \cos\left(\frac{2\pi kn}{N}\right), \quad \beta_k = \frac{1}{N}\sum_{n=0}^{N-1} p_n \sin\left(\frac{2\pi kn}{N}\right), \tag{5.27}$$

where $H_k = \alpha_k + i\beta_k$. The variance of the Fourier coefficients is obtained by error propagation

$$\sigma^2_{\alpha_k} = \frac{1}{N^2}\sum_{n=0}^{N-1} \sigma^2_{c_n} \cos^2\left(\frac{2\pi kn}{N}\right), \quad \sigma^2_{\beta_k} = \frac{1}{N^2}\sum_{n=0}^{N-1} \sigma^2_{c_n} \sin^2\left(\frac{2\pi kn}{N}\right), \tag{5.28}$$

where $\sigma^2_{c_i}$ is the variance of the count rate of the n^{th} phase bin, usually taken to be $\sigma^2_{p_n} = p_n$. An advantage of writing the pulse profile in terms of its Fourier

components is that we can low-pass filter our data. For instance, if only the first $N_{\rm harm}$ harmonics, where $N_{\rm harm} \leq N/2$, of a pulse profile are significant then we can smooth out our pulse profile by including only those harmonics in the summation in Eq. 5.25. Note that one must be careful of aliasing when one does such filtering. For instance the $N_{\rm harm}^{\rm th}$ harmonic in Equation 5.26 corresponds to $k = N_{\rm harm} + 1$ and $k = N - 2 - N_{\rm harm}$.

5.3.8 Phase-Coherent Timing

I discussed several methods to determine the pulsation frequency for individual observations. However, given that pulsar frequencies vary with time how does one characterize the long-term evolution of a pulsar's spin frequency? What was traditionally done in X-ray astronomy was to plot individual frequencies as a function of time and fit them to the Taylor expansion of the frequency (Eq. 5.21), including as many frequency derivatives as necessary to minimize a χ^2 statistic. A more precise method is to measure the pulse phase (Eq. 5.23) of each observation, plot it as a function of time including as many frequency derivatives as are necessary to minimize a statistic. The advantage of this technique is that we have an additional constraint that there must be an integer number of rotations between one observation and the next. In fact, we can account for every pulse rotation. There is the caveat that if there is a large gap between one observation and the next we could under- or overestimate the number of pulses by an integer number of rotations. Unambiguous pulse numbering is made possible by obtaining monitoring observations spaced so that the best-fit model parameters have a small enough uncertainty to allow prediction of the phase of the next observation to within ~ 0.2. Typically this requires two closely spaced observations (within a few of hours of each other) followed by one spaced a few days later, and regular monitoring thereafter, as long as phase coherence can be maintained. The following section describes the technique we used to determine the pulse phase.

Cross Correlation

Cross correlation involves comparing two pulse profiles in order to determine the phase offset between them. In order to determine this phase offset we must first fold the data at some reference epoch (t_0). By looking at Fig. 5.5 we see that the peak of the pulse arrived at phase ~0.1 cycles. This is easily read off the figure because it is a high S/N profile. In order to measure the pulse phase in a low S/N profile accurately, we cross-correlate a high S/N profile template with the pulse profile of our observation. The template could either be a long-exposure observation, a sum of many phase-aligned profiles, or a simulated profile with a distinct peak. The cross correlation, of a signal $f(\phi)$ and a high signal-to-noise template $g(\phi)$, is given by

$$C(f,g) = \int_{-\infty}^{\infty} f(\phi)g(\phi + \delta\phi)d\phi. \tag{5.29}$$

The value of $\delta\phi$ which maximizes the above is the optimal phase offset between f and g. Now, via the convolution theorem we can conveniently write the correlation of the two functions in terms of their Fourier transforms,

$$\int_{-\infty}^{\infty} f^*(\phi)g(\phi + \delta\phi)d\phi = \mathcal{FT}\left(\mathcal{FT}(f)\mathcal{FT}(g)\right), \tag{5.30}$$

where $\mathcal{FT}$ represents the Fourier transform. Now, because f is a real function $f = f^*$, so we have

$$C(f,g) = \mathcal{FT}\left(\mathcal{FT}(f)\mathcal{FT}(g)\right). \tag{5.31}$$

The advantage of writing the correlation this way is we can easily apply a low-pass Fourier filter to our profiles. In other words we can set the insignificant Fourier coefficients of f and g to zero as was discussed in § 5.3.7.

Phase Connecting

We can use the phase offset from the peak of the template, $\delta\phi$, to determine the time-of-arrival (TOA) of the pulse peak,

$$TOA = t_0 + \delta\phi/\nu(t_0), \tag{5.32}$$

where t_0 is the reference epoch used to fold the data, and the frequency $\nu(t_0)$ can be determined from Eq. 5.21. Since the phase evolution is modeled as a polynomial (Eq. 5.23) the TOAs can be fit to a polynomial using the pulsar timing software package `TEMPO`[8]. `TEMPO` tries to minimize the following statistic

$$\chi^2 = \sum_{i=1}^{N} \left(\frac{\phi_i - \phi(t)}{\sigma_{\phi_i}} \right)^2, \tag{5.33}$$

where N is the number of TOAs, $\phi(t_0)$ is the model predicted phase at the time of the TOA, ϕ_i is the observed phase with its corresponding error σ_{ϕ_i}. The error on the phase offset is determined by the following Monte-Carlo simulation: we generate 10000 simulated pulse profiles which are determined by adding to the template random noise which was drawn from a Poisson distribution with mean equal to the average of the observed pulse profile. The simulated profiles (template + random noise) are then cross-correlated with the ("noiseless") template and the resulting phase offsets are measured. We then generate a histogram of phase offsets and fit it to a Gaussian distribution, and quote the standard deviation of the distribution (i.e. the spread in phase offset) as the error on the phase.

5.3.9 Pulsed Flux

RXTE is not an imaging telescope; thus, we cannot directly isolate source counts from background counts. However, we can estimate the count rate of the pulsed emission, or pulsed flux, since any counts from the background (counts unrelated

[8] `http://pulsar.princeton.edu/tempo`

to the source) should be uniformly distributed across the pulse phase of the source. The methods described below for calculating pulsed flux follow Bildsten et al. (1997) and Woods et al. (2004)[9]. One way of measuring the pulsed flux is to integrate a folded profile from the pulse minimum to maximum. This way of calculating pulsed flux is usually referred to as the "peak-to-trough" flux. For example, if the count rate as a function of phase is given by $c(\phi)$, then the peak-to-trough pulsed flux is given by

$$\begin{aligned} F_{\rm pt} &= \int_0^1 (c(\phi) - c_{\rm min})\, d\phi \\ &= \langle c \rangle - c_{\rm min}, \end{aligned} \tag{5.34}$$

where $\langle\rangle$ denotes the average. For a sine wave of amplitude A, $c(\phi) = A\sin(2\pi\phi)$, the peak-to-trough pulsed flux is just the amplitude $F_{pt} = A$. A drawback of calculating the pulsed flux in this manner is that this method is very sensitive to deviations from phase bins with large uncertainties. A more robust way of calculating the pulsed flux is to calculate the root mean-square (RMS) of the signal, or RMS pulsed flux. In this case the pulsed flux is defined as

$$\begin{aligned} F_{\rm RMS} &= \left(\int_0^1 (c(\phi) - < c >)^2\, d\phi \right)^{1/2} \\ &= \left(\langle c^2 \rangle - \langle c \rangle^2 \right)^{1/2}. \end{aligned} \tag{5.35}$$

For a sine wave of amplitude A, $c(\phi) = A\sin(2\pi\phi)$, the RMS pulsed flux is just $F_{\rm RMS} = \frac{1}{\sqrt{2}}A$. For reasons that will become clear later, we can write the RMS pulsed flux in terms of the Fourier coefficients of the signal. To do this, first we make use of Parseval's theorem, which states that

$$\langle c^2 \rangle = \sum_{k=-N/2}^{N/2-1} |H_k|^2, \tag{5.36}$$

[9]In Equation 1 of Woods et al. (2004) there is a typographical error of a factor of 2 missing from the coefficients α_k and β_k; similarly a factor of 4 is missing from their respective variances. The calculations in that paper however, used the correct form of the equation.

where the H_k are the complex Fourier coefficients of $c(t)$, see Equation 5.15. Now recall that $H_0 = \langle c \rangle$ and because of aliasing $|H_k|^2 = |H_{-k}|^2$, so we have

$$\langle c^2 \rangle = \langle c \rangle^2 + 2 \sum_{k=0}^{N/2-1} |H_k|^2 . \tag{5.37}$$

Using the above we can rewrite the RMS pulsed flux as

$$F_{\mathrm{RMS}} = \left(2 \sum_{k=1}^{N/2-1} |H_k|^2 \right)^{1/2} . \tag{5.38}$$

This Equation is equivalent to Eq. 5.35, however writing the RMS pulsed flux in this manner has the advantage that we can low-pass filter our pulse profile by simply cutting off our summation at the highest harmonic we wish to include. Thus Eq. 5.38 becomes

$$F_{\mathrm{RMS}} = \left(2 \sum_{k=1}^{N_{\mathrm{harm}}} |H_k|^2 \right)^{1/2} , \tag{5.39}$$

where N_{harm} is the number of harmonics of $c(t)$ that we wish to include, $1 \leq N_{\mathrm{harm}} \leq N/2 - 1$. We can also express the flux in terms of sine and cosine coefficients, $H_k = \alpha_k + i\beta_k$:

$$F_{\mathrm{RMS}} = \left(2 \sum_{k=1}^{N_{\mathrm{harm}}} \left(\alpha_k^2 + \beta_k^2 \right) \right)^{1/2} . \tag{5.40}$$

The variance of F_{RMS}, obtained by propagating the errors, is given by

$$\sigma^2_{F_{\mathrm{RMS}}} = \frac{4}{F^2_{\mathrm{RMS}}} \sum_{k=1}^{\infty} \left(\alpha_k^2 \sigma^2_{\alpha_k} + \beta_k^2 \sigma^2_{\beta_k} \right) , \tag{5.41}$$

where the variances of the Fourier coefficients are given by Equations 5.28 and 5.28.

If we can convert the flux from a count rate to a flux in CGS units we can then compare it to the total flux from the source, obtained from an imaging telescope,

and in turn we can compute the pulse fraction. The pulse fraction is simply the fraction of the total flux which is pulsed,

$$\mathcal{PF} = \frac{F_{\rm max} - F_{\rm min}}{F_{\rm max} + F_{\rm min}}, \tag{5.42}$$

where $F_{\rm max}$ denotes the total flux and $F_{\rm min}$ denotes the "unpulsed" flux (total flux − pulsed flux). In order to convert the pulsed flux from a count rate to CGS units (erg/s) we need to model the spectrum of the source, which brings us to the following section.

5.4 Spectral Analysis

This section reviews how one goes about analyzing spectra from *RXTE*. As mentioned in § 4.2, the PCA on board *RXTE* is capable of returning the channel a photon was detected in, and there are a total of 256 spectral channels corresponding to the energy range ~2−60 keV. The channel-to-energy mapping, which varies with time, is calibrated by the *RXTE* team. One deals with spectra in the following way: if we have a model $M(E)$ which is a function of energy, then the observed spectrum, as a function of spectral channel, S, is given by

$$c(S) = \int_0^\infty M(E) R(S, E) dE. \tag{5.43}$$

Here $R(S, E)$ is the instrumental response, and it corresponds to the probability of observing a photon with energy E in spectral channel S. The instrumental response is usually a smooth function of energy but it is converted to discrete form for computational feasibility.

$$R_{ij} = \frac{1}{E_j - E_{j-1}} \int_{E_{j-1}}^{E_j} R(S_i, E) dE. \tag{5.44}$$

The above is referred to as the response matrix, and its elements correspond to the probability of observing a photon with energy E_j in channel S_i. In discrete

form Equation 5.43 can be written as

$$c_i = \sum_j R_{ij} M(E_j). \tag{5.45}$$

Notice that $c(S)$ is what we observe, however given the response matrix we need to make some guess of the model spectrum and see if it can reproduce the observed spectrum $c(S)$. The inverse of using the response and the observed spectrum to determine the model spectrum, which at first glance may seem more intuitive, is in fact much more problematic; solving for the model spectrum in this way leads to more than one solution and is very sensitive to small perturbations in the observed spectrum.

The model spectrum can either be due to thermal or non-thermal emission from the source, or both. Thermal emission is usually modeled as a blackbody:

$$M(E) = 8.0525A \left(\frac{E^2}{(kT)^4 \left(\exp(E/kT) - 1\right)} \right) dE, \tag{5.46}$$

where A is in units of photons keV^{-1}, $A = (L/10^{39}$ erg s$^{-1})/(d/10$ kpc$)^2$, where L is the luminosity and d is the distance to the source; kT is in units of keV, T is the effective temperature and k is Boltzmann's constant. Many non-thermal high energy astrophysical processes, such as inverse Compton scattering and synchrotron radiation, have power-law distributions

$$M(E) = A \left(\frac{E}{1 \text{ keV}} \right)^{-\Gamma}, \tag{5.47}$$

where Γ is the photon index of the power law and A is the normalization in units of photons keV^{-1} cm^{-2} s^{-1} at 1 keV.

Now an important consideration in spectral fitting is that as photons travel through the interstellar medium they are photoelectrically absorbed. The fraction of the flux that is absorbed is given by

$$dF = -\sigma(E) n_H F d\ell, \tag{5.48}$$

where F is the flux, $\sigma(E)$ is the energy-dependent photoelectric cross-section, n_H is the number density of Hydrogen atoms and ℓ is the distance between the source and the observer. Now, integrating Equation 5.48 from the actual flux F_0 to the observed flux F we find

$$F = F_0 e^{-\sigma(E)\int n_H d\ell}, \tag{5.49}$$

this is usually written as

$$F = F_0 e^{-\sigma(E)N_H}, \tag{5.50}$$

where $N_H = \int n_H d\ell$ is the neutral hydrogen column-density between the source and the observer. The photoelectric cross-section tends towards zero for energies above ~1 keV, so fitting for N_H with *RXTE* data is very difficult since *RXTE* is only sensitive to photons above 2 keV. In spectral fitting we usually rely on N_H measurements made with telescopes which are sensitive to softer photons.

Once a model spectrum is chosen, and a response matrix generated, the spectral fitting program `XSPEC`[10] fits for the parameters in the model spectrum by simply minimizing a χ^2 statistic

$$\chi^2 = \sum_i \frac{\left(c_i - b_i - \sum_j R_{ij} M(E_j)\right)^2}{\sigma_{c_i}^2 + \sigma_{b_i}^2}. \tag{5.51}$$

Here c_i is the observed counts, with variance $\sigma_{c_i}^2$; b_i are the background counts with variance $\sigma_{b_i}^2$; R_{ij} is the response matrix and $M(E_j)$ is the model spectrum. `XSPEC` provides a whole slew of model spectra one can choose, and also allows the user to program their own. The response matrix is generated by the `FTOOL` `pcarsp` and only requires as input the observed spectrum and information about how the observation was filtered.

[10] `http://xspec.gsfc.nasa.gov`

Chapter 6

Magnetar-like X-ray Bursts from an Anomalous X-ray Pulsar

The work presented in this chapter originally appeared in: *Gavriil, F. P., Kaspi, V. M., & Woods, P. M. Magnetar-like X-ray Bursts from an Anomalous X-ray Pulsar. Nature, 419, 142–144, 2002.* References to this chapter should be considered as references to Gavriil et al. (2002) as well.

6.1 Introduction

The suggestion that Anomalous X-ray Pulsars AXPs are magnetars has been controversial (see § 1.5.2, Chapter 3 and references therein). Soft Gamma Repeaters (SGRs) are believed to be magnetars because the high magnetic field provides the torque for their rapid spin-down, as well as the energy to power their bursts and quiescent X-ray emission (Thompson & Duncan, 1995). For a review of AXPs and SGRs see § 1.5 and § 1.6 respectively. AXPs have been suggested to be magnetars, albeit less active, because of their similar spin periods, rates of spin down, location in the Galactic plane, and similar though somewhat softer X-ray spectra to those of SGRs in quiescence (Thompson & Duncan, 1996). The physical difference between the two classes is unknown, but, in the magnetar model, is likely related to the magnitude or distribution of the stellar magnetic field. However, the apparent absence of any bursting behavior in AXPs has led to suggestions that they could be powered, not by magnetism, but by accretion from a disk of material remaining after the birth supernova event (Chatterjee et al., 2000). If so, the observational similarities between AXPs and SGRs must

be purely coincidental. For a review of the magnetar and fall-back disk model see Chapter 2 and Chapter 3 respectively.

Here we report the discovery, from the direction of AXP 1E 1048−5937, of two X-ray bursts that have many properties similar to those of SGR bursts. These events imply a close relationship between AXPs and SGRs, with both being magnetars.

6.1.1 1E 1048.1–5937: an Unusual AXP

The eventual observation of bursts from 1E 1048.1–5937 was predicted by Kaspi et al. (2001) because of the unusual nature of this particular AXP as compared to the others. 1E 1048.1–5937 is a very unstable rotator. Despite periods of instability and glitches all the other AXPs have shown rotational stability lasting more than a few years – making phase-coherent timing possible. 1E 1048.1–5937 is exceptional in that it can only be phase connected for periods of a few months. This level of noisy spin-down is very reminiscent of the rotationally unstable SGRs. 1E 1048.1–5937's pulse profile is also unusual in that it is very sinusoidal, i.e. it shows virtually no harmonic content. Conversely, the other AXPS pulse profiles of the other AXP are rich in harmonic content; in fact AXP 1E 2259+586's pulse profile has more power in its 1st harmonic than in its fundamental. 1E 1048.1–5937's very sinusoidal profile is analogous to the highly sinusoidal pulse profile of the SGRs (however SGRs can show huge morphology changes). Gavriil & Kaspi (2002) also noted that the pulse profiles of all AXPs, except 1E 1048.1–5937, show some level of energy dependence. 1E 1048.1–5937's hard spectrum is also within the SGR range. All these properties led Kaspi et al. (2001) to conclude that 1E 1048.1–5937 might be an AXP-SGR transition object.

6.2 Observations and Analysis

As part of our long-term monitoring program (see § 5.1) of AXPs with the *Rossi X-ray Timing Explorer (RXTE)*, motivated by the existence of SGR bursts, we also searched our AXP monitoring data for bursts. The *RXTE* AXP data set

consists of short (~3 ks) snapshots, as well as longer archival observations, all taken in the PCA `GoodXenonwithPropane` mode (§ 4.4.1), which records photon arrival times with 1-μs resolution, and bins photon energies into 256 channels. See § 4.4 for more details on *RXTE* data. Time series were initially created with 31.25-ms resolution from photons having energies in the range 2–20 keV for each PCA Proportional Counter Unit (PCU) separately, using all xenon layers. Photon arrival times at each epoch were adjusted to the solar system barycenter (§ 5.3.2).

6.2.1 The Burst Search Algorithm

To search for bursts in the resulting time series the following procedure was performed separately for each PCU. First, for each data set, the number of counts in the i^{th} time bin was compared to a local mean λ_i. The local mean was calculated over a ~7 ms stretch of data centered around the time bin being evaluated. A window of ~ 0.6 s was also administered so that counts directly from, and immediately around, the point under investigation would not contribute to the local mean. For the number of counts in a time bin (n_i) greater than the local mean (λ_i), the probability (assuming Poissonian statistics) of those counts occurring by random chance is given by

$$P_i(\mu_i) = \frac{\lambda_i^{n_i} e^{-\lambda_i}}{n_i!}. \tag{6.1}$$

As the probability P_i for each PCU is independent, we calculated the total probability (P_{tot}) of observing a burst simultaneously by all operational PCUs as

$$P_{i,tot} = \prod_{i=0}^{4} P_{i,k}, \tag{6.2}$$

and k corresponds to the PCU under consideration. If a particular PCU were inoperable we set $P_{i,k} = 1$. Events which registered a value of $P_{tot} \leq 0.01/N$, where N is the total number of time bins searched, were flagged as bursts, and were subject to further investigation.

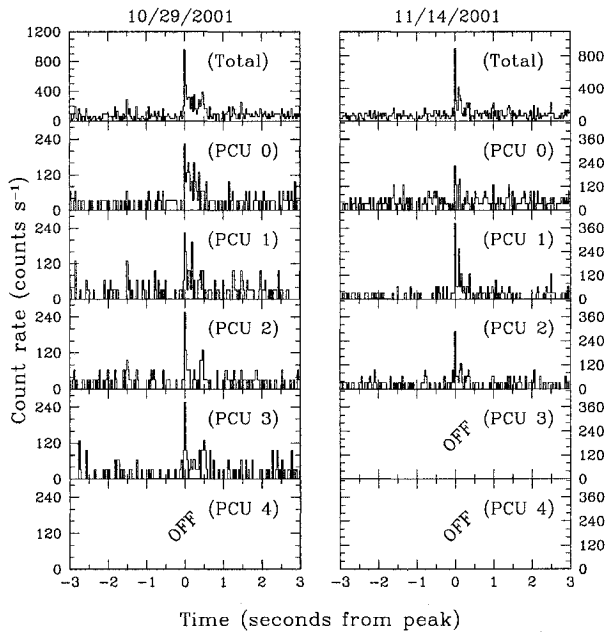

Figure 6.1: Light curves of the observed bursts in separate PCUs. Notice that the bursts are equally significant in all operational PCUs.

6.3 Results

We discovered two highly significant bursts from the direction of AXP 1E 1048.1–5937 using the method described above. The first (hereafter Burst 1) occurred during a 3-ks PCA observation obtained on 2001 October 29 with chance probability $P_{tot} \simeq 6 \times 10^{-18}$ after accounting for the number of trials. A second burst (hereafter Burst 2) was found in a 3-ks observation obtained on 2001 November 14, with analogous probability $P_{tot} \simeq 2 \times 10^{-9}$. No other significant ($\geq$99.9%) bursts were found toward 1E 1048−5937. The total PCA time searched for bursts toward this source was 380 ks in observations obtained from 1996-2002. We verified that there was no significantly enhanced signal from PCA events not flagged as "good" at the times of the bursts (such as those that do not enter through the PCA aperture) in the *RXTE* "Standard 1" (§ 4.4.1) event files. We also verified that both events were clearly detected in all operational PCUs (see Fig. 6.1). Hence the events are unlikely to be instrumental in origin.

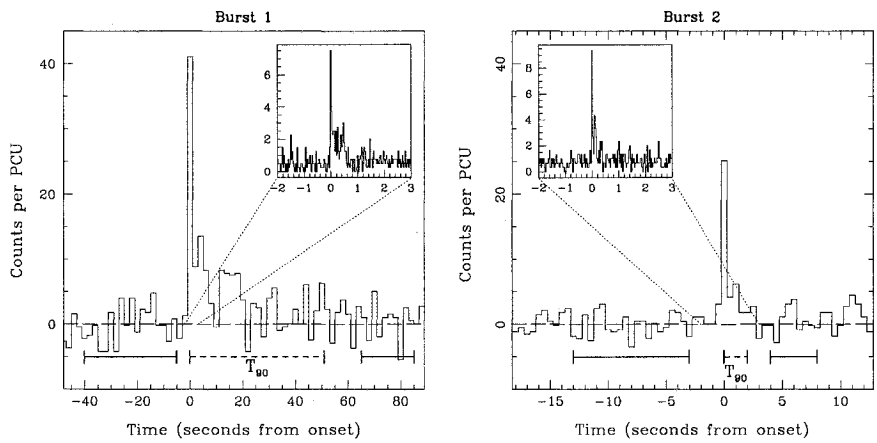

Figure 6.2: Lightcurves for the observed bursts. Left Panel: Background subtracted 2-20 keV lightcurves for Burst 1, displayed with 2-s time resolution. The solid horizontal lines before and after the bursts are the boundaries of the pre- and post-background intervals used for calculating T_{90} and for spectral modeling. The T_{90} interval is shown as a horizontal dashed line. Right Panel: Same but for Burst 2, and with 0.5-s time resolution in the main panel. The insets show the peak of each burst with 31.25-ms time resolution.

6.3.1 Burst Temporal properties

The burst profiles are shown in Figure 6.2. Both are characterized by fast rises and slow decays (see Table 6.1). The burst rise times were determined by a maximum likelihood fit to the unbinned data using a piecewise function having a linear rise and exponential decay. The burst duration, T_{90}, is the interval between when 5% and 95% of the total 2–20 keV burst fluence was received. The background regions used for this calculation are shown in Figure 6.2. Burst 1 appears to have a long, low-level tail that is just above the PCA background as determined by intervals selected before and after the bursts (see Fig. 6.2), while Burst 2 is much shorter. Both bursts arrived at the peak of the AXP pulse within uncertainties in burst arrival time and definition of pulse peak. The probability of this occurring by random chance is $\sim$1%. We note a marginal ($\sim 3\sigma$) increase in the pulsed flux from 1E 1048.1−5937 that commenced with the observation in which Burst 1 was detected, and which lasted $\sim$4 weeks. For a more detailed discussion of this source's long-term pulsed flux evolution see Chapter 9.

Table 6.1: AXP Burst Timing and Spectral Properties.

	Burst 1	Burst 2
Temporal Properties		
Burst day, (MJD)	52211	52227
Burst start time[a], (fraction of day, UT)	0.2301949(24)	0.836323379(68)
Burst rise time, t_r (ms)	21^{+9}_{-5}	$5.9^{+2.0}_{-1.2}$
Burst duration, T_{90} (s)	51^{+28}_{-19}	$2.0^{+4.9}_{-0.7}$
Burst phase[b]	-0.018 ± 0.034	0.051 ± 0.032
Fluxes and Fluences[c]		
T_{90} fluence (counts)	485 ± 118	101 ± 15
T_{90} fluence ($\times 10^{-10}$ erg cm^{-2})	20.3 ± 4.8	5.3 ± 1.2
1-s fluence (counts)	117 ± 13	69 ± 10
1-s fluence ($\times 10^{-10}$ erg cm^{-2})	$5.9^{+8.6}_{-1.9}$	$4.0^{+3.5}_{-0.8}$
Peak flux for 64 ms ($\times 10^{-10}$ erg s^{-1} cm^{-2})	31^{+45}_{-10}	26^{+23}_{-5}
Peak flux for t_r ms ($\times 10^{-10}$ erg s^{-1} cm^{-2})	54^{+79}_{-17}	114^{+100}_{-23}
Spectral Properties[d]		
Power law:		
power law index	$0.89^{+1.8}_{-0.71}$	$1.38^{+0.75}_{-0.62}$
power law flux ($\times 10^{-10}$ erg s^{-1} cm^{-2})	$2.0^{+8.4}_{-1.8}$	$4.0^{+3.5}_{-0.8}$
line energy (keV)	13.9 ± 0.9	...
line width, σ (keV)	$2.2^{+1.3}_{-1.0}$	...
line flux ($\times 10^{-10}$ erg s^{-1} cm^{-2})	$3.9^{+2.2}_{-1.6}$	...
reduced χ^2/degrees of freedom	1.24/15	0.77/5
Black body:		
kT (keV)	$3.9^{+3.7}_{-2.7}$	$3.6^{+2.2}_{-1.3}$
black body flux ($\times 10^{-10}$ erg s^{-1} cm^{-2})	$2.4^{+5.0}_{-2.1}$	$3.8^{+3.3}_{-1.5}$
line energy (keV)	$14.2^{+1.1}_{-1.2}$	...
line width (keV)	$2.1^{+1.5}_{-1.3}$	...
line flux ($\times 10^{-10}$ erg s^{-1} cm^{-2})	$3.7^{+2.2}_{-1.9}$	...
reduced χ^2/degrees of freedom	1.23/15	1.66/5

Uncertainties in the Table are 68% confidence intervals, except for those reported for the CGS-unit fluences and fluxes, as well as the spectral model parameters, for which we report 90% confidence intervals.

(a) The uncertainty on the burst start time is the burst rise time t_r and is given in parenthesis as the uncertainty in the last digits shown; (b) burst phase is defined such that the peak of the periodic pulsation is at phase 0/1; (c) all fluences and fluxes are in the 2–20 keV range; (d) the spectral parameters are derived from fits to a single-component model (power law or blackbody). Because *RXTE* is only sensitive to photons $\geq$2 keV and because of the limited statistics of the burst a two-component fit was not feasible.

6.3.2 Burst Spectral Properties

For all spectral analyses, we first created spectral files having 256 channels across the full PCA energy range (~0.2–60 keV). The burst and background intervals were used as input to the X-ray spectral fitting package `XSPEC`[1] `v11.1.0` (Arnaud, 1996). Response matrices were created using the `FTOOL pcarsp` [2]. For further details on *RXTE* data spectral analysis see § 5.4. To determine the bursts' spectral properties, we first established that neither burst exhibited significant spectral evolution with time by computing hardness ratios (the ratio of 10–60 keV counts to 2–10 keV counts) for the first 0.5-s and subsequent 1.5-s burst intervals. No significant change in hardness was detected, though marginal spectral softening with time was detected after the first 2.5 s of Burst 1. Hardness ratios for Burst 1 and 2 for the 1 s after burst onset were 2.8 ± 0.8 and 1.0 ± 0.3, respectively. We then fit the spectra from the first 1 s of each burst to two one-component models, a power law and a black body (see Table 6.1). Spectral modeling was done using photons in the 2–40 keV range. The spectral rebinning method used in all spectral modeling for Burst 1 was to group the 256 PCA channels by a factor of 4, while for Burst 2, we demanded at least 20 counts per spectral bin. For all spectral fits, the equivalent neutral hydrogen column density was held fixed at 1.2×10^{22} cm^{-2}, the value determined from recent XMM observations (Tiengo et al., 2002).

Continuum models provided an adequate characterization of the Burst 2 spectrum but not of the Burst 1 spectrum. As seen in Figure 6.3, the spectrum for the 1 s after the Burst 1 onset exhibits a feature near 14 keV. This feature is clear in all binning schemes and is prominent throughout the first ~1 s of the burst. No known PCA instrumental effect produces a feature at this energy (K. Jahoda, personal communication). The F-test determines the significance of the addition of an extra model component. If $\chi^2_{\nu_1}$ and ν_1 is the initial reduced χ^2 and the degrees of freedom (d.o.f) of the fit respectively, and if $\chi^2_{\nu_2}$ and ν_2 is the reduced χ^2 and d.o.f of the fit after the addition of an extra model component,

[1] `http://xspec.gsfc.nasa.gov`

[2] `http://heasarc.gsfc.nasa.gov/docs/xte/recipes/pca_response.html`

then the F statistic is given by

$$F = \frac{\chi^2_{\nu_1}/\nu_1}{\chi^2_{\nu_2}/\nu_2}. \tag{6.3}$$

The F-test shows that the addition of a line of arbitrary energy, width and normalization to a simple power law model improves the fit significantly, with a chance probability of this occurring of 0.0032. Monte Carlo simulations in XSPEC were done to verify this conclusion: 10,000 simulations of similar data sets were produced assuming a simple power-law energy distribution, then fit with a power law plus Gaussian line of arbitrary energy, width and normalization. This procedure is conservative, since it ignores that the observed large line has flux comparable to the measured continuum. In 10,000 trials, we found 1 trial with the same or smaller chance occurrence probability as judged by the F-test, indicating that the probability of the line we observed being due to random chance is < 0.0001. We repeated this procedure for data having a black-body spectrum, with similar results, namely the probability of the line being due to chance is < 0.0008. The spectrum also shows possible additional features at $\sim$7 keV and $\sim$30 keV (suggestive of lines at multiples of 1, 2 and 4 of $\sim$7 keV). These additional features are not apparent in all binning schemes and are not statistically significant.

6.3.3 Burst Fluxes and Fluences

T_{90} fluences[3] in CGS units were calculated assuming a power-law spectral model and spectral grouping that demanded a minimum of 20 counts per spectral bin. The 1-s fluences in CGS units correspond to the fluxes found in the spectral modeling. Peak fluxes on the short time scales were determined by scaling the 1-s fluxes by number of counts. The fluxes and fluences of the bursts for various timescales are listed in Table 6.1.

[3]A fluence is a flux integrated over time. It is in units of energy per area.

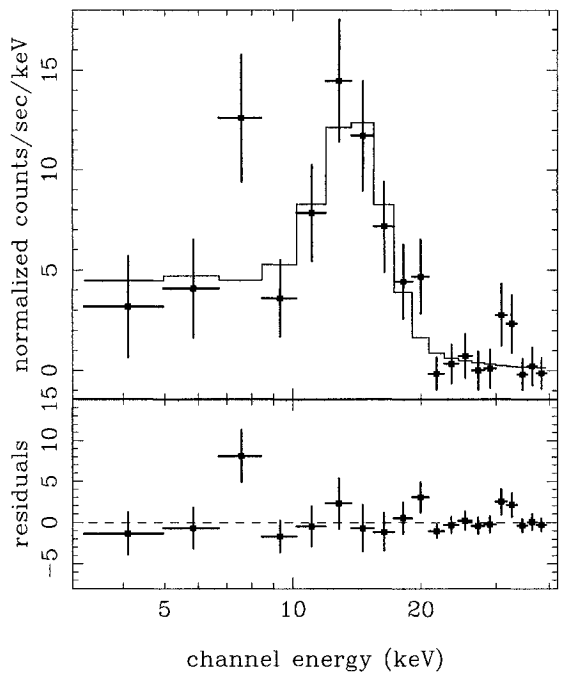

Figure 6.3: X-ray spectrum in the 2–40 keV range for the 1 s after the onset of Burst 1. The spectrum of the first 1 s after Burst 1 onset is not well characterized by any continuum model. The best fit power-law plus Gaussian line model is shown as a solid line. The spectrum also shows possible additional features at ~7 keV and ~30 keV (suggestive of of lines at multiples of 1, 2 and 4 of ~7 keV). These additional features are not apparent in all binning schemes and are not statistically significant.

6.4 Discussion

Due to the wide (~1°) field-of-view (FOV) and lack of imaging capabilities of the PCA, we cannot verify that the bursts originated from the location of the AXP. The low peak X-ray fluxes of the events (see Table 6.1) preclude determining the source's location using data from other, better imaging instruments that were contemporaneously observing the X-ray sky, such as the *RXTE* All Sky Monitor, or the Wide Field Camera aboard *BeppoSAX*. We must therefore consider other possible origins from the bursts before concluding they were from the AXP.

The bursts' short rise times (Table 6.1) require emission regions of less than

a few thousand km, implying a compact object origin. So-called Type I X-ray bursts (see § 1.4) are a well-studied phenomenon that result from unstable helium burning just below the surface of a weakly magnetized neutron star that is accreting material in a low-mass X-ray binary (LMXB) (Lewin et al., 1995). However, Type I bursts from an LMXB in the same FOV as 1E 1048.1−5937 are unlikely to explain our observed bursts because (i) the burst rise times are much shorter than those of Type I bursts; (ii) the burst spectra are much harder than those of Type I bursts; (iii) Burst 2 shows no evidence for spectral softening with time and no Type I burst has ever exhibited a spectral feature like the one detected in Burst 1; (iv) the bursts are extremely faint, implying a source location well outside the Milky Way for Type I burst luminosities (v) there are no known LMXBs in the FOV (Liu et al., 2001). Type II X-ray bursts (Lewin et al., 1995) are a much rarer and less well understood phenomenon observed thus far in only two sources, both accreting binaries. The bursts we have observed are unlikely to be Type II bursts from an unknown X-ray binary in the PCA FOV because (i) of the rarity of such events; (ii) Type II bursts have longer rise times than do our bursts; (iii) no Type II burst has exhibited a spectral feature like that seen in Burst 1.

Classical gamma-ray bursts (GRBs) introduced in § 1.6 sometimes exhibit prompt X-ray emission that can have temporal and spectral signatures similar to those we have observed (Heise et al., 2001). However, the likelihood of two GRBs occurring within 1° of each other is small, and GRBs are not known to repeat. Conservatively assuming GRB spectral model parameters that result in low gamma-ray fluxes and extrapolating the GRB rate (Stern et al., 2001) as measured with the Burst and Transient Source Experiment (BATSE Fishman et al., 1993) assuming homogeneity below the BATSE threshold, we estimate a probability that these events are unrelated GRBs that occurred by chance in the same *RXTE* FOV during our 1E 1048.1−5937 monitoring observations (conservatively neglecting that they occurred within two weeks of each other) of $\sim 9 \times 10^{-5}$.

The observed burst properties are in many ways similar to those seen from

SGRs (Göğüş et al., 2001). The fast rise and slow decay profiles are consistent with SGR time histories, as are the burst durations (neglecting the long, low-level tail of Burst 1). Both AXP and SGR bursts are spectrally much harder than is their quiescent pulsed emission. The burst peak fluxes and fluences fall within the range seen for SGRs, and the spectrum of Burst 2 is consistent with SGR burst spectra of comparable fluence. Burst 1 has characteristics unlike nearly all SGR bursts, specifically its long tail and spectral feature. However, we note that a single event from SGR 1900+14 was shown (Ibrahim et al., 2001; Strohmayer & Ibrahim, 2000) to possess each of these properties. The marginal increase in the pulsed fraction that we observed at the burst epochs is consistent with SGR pulsed flux increases seen during bursting episodes (Woods et al., 2001). Finally, the fact that in spite of several years of monitoring, the only two bursts detected occurred within two weeks of each other suggests episodic bursting activity, the hallmark of SGRs. Thus, the characteristics of these events match the burst properties of SGRs far better than any other known burst phenomenon.

In the magnetar model for SGRs (see Chapter 2 and references therein), bursts are a result of sudden crustal yields due to stress from the outward diffusion of the huge internal magnetic field. Such yields cause crust shears which twist the external magnetic field, releasing energy. Thompson & Duncan (1996) who, upon suggesting that AXPs are also magnetars, predicted X-ray bursts should eventually be seen from them. By contrast, in no AXP accretion scenario, whether binary or isolated fall-back disk, are SGR-like bursts expected.

The large 14-keV spectral line in Burst 1 is intriguing. An electron cyclotron feature at this energy E implies a magnetic field of $B \simeq 1.2 \times 10^{12}$ G (calculated via Eq. 1.26 using $m = m_e$, where m_e is the electron mass), while a proton cyclotron feature implies $B \simeq 2.4 \times 10^{15}$ G. The former is significantly lower than is implied from the source's spin-down and is typical of conventional young neutron stars, rather than magnetars. The latter is higher than is implied by the spin-down yet reasonable for the magnetar model as the spin-down torque is sensitive only to the dipolar component of the magnetic field. Spectral features have also been seen in SGR bursts. Ibrahim et al. (2002) discovered a 5.0 keV

absorption feature in a burst from SGR 1806−20. The burst's spectrum had evidence for features at higher harmonics of 5.0 keV. The SGR spectral feature was much narrower (σ =0.2 keV) than the one reported here (σ=2 keV). Ibrahim et al. (2002) also interpreted their feature as a proton-cyclotron feature, which implied a magnetic field of 1.0×19^{15} G for SGR 1086−20. This value is in good agreement with the one measured from the spin-down of this source (8×10^{14} G). If confirmed, features such as the one reported by Ibrahim et al. (2002) and the one reported here will provide independent evidence for magnetar-strength fields in SGRs and AXPs.

Why do the burst rates of AXPs and SGRs differ so markedly, in spite of their common magnetar nature? One possibility is that AXP internal magnetic fields are much larger than those of SGRs; if so, AXP crusts can undergo plastic deformation rather than brittle fracturing (Thompson & Duncan, 1996). However, this is opposite to what is inferred from the two classes' spin-down rates, suggesting the latter is an unreliable internal field indicator. This could help reconcile the contrasting radiative properties of AXPs and apparently high-magnetic field radio pulsars (Pivovaroff et al., 2000). It also suggests that AXPs are SGR progenitors, with bursting behavior commencing as the field decays. This is consistent with the smaller AXP ages implied by their more numerous associations with supernova remnants (Gotthelf et al., 1999), but does not explain why AXPs and SGRs have similar spin period distributions, since AXPs spin down as they age (Gaensler et al., 2001). This aspect of magnetar physics remains a puzzle.

6.5 Summary

This Chapter reported on the discovery of two X-ray bursts from the direction AXP 1E 1048.1–5937 using *RXTE*. This was the first time such a phenomenon was observed from any AXP. Unfortunately, we could not unambiguously identify 1E 1048.1–5937 as the burster because of the large (1°×1°) FOV of *RXTE*, but after evaluating other possible origins for the bursts we concluded that the AXP was the most likely source. The bursts were very similar to those seen uniquely

from SGRs. SGR bursts can only be explained within the context of the magnetar model, thus if the bursts from 1E 1048.1–5937 are confirmed this marks a major advance for the magnetar model for AXPs. In the next chapter we will report on a major outburst involving over 80 bursts from another AXP, 1E 2259+586. As well as bursts the outburst consisted of several changes to the source's persistent and pulsed emission.

Chapter 7

A Major SGR-like Outburst and Rotation Glitch in the No-Longer-So-Anomalous X-ray Pulsar 1E 2259+586

The work presented in this chapter originally appeared in: *Kaspi, V. M., Gavriil, F. P., Woods, P. M., Jensen, J. B., Roberts, M. S. E., & Chakrabarty, D. A Major SGR-like Outburst and Rotation Glitch in the No-Longer-So-Anomalous X-ray Pulsar 1E 2259+586. Astrophysical Journal Letters. 588, L93–L96, 2003.* References to this chapter should be considered as references to Kaspi et al. (2003) as well.

7.1 Introduction

As reported in the previous chapter, the detection of two weak X-ray bursts from the direction of AXP 1E 1048.1–5937 argued for AXPs being magnetars. That AXP had previously been identified as one that was most likely to burst on the basis of its unstable timing behavior which was reminiscent of that seen in SGRs, and because of its SGR-like spectrum (Kaspi et al., 2001).

1E 2259+586, a 7-s AXP in the supernova remnant CTB 109 (Fahlman & Gregory, 1981), in contrast to 1E 1048.1–5937, has shown remarkably stable timing behavior and pulsed X-ray fluxes in the past 5.6 yr (Kaspi et al., 1999; Gavriil & Kaspi, 2002). It also has the smallest inferred surface dipolar magnetic field of all AXPs (and SGRs for which it has been determined), and has an X-ray spectrum softer than those of the SGRs. Past observations have suggested, however, that the pulsar may experience epochs of activity, including flux, timing,

and pulse profile variations (Iwasawa et al., 1992; Corbet et al., 1995; Baykal & Swank, 1996).

Here we report a major SGR-like outburst from the AXP 1E 2259+586, in which over 80 X-ray bursts were detected along with a variety of significant changes to the pulsed and persistent emission. Simultaneously the pulsar suffered a large spin-up glitch (§ 1.3.4), and subsequent enhanced spin-down. We also report on infrared and radio observations made just after the outburst. This discovery demonstrates that *any* AXP can burst, and conclusively confirms the connection between AXPs and SGRs, as was proposed in the magnetar model by Thompson & Duncan (1995).

7.2 Observations and Results

The 1E 2259+586 outburst was detected in an observation that was made as part of our long-term *Rossi X-ray Timing Explorer (RXTE)* AXP monitoring program (see § 5.1). Unexpectedly, bursts were seen during a 14.4 ks observation on June 18, 2002 (UT 15:39). The total on source exposure time was 10.7 ks. Data were taken with the Proportional Counter Array (PCA) in `GoodXenonwithPropane` mode (§ 4.4.1), which records photon arrival times with 1-μs resolution, and bins photon energies into 256 channels. In subsequent analysis, photon arrival times at each epoch were adjusted to the solar system barycenter (§ 5.3.2). The resulting time series were analyzed in a variety of ways. Figure 7.1 shows the lightcurve binned with 125 ms time resolution, along with time series of several properties of the pulsed and persistent emission (see below). The decreasing burst rate and flux throughout our observation clearly indicates that we observed only the end of an event that commenced prior to the start of our observations. Lightcurves in the three operational PCUs look similar. Only the largest burst showed any excess in the PCA Standard 1 (§ 4.4.1) "Remaining Counts," however, the flux correction due to deadtime is minimal (~10%). A detailed description of the bursts as well as how they were identified is given in Chapter 8. Follow-up *RXTE* observations on June 20 revealed no further bursts, nor have any of the

15 observations, each of duration 7–8 ks, obtained every ~10 days since. Neither target-of-opportunity observations obtained with the *XMM-Newton* satellite on June 21, nor *XMM-Newton* observations scheduled fortuitously 7 days prior to the burst, revealed any additional bursts (Woods et al., 2004). The *RXTE* All Sky Monitor observed the field on June 18 at UTs 03:50 and 14:43 for ~90 s per observation but detected no enhanced flux, with 99% confidence upper limits of 1×10^{-9} erg s^{-1} cm^{-2} (2–10 keV).

In spite of the large (1°×1°) field of view of the PCA, we are certain that the AXP is the origin of the bursts, as many properties of the pulsed emission were simultaneously observed to change dramatically (Fig. 7.1). The persistent flux evolution was determined as follows. A spectral analysis was done using the `XSPEC` software package v11.2.0 [1], in which the preburst PCA data for 1E 2259+586 were modeled using the best available background models made with the `FTOOL` `pcabackest`[2], the pulsar spectrum as determined using a *XMM-Newton* observation of the pulsar made 1 week before the burst observation (Woods et al., 2004), and an additional component to account for the remaining emission in the PCA field-of-view. The burst data were modeled by a blackbody plus power-law component, while holding the pulsar equivalent neutral hydrogen column density and the remaining emission model fixed. The resulting persistent fluxes are shown in Figure 7.1 (second panel from the top). The pulsed flux evolution, also shown in in Figure 7.1 (second panel from the top) was calculated by first folding ~200 s long data segments with the spin ephemeris (Table 7.1), then summing the first six harmonics of the normalized Fourier powers of the resulting pulse profiles (see Eq. 5.40). The total 2–10 keV fluence over and above the quiescent flux is 2×10^{-6} erg cm^{-2}, two orders of magnitude above that in the bursts. As is also seen in Figure 7.1, the pulsar spectrum clearly hardened during the outburst, and relaxed back toward the quiescent spectral parameters during the course of the observation. The fitted blackbody radius remained approximately constant throughout. Interestingly, the same cannot be said of the ratio of power-law to

[1] `http://xspec.gsfc.nasa.gov`
[2] `http://heasarc.gsfc.nasa.gov/docs/xte/recipes/p2.html`

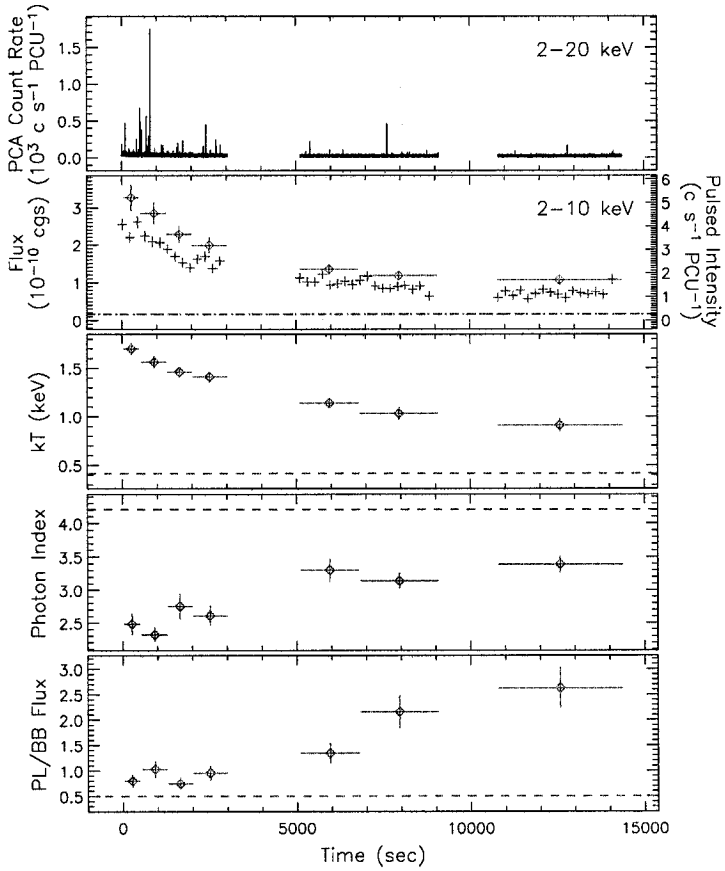

Figure 7.1: Lightcurve and time evolution of persistent and pulsed emission during the burst observation. Top panel: 2–20 keV *RXTE/PCA* lightcurve for 1E 2259+586 on June 18, 2002, at 125 ms resolution. The gaps are Earth occultations. 2nd panel: Unabsorbed persistent (diamonds) and pulsed (crosses) fluxes in the 2–10 keV band. The vertical scale of each parameter has the same relative range to show the lower pulsed fraction within this observation relative to the pre-burst value. The horizontal dashed (dotted) lines denote the quiescent (pre-burst) levels of each parameter. 3rd panel: Blackbody temperature of the persistent and pulsed emission spectrum assuming a two-component model consisting of the blackbody and a power law. The same spectral fits show that the blackbody radius remained at $\sim$1 km throughout. 4th panel: Power-law photon index of the persistent and pulsed emission spectrum for same model as in the 3rd panel. 5th panel: Ratio of the unabsorbed 2–10 keV power-law flux and the bolometric blackbody flux.

Table 7.1: Spin Parameters for 1E 2259+586

Parameter	Value[a]
No. TOAs	112
Range (MJD)	50356–52575
Epoch (MJD)	52400.0000
ν (Hz)	0.1432870351(3)
$\dot{\nu}$ ($\times 10^{-15}$ Hz s^{-1})	$-9.811(8)$
$\ddot{\nu}$ ($\times 10^{-24}$ Hz s^{-2})	1.28(9)
Glitch Epoch (MJD)	52443.9(2)
$\Delta\nu$ ($\times 10^{-7}$ Hz)	5.88(4)
$\Delta\dot{\nu}$ ($\times 10^{-14}$ Hz s^{-1})	$-1.09(7)$
rms Residual (ms)	102

(a) Numbers in parentheses are TEMPO-reported 1σ uncertainties.

blackbody flux; as is seen in the bottom panel of Figure 7.1, the latter continued evolving away from the quiescent state during our observation.

A significant change in the pulse morphology was observed at the burst epoch, as shown in Figure 7.2. During the outburst, the amplitudes of the peaks relative to the pre- and post-outburst profiles are clearly reversed. The relative phase displayed above is that successfully used in our timing analysis (see § 5.3.8). The profile change is similar in different energy bands. This different pulse profile persisted for at least 2 days following the outburst, and gradually returned to its pre-outburst morphology after ~6 days (Woods et al., 2004).

The star underwent a sudden spin up or "glitch" (§ 1.3.4) at the outburst epoch. Briefly, time series were folded at the nominal pulse period to yield pulse profiles at each observing epoch. These profiles were then cross-correlated with a high signal-to-noise average template, obtained by summing all available *RXTE* from pre-outburst epochs, to yield times-of-arrival (TOAs). TOAs were modelled using the TEMPO[3] software package. For details regarding how the timing analysis was done, see § 5.3.8 and Gavriil & Kaspi (2002). For the burst and immediate post-outburst data, the pulse profile changes described above resulted

[3]http://www.atnf.csiro.au/research/pulsar/timing/tempo

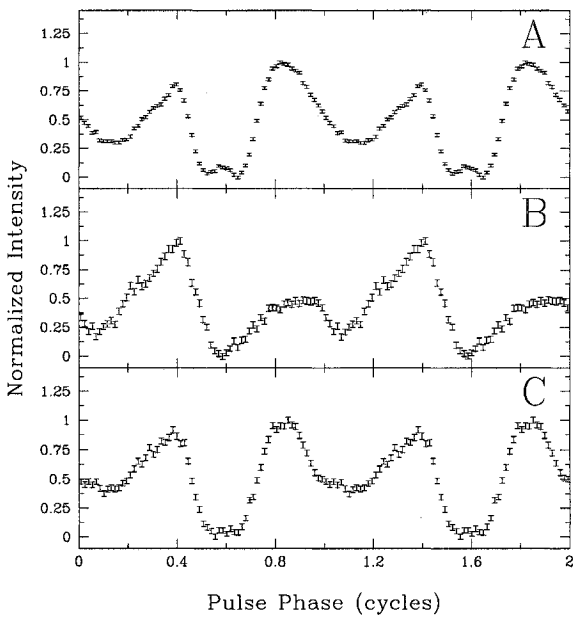

Figure 7.2: Average pulse profiles of 1E 2259+586 in the 2.5–9.0 keV band. Two cycles are plotted for clarity. (A) Average profile before the outburst (total exposure time: 764 ks). (B) Average profile during the outburst, with bursts omitted (total exposure time: 11 ks). (C) Average profile beginning 12 days after the outburst (total exposure time: 108 ks).

in obvious phase jumps corresponding to the two peaks being swapped in the cross-correlation. The glitch epoch was determined by requiring zero phase jump between pre- and post-outburst ephemerides. The *RXTE* data obtained during and after the burst are well characterized (rms residual 1.5% of the period for the full data set) by $\Delta\nu/\nu = (4.10 \pm 0.03) \times 10^{-6}$, similar to that observed in radio pulsar glitches (Lyne & Smith, 1990). The best-fit glitch epoch is consistent at the $< 1\sigma$ level with having occurred during our observation. Additionally, the spin-down rate can be modeled as having approximately doubled abruptly. Precise spin parameters are given in Table 7.1. Residuals from the last ~100 days of timing suggest that the spin-down rate may have relaxed back to near its pre-burst value by ~60 days post-outburst, however additional observations are required to confirm this.

The following infrared data analysis was performed by Joseph B. Jensen (see

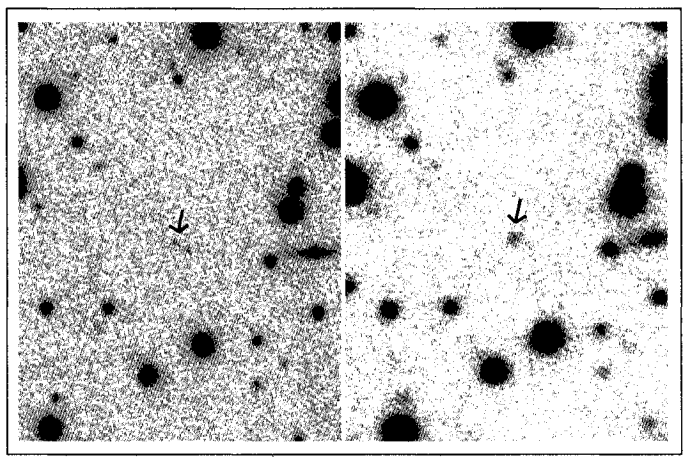

Figure 7.3: Near-infrared images of the 1E 2259+586 field pre- (left) and post-outburst (right). The AXP position is indicated by an arrow. The left image (Hulleman et al., 2001b) is that obtained at the *Keck* observatory in September, 2000 (courtesy F. Hulleman).

the preface of this thesis). Target-of-opportunity near-infrared observations were made using the NIRI instrument at the 8-m *Gemini*-North telescope in Hawaii on June 21 at UT 14:44 using a K_s filter (0.15 μm wide centered on 2.15 μm). The observation had total exposure 1530 s with 0.7″ seeing and light cirrus. The data were reduced using the *Gemini* `IRAF` package and photometry performed using standard `IRAF` procedures. The proposed infrared counterpart (Hulleman et al., 2001b) of 1E 2259+586 had magnitude 20.36 ± 0.15, 1.33 ± 0.22 mag (factor of $3.40^{+0.77}_{-0.62}$) brighter 3 days after the outburst than was observed in a 2000 *Keck* telescope observation (Hulleman et al., 2001b). This can be seen clearly in Figure 7.3. A second *Gemini*/NIRI observation was obtained on June 28 at UT 14:51, with 900 s of exposure and 0.55″ seeing. This time, the AXP counterpart had faded to magnitude 21.14 ± 0.21, for a difference relative to the 2000 *Keck* observation of 0.56 ± 0.29 mag (factor of $1.67^{+0.52}_{-0.39}$ in brightness). Photometric measurements on 7 reference objects in the field agreed with those obtained at *Keck* to within 0.007 mag and 0.028 mag for the first and second nights, respectively.

The following radio data analysis was performed by Mallory S. E. Roberts (see the preface of this thesis). Target-of-opportunity radio observations were also made using the *Very Large Array* in New Mexico on June 20, 2002. The 1E 2259+586 field was observed for 2420 s in B array at a central observing frequency of 1424.3 MHz. After standard calibration, imaging and cleaning using the `MIRIAD` software package, an rms noise level of 15 μJy/beam ($4.6'' \times 3.9''$ beam) was achieved. No emission was detected. We place a 3σ upper limit of 50 μJy on the radio flux for this epoch.

7.3 Discussion

The X-ray phenomenology we have observed in this major AXP outburst is all reminiscent of that seen in SGR bursts. The short bursts (Fig. 7.1) are very similar to short SGR bursts. The long, thermally evolving tail is similar to that seen in a handful of SGR bursts (Lenters et al., 2003). A timing anomaly in SGR 1900+14 was seen at the time of the giant flare in 1998 (Woods et al., 2002), as was a pulse profile change and enhanced pulsed and persistent flux (Göğüş et al., 2001). Thus, this AXP has shown uniquely SGR-like bursting behavior. 1E 2259+586 showed the most stable timing behavior of all AXPs in the 5.6 yr prior to this event (Gavriil & Kaspi, 2002), while 1E 1048.1–5937, the only other AXP seen to burst (Chapter 6), showed the least stable behavior, as well as the hardest AXP spectrum (Kaspi et al., 2001). Thus it seems any AXP can burst.

The properties of the outburst solve a number of previously outstanding AXP problems. A similar pulse profile change was claimed previously in data for 1E 2259+586 from the *Ginga* mission in 1989 (Iwasawa et al., 1992). The archival *Ginga* data show no evidence of bursts. The *Ginga* observation probably took place just after an outburst, consistent with the reported timing anomaly at the same epoch (Iwasawa et al., 1992). This suggests that such outbursts occur on decade time scales (Heyl & Hernquist, 1999). In addition, previously reported large X-ray flux variations in 1E 2259+586 and 1E 1048.1–5937 (Iwasawa et al., 1992; Baykal & Swank, 1996; Oosterbroek et al., 1998) that were

called into question by the flux stability observed in the ~5 yr prior to June 2002 (Gavriil & Kaspi, 2002; Tiengo et al., 2002) are now more understandable as enhanced emission due to bursting episodes. Pulsations from the AXP candidate AX J1845−0258 have been detected only once, in spite of multiple observations (Vasisht et al., 2000). This may have been following a similar outburst (though there is no evidence for bursts in the archival *ASCA* data).

The 1E 2259+586 outburst likely resulted from a sudden event in the stellar crust, such as a crustal fracture, which simultaneously affected both the superfluid interior and the magnetosphere. The large spin-up can be explained by the coupling of the faster-rotating superfluid inside the star with the crust, following the unpinning of angular momentum vortices from crustal nuclei (see § 1.3.4 and references therein). The fractional frequency increase is similar to that observed in many radio pulsars (Lyne & Smith, 1990) but is smaller than could have been detected in SGR timing data. However, the factor of two increase in the spin-down rate is unprecedented for radio pulsars, though possibly not for SGRs (Woods et al., 2002). According to glitch theory (Alpar et al., 1993), when the glitch occurs, a portion of the superfluid decouples, decreasing the effective moment of inertia of the star. For fixed external torque, an increase in spin-down rate results. For radio pulsars, the decoupled portion amounts to ~1% of the stellar moment of inertia, corresponding to the observed ~1% increases in spin-down rates (Alpar et al., 1993). For 1E 2259+586, however, most of the stellar moment of inertia would have had to decouple. This could imply a decoupling of core, as opposed to crustal, superfluid.

Alternatively, the external torque could have changed, due to a restructuring of the magnetosphere. Indeed the enhanced X-ray luminosity is too large to be explained as energy dissipated by vortex unpinning (Thompson & Duncan, 1996) or crustal elastic energy (Ruderman, 1991). A decaying magnetar-strength magnetic field can cause severe stress on the crust. A large-scale fracture could trigger vortex unpinning, and, simultaneously, shift magnetic field footpoints, resulting in a magnetospheric reconfiguration (Thompson & Duncan, 1995). The pulse profile variation is unlikely to be a result of the change in magnetospheric

structure (Thompson et al., 2002), since the torque change is much longer-lived. Rather, the profile change probably occurred at the surface; the effective blackbody radius of $\sim$1 km as determined from the spectral fits supports a localized enhancement.

Notably, there is no evidence for an accompanying giant soft gamma-ray flare, as might be expected from a sudden restructuring of the surface magnetic field of a magnetar (Woods et al., 1999). From the *Interplanetary Network* spacecraft, an upper limit on the fluence of a soft gamma-ray flare from 1E 2259+586, near the time of the X-ray outburst, is 5×10^{-7} erg cm^{-2} (25-150 keV) on time scales 0.25-0.5 s (K. Hurley 2002, personal communication). This corresponds to an energy 5×10^{38} erg, six orders of magnitude below that released in the giant SGR flares. This is consistent with the absence of any radio emission post-outburst from 1E 2259+586, as well as with the absence of bright soft gamma-ray flares from this source in the past. Thompson & Duncan (1996) showed that the absence of a large flare in the event of a glitch requires the neutron star crust to have deformed plastically. This demands a magnetic field roughly two orders of magnitude greater than that implied by the spin-down of 1E 2259+586. This could be explained by higher order multipole moments which are negligible at the light cylinder (§ 1.3.3; Eq. 1.56), where the spin-down torque arises.

The characteristic age $\tau \simeq 100-200$ kyr (estimated via Eq. 1.44) of 1E 2259+586 is much larger than the inferred age ($\sim$ 10 kyr) of the supernova remnant CTB 109 in which it resides (Rho & Petre, 1997). It is tempting to explain this discrepancy as being due to the pulsar having episodes of transient accelerated spin-down such as we observed post-outburst. However at least in this instance, the increased spin-down rate could be roughly compensated by the sudden spin-up.

The near-infrared enhancement post-outburst is intriguing. Currently, the magnetar model does not address the origin of such emission. In conventional rotation-powered pulsars, infrared emission is thought to arise from a population of synchrotron radiating electron/positron pairs in the outer magnetosphere (see Lyne & Smith (1990) and references therein). An enhancement is therefore consistent with a change in the magnetospheric field structure suggested by the

torque change. Future observations can test this by comparing infrared variations to the torque evolution.

7.4 Summary

This Chapter reported on a major outburst from AXP 1E 2259+586 involving over 80 bursts as well as several changes to the source's persistent and pulsed emission. The changes included a flux enhancement, a rotational anomaly, a pulse morphology change and spectral variability. This was the second AXP ever observed to burst. The first was 1E 1048.1–5937 (Chapter 6); however, only two weak burst were observed from that source and *RXTE*'s large FOV did not allow us to unambiguously identify 1E 1048.1–5937 as the burster. Here, the numerous changes to 1E 2259+586's persistent and pulsed emission established without a shadow of a doubt that the bursts emanated from 1E 2259+586. The radiative changes in 1E 2259+586 were very similar to the changes observed during SGR-like outbursts. In the next chapter we will show that not only were the bursts qualitatively similar to those of SGRs but also quantitatively similar.

Chapter 8

A Comprehensive Study of the X-ray Bursts from the Magnetar Candidate 1E 2259+586

The work presented in this chapter originally appeared in: *Gavriil, F. P., Kaspi, V. M., & Woods, P. M. A Comprehensive Study of the X-ray Bursts from the Magnetar Candidate 1E 2259+586. Astrophysical Journal, 607, 959–969, 2004.* References to this chapter should be considered as references to Gavriil et al. (2004) as well.

8.1 Introduction

As discussed in the previous chapters, the magnetar model for AXPs was given a boost when SGR-like bursts were detected from two AXPs. Chapter 6 reported on the discovery of two X-ray bursts in observations obtained in the direction of AXP 1E 1048.1–5937. The temporal and spectral properties of those bursts were similar only to those seen exclusively in SGRs. However, the AXP could not be definitely identified as the burster. On 2002 June 18, a major outburst was detected unambiguously from AXP 1E 2259+586, involving over 80 bursts as well as significant spectral and timing changes in the persistent emission (see Chapter 7). Those bursts demonstrated that AXPs are capable of exhibiting behavior observed, until now, uniquely in SGRs, therefore implying a clear connection between the two source classes. Such a connection was predicted only by the magnetar model (Thompson & Duncan, 1996). However, the physical difference between the source classes is as yet unclear; In Chapter 6 and 7 we suggest that AXPs have higher surface magnetic fields than do SGRs, in spite of

the evidence to the contrary from their spin-down properties.

In this chapter, we consider the statistical properties of the 1E 2259+586 bursts in detail, in order to compare them quantitatively with SGR bursts, both to confirm that they have properties sufficiently similar that the two phenomena can definitely be unified, as well as to look for subtle differences that may offer clues regarding the physical distinction between the two classes. Statistical studies of magnetar bursts (e.g. Gögüs et al., 1999; Gögüs et al., 2000; Göğüş et al., 2001) have the potential to yield important information regarding the burst energy injection and radiation mechanisms. Correlations between different burst properties, whether temporal and spectral, can be powerful model discriminators. Burst statistical properties can be compared with other physical phenomenon in order to assist in identifying their underlying cause; for example, they have been used to argue for important similarities between SGR bursts and earthquakes (Cheng et al., 1996).

In this chapter we present a comprehensive analysis of the properties of the bursts seen in the 2002 June 18 outburst of 1E 2259+586. A study of the detailed outburst and post-outburst properties of the persistent and pulsed emission of 1E 2259+586 was presented in Woods et al. (2004).

8.2 Observations and Analysis

The results presented here were obtained using the PCA on board *RXTE*. On 2002 June 18, during one of our regular monitoring observations (*RXTE* observation identification 70094-01-03-00) that commenced at UT 15:39:18, the AXP 1E 2259+586 exhibited an SGR-like outburst (see Figures 7.1 and 8.1). The bursting behavior was detected by online *RXTE* monitors during the observation, and is clearly visible in the PCA "Standard 1" (§ 4.4.1) data. The observation spanned three orbits and had total on-source integration time 10.7 ks. Although some PCUs turned on/off during our observation, there were exactly three PCUs operational at all times. In addition to the standard data modes, data were collected in the `GoodXenonwithPropane` mode (§ 4.4.1), which records the arrival

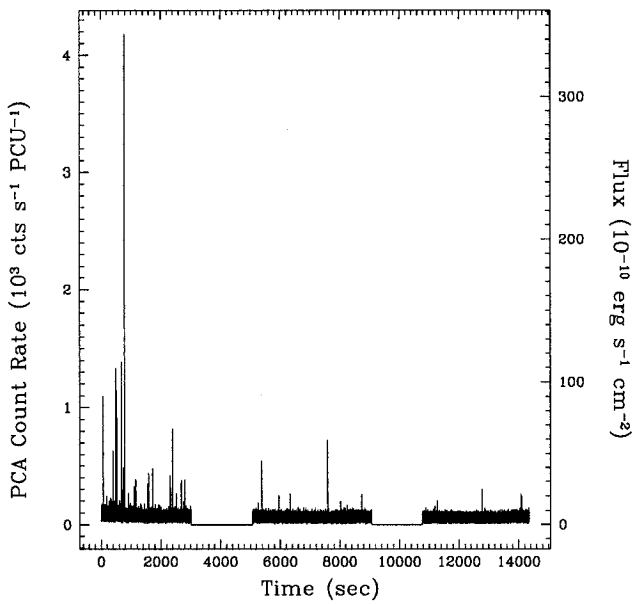

Figure 8.1: 2–60 keV *RXTE*/PCA light curve for 1E 2259+586 on 2002 June 18, at 62.5-ms resolution. The gaps are Earth occultations.

time (with 1-μs resolution) and energy (with 256-channel resolution) of every unrejected xenon event as well as all the propane layer events. Processing of these data was done using software that operated directly on the the raw telemetry data. Photon arrival times were adjusted to the solar system barycenter (§ 5.3.2) using the source position (J2000) given in Table 1.1 and the JPL DE200 planetary ephemeris. Note that following the outburst, Target of Opportunity observations of the source were initiated the next day and continued at different intervals over the subsequent weeks, however no more bursts were seen.

8.2.1 The Adjusted Burst Identification Algorithm

To study the bursts quantitatively, we made use of the `GoodXenonwithPropane` data. Time series were created separately for each PCU using all xenon layers (§ 4.3.2). Light curves of various time bin widths (1/1024 s, 1/256 s, 1/64 s, 1/32 s and 1/16 s) were created to allow sensitivity to bursts on a range of time

scales. The FTOOLs `xtefilt` and `maketime` were used to determine the intervals over which each PCU was off. We further restricted the data set by including only events in the energy range 2–20 keV. We used this energy range, which is larger than that used to study the quiescent pulsations (Gavriil & Kaspi, 2002; Woods et al., 2004), because of the much harder spectra of the bursts relative to the quiescent emission.

We had to slightly modify the burst searching algorithm described in § 6.2.1 to identify bursts here, because during the outburst there was an increase in the pulsed flux (Chapter 7; Fig. 7.1), such that coherent pulsations were visible in our binned light curves. Because of this, the apparent significance of bursts falling near a pulse peak would be artificially enhanced. We compensated for this effect by adjusting the local mean (λ_i) in Eq. 6.1 in the following way: first, for each data set, the number of counts in the $i^{\rm th}$ time bin was compared to a (unadjusted) local mean μ_i. The local mean was calculated over a ~28 s (four pulse periods) stretch of data centered around the time bin being evaluated. A window of ~7 s (one pulse cycle) was also administered so that counts directly from, and immediately around, the point under investigation would not contribute to the local mean. We then modeled the counts per time bin due to pulsations as:

$$p_i = A(\phi_i, t_i)\left[Ce^{-t_i/\tau}\right], \tag{8.1}$$

where $A(\phi, t)$ is the normalized amplitude of the pulsations as a function of pulse phase ϕ and time t. The parameters C and τ are from an exponential fit to the pulsed flux evolution. To verify that our model adequately accounted for the pulsations we Fourier transformed our binned time series with the above model subtracted, see Fig. 8.2. We then calculated an adjusted local mean in the following way:

$$\lambda_i = \mu_i + p_i - \sum_j p_j, \tag{8.2}$$

where the index j spans the windowed stretch of data used to calculate the local mean. Using this adjusted local mean we were now able to follow the rest of the procedure outlined in § 6.2.1.

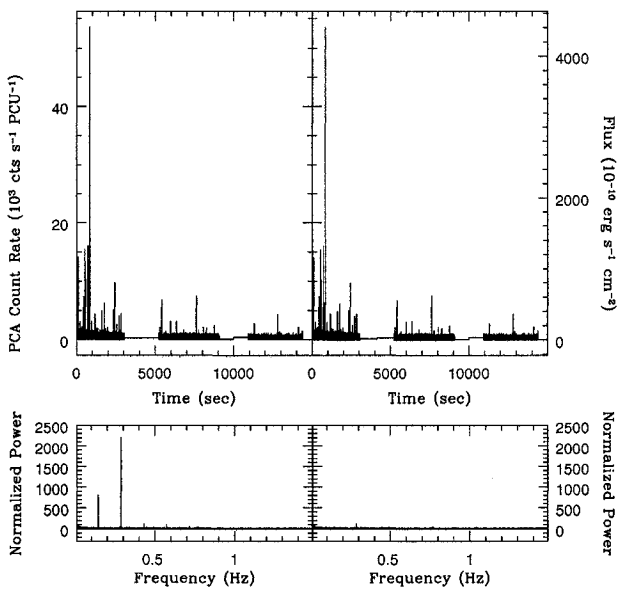

Figure 8.2: Left: 2–60 keV *RXTE*/PCA light curve for 1E 2259+586 on 2002 June 18, at 62.5-ms resolution and its Fourier power spectrum displayed below. Right: Same as left panel but with 1E 2259+586's pulsations (as modeled by Eq. 8.1) removed.

The significance of the number of counts in a time bin can be underestimated if there are one or more bursts in the interval used as the local mean. For this reason, once a burst was identified it was removed from the light curve, and the burst identifying procedure was repeated until there were no additional bursts returned.

8.3 Results

8.3.1 Burst Statistics

Our burst searching algorithm returned 80 significant bursts from the 2002 June 18 observation –this is the total number of unique bursts identified on all time scales we searched. The number of bursts identified depended on the time resolution used: 26%, 55%, 76%, 83% and 74% of all identified bursts were flagged

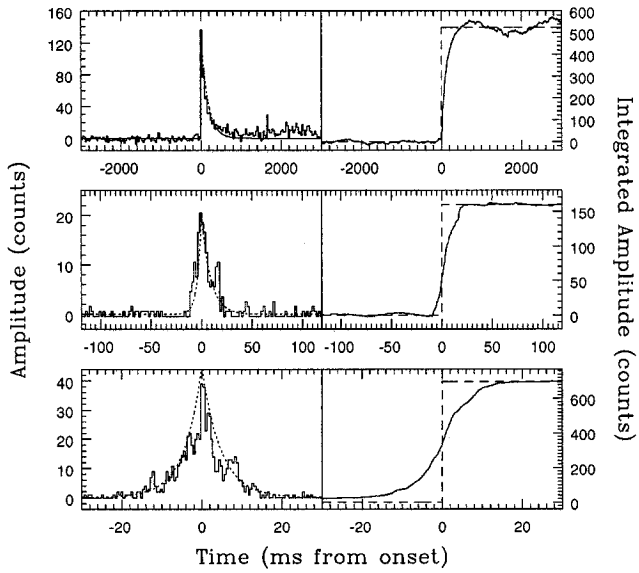

Figure 8.3: Three different examples of bursts seen in the 2002 June 18 outburst of 1E 2259+586. Left: Sample background-subtracted light curves in the energy range 2–60 keV with 1/32 s (top), 1/512 s (middle) and 1/2048 s (bottom) time resolution. The dotted line shows the model fit to the data in order to measure burst rise and fall times (see §8.3.1 for details). Right: Cumulative background-subtracted counts for each burst. The vertical dotted line shows the location of the burst peak. The horizontal dotted line shows the level used in determining the burst fluence. See §8.3.1 for details.

at 1/1024 s, 1/256 s, 1/64 s, 1/32 s and 1/16 s time resolution, respectively. The bursts were single-peaked and had durations $\lesssim$1 s. A small handful ($\sim$12) were bright and had clear fast-rise, exponential decay morphology. In four instances we could not analyze bursts independently because one would fall on the long tail of another. A variety of burst morphologies is shown in Figure 8.3. Some bursts ($\sim$5%) were approximately symmetric, a few ($\sim$3%) fell faster than they rose while most fell more slowly than they rose (see §8.3.1).

Burst Event Times and Phase

The time of each burst was initially defined, using binned light curves, to be the midpoint of the bin having the most counts. To increase the precision of the burst time we refined this value, using the event data which comprised this time bin, to be the midpoint of the times of the events having the smallest temporal separation. We also calculated the occurance in pulse phase for each burst using the time of the burst peak and the rotational ephemeris given in Table 7.1. Comparing the burst phase distribution to the pulse profile of 1E 2259+586 at the time of the outburst, a correlation is seen (Fig. 8.4). To quantify it, we binned the pulse intensity with the same number of phase bins as the burst phase distribution. Least-squares fitting to a straight line yields reduced $\chi^2 = 0.6$. Although when comparing our burst phase distribution to the mean number of bursts per phase bin we find reduced $\chi^2 = 1.5$, the fact that most of the bursts tend to occur when the pulsed intensity is high is very suggestive. We note that the two bursts seen from the AXP 1E 1048.1–5937 (see Chapter 6) were also coincident with the pulse peak, which strengthens the argument that 1E 1048.1–5937 was the source of those bursts. We do not find any other significant correlation between burst phase and any another burst property discussed below.

Burst Durations and Fluence

The T_{90} duration is the time between when 5% and 95% of the total background-subtracted burst counts have been accumulated (e.g. Göğüş et al., 2001). The background count rate was determined by averaging a hand-selected burst-free region before and after the burst. This typically consisted of two intervals of 1 s before and after the burst in question. The integrated background-subtracted counts were then fit to a step function plus a linear term using least-squares fitting. The height of the step-function corresponds to the total burst fluence F (in counts) and the slope of the line corresponds to any background counts that were improperly subtracted.

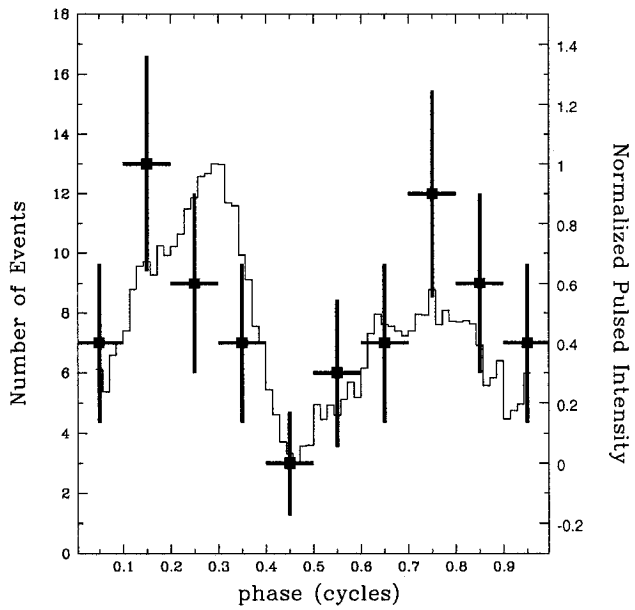

Figure 8.4: Distribution of the pulse phases of 1E 2259+586 which correspond to the times of the burst peaks (solid points). The solid curve is the folded 2–60 keV light curve of the 2002 June 18 observation with the bursts omitted.

SGR T_{90} distributions follow a log-normal distribution, defined as

$$P(T_{90}, \mu, \hat{\sigma}) = \frac{1}{\log \hat{\sigma}\sqrt{2\pi}} \exp\left[-\frac{1}{2}\left(\frac{\log T_{90} - \log \mu}{\log \hat{\sigma}}\right)^2\right] \tag{8.3}$$

whose mean and standard deviation vary with source (e.g. Göğüş et al., 2001). At first we fit the measured values of T_{90} for the 1E 2259+586 bursts with this model and found it to characterize the distribution well. In Equation 8.3 the parameters $\log \mu$ and $\log \hat{\sigma}$ correspond to the mean and standard deviation of the $\log T_{90}$ values. The mean of the T_{90} values is given by μ and the range for one standard deviation corresponds to $(\mu\hat{\sigma}^{-1}, \mu\hat{\sigma})$. The best-fit μ and $\hat{\sigma}$ were determined by maximum likelihood testing. The latter allowed us to extract model parameters that are independent of the arbitrarily chosen histogram bin widths. Specifically,

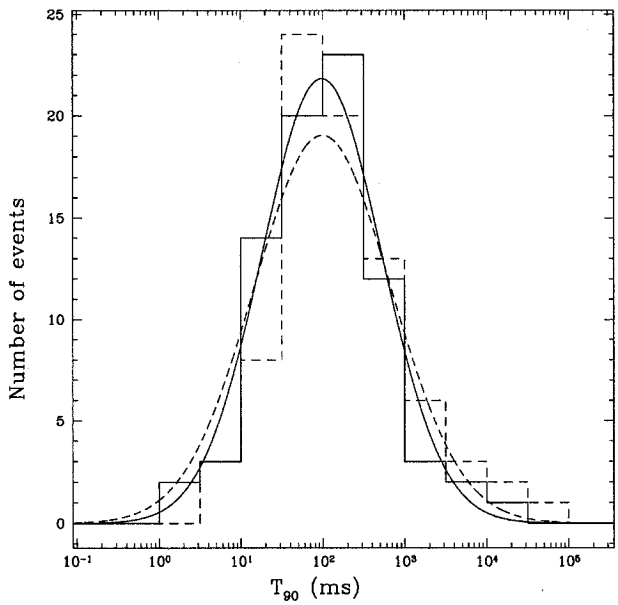

Figure 8.5: Distribution of T_{90} durations for the bursts observed from 1E 2259+586. The solid histogram line shows the observed binned distribution (see §8.3.1), while the dashed histogram line shows the corrected distribution (see §8.3.1). The solid curve represents the best-fit log-normal model for the observed data, as determined by maximum-likelihood testing. The dashed curve is the best-fit log-normal model for the corrected data. This fit has mean 99.31 ms and standard deviation of a factor of 6.9.

the best-fit parameters were those which maximize the statistic

$$\mathcal{M} = \sum_{i=1}^{N} \log P(\mathrm{T}_{90,i}, \mu, \hat{\sigma}), \tag{8.4}$$

where N is the number of bursts. Figure 8.5 shows the distribution, and best-fit log-normal model for the measured values. We found that our T_{90} distribution has mean $\mu = 97.9$ ms with a range of 18.2–527.2 ms for one standard deviation. Note however that for low signal-to-noise bursts, T_{90} can be substantially underestimated. We describe how we corrected for this problem and obtained slightly modified best-fit log-normal parameters in §8.3.1 below.

The fluences measured as described above were then grouped in equispaced

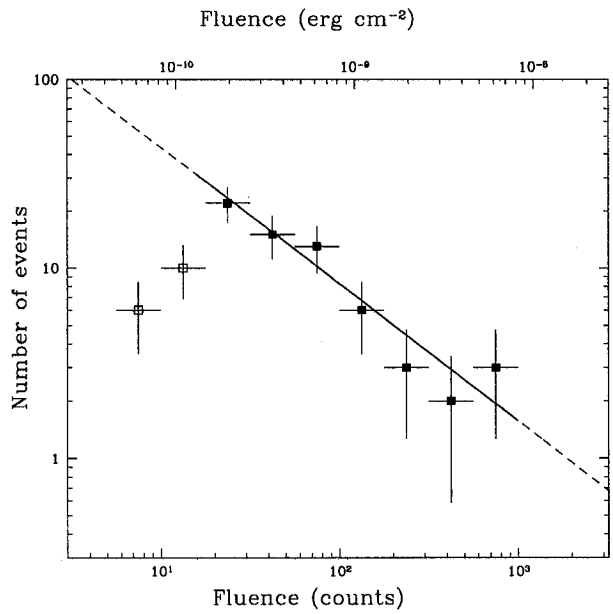

Figure 8.6: Distribution of the 2–60 keV fluence F for each burst observed from 1E 2259+586. Solid points represent average values of fluence in equispaced logarithmic bins for which our observations had full sensitivity. The open points suffered from reduced sensitivity. The best-fit line was determined using the solid points only and is shown as a solid line; the dashed lines are its extrapolation. The slope of this line is -0.7 ± 0.1, which corresponds to $\mathrm{d}N/\mathrm{d}F \propto F^{-1.7}$.

logarithmic bins. The distribution of burst fluences is displayed in Figure 8.6. The low-end fluences are underrepresented because of sensitivity drop-off. Excluding the points having fluence $\lesssim$20 PCA counts, the distribution is well modeled by a simple power law. Using least-squares fitting we find a best-fit power-law index of -0.7 ± 0.1, which corresponds to a differential spectrum $\mathrm{d}N/\mathrm{d}F \propto F^{-1.7\pm0.1}$. From the plot, it is clear that the fluences span approximately two orders of magnitude. For our calibration of the fluences in CGS units, see §8.3.2.

Göğüş et al. (2001) also find a clear correlation between burst durations and total burst fluence. In Figure 8.7, we plot fluence versus $\mathrm{T_{90}}$. A correlation can be seen. To quantify it, we grouped the $\mathrm{T_{90}}$ values in equispaced logarithmic bins and determined group-averaged fluences for each bin. Least-squares fitting to a simple power-law model yields $F \propto \mathrm{T_{90}}^{+0.54\pm0.08}$, with reduced $\chi^2 = 1.0$.

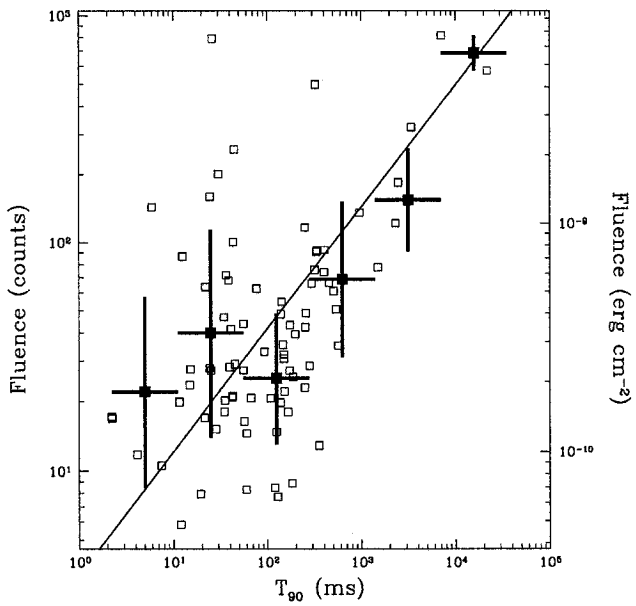

Figure 8.7: Burst 2–60 keV fluence versus T_{90}. The open points represent individual bursts. The solid points represent binned averages. The solid line represents the best-fit power law for the binned averages. The slope of the line is $+0.54 \pm 0.08$.

Burst Peak Fluxes

Burst peak fluxes were determined from the event data using the following algorithm. A box-car integrator of width 62.5 ms was translated through the event data. The procedure began and ended when the center of the box-car was at half a box-car width before and after the time of the burst peak (as determined in § 8.3.1). At each box-car step a flux measurement was made by integrating the number of events and dividing by the box-car width. The burst peak flux was assigned the largest such flux measurement. We then grouped our peak fluxes in equispaced logarithmic bins. The distribution of peak fluxes is shown in Figure 8.8.

Our burst-identifying algorithm is less sensitive to bursts of smaller peak flux. To compensate for this effect, we ran the following simulation. We took a hand-selected 1-ks long burst-free region from our observed 1E 2259+586 light curve

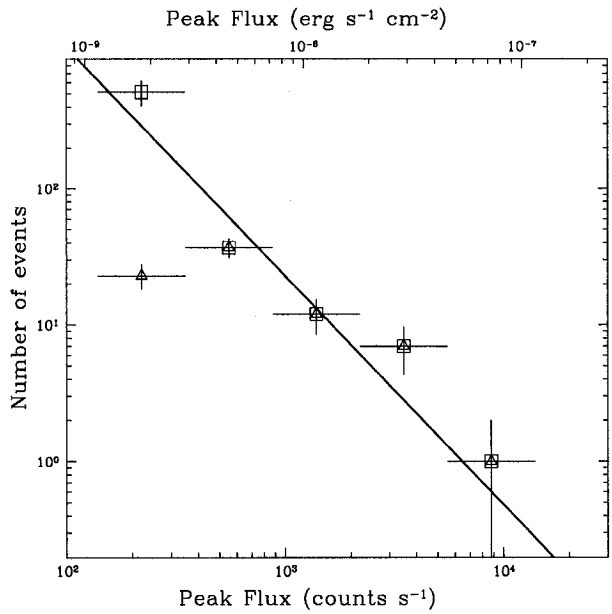

Figure 8.8: Distribution of burst peak flux for 62.5-ms time binning. The diamonds are observed averages in equispaced logarithmic bins. Our sensitivity is significantly reduced at low peak fluxes. The corrected values, determined using simulations described in § 8.3.1 are shown by open squares. The corrected flux bins were fit with a power law, shown by a line. The slope is -1.42 ± 0.13.

binned with 62.5-ms resolution. We then injected a simulated burst having peak flux f_p at a random position in the light curve. We modeled the burst by a top-hat function of width 62.5 ms (one time bin) and height $f_p \times 62.5$ ms. We then ran our burst-identifying algorithm as described in § 8.2.1. We repeated this procedure for N_i iterations and determined N_s, the number of successful burst identifications for that simulated peak flux. We repeated the procedure for various peak fluxes and determined the probability of detecting a burst $P = N_s/N_i$ as a function of peak flux f_p. We found that P could be well modeled by the following analytic function

$$P(f_p) = \frac{1}{2}\left[1 + \tanh\left(\frac{f_p - f_0}{k}\right)\right], \tag{8.5}$$

with $f_0 = 309.84$ cts s^{-1} and $k = 58.21$ cts s^{-1}. We then used this function to correct our peak flux distribution (see Fig. 8.8, boxes). Using least-squares fitting

we found that the corrected distribution is well modeled by a simple power law with index -1.42 ± 0.13. For our calibration of these peak fluxes in CGS units, see §8.3.2.

Burst Rise Times and Fall Times

Burst rise and fall times were obtained from the event data by maximizing the likelihood of the assumed probability distribution

$$P(t) = \begin{cases} A(C_p e^{(t-t_p)/t_r} + B) & t \leq t_p \\ A(C_p e^{-(t-t_p)/t_f} + B) & t > t_p \end{cases}, \tag{8.6}$$

where B represents the background count rate, C_p represents the background-subtracted count rate at the time of the burst peak t_p, and t_r and t_f represent the burst rise and fall times, respectively. The parameter A is a normalizing factor ensuring unit probability over the interval of interest. This model characterized the bursts well – see the left panels of Figure 8.3 (dotted line) for examples. Burst rise and fall time distributions are displayed in Figure 8.9, with best-fit log-normal models determined via maximum-likelihood testing. For the rise time distribution, we find a mean of 2.43 ms and a range of 0.51–11.51 ms for one standard deviation, with reduced $\chi^2 = 1.3$. For the fall time distribution, we find mean 13.21 ms and a range of 3.52–49.55 ms for one standard deviation, and a reduced $\chi^2 = 0.2$. In order to better quantify burst morphologies we also show the ratio of burst rise times to fall times (t_r/t_f; Fig. 8.9). On average, bursts rise faster than they fall, however this is not universally true. Again fitting a log-normal distribution, we find mean 0.18 and a range of 0.03–1.08 for one standard deviation, with reduced $\chi^2 = 3.7$. The latter fit is poor because the distribution is clearly skewed toward shorter rise times. The asymmetry of the typical burst can also be seen in Figure 8.10, where the distribution of t_r/T_{90} is plotted.

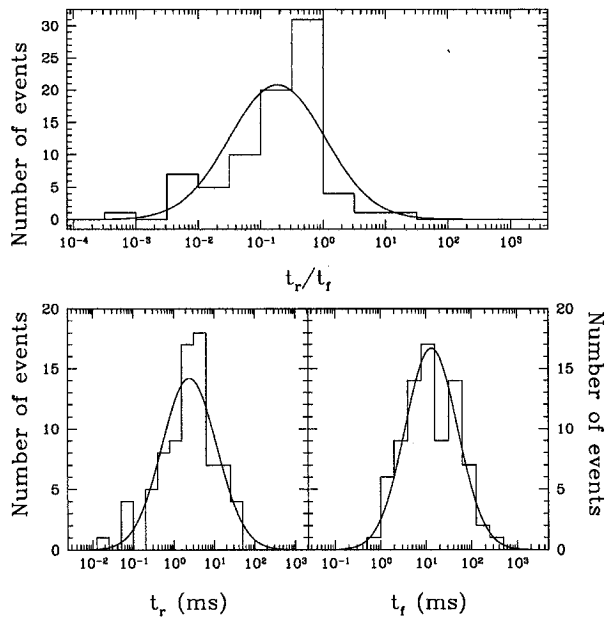

Figure 8.9: Distribution of burst rise (t_r) and fall (t_f) times (see §8.3.1). Bottom left: Distribution of fall times t_r. Bottom right: Distribution of fall times t_f. Top: Distribution of t_r/t_f. In all cases, the solid line represents the best fit log-normal model, as determined by maximum-likelihood testing.

Corrected T_{90} Values

Göğüş et al. (2001) showed that in the low signal-to-noise regime, the value of T_{90} can be underestimated. To account for this, a model light curve was generated for each burst, having the form of Equation 8.6. Peak flux, rise time and fall time were fixed at the values measured for that particular burst. The simulated light curve was then integrated and the model duration ($T_{90,m}$) was measured by the same procedure outlined in §8.3.1. We then repeated the procedure with noise added to the simulated light curve. The noise was drawn from a Poissonian distribution having mean equal to the measured background rate of the burst under investigation. We repeated the procedure for 200 realizations of noise. For each iteration (i) we measured the duration ($T_{90,i}$). The simulated durations ($T_{90,i}$) were normally distributed and the mean of this distribution ($T_{90,s}$) allowed us to calculate a correction factor $\mathcal{FD} \equiv 1 - T_{90,m}/T_{90,s}$. The corrected T_{90}

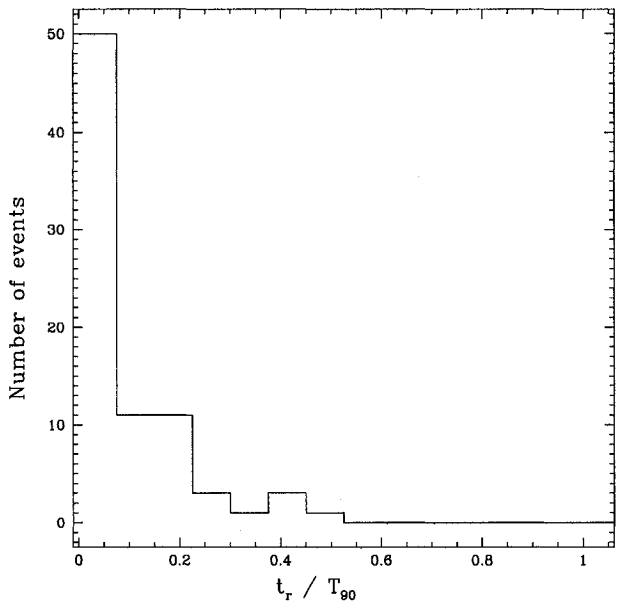

Figure 8.10: Distribution of the ratio of burst rise time t_r to duration T_{90}.

distribution is shown in Figure 8.5. The best-fit mean is 99.31 ms with a range of 14.4–683.9 ms for one standard deviation.

Burst Waiting Times

SGR waiting times (ΔT), defined as the temporal separations of adjacent bursts, are found to follow log-normal distributions (Gögüs et al., 1999; Gögüs et al., 2000). We measured the waiting time for the 1E 2259+586 events, excluding those interrupted by Earth occultations. Figure 8.11 displays our ΔT distribution with the best-fit log-normal model as determined by maximum likelihood testing. The best-fit parameters are mean of 46.7 s and a range of 10.5–208.4 s for one standard deviation, with reduced $\chi^2 = 0.6$. We find no correlation between the burst energy, duration and the waiting time until the next burst, nor with the elapsed time since the previous burst.

Note however that the burst rate clearly decreased during the observation (see Fig 8.1). This is made clear by the bottom panel of Figure 8.11 which shows a

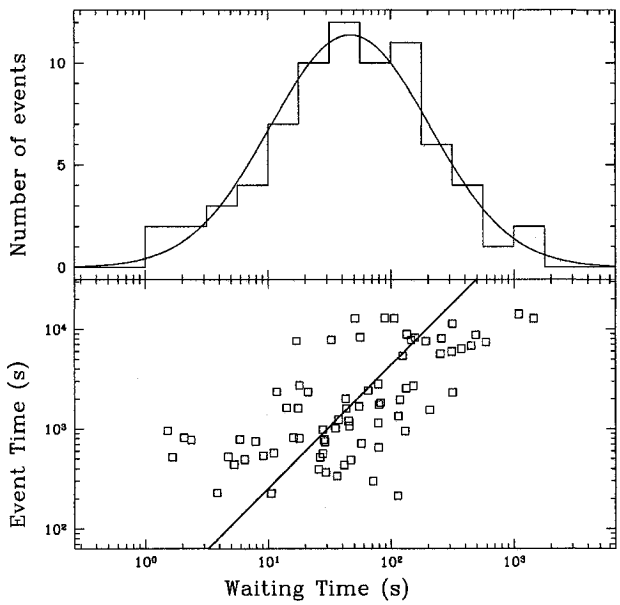

Figure 8.11: Top: Distribution of the waiting time between successive bursts. The solid line represents the best fit log-normal model, as determined by maximum-likelihood testing. The mean is 46.8 s, and standard deviation of a factor 4.4. Bottom: Waiting time as a function of event time. The line represents the best-fit power law model. The gaps in the event times are Earth occultations.

correlation between the waiting time (ΔT) and the burst peak time (t_p). We fit this correlation to a power-law model using least-squares fitting, which reveals that $\Delta T = 0.11 \times {t_p}^{0.81}$. This correlation implies that the mean of our waiting time distribution depends on the time at which we started observing the outburst. We find no correlation between the burst energy, duration and when the bursts occur.

8.3.2 Burst Spectroscopy

Individual Burst Spectra

Spectra for each burst were extracted with the 256 spectral bins over the PCA range grouped by a factor of 4 in order to increase the signal-to-noise ratio per spectral bin. The same background intervals selected in measuring T_{90} were used

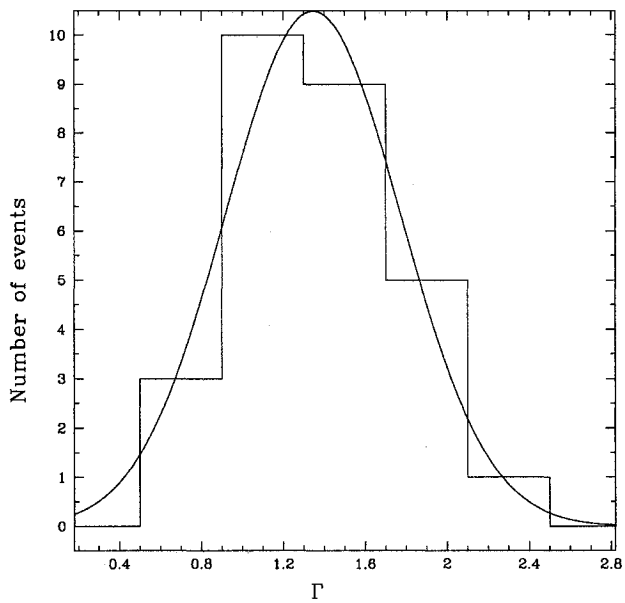

Figure 8.12: Distribution of photon indices (Γ) for the 28 most fluent bursts. See §8.3.2 for details. The curve is the best-fit Gaussian model. This fit has mean 1.35 and standard deviation 0.43.

in the spectral analysis. In all spectral analyses, energies below 2 keV and above 60 keV were ignored, leaving on average 33 spectral channels for fitting. The regrouped spectra along with their background estimators were used as input to the X-ray spectral fitting software package `XSPEC`[1]. Response matrices were created using the `FTOOLs` `xtefilt` and `pcarsp`. We fit the 28 most fluent bursts with a photoelectrically absorbed power law of index Γ, holding only N_H fixed at 0.93×10^{22} cm^{-2} (the value found by Patel et al., 2001). For more details on spectral analysis of *RXTE* data see § 5.4. The distribution of photon indices is shown in Figure 8.12. We find a mean photon index of $\Gamma = 1.35$ with standard deviation 0.43.

[1]http://xspec.gsfc.nasa.gov

Hardness Ratios

Göğüş et al. (2001) noted that SGR bursts tend to soften with increasing burst energy. We studied the hardness ratio/fluence relationship by extracting spectra and creating response matrices separately for each burst. Hardness ratios were defined as the ratio of the counts in the 10–60 keV band to those in the 2–10 keV band as in Göğüş et al. (2001). Also following Göğüş et al. (2001), we divided the bursts into equispaced logarithmic fluence bins and calculated a weighted average hardness ratio for each bin. Figure 8.13 shows the weighted mean hardness ratios as a function of fluence. A clear positive correlation is seen. We repeated the procedure for different definitions of hardness ratio and found similar correlations. We further confirmed this trend by considering the 28 most fluent bursts for which photon indexes Γ could be reliably and precisely constrained. All had Γ well below the mean value.

Absence of Spectral Lines and the Average Burst Spectrum

Possible spectral features have been reported in a burst from the AXP 1E 1048.1–5937 (see Fig. 6.3) and from bursts from two SGRs (Strohmayer & Ibrahim, 2000; Ibrahim et al., 2002, 2003). In no spectrum of any burst for 1E 2259+586 did we detect a significant feature. In order to amplify any low-level spectral feature common to all bursts, we combined individual burst spectra to create a grand average spectrum. We summed the burst and background spectra described in the previous section using the `FTOOL sumpha`. Response matrices were scaled and added using the `FTOOL addpha`. Energies below 2 keV and above 60 keV were ignored, spectral bins were grouped by a factor of two, leaving 65 spectral channels for fitting. In order to search for features in the residuals, we fit the combined spectrum to a simple photoelectrically absorbed power law. The fit had reduced $\chi^2 = 1.3$ for 63 degrees of freedom. The residuals showed no evidence of significant spectral features.

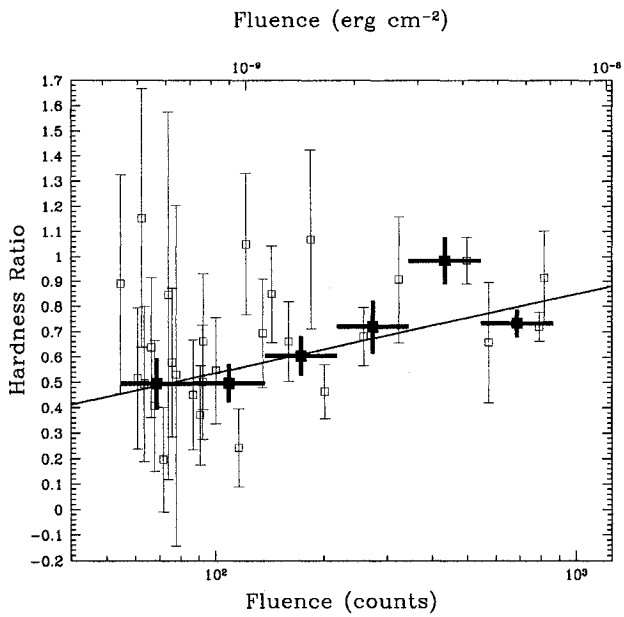

Figure 8.13: Hardness ratio (H) versus fluence (F). Hardness ratio is defined as the ratio of the number of PCA counts in the 10–60 keV band to that in the 2–10 keV band. The open points are hardness ratio measurements for individual bursts. The solid points are weighted averages of hardness ratios for bursts in equispaced logarithmic fluence bins. The line represents the best-fit logarithmic function for the weighted averages, $H = 0.31 \times \log F - 0.09$.

Calibrating Fluence and Flux

Determining peak flux and total fluence distributions in CGS units requires spectral fitting. However most bursts were too faint to allow spectral parameters to be determined with interesting precision. The problem was worse for the peak fluxes since even the brighter bursts generally had too few counts to meaningfully constrain the spectrum. Therefore, we devised an alternate way of converting between PCA counts and CGS units. We took the spectra of the 40 most luminous bursts extracted over their T_{90} duration and fit them with photoelectrically absorbed power laws. However this time, for consistency, we held Γ fixed at

the mean of our photon index distribution. We multiplied the flux (in units of erg s^{-1} cm^{-2}) in the 2–60 keV range returned by the fit by its respective T_{90} duration to obtain a fluence in erg cm^{-2}. We then considered the 2–60 keV fluence in counts as determined in §8.3.1 as a function of the fluence in CGS units and determined the proportionality constant between the two using least-squares fitting. This constant was found to be 8.226×10^{-12} erg cm^{-2} cts^{-1}. In §8.3.2 we found significant spectral evolution as a function of fluence. A change of 1σ in photon index Γ corresponds to a change by a factor of ~ 1.5 in our calibration constant. The same procedure and constant applies for the peak fluxes. The CGS energy scales are shown at the top of Figures 8.6 and 8.8. The fluences in the 2–60 keV band range from $\sim 5\times10^{-11}$ to $\sim 7\times10^{-9}$ erg cm^{-2}. These imply burst energies in the range $\sim 5\times10^{34}$ to $\sim 7\times10^{36}$ erg, assuming isotropic emission and a distance of 3 kpc to the source (Kothes et al., 2002). The sum total of all burst fluences is 5.6×10^{-8} erg cm^{-2}, corresponding to energy 6.0×10^{37} erg (2–60 keV). Peak fluxes in a 61.25-ms time bin range from $\sim 1 \times 10^{-9}$ to $\sim 1 \times 10^{-7}$ erg cm^{-2} s^{-1}, which imply peak luminosities in the range $\sim 1 \times 10^{36}$ to $\sim 1 \times 10^{38}$ erg s^{-1}. On shorter time scales we find 5 bursts with peak fluxes which are super-Eddington (§ 1.4.2; Eq. 1.70). The peak fluxes in a 1/2048 s time bin for these bursts range from $\sim 2 \times 10^{38}$ to $\sim 8 \times 10^{38}$ erg s^{-1}.

8.4 Discussion

Here we compare the various measured quantities for the AXP and SGR bursts. Note that our comparisons focus primarily on PCA observations of SGRs 1806−20 and 1900+14 for consistency of spectral and temporal response. Göğüş et al. (2001) observed SGR 1900+14 using *RXTE* between 1996 November 5 and 18. Their observations had a total integration time of 224.1 ks, and a total of 837 bursts were identified using the full PCA band-pass. In their statitstical analysis they concentrated on 679 bursts clustered together during two very burst active epochs. Similarly, Göğüş et al. (2001) observed SGR 1806−20 using *RXTE* between 1998 June 2 and December 21. These observations had a total integration

time of 136.8 ks, and a total of 290 bursts were identified using the full PCA band-pass. In their analysis for this source they focused on 268 bursts clustered together during a very burst active period of the source between 1998 August 29 and September 2.

8.4.1 Similarities between AXP and SGR bursts

As we describe below, many of the properties of the bursts seen from 1E 2259+586 during its 2002 June 18 outburst are very similar to those seen in SGRs. Specifically:

- the burst T_{90} durations follow a log-normal distribution which peaks at 99.31 ms
- the differential burst fluence spectrum is well described by a power law of index -1.7, similar to those seen in SGRs (and earthquakes and solar flares)
- burst fluences are positively correlated with burst durations
- the distribution of waiting times is well described by a log-normal with mean 46.7 s
- the burst morphologies are generally asymmetric, with rise times usually shorter than burst durations

The mean T_{90} value of 99.31 ms (see §8.3.1 and Fig. 8.5) is very similar to those seen for SGRs 1806−20 and 1900+14: 161.8 ms and 93.9 ms, respectively. Göğüş et al. (2001) suggested that the difference between these values for the two SGRs is a result of a different intrinsic physical property of the sources, such as the strength of the magnetic field, or the size of the active region. Given the generally softer persistent emission spectra of AXPs compared to SGRs, as well as the less frequent outbursts of the AXPs, it is reasonable to suspect that the two source classes differ also by some physical property; age (Kouveliotou et al., 1998; Gaensler et al., 2001), magnetic field (Chapter 6 and 7 and progenitor mass (Gaensler, 2004) have been proposed. The similarity of the burst durations of

all three sources implies, however, that the physical property resulting in different mean burst durations must be different from that which results in different average spectra and outburst frequency.

The distribution of burst fluences for 1E 2259+586 is remarkably similar to those seen in SGRs. For the 1E 2259+586 bursts, we find a fluence distribution $\mathrm{d}N/\mathrm{d}F \propto F^{-1.7\pm0.1}$ (Fig. 8.6). Gögüs et al. (2000) showed that for the PCA, the fluence distribution for SGR 1806−20 is well described by a power law of index -1.43 ± 0.06, while at higher burst energies, the index steepens to -1.7. For SGR 1900+14, Gögüs et al. (1999) found an index of $-1.66^{+0.13}_{-0.12}$ extending over the full range of burst fluences. The good agreement of the fluence distribution indices shows that for a given outburst intensity (i.e. the normalization of the fluence distribution), the average burst energy is the same for 1E 2259+586 as it is for these two SGRs. The difference between the SGR outbursts that are routinely detected by the Interplanetary Network (IPN) detectors and this outburst from 1E 2259+586 which was not detected by the IPN is the SGR outbursts have shown higher outburst intensities. Since we know that the SGRs spend most of their time in quiescence when the fluence distribution normalization is zero (or near zero), the dynamic range of the outburst intensities in SGRs is larger than has been observed thus far in 1E 2259+586. This difference in range is intrinsically even larger when one considers that 1E 2259+586 is believed to be significantly closer (3 kpc) than either of these two SGRs (∼15 kpc, Vrba et al., 2000; Corbel et al., 1997).

Cheng et al. (1996) noted the similarity of the fluence distribution index for SGR 1806−20 with that determined empirically for earthquakes (Gutenberg & Richter, 1956a,b, 1965), and also for the distribution of earthquake energies found in computer simulations (Katz, 1986). However, solar flares also show a size distribution with exponents ranging from 1.53 to 1.73 (Crosby et al., 1993; Lu et al., 1993). Magnetars are not clearly physically analogous to either system; in magnetars, magnetic stresses are thought to result in stellar crust cracking, which is not the case for earthquakes. The bursts could be magnetic reconnections as in solar flares (Lyutikov, 2002), however in the solar case there is no solid crust to

yield, unlike in magnetars. The similarity of the distributions could be explained as being a result of the phenomena of self-organized criticality (Bak et al., 1988), in which a system is dynamically attracted (i.e. self-organized) to a critical, spatially self-similar state which is just barely stable to perturbations. In other words, the burst statistics alone do not constrain their physical origin.

It is not possible to compare peak flux distributions as none are published for SGRs. For the AXP, the range of 2–60 keV peak flux for the 62.5-ms time scale spans a factor of ∼100, ranging from $\sim 1 \times 10^{-9}$ to $\sim 1 \times 10^{-7}$ erg cm^{-2} s^{-1}, which, for a distance of 3 kpc, corresponds to luminosities of $\sim 1 \times 10^{36}$ to $\sim 1 \times 10^{38}$ erg s^{-1}. At time scales as short as 1/2048 s we find peak fluxes as high as $\sim 8 \times 10^{38}$ erg s^{-1}. Thus 5 bursts are above the Eddington limit (§ 1.4.2; Eq. 1.70) on this time scale.

The waiting time distributions of the AXP and SGRs are very similar. All are well described by log-normal distributions. This is similar to what is seen in other self-organized critical systems, such as earthquakes (Nishenko & Buland, 1987). For 1E 2259+586, we find a mean waiting time between bursts of 47 s, and range of 10–208 s. Gögüs et al. (1999) found ∼49 s for SGR 1900+14, and Gögüs et al. (2000) found ∼97 s for SGR 1806−20, with range between ∼0.1 and 1000 s for both, very similar to our results. The absence of correlation of waiting time and burst fluence for the AXP is similar to that seen for SGRs (Gögüs et al., 1999; Gögüs et al., 2000), although Gögüs et al. (1999) report an anticorrelation between time since the previous burst and burst energy. We do not see this for the AXP, nor do Gögüs et al. (2000) observe it for SGR 1806−20.

The morphologies of the AXP and SGR bursts are similar, with most being asymmetric, with faster rises than decays. Rise and fall time distributions for the SGRs have not been published, so we cannot compare those parameters directly, nor the ratio of the two. Göğüş et al. (2001) showed the distribution of the ratio t_r/T_{90} for SGRs 1806−20 and 1900+14; the same plot for 1E 2259+586 looks similar (Fig. 8.10). We note that two bursts had T_{90} durations greater than the spin-period of the source. These bursts have similar profiles to others and we do not see any evidence for breaks in their profiles due to the occultation by the

star.

8.4.2 Differences between AXP and SGR bursts

As shown above, many of the properties of the bursts seen from 1E 2259+586 during its 2002 June 18 outburst are very similar to those seen by Göğüş et al. (2001) in SGRs 1900+14 and 1806−20. However, there are some quantitative differences between the properties of the AXP and SGR bursts. The differences can be summarized as:

- there is a significant correlation of burst phase with pulsed intensity, unlike in SGRs (see Palmer, 1999, 2002; Lenters et al., 2003).
- the AXP bursts have a wider range of burst duration (though this may be partly due to different analyses procedures)
- the correlation of burst fluence with duration is flatter for AXPs than it is for SGRs (although when selection effects are considered, this correlation should really be seen as an upper envelope for AXPs and SGRs)
- the fluences for the AXP bursts are generally smaller than are in observed SGR bursts
- the more energetic AXP bursts have the hardest spectra, whereas for SGR bursts, they have the softest spectra
- under reasonable assumptions, SGRs undergo outbursts much more frequently than do AXPs

The standard deviation of the T_{90} distribution for the 1E 2259+586 bursts is much larger than is seen for the SGR bursts. For 1E 2259+586, the 1σ range is from ∼14 ms to ∼684 ms or 1.7 magnitudes. For SGRs 1806−20 and 1900+14, the corresponding range in durations is 0.68 and 0.70 magnitudes. The lower bound on the 1E 2259+586 distribution may be artificially lower due to the shorter time scales searched in this work as compared to Göğüş et al. (2001) who

searched for SGR bursts on the 0.125 s time scale. However, such a wide range of durations is seen even when faint bursts are omitted from the T_{90} distribution of 1E 2259+586. Göğüş et al. (2001) argued that if the "trapped fireball" model, which describes the giant SGR bursts well, also applies to the fainter bursts, then the narrowness of the T_{90} distribution compared with the wide range of fluences demands a planar fireball geometry. This is because the duration of the burst is limited by the rate of cooling through the radiative fireball surface layer. For 1E 2259+586, the T_{90} range is larger than the fluence range, indicating that if the fireball model applies, a planar fireball geometry is not supported. For more details on fireballs within the context of the magnetar model see § 2.4 and references therein.

As in SGRs, the fluences of the 1E 2259+586 bursts are significantly positively correlated with T_{90} (Fig. 8.7). However there is one difference: for the AXP, the relationship is well described by a power law of index $+0.54 \pm 0.08$, while for SGRs 1806−20 and 1900+14, Göğüş et al. (2001) found $+1.05 \pm 0.16$ and $+0.91 \pm 0.07$, respectively. Thus the power-law index for AXPs is half that seen in SGRs. It is important to recognize, however, that severe selection effects are at work here. Specifically, as discussed in §8.3.1, we are less sensitive to low-fluence bursts. This is particularly true for bursts having long rise times, which will tend to have long T_{90} values. Thus there are severe selection effects against finding bursts in the bottom right-hand portion of Figure 8.7, as there are in similar analyses for SGRs. Therefore the above correlation should really be seen as an upper envelope to the phase space available to the burst. By contrast, our sensitivity to bursts that would sit in the upper left-hand corner of the plot is generally enhanced relative to the populated region, indicating the absence of bursts in this part of phase space is genuine.

One striking difference between the AXP and SGR bursts is in the relationship between spectral hardness ratio and fluence. For SGR 1806−20, Göğüş et al. (2001) found that the more energetic bursts are spectrally softer, regardless of burst morphology. This was not seen for SGR 1900+14, however. Our analysis (see Fig. 8.13) shows the opposite behavior to that seen in SGR 1806−20, with

the more energetic bursts having harder spectra. Göğüş et al. (2001) argued that the behavior seen for SGRs could be explained either by the emitting plasma being in local thermodynamic equilibrium, having radiative area decreasing for lower fluences, or by the spectral intensity of the radiation field being below that of a blackbody, hence the emitting plasma temperature T remaining in a narrow range, being higher at lower luminosities. Which of these two applies depends on the rate of energy injection into the magnetosphere; the latter applies only if the luminosity is less than $\sim 10^{42}(V^{1/3}/10\,\mathrm{km})$ erg s^{-1} where V is the injection region, assuming a spherical geometry. Clearly neither can apply for the AXP. Göğüş et al. (2001) imply that blackbody emission from a constant radius predicts the relationship between hardness and fluence that we find for the AXP. However for the AXP, naively taking Figure 8.7 at face value, $F \propto \mathrm{T}_{90}^{0.5}$. Hence $L_a \propto F^{-1}$, so blackbody emission from a constant radius predicts $T \propto F^{-1/4}$, the opposite to what we have observed. We note further that the range of hardness ratios for the AXP bursts is slightly greater than it is for the SGRs. For 1E 2259+586, hardness ratios (for bursts having 10^2–10^3 counts) range from ~0.54–0.85, while the range is ~0.82–0.95 for SGR 1806−20, and ~ 0.63–0.67 for SGR 1900+14 (Göğüş et al., 2001). It should be noted however that we identified bursts (see §8.2.1) using a different energy range (2–20 keV) than Göğüş et al. (2001), who used the full bandpass of the PCA. This would make us more sensitive to softer bursts which would affect the dynamic range of the hardness ratios we measured. Perhaps interestingly, for the SGRs, $F \propto \mathrm{T}_{90}$, so the $L_a \equiv F/\mathrm{T}_{90} \simeq$ constant, and for constant radiative area and blackbody emission, one expects $T \simeq$ constant, closer to what is observed for SGRs than for AXPs. Thus, although blackbody emission from a constant radius (not surprisingly) does not describe any of the data well, it does seem possible that the flatter dependence of fluence on T_{90}, the inverted dependence of hardness on fluence relative to the SGRs, and the greater range of hardness in the AXP bursts may all be related phenomena telling us something interesting about the physical distinction between these closely related sources.

We have stated that outbursts from AXPs similar to or larger than the one studied here are less frequent than are those from SGRs. Of course, given that we

have observed only one AXP outburst, and that this outburst was energetically smaller and fainter than observed SGR outbursts, making a meaningful comparison of their outburst rate is very difficult. We can estimate the rate of AXP outbursts of the magnitude of the 2002 June 18 event as follows. We consider data from only our *RXTE* PCA monitoring program, as it provides a consistent quasi-regularly sampled data set with a single instrument. The monitoring program for 1E 2259+586 has extended over nearly 7 yr with only one such outburst detected; even though the bursting appears to have been relatively short-lived, the effects of a glitch of even much smaller size would easily have been detected throughout the data span. We make the admittedly speculative assumption that all such outbursts are accompanied by comparably sized glitches. A comparable glitch in AXP 1RXS J1708–4009 was recently detected in 5.4 yr of monitoring without evidence for radiative outburst, however the sparse observations could have missed one (Kaspi & Gavriil, 2003; Dall'Osso et al., 2003). Two small bursts have been seen in 6.8 yr of timing of AXP 1E 1048.1–5937 (Chapter 6), all the measured properties of these two bursts fall within the range of burst properties found for 1E 2259+586. The timing behavior of 1E 1048.1–5937 suggests that many glitches could be occurring (Kaspi et al., 2001), however no other evidence for radiative outbursts has been found. No activity of any kind, apart from apparently simple timing noise, has been seen in 6.5 yr of timing of 4U 0142+61 (Gavriil & Kaspi, 2002) or in 4.3 yr of timing 1E 1841–045 (Gotthelf et al., 2002). If we omit 1E 1048.1–5937 whose timing behavior we do not fully understand, we can estimate a rough AXP outburst rate of one every 11 yr, assuming that the glitch in 1RXS J1708–4009 was indeed a similar outburst, or one every $\sim$22 yr if not. SGRs, by contrast, burst much more frequently, reach higher intensities, and persist for longer periods of time. The monitoring of the SGRs with the *RXTE* PCA has not been as regular as for the AXPs due to less optimal observing conditions for the SGRs (lower pulsed fractions, source flux, stronger timing noise, etc.), therefore, we cannot make a direct comparison of the outburst recurrence rate using the PCA data. We can, however, make a rough estimate of the recurrence rate using results obtained with the Burst and Transient Source

Experiment (BATSE) that flew aboard the *Compton Gamma-Ray Observatory.* The advantage of using BATSE to estimate the SGR outburst rate is its uniform and dense coverage in time due to its "all-sky" FOV. The disadvantage is that BATSE is much less sensitive to SGR bursts than is the PCA (e.g. Gögüs et al., 1999). Since SGR/AXP burst energies follow a steep power-law distribution, the outburst recurrence rate is a strong function of detector sensitivity. It follows that an outburst recurrence rate determined by BATSE will then be a lower limit to the rate for the more sensitive PCA. Moreover, the relative distances of AXPs and SGRs must be considered when determining intrinsic source rates for a given luminosity or total energy as opposed to peak flux and fluence. With these factors in mind, we now estimate the SGR outburst recurrence rate at the BATSE sensitivity level. BATSE was in operation for 9.1 yr from 1991 April through 2000 June. During that time, three of the four known SGRs entered outburst (Kouveliotou et al., 1993; Kouveliotou & 10 others, 1994; Woods et al., 1999; Göğüş et al., 2001), some multiple times. Here, we define an outburst as a collection of bursts (i.e. more than two) where the separation between consecutive bursts never exceeds one month. Using the results reported in Göğüş et al. (2001), the number of SGR outbursts detected during this time interval is 14. This yields an outburst rate for the SGRs of once every ~2.6 years. Recall, this is a lower limit to the rate at the PCA sensitivity level. Thus the SGRs clearly undergo outbursts more frequently than do AXPs.

8.5 Summary

In this chapter we presented a statistical analysis of the bursts observed during the SGR-like outburst from 1E 2259+586first reported on in Chapter 7. We found that the temporal and energetic properties of the bursts were quantitatively similar to those of the SGRs. We did however find some interesting differences, but nevertheless, the bursts were sufficiently similar to support the conclusion that AXPs and SGRs are unified as a source class.

In the previous chapter we saw that during 1E 2259+586's outburst the pulsar

exhibited an abrupt rise in flux which lasted for several months. In the next chapter we report on the discovery of two pulsed flux enhancements from another AXP, 1E 1048.1–5937. However, the flux enhancements in this source were very different from the one in 1E 2259+586.

Chapter 9

Anomalous X-ray Pulsar 1E 1048.1–5937: Pulsed Flux Flares and Large Torque Variations

The work presented in this chapter originally appeared in: *Gavriil, F. P. & Kaspi, V. M. Anomalous X-ray Pulsar 1E 1048.1–5937: Pulsed Flux Flares and Large Torque Variations. Astrophysical Journal Letters. 609, L67–L70, 2004.* References to this chapter should be considered as references to Gavriil & Kaspi (2004) as well.

9.1 Introduction

A mystery in AXP research has been their flux stability, see § 1.5.1 for a more detailed discussion of this issue. A possible solution to this puzzle came with the discovery of a large ($> 10\times$), long-lived flux enhancement from 1E 2259+586 at the time of a major outburst in 2002 June 18 (Chapter 7). This event was accompanied by many other radiative changes as well as by a large rotational spin-up (Chapter 7; Woods et al., 2004). This suggests that past flux variability reported in AXPs could be attributed to similar outbursts that went undetected.

We report here, using data from our continuing *RXTE* monitoring program (see § 5.1), the discovery of significant pulsed flux variability in 1E 1048.1–5937. This variability is mainly characterized by two long-lived pulsed flux flares, having well resolved, few-week-long rises. These are unlike any previously seen flux enhancements in AXPs and SGRs and thus likely represent a distinct physical phenomenon. We find no evidence for any major associated bursting behavior. We also report large variations in the spin-down torque on few-week/month time

scales. We find only a marginal correlation between the flux and torque variations. We argue that this poses another significant challenge to any disk-accretion model for AXPs, but is not inconsistent with the magnetar model. For more details on the fall-back disk and magnetar model see § 3 and Chapter 2 respectively.

9.2 Analysis and Results

All observations reported here were obtained with the PCA aboard *RXTE*. The timing observations described below are a continuation of those reported by Kaspi et al. (2001). The reader is referred to § 5.3.8 for details of the timing analysis procedure. Our *RXTE* monitoring program has shown that, in general, AXPs have sufficient stability for phase coherent timing (see § 1.5.1 and Kaspi & Gavriil, 2004, for a review). 1E 1048.1–5937 is an exception. For this pulsar, we have achieved phase-coherent timing only over relatively short data spans. In 2002 March, we adopted the strategy of observing this source every week with 3 short (∼2 ks) observations. These closely spaced observations allow us to measure the spin frequency with high precision weekly without phase connecting over long baselines. This therefore allows us to determine the spin-down rate with interesting precision on time scales of a few weeks. Figure 9.1A shows the long-term spin history of 1E 1048.1–5937 as measured by *RXTE*.

Figure 9.2A, shows the spin-down rate $\dot{\nu}$ as a function of time over the interval for which we can make this measurement. Plotted values of $\dot{\nu}$ were calculated by measuring the slopes of each 5 adjacent values of ν. Note how $\dot{\nu}$ clearly varies greatly during our observations, on all time scales to which we are sensitive. From MJD 52400 to MJD 52620 $\dot{\nu}$ had changed by a factor of ∼12. During the ∼120-day interval from MJD 52620 through 52740, $\dot{\nu}$ was a factor of ∼4 larger than the long-term average spin-down ($\langle\dot{\nu}\rangle = -6.48 \times 10^{-13}$ Hz s^{-1}). This was followed by an abrupt decrease in magnitude by a factor of ∼2, which was not resolved, and by subsequent additional variations. At no time did we observe any episode of spin-up.

We also monitor the pulsed flux of this source. In this analysis, data from

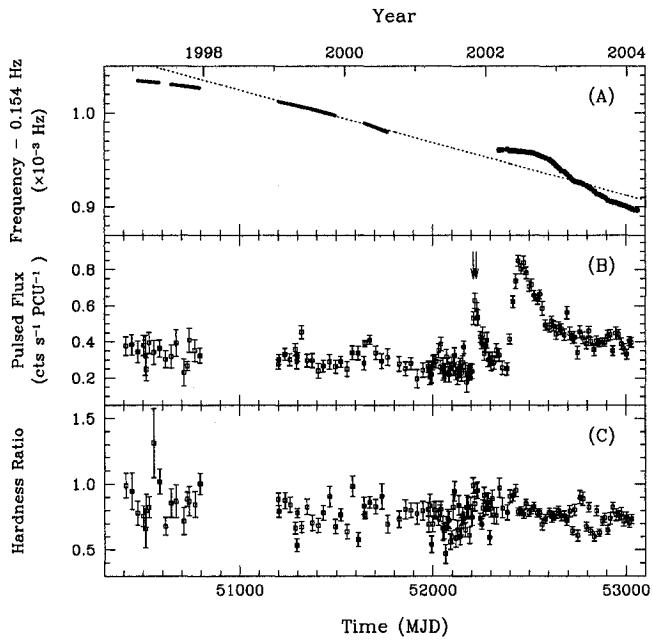

Figure 9.1: Spin, flux and spectral history of 1E 1048.1–5937. A: observed spin frequencies versus time. The points represent individual frequency measurements. The solid lines represent the phase-connected intervals as reported by Kaspi et al. (2001). The dashed line is the long-term average spin down. B: pulsed flux time series in the 2–10 keV band. Arrows indicate the times at which the bursts reported in Chapter 6 occurred. C: hardness ratio as a function of time. The hardness ratios displayed were computed for the pulsed flux in the energy range (4–6 keV)/(2–4 keV).

each observing epoch were also folded at the optimal pulse period. We calculated the RMS pulsed flux using the method described in § 5.3.9 Given 1E 1048.1–5937's highly sinusoidal pulse profile we only used the first two harmonics to calculate the pulsed flux. Figure 9.1B shows our pulsed flux time series in the 2–10 keV band. Pulsed flux time series in the 2–4 and 4–6 keV bands look similar. The pulsed flux time series clearly has significant structure. The most obvious features are two long-lived flares. The first flare was smaller and shorter-lived than the second. The latter clearly displayed significant structure in its decay. In estimating the following flare properties, we define the first flare as having occurred between MJDs 52198 and 52318, and the second having started

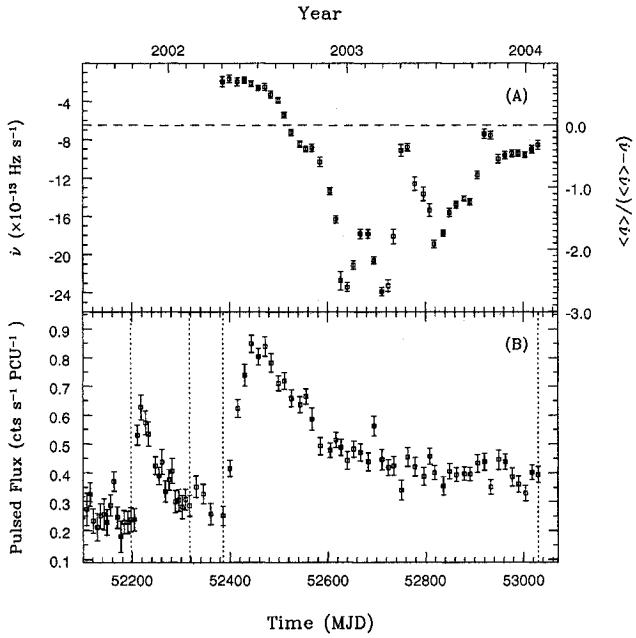

Figure 9.2: A: $\dot{\nu}$ versus time over the interval for which our data allow the measurement. The horizontal dashed line denotes the long-term average spin-down rate, $\langle\dot{\nu}\rangle$. The right-hand scale is the fractional difference of $\dot{\nu}$ and the long-term average spin-down rate. B: zoom-in of the pulsed flux time series in the 2–10 keV band. Vertical dotted lines denote the chosen start and end ranges for characterizing the two principal flares.

on MJD 52386, and we take its end to be our last observation on MJD 53030, although it clearly has not yet ended (see Fig. 9.2). We estimate that the first flare had a peak flux of 2.21 ± 0.16 times the quiescent pulse flux, with the peak occurring at MJD 52218.8 ± 4.5. Its rise time was 20.8 ± 4.5 days, and its fall time 98.9 ± 4.5 days. The second flare peak was on MJD 52444.4 ± 7.0, and had a peak value of 3.00 ± 0.13 times the quiescent pulsed flux. Its rise time was 58.3 ± 7.0 days, and its fall time is > 586 days. We estimate 2–10 keV fluences of $(111 \pm 12) \times 10^4$ cts PCU^{-1} and $(1136 \pm 38) \times 10^4$ cts PCU^{-1} for the first and second flare, respectively. Tiengo et al. (2002) measured a total flux in the 2–10 keV energy range of $\sim 5 \times 10^{-12}$ erg cm^{-2} s^{-1} and a pulsed fraction of $\sim 94\%$ (for energies > 2 keV) from *XMM-Newton* observations of 1E 1048.1–5937. This information, along with our measured quiescent pulsed flux, allows us to scale our

fluences to estimate the total energy released in each flare. Assuming a distance of 5 kpc (see discussion in Özel et al., 2001), we find a total energy release of $\sim 2.7 \times 10^{40}$ erg for the first flare, and $\sim 2.8 \times 10^{41}$ erg for the second flare, both in the 2–10 keV band.

Although we clearly detect both large flux variations and large changes in the spin-down rate, the correlation between the two is marginal. The Spearman rank order correlation coefficient $r_s = 0.28$, where 0 indicates no correlation and 1 indicates total correlation. The probability of obtaining this value of r_s or higher by random chance is 6%. Thus, there is marginal evidence of some correlation, equivalent to a $\gtrsim 2\sigma$ result. From Figure 2, it is clear why any correlation is not strong: for example, $\dot{\nu}$ changes very little during the rise of the second flare, in the interval MJD 52380–52420. Also, there is no short-term flux change when $\dot{\nu}$ suddenly reaches its maximum absolute value (near MJD 52620), nor when it abruptly changes by a factor of $\sim$2 around MJD 52740.

Hardness ratios (HRs) were measured by comparing the pulsed flux, as measured by the method described above, in the 2–4 keV band to that in the 4–6 keV band. Figure 9.1C shows our HR measurements. The mean HR is 0.78. There is evidence for spectral variability. The reduced χ^2 of the HR time series is 3.6 for 143 degrees of freedom. However, there is no evidence for any correlation of HR with pulsed flux or torque. Our uncertainties however are quite large; monitoring observations with an imaging instrument would improve this situation.

Intriguingly, the peak of the first flare was coincident with the epochs during which we observed two SGR-like X-ray bursts from the direction of this source in 2001 (indicated by arrows in Fig. 9.1; see Chapter 6). However, we found no other SGR-like bursts in any of the remaining data. For a detailed description of our burst searching algorithm see § 6.2.1. We also searched our folded time series for pulse morphology variations using the method described in Gavriil & Kaspi (2002). We find no evidence for significant pulse profile changes at any epoch in our data set.

9.3 Discussion

The long-lived flux enhancements with well-resolved rises that we have observed in 1E 1048.1–5937 are very different from previously detected X-ray flux variations in AXPs and SGRs, which show very abrupt rises associated with major outbursts (see Fig. 7.1; Woods et al., 2004). The long-lived flux decay in those sources has been attributed to burst afterglow, that is cooling of the crust following an impulsive heat injection from magnetospheric bursts (Lyubarsky et al., 2002). The much more gradual flux rises we have observed in 1E 1048.1–5937 comprise a new phenomenon not yet observed in any other AXP despite several years of careful and frequent *RXTE* monitoring. These flux variations may provide a new diagnostic of the physical origin of the persistent non-thermal emission in SGRs and AXPs, since they are not contaminated by burst afterglow. Also interesting are the large variations in spin-down rate or torque. Torque variations by nearly a factor of 5 were already reported from *RXTE* observations (Kaspi et al., 2001), on time scales of years. Here we have shown that the torque can change by at least a factor of $\sim$2 more, and on much shorter time scales, namely few-weeks to months.

In considering the observed pulsed flux and torque variations, whether they are correlated is an important issue. Our weekly monitoring of the source unfortunately commenced only after most of the first flare decayed. Prior to that, the monthly observations, taken in the form of brief snapshots, did not allow anything about the rotational behavior of the source to be determined when phase-coherent timing was not possible. This was the case during the first flare. During the second flare, the spin frequency was, interestingly, *most* stable during the rise and peak of the flare. Furthermore, the stable spin-down rate was at a lower magnitude than the long-term average. Subsequently, $\sim$ 60 days after the flux began to decay, the rate of spin-down began to increase. Given timing observations during only one flare, it is unclear whether these features are coincidences or not. However, there is no strong evidence to support otherwise; similar torque variations were seen in the past and were not accompanied by any flaring (see Fig. 9.1). Significant torque variations unaccompanied by severe flux variability

have been noted for 1E 1048.1–5937 prior to our *RXTE* monitoring (e.g. Paul et al., 2000). Nevertheless, statistically, the probability that they are uncorrelated is only 4%; studying Figure 9.2 suggests that if anything, slope transitions are correlated, if not the slopes between transitions. Continued *RXTE* monitoring will help identify any true correlations, particularly if the source exhibits more variability.

Can the magnetar model explain such behavior? The persistent emission in magnetars has a spectrum that is well described by a two-component model, consisting of a blackbody plus a hard power-law tail. The thermal component is thought to arise from heat resulting from the active decay of a high internal magnetic field (Thompson & Duncan, 1996), however thermal X-ray flux changes are not expected on as short a time scale as we have measured in the absence of major bursts. Thompson et al. (2002) put forth a model in which the non-thermal component arises from resonant Compton scattering of thermal photons by currents in the magnetosphere. In magnetars, these currents are maintained by magnetic stresses acting deep inside its highly conducting interior, where it is assumed that the magnetic field lines are highly twisted. These magnetospheric currents in turn twist the external dipolar field in the lesser conducting magnetosphere (for more details on the "twisted" magnetosphere model see § 2.6 and references therein). These magnetic stresses can lead to sudden outbursts or more gradual plastic deformations of the rigid crust, thereby twisting the footpoints of the external magnetic field and inducing X-ray luminosity changes. The persistent non-thermal emission of AXPs is explained in this model as being generated by these currents through magnetospheric Comptonization and surface back-heating (Thompson & Duncan, 1996; Thompson et al., 2002). Changes in X-ray luminosity, spectral hardness, and torque have a common physical origin in this model and some correlations are expected. Larger twists correspond to harder persistent X-ray spectra, as is observed, at least when comparing the harder SGR spectra to those of the softer AXPs. As noted by Kaspi et al. (2001), 1E 1048.1–5937's hard photon index ($\Gamma = 2.9 \pm 0.2$) suggests it is a transition object between the AXPs ($\Gamma \simeq 3 - 4$) and the SGRs ($\Gamma = 2.2 - 2.4$). Hence if during the flares

1E 1048.1–5937's magnetosphere was twisted to the SGR regime, we expect photon index variations of ~ 0.5. Spectral measurements of such precision are not feasible with our short *RXTE* monitoring observations.

Decoupling between the torque and the luminosity can be accounted for in the magnetar model. According to Thompson et al. (2002) the torque is most sensitive to the current flowing on a relatively narrow bundle of field lines that are anchored close to the magnetic pole, and so only a broad correlation in spin-down rate and X-ray luminosity is predicted, and in fact is observed for the combined population of SGRs and AXPs (Marsden & White, 2001; Thompson et al., 2002). However for a single source, whether an X-ray luminosity change will be accompanied by a torque change depends on where in relation to the magnetic pole the source of the enhanced X-rays sits. Similarly, large torque variations, as we have observed, may occur in the absence of luminosity changes if the former are a result of changes in the currents flowing only in the small polar cap region.

Note that energetically, the total release in these flares is comparable to, though somewhat less than that in the afterglows seen in SGRs and in AXP 1E 2259+586 (see Woods et al., 2004, for a summary). It can easily be accounted for given the inferred magnetic energy of the star.

Although the magnetar model for AXPs has been spectacularly successful in explaining their most important phenomenology, the anomalous behavior noted for 1E 1048.1–5937 raises the possibility that perhaps it has a physical nature different from other AXPs. It has also been suggested that AXPs might be powered by accretion from fossil disks (Chatterjee et al., 2000; Alpar, 2001). An increase in luminosity L_x can easily be explained in accretion models by an increase in the mass accretion rate $\dot{M}$, given that $L_x \propto \dot{M}$ (Eq. 1.64, 1.86). Transient changes $\dot{M}$ are perhaps not unreasonable to expect in fossil disk models, given the huge variations seen in $\dot{M}$s of conventional accreting sources. However, in an accretion scenario, we expect correlations between luminosity and torque. In conventional disk-fed accreting pulsars undergoing spin-up, one expects $\dot{\nu} \propto L_x^{6/7}$ (see Eq. 1.100). Such a correlation is seen approximately in accreting pulsars, with

discrepancies possibly attributable to changed beaming or improper measurement of bolometric luminosities, the former due to pulse profile changes, and the latter due to finite bandpasses (Bildsten et al., 1997). As discussed in § 3.1.6 (see also Kaspi et al., 2001), for a source undergoing regular *spin-down* as in 1E 1048.1–5937, the prediction is less clear; the form of the correlation depends on the unknown functional form of the torque. For the propeller torque prescription of Chatterjee et al. (2000), we find that $L_x \propto \dot{\nu}^{7/3}$ (see Eq. 3.12), a much stronger correlation than in the conventional spin-up sources. For a change in L_x by a factor of $\sim$3 as we have seen in the rise of the second flare, we would expect a simultaneous change in $\dot{\nu}$ by $> 50\%$, clearly ruled out by our data. Conversely, for the abrupt change of $\dot{\nu}$ by a factor of $\sim$2 (near MJD 52740), we expect a change in L_x by a factor of $\sim$5, definitely not seen. This appears to pose a significant challenge to fossil-disk accretion models for 1E 1048.1–5937.

Two infrared observations taken on MJD 52324 (Israel et al., 2002) and MJD 52372 (Wang & Chakrabarty, 2002) have shown that the IR counterpart of this source is variable. However the pulsed X-ray flux at both those epochs was consistent with the quiescent value. Furthermore even though the X-ray flux has not yet returned to its quiescent value, recent observations show that the source's proposed IR counterpart is consistent with the fainter of the two previous observations (Durant et al., 2004). This decoupling between the IR and the X-ray flux contrasts with what was observed in AXP 1E 2259+586, whose IR flux increased then decayed in concert with the X-ray flux at the time of its 2002 outburst (Chapter 7; Tam et al., 2004). This is puzzling and suggestive of more than one mechanism for producing IR emission in AXPs.

9.4 Summary

In this chapter we reported on the discovery of two slow-rising, long-lasting pulsed flux enhancements from AXP 1E 1048.1–5937. The flux enhancements in this source were very different from the one discovered in 1E 2259+586(Chapter 7). The abrupt, long-lasting flux enhancement in 1E 2259+586 was explained as be-

ing the afterglow of energy injected into the surface from magnetospheric bursts. The flux enhancements in 1E 1048.1–5937 cannot be explained as burst afterglow because of their long rises and the absence of any obvious major bursting activity. Slow-rising flux enhancements such as these have never before been seen in any AXP or SGR.

In the next Chapter we report on the discovery of a third burst from 1E 1048.1–5937. We also discovered a short-term pulsed flux enhancement (not to be confused with the long-term pulsed flux enhancements reported on in this chapter) at the time of the burst.

Chapter 10

A Burst and Simultaneous Short-Term Pulsed Flux Enhancement from the Magnetar Candidate 1E 1048.1–5937

The work presented in this chapter has been accepted for publication in the Astrophysical Journal: *Gavriil, F. P., Kaspi, V. M., & Woods, P. M. A Burst and Simultaneous Short-Term Pulsed Flux Enhancement from the Magnetar Candidate 1E 1048.1–5937. Astrophysical Journal, in press.*

10.1 Introduction

We report here, using data from our continuing *RXTE* monitoring program (§ 5.1), the discovery of another X-ray burst from AXP 1E 1048.1–5937. We show that the pulsed emission increased in the tail of the burst, indicating that the AXP was unambiguously the source of the burst. The identification of 1E 1048.1–5937 as the burst source for this event and the similarities between this burst and the previous two lends further support to the AXP having also been the emitter of the two bursts reported in Chapter 6.

10.2 Results

10.2.1 *RXTE* Observations

The results presented here were obtained using the PCA on board *RXTE*. On 2004 June 29, during one of our regular monitoring observations (*RXTE* obser-

vation identification 90076-02-09-02) that commenced at UT 06:29:28, the AXP 1E 1048.1–5937 exhibited an SGR-like burst.

The burst was identified using the burst searching algorithm described in § 6.2.1. To summarize briefly, time series were created separately for each PCU using all xenon layers. Light curves with time bin widths of 1/32 s were created. The FTOOLs `xtefilt` and `maketime` were used to determine the intervals over which each PCU was off. We further restricted the data set by including only events in the energy range 2–20 keV. Time bins with significant excursions from a running mean were flagged and subject to further investigation. The observation had total on-source integration time of 2.0 ks. There were exactly three PCUs operational at all times and the burst was equally significant in all three PCUs. Data were collected in the `GoodXenonwithPropane` mode (§ 4.4.1), which records the arrival time (with 1-μs resolution) and energy (with 256-channel resolution) of every unrejected xenon event as well as all the propane layer events. Photon arrival times were adjusted to the solar system barycenter using the source position (J2000) given in Table 1.1 and the JPL DE200 planetary ephemeris. Note that following the burst we initiated a 20.2 ks long *RXTE*/PCA Target of opportunity (ToO) observation on 2004 July 8. Similarly, on 2004 July 10, we initiated 3 more *RXTE*/PCA ToO observations which had integration times of 3.6 ks, 15.0 ks and 20.2 ks respectively. No more bursts or other unusual behavior were seen in the ToO observations or in any of the monitoring observations since the burst.

Burst Temporal Properties

We analyzed the temporal properties of the burst in order to compare them to those of other bursts from AXPs and SGRs. The analysis methods are explained in greater detail in Chapter 6 and 8. The burst profile is shown in Figure 10.1 and its measured properties are summarized in Table 10.1. The burst peak time was initially defined, using a time series binned with 1/32 s resolution, as the midpoint of the bin with the highest count rate. We redefined this value, using the event timestamps within this time bin, as the midpoint of the two events

Table 10.1: Burst Timing and Spectral Properties

Temporal Properties	
Burst day, (MJD)	53185
Burst start time, (UT)	6:52:33.63(18)
Burst rise time, t_r (ms)	$18.2^{+5.8}_{-4.4}$
Burst duration, T_{90} (s)	> 699
Burst phase	-0.078 ± 0.016
Fluxes and Fluences	
T_{90} fluence[a] (counts)	> 5387
T_{90} fluence[a] ($\times 10^{-10}$ erg cm^{-2})	> 330
Peak flux for 64 ms[a] ($\times 10^{-10}$ erg s^{-1} cm^{-2})	59 ± 9
Peak flux for t_r ms[a] ($\times 10^{-10}$ erg s^{-1} cm^{-2})	105 ± 20
Spectral Properties[b]	
Power law:	
Power law index	$1.06^{+0.14}_{-0.12}$
Power law flux ($\times 10^{-11}$ erg s^{-1} cm^{-2})	2.6 ± 0.9
Reduced χ^2/degrees of freedom	1.00/62
Blackbody:	
kT (keV)	$2.99^{+0.25}_{-0.23}$
Blackbody flux ($\times 10^{-11}$ erg s^{-1} cm^{-2})	2.4 ± 0.3
Reduced χ^2/degrees of freedom	0.78/62

(a) Fluxes and fluences calculated in the 2–20 keV band; (b)the spectral parameters are derived from fits to a single-component model (power law or blackbody). Because *RXTE* is only sensitive to photons $\geq$2 keV and because of the limited statistics of the burst a two-component fit was not feasible.

having the shortest separation.

Using the burst peak time, we determined the occurrence of the burst in pulse phase. We split our observation into four segments and phase-connected these intervals using the burst peak time as our reference epoch. We then folded our data using the resulting ephemeris and cross-correlated our folded profile with a high signal-to-noise template whose peak was centered on phase $\phi = 0$, where ϕ is measured in cycles (for a review of our timing techniques see § 5.3.8). We find that the burst occurred near the peak of 1E 1048.1–5937's pulse profile, at $\phi = -0.078 \pm 0.016$.

The burst rise time was determined by a maximum likelihood fit to the un-

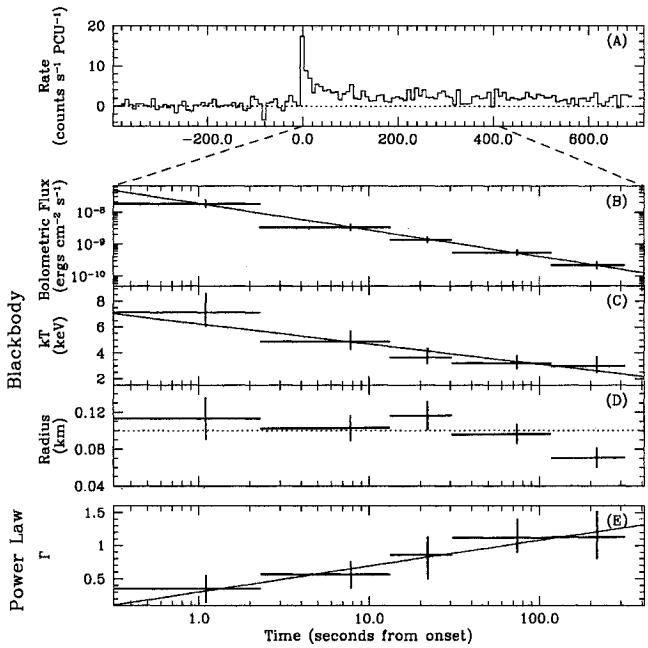

Figure 10.1: Lightcurve and spectral evolution of the burst. A: Background subtracted burst time series in the 2–20 keV band binned with 8-s time resolution. B: Bolometric flux (F) time series. The line represents the best-fit power law, $F = 1.84 \times 10^{-8}(t/1\text{ s})^{-0.82}$ erg cm^{-2} s^{-1}. C: Blackbody temperature (kT) time series. The line represents the best-fit logarithmic function, $kT = 6.24 - 1.55\log(t/1\text{ s})$ keV. D: Blackbody radius versus time. The dotted line represents the average emission radius, $R = 0.10$ km assuming a distance of 5 kpc. E: Power-law index (Γ) time series. The line represents the best-fit logarithmic function, $\Gamma = 0.30 + 0.39\log(t/1\text{ s})$.

binned data using a piecewise function having a linear rise and exponential decay. The burst rise time, t_r, was defined as the time from the peak to when the linear component reached the background (§ 10.2.1 discusses how the background was estimated). The burst duration, T_{90}, is the interval between when 5% and 95% of the total 2–20 keV burst fluence was received. As we will note in § 10.2.1, the burst did not fade away before the end of our observation. Thus we could only place an upper limit of > 699 s on the burst duration, which is the time from the burst's peak to the end of our observation. This very long tail can be seen in the burst profile in Figure 10.1, which shows a significant excess from the burst's peak to the end of our observation.

Burst Spectral Evolution

Significant spectral evolution has been noted for the first burst discovered from this source (see § 6.3.2) as well as for bursts from AXP XTE J1810–197 (Woods et al., 2005) and bursts from SGRs (Ibrahim et al., 2001; Lenters et al., 2003). Motivated by these observations we extracted spectra at different intervals within the burst's duration. We increased the integration time of the spectra as we went further away from the burst to maintain adequate signal-to-noise. A background spectrum was extracted from a 1000-s long interval which ended 10 s before the burst. From each of the burst intervals and the background interval we subtracted the instrumental background as estimated from the tool `pcabackest`. Each burst interval spectrum was grouped so that there were never fewer than 20 counts per spectral bin after background subtraction. The regrouped spectra along with their background estimators were used as input to the X-ray spectral fitting software package `XSPEC`[1]. Response matrices were created using the `FTOOLs` `xtefilt` and `pcarsp`. All channels below 2 keV and above 30 keV were ignored leaving 10–24 spectral bins for fitting. We fit the burst spectra to a photoelectrically absorbed blackbody model which adequately characterized the data. In all fits, the column density was held fixed at the average value of our *Chandra* and *XMM-Newton* observations (see § 10.2.2 and Table 10.2). The burst's bolometric flux, blackbody temperature and radius evolution are shown in Figure 10.1. The bolometric flux decayed as a power law in time, $F = F_1(t/1\ \mathrm{s})^{\beta}$, where $F_1 = 1.84 \pm 0.36 \times 10^{-8}$ erg cm^{-2} s^{-1} and $\beta = -0.82 \pm 0.05$. The blackbody temperature decayed as $kT = kT_1 - \alpha \log(t/1\ \mathrm{s})$, where $kT_1 = 6.24 \pm 0.71$ keV and $\alpha = 1.55 \pm 0.41$ keV. The blackbody emission radius (calculated via Eq. 2.55 using the luminosity and temperature returned from the fits) remained relatively flat with an average value of $R = 0.100 \pm 0.01$ km. The blackbody radius was calculated assuming a distance of 5 kpc to the source. We repeated the above procedure using a power-law model, which also adequately characterized the data. Our power-law photon index time series is shown in Figure 10.1, where we see

[1] `http://xspec.gsfc.nasa.gov`

Table 10.2: Phase-averaged spectral fit parameters and pulsed fractions of 1E 1048.1–5937.

Parameter[b]	July 8	July 10	July 15
N_H (10^{22} cm^{-2})	1.18(4)	1.18(4)	1.23(5)
kT (keV)	0.619(14)	0.585(12)	0.585(12)
Γ	3.30(9)	3.08(11)	3.23(12)
Flux[c] (10^{-12} ergs cm^{-2} s^{-1})	7.51	7.91	7.51
Unabs Flux[d] (10^{-12} ergs cm^{-2} s^{-1})	9.07	9.56	9.20
χ^2/dof	307/306	293/286	306/278
Pulsed Fraction[e]	0.561(7)	0.563(9)	0.551(10)

(a) The spectral parameters are derived from fits to two-component models (power law + blackbody); (b) numbers in parentheses indicate the 1σ uncertainty in the least significant digits of the spectral parameter. Note that these uncertainties reflect the 1σ error for a reduced χ^2 of unity; (c) observed flux from both spectral components 2–10 keV; (d) unabsorbed flux from both spectral components 2–10 keV; (e) RMS pulsed fraction (2.0–10.0 keV) following the definition in Woods et al. (2004).

that the initial spike of the burst is very hard, with the burst gradually softening as the flux decays. Fitting a logarithmic function to the power-law photon index time series we find $\Gamma = \Gamma_1 + \alpha \log(t/1\text{ s})$, where $\Gamma_1 = 0.30 \pm 0.18$ and $\alpha = 0.39 \pm 0.13$.

Possible spectral features have been reported in bursts from AXPs 1E 1048.1–5937 (see Fig. 6.3) and XTE J1810–197 (Woods et al., 2005) and from bursts from two SGRs (Strohmayer & Ibrahim, 2000; Ibrahim et al., 2002, 2003). We searched for features by extracting spectra of different integration times as was done for the spectral evolution analysis. The spectra were background-subtracted and grouped in the exact same fashion as in the spectral evolution analysis. Energies below 2 keV and above 30 keV were ignored, leaving 13 spectral channels for fitting. Regrouped spectra, background estimators and response matrices were fed into `XSPEC`. Spectra were fit with a photoelectrically absorbed blackbody model, holding only N_H fixed at the same value used in the spectral evolution analysis. The first 8 s of the burst spectrum was poorly fit by a continuum

model, because of significant residuals centered near 13 keV. The apparent line feature was most significant if the first second of the burst was excluded. A simple blackbody fit had reduced $\chi^2_{\rm dof} = 1.61$ for 11 degrees of freedom (see Figure 10.2). The probability of obtaining such a value of χ^2 or larger under the hypothesis that the model is correct is very low, $P(\chi^2 \geq 17.75) = 0.088$. The fit was greatly improved by the addition of a Gaussian emission line; in this case the fit had $\chi^2_{\rm dof} = 0.56$ for 8 degrees of freedom (see Figure 10.2). The probability of obtaining such a value of χ^2 or larger under the hypothesis that the model is correct is $P(\chi^2 \geq 4.75) = .784$. The line energy was $E = 13.09 \pm 0.25$ keV. Note that in Chapter 6 a line at a similar energy was found in the first burst discovered from this source (see Table 6.1).

To firmly establish the significance of this feature, we performed the following Monte Carlo simulation in XPSEC. We generated 10000 fake spectra drawn from a simple blackbody model having the same background and exposure as our data set. We fit the simulated data to a blackbody model and to a blackbody plus emission line model and compared the χ^2 difference between the two. To ensure we were sensitive to narrow lines when fitting our blackbody plus emission line model we stepped through different line energies from 2 to 30 keV in steps of 0.2 keV and refit our spectrum holding the line energy fixed and recorded the lowest χ^2 value returned. In our simulations only 11 events had a χ^2 difference greater or equal to the one found from our data. Thus, the probability of obtaining a spectral feature of equal significance by random chance is ~ 0.0011. The significance of the spectral feature reported for this source in Chapter 6 at this energy was ~ 0.0008. Since these were independent measurements, the probability of finding two spectral features at the same energy by random chance is $\sim 8.8 \times 10^{-7}$, thus the emission line at ~13 keV is genuine.

Burst Energetics

In order to compare the energetics of this burst to those emitted in 2001 we measured its peak flux and fluence. The first step in this analysis was to model the background count rate. First we extracted an instrumental background for

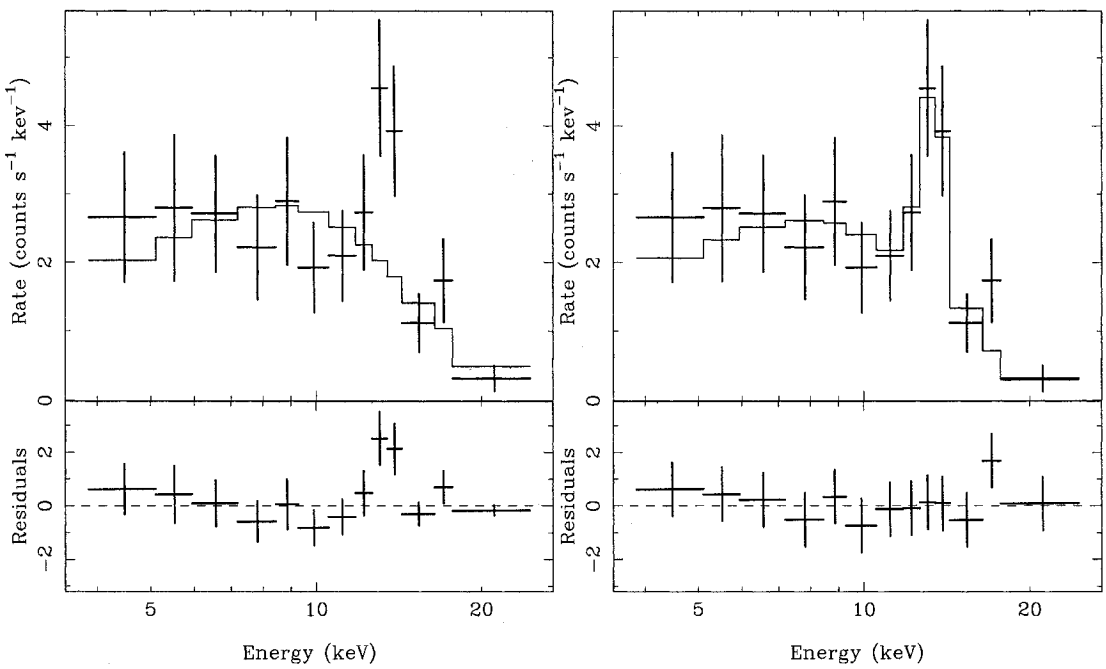

Figure 10.2: The spectrum of the burst tail. Left: An 8-s long spectrum starting 1 s after the peak of the burst fit with a simple blackbody model. The fit had $\chi_{\rm dof} = 1.6$ for 11 degrees of freedom. There is a possibility of a spectral feature at ~ 13 keV. Right: The same spectrum as on the left, but fit with a blackbody plus a Gaussian emission line. The fit had $\chi_{\rm dof} = 0.6$ for 8 degrees of freedom.

the entire observation using `pcabackest`[2]. The function `pcabackest` can only estimate the background rate every 16 s seconds, so we interpolated to finer resolution by modeling the background rate as a 5th order polynomial. We then added the average non-burst count rate to this model. We estimated this value by subtracting our interpolated `pcabackest` model from our data and then measuring the average count rate over the same interval used to estimate the background in the spectral evolution analysis. The 2–20 keV peak flux was determined from the event data using a box-car integrator of width $1/\Delta t$. We used $\Delta t = 64$ ms and $\Delta t = t_r$ (for details on the flux calculation algorithm, see § 8.3). At each step

[2]`http://heasarc.gsfc.nasa.gov/docs/xte/recipes/pcabackest.html`

of the boxcar we subtracted the total number of background counts as determined by integrating our background model over the boxcar limits. To convert our flux measurements from count rates to CGS units we extracted spectra whose limits were defined by the start and stop time of the boxcars. For each flux measurement we extracted a spectrum for the region of interest, a background spectrum and a response matrix, similar to what was done for the spectral evolution analysis. Each spectrum was fit to a photolectrically absorbed blackbody using `XSPEC` in order to measure the 2–20 keV flux in CGS units. The 2–20 keV total fluence was determined by integrating our background-subtracted time series. If the burst had emitted all of its energy during the observation, the integrated burst profile would eventually plateau. However, this is not what we observed. The integrated burst profile was still steadily rising even at the end of our observation, indicating that our observation finished before catching the end of the burst. Thus, we can only set an upper-limit on the total 2–20 keV fluence; see Table 10.1. To convert our fluence upper limit from counts to CGS units the exact procedure was followed as for the peak flux measurements.

Pulsed Flux Measurements

Magnetar candidates have been observed to be highly flux variable, which is why we regularly monitor the pulsed flux of this source (see § 9.2 for a detailed discussion of pulsed flux calculations for 1E 1048.1–5937). The pulsed flux during the entire observation in which the burst occurred was not significantly higher than in neighboring observations. However, in some AXPs and SGRs, short timescale ($\ll$ 1000 s) abrupt changes in pulsed flux have been observed in conjunction with bursts (e.g. Lenters et al., 2003; Woods et al., 2004, 2005). Motivated by such observations we decided to search for short-term pulsed flux enhancements around the time of the burst from 1E 1048.1–5937. We broke the observation into 10 intervals and calculated the pulsed flux for each. In order to avoid having the burst spike biasing our pulsed flux measurements we removed a 4 s interval centered on the burst peak. A factor of 3.5 increase in pulsed flux can be seen in the tail of the burst (see Fig. 10.3). This coupling between bursting activity and

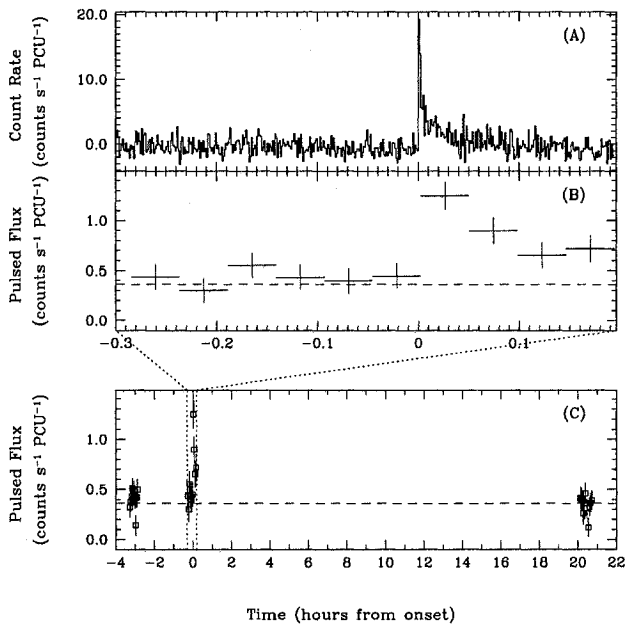

Figure 10.3: Burst lightcurve and 1E 1048.1–5937's pulsed flux evolution. A: Burst time series in the 2–20 keV band, binned with 4-s time resolution. B: Pulsed flux in the 2–10 keV band during the observation. The dashed line represents the average *quiescent* pulsed flux as measured from neighboring observations. C: Same as above except for a longer baseline.

pulsed flux establishes that 1E 1048.1–5937 is definitely the burst source.

10.2.2 Imaging X-ray Observations

The X-ray imaging data analysis presented in this section was performed by Peter M. Woods (see the preface of this thesis). The data were obtained from the *Chandra* X-ray observatory and the X-ray Multi-Mirror Mission (XMM), also know as *XMM-Newton*. These are X-ray imaging satellites with spectral capabilities. For more information on *Chandra* see the *Chandra* Proposers' Observatory Guide[3], and for more information on *XMM-Newton* see the *XMM-Newton* Users' Handbook[4].

[3] `http://cxc.harvard.edu/proposer/POG/index.html`
[4] `http://xmm.vilspa.esa.es/external/xmm_user_support/documentation/index.shtml`

Following the discovery of a new burst from the direction of 1E 1048.1–5937, we triggered observations of the source with imaging X-ray telescopes. The AXP was observed once with *XMM-Newton* on 2004 July 8 for 33 ks and twice with *Chandra* on 2004 July 10 and 15 for 29 and 28 ks, respectively. Simultaneous *RXTE* observations were performed during the *XMM-Newton* and the first *Chandra* observation to assist in the identification of bursts. For scheduling reasons the second *Chandra* observation could not be coordinated with simultaneous *RXTE* observations.

The *XMM-Newton* data were processed using the *XMM-Newton* Science Analysis System[5] (SAS) v6.0.0. The scripts `epchain` and `emchain` were run on the Observation Data Files for the PN and MOS data, respectively. For the *Chandra* data, we started from the filtered event 2 list for all results presented here. Standard analysis threads were followed to extract filtered event lists, light curves and spectra from the processed data. See below for more details. The approximate count rates for the *XMM-Newton* PN observation was 2.69 ± 0.01 counts s^{-1} in the 0.5–12 keV band. The first and second *Chandra* observation had a count rate of 1.344 ± 0.007 counts s^{-1} and 1.302 ± 0.007 counts s^{-1}, respectively, in the 0.5–10 keV band.

Burst Search

The *XMM-Newton* PN camera and *Chandra* ACIS detectors (S3 chip) were operated in similar modes (`TIMING` for PN and `CC mode` for ACIS) to optimize the time resolution in order to search for short X-ray bursts (5.96 ms for PN and 2.85 ms for ACIS). Filtered source event lists (0.5−12.0 keV for PN and 0.5−10.0 keV for ACIS) were extracted for each observation to create light curves at three different time resolutions: 1, 10 and 100 times the nominal time resolution of the data. No bursts were found in any of the light curves. Moreover, no bursts were seen within the *RXTE* PCA data of the simultaneous observations of 1E 1048.1–5937. Aside from the regular X-ray pulsations, the intensity of 1E 1048.1–5937 does not vary significantly within these observations.

[5] `http://xmm.vilspa.esa.es/external/xmm_sw_cal/sas.shtml`

Persistent Emission Properties

Motivated by the sometimes dramatic changes in the persistent, pulsed X-ray emission of SGRs and AXPs following burst activity (e.g. Woods et al., 2004), we investigated both the spectral and temporal properties of the X-ray emission from 1E 1048.1–5937 using the *XMM-Newton* and *Chandra* data. Admittedly, only a single, relatively weak burst was observed from 1E 1048.1–5937 on 2004 June 29, so significant changes in these properties are not necessarily expected. However, this particular source has shown significant variability in its pulsed flux and pulsed fraction over the last several years apparently independent of strong burst activity (Chapter 9; Mereghetti et al., 2004), so searching for continued evolution in these properties is of interest.

The `TIMING` mode for PN data is not yet well calibrated for spectral analysis, so we accumulated a spectrum from the MOS1 camera which was operated in `SMALL WINDOW` mode. The source spectrum was extracted from a circular region centered on the AXP with a radius of 35″. A background spectrum was extracted from a circular (radius = 80″), source free region on CCD #3, closest to the center of the field of view. The calibration files used to generate the effective area file and response matrix were downloaded on 2004 August 3. The source spectrum was grouped to contain no fewer than 25 counts per channel and fit using `XSPEC`. We obtained a satisfactory fit to the energy spectrum (0.3−12.0 keV) using the standard blackbody plus power-law (BB+PL) model. Fit parameters are given in Table 10.2. For a detail analysis of 1E 1048.1–5937's spectrum above 0.6 keV (for which the `TIMING` mode is better calibrated) including the `TIMING` mode data see Tiengo, Mereghetti, Turolla, et al. (2005).

For the *Chandra* observations, source spectra were extracted from a rectangular region centered on the source with a dimension along the ACIS-S3 readout direction of 16 pixels (∼8″). Background spectra were extracted from 40 pixel wide rectangular regions on either side of the source with a gap of 7 pixels in between the source and background regions. Effective area files and response matrices were generated using CALDB v2.23. Similar to the *XMM-Newton* spectral analysis, the *Chandra* spectra were grouped and fit to the BB+PL model.

We were unable to obtain a satisfactory fit to either *Chandra* data set due to the presence of an emission line at 1.79 keV. This feature is instrumental in origin caused by an excess of Silicon fluorescence photons recorded in the CCD (Morii et al., 2003). To avoid this feature and calibration uncertainties between 0.3 and 0.5 keV that give rise to large residuals in this range, we restricted our spectral fits to 0.5−1.67 and 1.91−10.0 keV. See Table 10.2 for fit parameters.

Using the PN data from *XMM-Newton* and the ACIS data from *Chandra*, we measured the root-mean-square (rms) pulsed fraction of 1E 1048.1–5937 during each of the three observations for different energy bands. For the PN data, a source event list was extracted from a 5.6 pixel wide rectangular region centered on the AXP[6] and the times were corrected to the solar system barycenter. A background event list was extracted from two 10 pixel wide rectangles on either side of the source with a 10 pixel gap between the source and background regions. The same source and background regions used for the spectral analysis of the *Chandra* data were used here for the pulse timing analysis. The *Chandra* photon arrival times were corrected for instrumental time offsets[7] and to the solar system barycenter. Best-fit frequencies were measured independently for each observation and found to be consistent with the more precise *RXTE* spin ephemeris. We constructed background-subtracted folded pulse profiles for each observation for different energy ranges and measured the RMS pulsed fraction following Woods et al. (2004) using the Fourier power from the first 3 harmonics. The pulsed fraction increases with energy from 46.6±0.5% in the 0.5−1.7 keV range to 56.8±1.0% in the 3.0−7.0 keV range. The 2.0−10.0 keV pulsed fractions are listed in Table 10.2.

Comparing our results to those of Mereghetti et al. (2004), we find that both the flux and the pulsed fraction are intermediate between the *XMM-Newton* observations in 2000 December and 2003 June (Figure 10.4). The definition of pulsed fraction introduced by Mereghetti et al. (2004) is significantly different from ours. Therefore, we analyzed each of the archival *XMM-Newton* data sets for

[6] `http://wave.xray.mpe.mpg.de/xmm/cookbook/EPIC_PN/timing/timing_mode.html`
[7] `http://wwwastro.msfc.nasa.gov/xray/ACIS/cctime/`

this source in the same manner as described above for the 2004 data set. Similar to the behavior seen in 2004, we find that the pulsed fraction increases significantly with energy within each archival data set. The average pulsed fractions during these observations, however, are significantly different from 2004. We measure rms pulsed fractions (2.0−10.0 keV) of 76.0 ± 2.3% and 43.9 ± 0.4% for the respective observations. The observation in 2000 took place well before the onset of the first pulsed flux flare (Chapter 8; Fig. 9.1B) and the two bursts seen near the peak of that flare (Chapter 6). The observation in 2003 took place during the decay of the second flare which peaked one year earlier. We conclude that both the flux and pulsed fraction that changed so drastically during these extended flares appear to be returning to their "nominal" pre-flare levels. It is interesting to note that the pulsed fraction decreases during these flares showing a possible anti-correlation with the phase-averaged flux. Thus, the relative increase in the phase-averaged flux is actually much larger than the increase in pulsed flux seen in the *RXTE*/PCA light curve (i.e. the phase-averaged flux time history may have exhibited a stronger peak).

10.3 Discussion

We have discovered the longest, most luminous and most energetic burst from 1E 1048.1–5937 thus far. The short-term pulsed flux enhancement at the time of the burst establishes that 1E 1048.1–5937 is definitely the burst source and in all likelihood was the source of the 2001 bursts as well.

An interesting property of all three bursts from 1E 1048.1–5937 is that they occur preferentially at pulse maximum. A similar trend was found for the transient AXP XTE J1810–197 for which four bursts occurred near pulse maximum (Woods et al., 2005). Furthermore, in Chapter 8 we found that bursts occurred preferentially at pulse phases for which the pulsed emission was high (see Fig. 8.4, note that the pulse profile of 1E 2259+586 is double-peaked as opposed to the quasi-sinusoidal profiles of 1E 1048.1–5937 and XTE J1810–197). SGR bursts on the other hand show no correlation with pulse phase. Palmer (2002) found

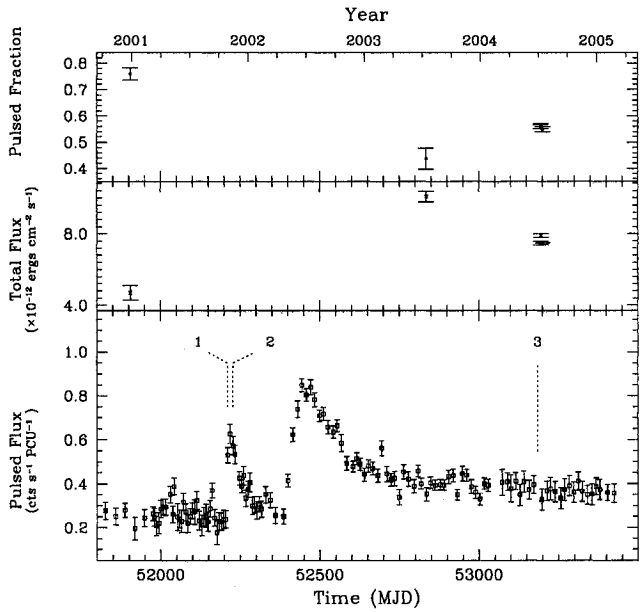

Figure 10.4: 1E 1048.1–5937's total and pulsed flux evolution. Top: 2–10 keV pulsed fraction as measured by *XMM-Newton* and *Chandra* (see Woods et al., 2004, for our particular definition of pulsed fraction). Middle: 2–10 keV total flux as measured by *XMM-Newton* and *Chandra*. Bottom: 2–10 keV pulsed flux as measured by *RXTE* (for details on the analysis see § 9.2). The epochs of the three bursts observed from 1E 1048.1–5937 are indicated by their respective numbers.

that hundreds of bursts from SGR 1900+14 were distributed uniformly in phase. However as discussed in Chapter 8, Woods et al. (2005) and below, this is not the only difference between SGR and AXP bursts.

If AXP bursts do occur at specific pulse phases then they must be associated with particularly active regions of the star. This would imply that AXPs burst much more frequently than is observed, but the bursts go unseen because they are beamed away from us. However, even if a burst is missed, it may still leave two characteristic signatures. One is a very long tail: those observed in 1E 1048.1–5937 and XTE J1810–197 lasted several pulse cycles. Second, short-term increases in pulsed flux like those observed here would be an indication of a burst whose onset went unobserved. A search for "naked tails" or short time scale pulsed flux

enhancements could in principle demonstrate the existence of missed bursts.

The very long tail (> 699 s) of the burst reported here makes it very similar to one burst observed from 1E 1048.1–5937, some of the bursts seen in AXP 1E 2259+586, and to those observed in XTE J1810–197. Their long durations set these bursts apart from the brief $\sim$ 0.1 s burst observed in SGRs. As argued by Woods et al. (2005), bursts from 1E 1048.1–5937, XTE J1810–197 and 1E 2259+586, which have very long tails and occur close to pulse maximum, might constitute a new class of bursts unique to AXPs. Although there were two bursts with extended tails observed from SGR 1900+14, many of their properties differ from those of the long-duration AXP bursts. The first extended-tail SGR burst occurred on 1998 April 29 (Ibrahim et al., 2001) and the second on 2001 April 28 (Lenters et al., 2003). In both cases an obvious distinction could be made between the initial "spike" and the extended "tail" component of the burst. For the AXP bursts which have a fast rise and smooth exponential decay morphology, there is no point which clearly marks the transition between initial spike and extended tail. Furthermore in both of these extended-tail SGR bursts, the majority of the energy was in the initial spike, not the tail. In fact, from the time of their peaks to $\sim$ 1% of their total duration, $\sim$ 98% of their total energy was released. By contrast, in the AXP bursts, virtually all the energy is in what would be considered the tail component. For the burst reported here, from the time of its peak to $\sim$ 1% of its total duration $<$ 37% of its total energy was released. Also, unlike the long-duration AXP bursts which all occurred near pulse maximum, the extended-tail SGR bursts occurred 180° apart in pulse phase, i.e., the first burst occurred near pulse maximum and the second burst near pulse minimum (Lenters et al., 2003). Last, the long-tailed SGR bursts only occurred following high-luminosity flares: the first followed the 1998 August 27 SGR 1900+14 event and the second followed the 2001 April 18 event (Guidorzi et al., 2001). No such high-luminosity flares have ever been observed in an AXP.

From its earliest stages, the magnetar model put forward by Thompson & Duncan (1995) offered a viable burst mechanism for SGRs and AXPs. In a magnetar, the magnetic field is strong enough to crack the crust of the neutron

star (see § 2.3.1 and references therein). The fracturing of the crust disturbs the magnetic field foot-points and releases an electron-position-photon fireball into the magnetosphere. The fireball is trapped and suspended above the fracture site by closed field lines. The suspended fireball heats the surface, and in the initial version of this model, it was suggested that the burst duration would be comparable to the cooling time. In more recent work it has been suggested that burst durations can be extended by orders of magnitude via vertical expansion of the surface layers (Thompson et al., 2002) or deep crustal heating (Lyubarsky et al., 2002). The surface fracture mechanism can explain the very long durations of the bursts observed from 1E 1048.1–5937 and XTE J1810–197. Furthermore this mechanism also provides an explanation for the phase dependence of the AXP bursts, since the fracture sites are thought to be preferentially located near the magnetic poles. Hence the bursts would be associated with a particular active region on the surface, resulting in a correlation with pulse phase.

Lyutikov (2002) proposed another burst emission mechanism within the framework of the magnetar model. He suggested that the bursting activity of AXPs and SGRs is due to the release of magnetic energy stored in non-potential magnetic fields by reconnection-type events in the magnetosphere. In this model, bursts occur at random phases because the emission site is in the upper magnetosphere. Hence no bursts go unobserved (Lyutikov, 2002). This mechanism will produce harder and shorter bursts as compared to the ones due to surface fracturing. Softer and longer bursts are achieved by a combination of reconnection and a small contribution from surface cooling, as energetic reconnection events will precipitate particles which will heat the surface (Lyutikov, 2002). Since there is a duration-fluence correlation in both SGR (Göğüş et al., 2001) and AXP bursts (Fig. 8.7), this model suggests that the shorter (less-luminous) bursts are harder than the longer (more luminous) bursts. A hardness-fluence correlation was found for SGR bursts (Göğüş et al., 2001), but an anti-correlation was found for the 80 bursts from AXP 1E 2259+586, see Figure 8.13. It should also be noted that for 1E 1048.1–5937 and XTE J1810–197 the more energetic bursts are the hardest, although only three bursts have been observed thus far. Hence the aspects that

differentiate the surface-cooling model from the reconnection model for bursts seem to be the same aspects that separate the canonical SGR bursts from the long-duration AXP bursts. In the surface-cooling model one expects longer durations, a correlation with pulse phase and a fluence-hardness anti-correlation.

It is possible that both mechanisms (surface and magnetospheric) are responsible for creating AXP and SGR bursts, but that magnetospheric bursts are more common in SGRs. This is not unreasonable if we consider the twisted-magnetosphere model proposed by Thompson et al. (2002). In this extension to the magnetar model, Thompson et al. (2002) suggested that the highly twisted internal magnetic field of a magnetar imposes stresses on the crust which in turn twist the external dipole field. The twisted external fields induce large-scale currents in the magnetosphere. The inferred dipole magnetic field strengths, luminosity and spectra of SGRs all suggest that the global "twists" of their magnetic fields are greater than those of the AXPs. If the external fields of SGRs are much more "twisted" than those of the AXPs, that would make them more susceptible to reconnection type events in their magnetosphere. Furthermore, if SGRs have stronger magnetic fields than the AXPs, then they would be less susceptible to surface fracture events because at high field strengths the crustal motions are expected to become plastic (Thompson & Duncan, 1996, 2001).

What could make a burst tail last longer in AXPs? We can speculate that the energy is released very deep in the crust and the energy conducts to the surface on very long time scales. If we assume that most of the heat is absorbed by the core, then this scenario could explain why AXP bursts are in general dimmer than SGR bursts. However, how realistic this assumption is cannot be ascertained given the uncertainty of the composition of neutron star cores. In order for the above scenario to explain both the extended-tail SGR bursts and the long-duration AXP bursts one can imagine a hybrid scenario between the Lyutikov (2002) and Lyubarsky et al. (2002) model in which a sudden twist occurs, which deposits energy both in the magnetosphere and deep in the crust. The energy deposited in the magnetosphere gives rise to a spike and the energy deposited deep in the crust conducts to the surface on longer time scales. The

reason why no spike is seen in the AXPs is because the magnetospheric component is small. This reasoning applies to AXPs 1E 1048.1–5937 and XTE J1810–197 but it is not surprising that AXP 1E 2259+586 exhibits both types of bursts, because as argued by Woods et al. (2004) the best explanation for the bursts and contemporaneous flux, pulse profile and spin-down variability from this source was through a catastrophic event that simultaneously impacted the interior and the magnetosphere of the star.

The spectrum of the burst reported here is intriguing. First, although this burst is much harder given its luminosity when compared to SGR bursts (the SGRs show a luminosity-hardness anti-correlation), its spectral softening is very similar to those of the extended-tail bursts of SGR 1900+14 (Ibrahim et al., 2001; Lenters et al., 2003). Second, the evidence of a spectral feature at ~13 keV makes this burst very similar to the first burst detected from 1E 1048.1–5937 (compare Fig. 6.3 to Fig. 10.2). The probability of observing an emission line at ~13 keV in both bursts is exceedingly small, thus the line is almost certainly intrinsic to the source and has important implications. If it is a proton-cyclotron line then it allows us to calculate the surface magnetic field strength, $B = 2.1 \times 10^{15}\,(E/13\text{ keV})$ G (Eq. 1.26 with $m = m_p$, where m_p is the proton mass) where E is the energy of the feature. This value for the magnetic field strength is greater than that measured from the spin-down of the source, but the spin-down is only sensitive to the dipolar component of the field and it is plausible that the field is multipolar. It should be noted that this surface magnetic field strength estimation assumes the burst was a surface cracking phenomenon. An open question is why bursts from certain magnetar candidates exhibit spectral features and others do not. 1E 2259+586 exhibited over 80 bursts and no spectral features were seen, whereas 1E 1048.1–5937 showed only three bursts with 2 spectral features seen. Woods et al. (2005) reported a spectral feature at approximately the same energy in a burst from AXP XTE J1810–197 at a higher significance level than both of the 1E 1048.1–5937 spectral features.

We have argued that the bursts from 1E 1048.1–5937 are very similar to those of XTE J1810–197. Interestingly, the two sources show other similarities.

They both have sinusoidal profiles while all other AXPs exhibit rich harmonic content in their pulse profiles (see Fig. 1.4). They have shown long-lived (> months) pulsed flux variations which are not due to cooling of the crust after the impulsive injection of heat from bursts. Furthermore, their timing properties are the most reminiscent of the SGRs.

The pulsed fraction decrease we have observed lends further evidence that the pulsed flux variations we have observed in 1E 1048.1–5937 (Chapter 8; Fig. 9.1B) represent a new phenomenon seen exclusively in the AXPs. The fact that the pulsed fraction decreased as the pulsed flux increased without any pulse morphology changes implies that there was a greater fractional increase in the unpulsed flux than in the pulsed flux, in agreement with what was found by Mereghetti et al. (2004). Such a flux enhancement cannot be attributed to a particular active region. Thus we can rule out the flux enhancements were due to the injection of heat from bursts that were beamed away from us, because in that scenario one would expect a larger fractional change in pulsed flux than in total flux. Indeed, during the burst afterglow pulsed flux enhancement in SGR 1900+14, Lenters et al. (2003) found a pulsed flux and pulse fraction increase.

10.4 Summary

In this chapter we reported on the discovery of a third burst from AXP 1E 1048.1–5937. Two bursts were previously observed from the direction of this source in Fall 2001 (Chapter 6). However, because of the large FOV of *RXTE* we could not establish that 1E 1048.1–5937 was definitely the source of the bursts. Fortuitously, at the time of this burst the source also exhibited a simultaneous short-term pulsed flux enhancement which established the AXP as the burster. The similarities between this burst and the two others confirms that the AXP emitted all three. This is the second AXP confirmed to burst as part of this thesis work. Recently, Woods et al. (2005) discovered bursts from AXP XTE J1810–197 which means that to date half of the AXP population has been observed to burst. These bursts have a clear explanation within the context of the magnetar model.

The specific conclusions of this chapter, the previous chapters, as well as the conclusions of this thesis as a whole are given in the next chapter.

Chapter 11

Conclusions

Anomalous X-ray pulsars (AXPs) were a mystery because they did not fall into the two canonical categories for pulsars: rotation-powered or accretion-powered binaries. They are not rotation-powered because their observed X-ray luminosities are much greater than their loss of rotational kinetic energy. They are not accretion-powered binaries because they have no companions from which to accrete. Two competing models emerged in order to explain AXP emission. One was that AXPs are accreting from a disk made up of material left over from the supernova explosion – the fall-back disk model. The other model proposed that AXPs are young, isolated neutron stars powered by the decay of an enormous magnetic field – the magnetar model. Both models are able to account for their observed X-ray luminosities and their rapid spin-down. The fall-back disk model provides an explanation for the narrow range of AXP spin-periods, however it does not accurately describe the IR emission of AXPs – especially in one case where the IR emission is modulated at the spin frequency of the star with a pulsed fraction too high to be accounted for by a fall-back disk (4U 0142+61, Kern & Martin, 2002). The magnetar model for AXPs was favored because the emission of AXPs is very similar to that of another class of sources, the Soft Gamma Repeaters (SGRs), for which there exists independent evidence for being magnetars. The SGRs emit frequent bursts of hard X-ray/soft gamma-rays and three have emitted giant flares; these events can only be explained within the context of the magnetar model. Thus for many years the main difference between AXPs and SGRs was that SGRs were observed to burst while AXPs were not.

The magnetar model for AXPs was given a major boost with our discovery of two X-ray bursts from the direction of AXP 1E 1048.1–5937 in Fall 2001. These

bursts were very similar to those of SGRs: they had asymmetric profiles with very fast rise times and slow decay times; the bursts were spectrally harder than the persistent emission; the fluences and the peak fluxes of the bursts fell within the ranges observed for SGR bursts. The first burst, however, was unusual in that it had a very long tail ($\sim$ 51 s, while most SGR bursts have $\sim$0.1 s durations) and a spectral feature at around $\sim$13 keV. If this feature is interpreted as a proton-cyclotron line, then it confirms that this source has a magnetar-strength field. Furthermore, both bursts occurred near the peak of the source's pulse profile, while SGR bursts are uniformly distributed in pulse phase. Despite these differences the bursts were sufficiently similar to those of the SGRs. However, because of the $1^\circ \times 1^\circ$ field-of-view (FOV) of *RXTE* we could not unambiguously identify 1E 1048.1–5937 as the source of the bursts, which obliged us to consider alternate sources for the bursts. Gamma-ray bursts (GRBs) sometimes emit prompt X-ray emission. However, GRBs are not observed to repeat, thus the probability of observing two in the same FOV as 1E 1048.1–5937 is low. Low-mass X-ray binaries (LMXBs) are known to emit thermonuclear X-ray bursts, the so called Type I X-ray bursts. However, the spectral and temporal properties of Type I X-ray bursts are very different from those observed here; furthermore, there is no known LMXB in 1E 1048.1–5937's FOV. Thus, we conclude that 1E 1048.1–5937 is the most likely source of the bursts.

The open question of whether AXPs do in fact burst or not was answered on 2002 June 18 with the discovery of a major outburst from AXP 1E 2259+586. The outburst consisted of over 80 X-ray bursts within a four hour long *RXTE* observation, along with several changes to the persistent and pulsed emission of the pulsar – clearly identifying 1E 2259+586 as the burster. The variability exhibited by 1E 2259+586 at the time of the outburst included: an increase of the pulsed and persistent X-ray emission by over an order of magnitude relative to quiescent levels. Both decayed significantly during the course of the observation. Correlated spectral hardening was also observed, with the spectrum softening during the observation. In addition, we observed a pulse profile change, in which the amplitudes of the two peaks in the pulse profile were swapped. The profile

relaxed back to its pre-outburst morphology after ~6 days. The pulsar also underwent a sudden spin-up ($\Delta\nu/\nu = 4 \times 10^{-6}$), followed by a large (factor of ~2) increase in spin-down rate which persisted for >18 days. We also observed, using the *Gemini*-North telescope, an infrared enhancement, in which the K_s (2.15 μm) flux increased, relative to that measured in an observation made in 2000, by a factor of ~3, three days post-outburst. The IR counterpart then faded by a factor of ~2 a week later. All these simultaneous changes in the pulsar's emission undoubtedly establishes the AXP as the source of the bursts. Furthermore, the properties of the outburst were like those seen only in SGRs, thus conclusively unifying AXPs and SGRs – a connection uniquely predicted by the magnetar model.

Given that the radiative changes during 1E 2259+586's 2002 June 18 outburst were similar to those observed in SGRs, we decided to determine whether 1E 2259+586's bursts were similar to SGR bursts. We performed a comprehensive statistical analysis of the 1E 2259+586 bursts and compared our results with those obtained for the two best-studied SGRs, 1806−20 and 1900+14. Indeed, the bursts were quantitatively similar to those of SGRs in many ways, further confirming that AXPs and SGRs share a common nature. We found the following similarities: the burst durations followed a log-normal distribution which peaked at 99 ms, the differential burst fluence distribution was well described by a power law of index −1.7; the burst fluences were positively correlated with the burst durations, the distribution of waiting times were well described by a log-normal distribution of mean 47 s, and the bursts were generally asymmetric with faster rise than fall times. However, we also found some interesting quantitative differences between the 1E 2259+586 and SGR bursts, which may help shed light on the physical difference(s) between AXPs and SGRs. We found: the AXP bursts exhibited a wider range of durations; the correlation between burst fluence and duration was flatter than for SGRs; the observed AXP bursts were on average less energetic than observed SGR bursts; the more energetic AXP bursts had the hardest spectra – the opposite of what is seen for SGRs. Furthermore, unlike the SGRs, we found a correlation of burst phase with pulsed intensity. We conclude

that the bursts are sufficiently similar that AXPs and SGRs can be considered united as a source class yet there exists some interesting differences that may help determine what physically differentiates the two closely related manifestations of neutron stars.

The pulsed flux enhancement observed during 1E 2259+586's outburst was intriguing because it answered an important question: are AXPs flux variable? Answering this question was important because it has important implications on the current number of magnetars. There were past reports of flux variability (factors of $\sim$10 in some cases) in AXPs, however they were called into question because these data were taken with different instruments (some imaging some not) and because long-term monitoring of AXPs by Gavriil & Kaspi (2002) (before 1E 2259+586's outburst) showed that AXP fluxes are stable. The flux enhancement from 1E 2259+586 unambiguously determined that AXPs can be flux variable. It seemed however that flux variations were abrupt events (i.e., they have instantaneous rises) and associated with major outbursts. This idea was turned on its head when we discovered two slow-rising, long-lasting pulsed flux flares from AXP 1E 1048.1–5937. The flares had peak fluxes of 2.21 ± 0.16 and 3.00 ± 0.13 times the quiescent value. Both flares lasted several months and had well resolved few-week-long rises. The long rise times of the flares is a phenomenon not previously reported for this class of object. We had also found large (factor of $\sim$12) changes to the pulsar's spin-down rate on time scales of weeks to months, shorter than had been reported previously. In any accretion scenario one would expect a strong correlation between the spin-down rate and flux variations. However, we only found marginal evidence for such a correlation, with probability of non-random correlation 6%. The magnetar model can explain the abrupt flux enhancement seen in 1E 2259+586 (and in the SGRs) as afterglow after the impulsive injection of heat from magnetospheric bursts; but, can the magnetar model explain the flux flares observed in 1E 1048.1–5937? Well, according to Thompson et al. (2002) the internal magnetic field of a magnetar is believed to be highly twisted. As the highly twisted internal magnetic field diffuses to the exterior it stress the crust, which in turn twists the external

magnetic field lines. Twisting the external magnetic field lines allows large scale currents to flow, which enhance the X-ray emission. Thus, the pulsed flux flares observed from 1E 1048.1–5937 can be explained as being due to the unwinding of the highly-twisted internal magnetic field of a magnetar.

The mystery of whether AXP 1E 1048.1–5937 emitted the two bursts in Fall 2001 was finally solved with the discovery of a third burst from this source. Contemporaneously with the burst we discovered a pulsed-flux enhancement which unambiguously identified 1E 1048.1–5937 as the burst's origin. The clear identification of 1E 1048.1–5937 as the burster in this case argued that it was indeed the emitter of the two bursts discovered from the direction of this source in 2001, as already inferred by Gavriil et al. (2002). Recently, Woods et al. (2005) detected four X-ray bursts from AXP XTE J1810–197, all of which showed similar simultaneous short-term pulsed flux enhancements as 1E 1048.1–5937.

All three bursts from 1E 1048.1–5937 can only be explained within the context of the magnetar model, however many of their properties differentiate them from canonical SGR bursts. The first and third burst discovered from this source had very long tails, $\sim$51 s and $>$ 699 s respectively, as opposed to the $\sim$0.1 s duration SGR bursts. Two ks-long SGR bursts have been reported but we argued that they were a very different phenomenon (Ibrahim et al., 2001; Lenters et al., 2003). Specifically the extended-tail SGR bursts had very energetic initial spikes and the long tails were argued to be the afterglow of this initial injection of energy. However, in the AXP bursts no such spikes are present; in fact, most of the energy is in what would be considered the tail. All three bursts from 1E 1048.1–5937 occurred near pulse maximum, as opposed to the SGR bursts which are uniformly distributed in pulse phase. The spectral evolution of the third 1E 1048.1–5937 burst was very similar to the extended-tail SGR bursts with the trend going from hard to soft. However, at one part of the bursts tail there was an unusual spectral feature at $\sim$13 keV; just like in the first burst observed from this source. A similar feature was also discovered in a very high signal-to-noise burst from XTE J1810–197 (Woods et al., 2005). If more features such as these are confirmed they may provide direct estimates of the neutron

star's magnetic field especially if harmonic features can be positively identified.

All of the bursts discovered from 1E 1048.1–5937 and XTE J1810–197 as well as a handful of bursts from 1E 2259+586 share the following properties: they have long-tails (with no energetic spikes) and they occur near pulse maxima. As argued by Woods et al. (2005) bursts such as these might comprise a new burst class thus far unique to AXPs. The differences between the long- and short-duration bursts might be due to separate emission mechanisms. Two burst mechanisms have been proposed within the magnetar model: surface fracture and magnetospheric reconnection (Thompson & Duncan, 1995; Lyutikov, 2002). We argued that the long-tailed 1E 1048.1–5937 and 1E 2259+586 bursts are more likely surface fracture events which agrees with the conclusion reached by Woods et al. (2005) for the long-tailed bursts from XTE J1810–197. If in fact the two classes of bursts are due to emission mechanisms operating in two distinct regions (near the surface and in the upper magnetosphere), then AXP bursts provide opportunities to probe the physics of these separate regions of a magnetar.

Bursts from AXP 1E 1048.1–5937 were predicted by Kaspi et al. (2001) because this source is the most SGR-like of all the AXPs: it shows the most timing noise, it has a sinusoidal profile and a relatively hard spectrum. However, bursts from 1E 2259+586 were somewhat surprising because it showed prolonged timing stability, has the most harmonic content in its pulse profile, and the softest spectrum. The fact that we observed bursts from 1E 2259+586 suggests that any AXP can burst. Together with XTE J1810–197, three out of the seven confirmed AXPs have now been observed to burst – something predicted and explained uniquely by the magnetar model. Given the rarity of AXP bursts coupled with the unique information that detection of such bursts provide, observing more outbursts is obviously desirable. Continued monitoring is thus clearly warranted, and *RXTE* with its large area and flexible scheduling is the obvious instrument of choice.

As a final note, despite all the success of the magnetar model there are still some outstanding issues in the field. For example, the magnetar model does not explain why AXPs have spin periods in the narrow range of 5–12 s. Although

the fall-back disk cannot explain the bursts from AXPs and it struggles with the optical/IR emission, it does provide an explanation for the period clustering. In the fall-back disk model one expects to observe these sources when they are in the short-lived "tracking phase"; while in this phase the neutron star is spinning at its equilibrium spin period (Chatterjee et al., 2000). Another mystery is why there exists three large B-field ($B \sim 10^{13}$ G) radio pulsars which exhibit no AXP behavior (see McLaughlin et al., 2005). These pulsars exhibit no X-ray emission and the AXPs are radio-quiet. The magnetic fields of these high B-field radio pulsars are calculated using Eq. 1.39 which only determines the strength of the dipolar component of the field; hence, one can speculate that AXPs have stronger fields in higher multipoles. Nevertheless one would still expect a continuum of behavior between the two classes. Another issue is the optical/IR emission from AXPs. The fall-back disk model in some cases overpredicts and in other underpredicts the flux from AXPs. The magnetar model can energetically account for this emission but it does not make any *ab initio* predictions about where this emission is coming from. In the fall-back disk model, and possibly in the magnetar model, one expects a correlation between the X-ray and optical/IR flux. Indeed a definite correlation was seen for 1E 2259+586 (Tam et al., 2004) and possibly for XTE J1810–197 (Rea et al., 2004). However in AXP 1E 1048.1–5937 there is no obvious correlation; if anything the optical/IR and X-ray flux are anti-correlated (Durant & van Kerkwijk, 2005). If the optical/IR emission is purely magnetospheric, then any variations in the optical/IR emission should also be correlated to the photon index of the power-law component of AXP spectra which Thompson et al. (2002) proposed is moderated by magnetospheric currents. We have proposed to test this prediction using joint *Chandra* X-ray Observatory and *Hubble* Space Telescope observations. Perhaps future observations using telescopes operating in the mid-IR band such as the *Spitzer* Space Telescope will also provide new clues towards solving this mystery.

Bibliography

Alpar, M. A. 1999, http://xxx.lanl.gov/abs/astro-ph/9912228

—. 2001, ApJ, 554, 1245

Alpar, M. A., Chau, H. F., Cheng, K. S., & Pines, D. 1993, ApJ, 409, 345

Alpar, M. A., Cheng, K. S., & Pines, D. 1989, ApJ, 346, 823

Anderson, P. W. & Itoh, N. 1975, Nature, 256, 25

Arnaud, K. A. 1996, in Astronomical Data Analaysis Software and Systems V, ed. G. Jacoby & J. Barnes, Vol. 101 (San Fransisco: ASP), 17

Baade, W. & Zwicky, F. 1934, Proc. Nat. Acad. Sci., 20, 254

Bak, P., Tang, C., & Wiesenfeld, K. 1988, Phys. Rev. A, 38, 364

Bassani, L., Malizia, A., Stephen, J. B., Bazzano, A., Ubertini, P., Barlow, E. J., Bird, A. J., Dean, A. J., Hill, A. B., Shaw, S. E., Walter, R., Bodaghee, A., Belanger, G., Lebrun, F., Terrier, R., & Much, R. 2004, The Astronomer's Telegram, 232, 1

Baykal, A. & Swank, J. 1996, ApJ, 460, 470

Baym, G., Pethick, C., & Pines, D. 1969, Nature, 224, 673

Baym, G. & Pines, D. 1971, Ann. Phys. (U.S.A.), 66, 816

Bildsten, L., Chakrabarty, D., Chiu, J., Finger, M. H., Koh, D. T., Nelson, R. W., Prince, T. A., Rubin, B. C., Scott, D. M., Stollberg, M., Vaughan, B. A., Wilson, C. A., & Wilson, R. B. 1997, ApJS, 113, 367

Bowers, R. L. & Deeming, T. 1984, Astrophysics. Volume 1 - Stars (Research supported by the University of Texas, Los Alamos National Laboratory, and Digicon Geophysical Corp. Boston, MA, Jones and Bartlett Publishers, Inc., 1984, 343 p.)

Braithwaite, J. & Spruit, H. C. 2004, Nature, 431, 819

Brandt, N. & Podsiadlowski, P. 1995, MNRAS, 274, 461

Burwitz, V., Zavlin, V. E., Neuhäuser, R., Predehl, P., Trümper, J., & Brinkman, A. C. 2001, A&A, 379, L35

Cannizzo, J. K., Lee, H. M., & Goodman, J. 1990, ApJ, 351, 38

Carroll, B. W. & Ostlie, D. A. 1996, An introduction to modern astrophysics (Reading, Mass. : Addison-Wesley Pub., c1996.)

Chadwick, J. 1932, Nature, 129, 312

Chakrabarty, D., Bildsten, L., Grunsfeld, J. M., Koh, D. T., Prince, T. A., Vaughan, B. A., Finger, M. H., Scott, D. M., & Wilson, R. B. 1997, ApJ, 474, 414

Chandrasekhar, S. 1931, ApJ, 74, 81

Charbonneau, P. & MacGregor, K. B. 2001, ApJ, 559, 1094

Chatterjee, P., Hernquist, L., & Narayan, R. 2000, ApJ, 534, 373

Cheng, B., Epstein, R. I., Guyer, R. A., & Young, A. C. 1996, Nature, 382, 513

Chevalier, R. A. 1989, ApJ, 346, 847

Chiu, H. Y. & Salpeter, E. E. 1964, Phys. Rev. Lett., 12, 413

Corbel, S., Chapuis, S., Dame, T. M., & Durouchoux, P. 1999, ApJ, 526, L29

Corbel, S. & Eikenberry, S. S. 2004, A&A, 419, 191

Corbel, S., Wallyn, P., Dame, T. M., Durouchoux, P., Mahoney, W. A., Vilhu, O., & Grindlay, J. E. 1997, ApJ, 478, 624

Corbet, R. H. D. & Mihara, T. 1997, ApJ, 475, L127

Corbet, R. H. D., Smale, A. P., Ozaki, M., Koyama, K., & Iwasawa, K. 1995, ApJ, 443, 786

Cowling, T. G. 1934, MNRAS, 94, 768

Crosby, N. B., Aschwanden, M. J., & Dennis, B. R. 1993, Sol. Phys., 143, 275

Cumming, A., Arras, P., & Zweibel, E. 2004, ApJ, 609, 999

Dall'Osso, S., Israel, G. L., Stella, L., Possenti, A., & Perozzi, E. 2003, ApJ, 599, 485

den Hartog, P. R., Kuiper, L., Hermsen, W., & Vink, J. 2004, The Astronomer's Telegram, 293, 1

Dhillon, V. S., Marsh, T. R., Hulleman, F., van Kerkwijk, M. H., Shearer, A., Littlefair, S. P., Gavriil, F. P., & Kaspi, V. M. 2005, MNRAS, 363, 609

Duncan, R. C. & Thompson, C. 1992, ApJ, 392, L9

Durant, M. & van Kerkwijk, M. H. 2005, ApJ, 627, 376

Durant, M., van Kerkwijk, M. H., & Hulleman, F. 2004, in IAU Symposium, 251–+

Ekşı, K. Y. & Alpar, M. A. 2003, ApJ, 599, 450

Fahlman, G. G. & Gregory, P. C. 1981, Nature, 293, 202

Feroci, M., Caliandro, G. A., Massaro, E., Mereghetii, S., & Woods, P. M. 2004, ApJ, 612, 408

Fishman, G. J. et al. 1993, A&AS, 97, 17

Frail, D. A., Kulkarni, S. R., & Bloom, J. S. 1999, Nature, 398, 127

Frank, J., King, A. R., & Raine, D. J. 1985, Accretion Power in Astrophysics (Cambridge: Cambridge University Press)

Francischelli, G. J., Wijers, R. A. M. J. 2002, http://xxx.lanl.gov/abs/astro-ph/0205212

Göhler, E., Wilms, J., & Staubert, R. 2005, A&A, 433, 1079

Göğüş, E., Kouveliotou, C., Woods, P. M., Thompson, C., Duncan, R. C., & Briggs, M. S. 2001, ApJ, 558, 228

Gaensler, B. M. 2004, Advances in Space Research, 33, 645

Gaensler, B. M., Gotthelf, E. V., & Vasisht, G. 1999, ApJ, 526, L37

Gaensler, B. M., McClure-Griffiths, N. M., Oey, M. S., Haverkorn, M., Dickey, J. M., & Green, A. J. 2005, ApJ, 620, L95

Gaensler, B. M., Slane, P. O., Gotthelf, E. V., & Vasisht, G. 2001, ApJ, 559, 963

Gaensler, B. M., Slane, P. O., Gotthelf, E. V., & Vasisht, G. 2001, ApJ, 559, 963

Gavriil, F. P. & Kaspi, V. M. 2002, ApJ, 567, 1067

Gavriil, F. P. & Kaspi, V. M. 2004, ApJ, 609, L67

Gavriil, F. P., Kaspi, V. M., & Woods, P. M. 2002, Nature, 419, 142

—. 2004, ApJ, 607, 959

Gavriil, F. P., Kaspi, V. M., & Woods, P. M. 2006, ApJ, in press (astro-ph/0507047)

Gögüs, E., Woods, P. M., Kouveliotou, C., van Paradijs, J., Briggs, M. S., Duncan, R. C., & Thompson, C. 1999, ApJ, 526, L93

Gögüs, E., Woods, P. M., Kouveliotou, C., van Paradijs, J., Briggs, M. S., Duncan, R. C., & Thompson, C. 2000, ApJ, 532, L121

Goldreich, P. & Julian, W. H. 1969, ApJ, 157, 869

Goldreich, P. & Reisenegger, A. 1992, ApJ, 395, 250

Gotthelf, E. V., Gavriil, F. P., Kaspi, V. M., Vasisht, G., & Chakrabarty, D. 2002, ApJ, 564, L31

Gotthelf, E. V., Halpern, J. P., Buxton, M., & Bailyn, C. 2004, ApJ, 605, 368

Gotthelf, E. V. & Vasisht, G. 1998, New Astronomy, 3, 293

Gotthelf, E. V., Vasisht, G., & Dotani, T. 1999, ApJ, 522, L49

Griffiths, D. J. 1995, Introduction to quantum mechanics (Introduction to quantum mechanics/ David J. Griffiths. Englewood Cliffs, N.J.: Prentice Hall, c1995.)

—. 1999, Introduction to Electrodynamics (Upple-Saddle River, New Jersey : Prentice-Hall Inc., c1999.)

Guidorzi, C., Montanari, E., Frontera, F., Costa, E., Gandolfi, G., Feroci, M., Piro, L., Amati, L., in't Zand, J. J. M., D'Andreta, G., Kaptein, R., & Reboa, L. 2001, GRB Circular Network, 1041, 1

Gutenberg, B. & Richter, C. F. 1956a, Bull. Seism. Soc. Am., 46, 105

—. 1956b, Ann. Geophys., 9, 1

—. 1965, Seismicity of the Earth and Associated Phenomena (New York: Hafner)

Hailey, C. J. & Mori, K. 2002, ApJ, 578, L133

Halpern, J. P. & Gotthelf, E. V. 2005, ApJ, 618, 874

Heindl, W. A., Rothschild, R. E., Coburn, W., Staubert, R., Wilms, J., Kreykenbohm, I., & Kretschmar, P. 2004, in AIP Conf. Proc. 714: X-ray Timing 2003: Rossi and Beyond, 323–330

Heise, J., in't Zand, J., Kippen, M., & Woods, P. 2001 (Memorie della Societa' Astronomica Italiana), http://xxx.lanl.gov/abs/astro-ph/0111246

Hessels, J. W. T, Ransom, S. M., Stairs, I. H., Freire, P. C. C., Kaspi, V. M., & Camilo, F. 2006, Science, in press

Hewish, A., Bell, S. J., Pilkington, J. D. H., Scott, P. F., & Collins, R. A. 1968, Nature, 217, 709

Heyl, J. S. & Hernquist, L. 1999, MNRAS, 304, L37

Hjorth, J., Sollerman, J., Møller, P., Fynbo, J. P. U., Woosley, S. E., Kouveliotou, C., Tanvir, N. R., Greiner, J., Andersen, M. I., Castro-Tirado, A. J., Castro Cerón, J. M., Fruchter, A. S., Gorosabel, J., Jakobsson, P., Kaper, L., Klose, S., Masetti, N., Pedersen, H., Pedersen, K., Pian, E., Palazzi, E., Rhoads, J. E., Rol, E., van den Heuvel, E. P. J., Vreeswijk, P. M., Watson, D., & Wijers, R. A. M. J. 2003, Nature, 423, 847

Hulleman, F., Tennant, A. F., van Kerkwijk, M. H., Kulkarni, S. R., Kouveliotou, C., & Patel, S. K. 2001a, ApJ, 563, L49

—. 2001b, ApJ, 563, L49

Hulleman, F., van Kerkwijk, M. H., & Kulkarni, S. R. 2000, Nature, 408, 689

Hulleman, F., van Kerkwijk, M. H., & Kulkarni, S. R. 2004, A&A, 416, 1037

Hurley, K., Cline, T., Mazets, E., Barthelmy, S., Butterworth, P., Marshall, F., Palmer, D., Aptekar, R., Golenetskii, S., Ill'lnskii, V., Frederiks, D., McTiernan, J., Gold, R., & Trombka, T. 1999, Nature, 397, 41

Ibrahim, A. I., Markwardt, C. B., Swank, J. H., Ransom, S., Roberts, M., Kaspi, V. M., Woods, P. M., Safi-Harb, S., Balman, S., Parke, W. C., Kouveliotou, C., Hurley, K., & Cline, T. 2004, ApJ, 609, L21

Ibrahim, A. I., Safi-Harb, S., Swank, J. H., Parke, W., Zane, S., & Turolla, R. 2002, ApJ, 574, L51

Ibrahim, A. I., Strohmayer, T. E., Woods, P. M., Kouveliotou, C., Thompson, C., Duncan, R. C., Dieters, S., Swank, J. H., van Paradijs, J., & Finger, M. 2001, ApJ, 558, 237

Ibrahim, A. I., Swank, J. H., & Parke, W. 2003, ApJ, 584, L17

Israel, G. L., Covino, S., Perna, R., Mignani, R., Stella, L., Campana, S., Marconi, G., Bono, G., Mereghetti, S., Motch, C., Negueruela, I., Oosterbroek, T., & Angelini, L. 2003, ApJ, 589, L93

Israel, G. L., Covino, S., Stella, L., Campana, S., Haberl, F., & Mereghetti, S. 1999, ApJ, 518, L107

Israel, G. L., Covino, S., Stella, L., Campana, S., Marconi, G., Mereghetti, S., Mignani, R., Negueruela, I., Oosterbroek, T., Parmar, A. N., Burderi, L., & Angelini, L. 2002, ApJ, 580, L143

Israel, G. L., Mereghetti, S., & Stella, L. 1994, ApJ, 433, L25

Israel, G. L., Rea, N., Mangano, V., Testa, V., Perna, R., Hummel, W., Mignani, R., Ageorges, N., Lo Curto, G., Marco, O., Angelini, L., Campana, S., Covino, S., Marconi, G., Mereghetti, S., & Stella, L. 2004, ApJ, 603, L97

Iwasawa, K., Koyama, K., & Halpern, J. P. 1992, PASJ, 44, 9

Jones, P. B. 1988, MNRAS, 233, 875

Juett, A. M., Marshall, H. L., Chakrabarty, D., & Schulz, N. S. 2002, ApJ, 568, L31

Kaspi, V. M., Chakrabarty, D., & Steinberger, J. 1999, ApJ, 525, L33

Kaspi, V. M. & Gavriil, F. P. 2003, ApJ, 596, L71

Kaspi, V. M. & Gavriil, F. P. 2004, in The Restless High-Energy Universe, ed. E. van den Heuvel, J. in't Zand, & R. Wijers (Elsevier), in press (astro-ph/0402176)

Kaspi, V. M., Gavriil, F. P., Chakrabarty, D., Lackey, J. R., & Muno, M. P. 2001, ApJ, 558, 253

Kaspi, V. M., Gavriil, F. P., Woods, P. M., Jensen, J. B., Roberts, M. S. E., & Chakrabarty, D. 2003, ApJ, 588, L93

Kaspi, V. M., Lackey, J. R., & Chakrabarty, D. 2000, ApJ, 537, L31

Kaspi, V. M, Roberts, M. S. E. & Harding, A. K. 2004, http://xxx.lanl.gov/abs/astro-ph/0402136

Katz, J. I. 1986, J. Geophys. Res., 91, 10412

Kern, B. & Martin, C. 2002, Nature, 415, 527

Klose, S., Henden, A. A., Geppert, U., Greiner, J., Guetter, H. H., Hartmann, D. H., Kouveliotou, C., Luginbuhl, C. B., Stecklum, B., & Vrba, F. J. 2004, ApJ, 609, L13

Kosugi, G., Ogasawara, R., & Terada, H. 2005, ApJ, 623, L125

Kothes, R., Uyaniker, B. ., & Yar, A. 2002, ApJ, 576, 169

Kouveliotou, C. & 10 others. 1994, Nature, 368, 125

Kouveliotou, C., Dieters, S., Strohmayer, T., van Paradijs, J., Fishman, G. J., Meegan, C. A., Hurley, K., Kommers, J., Smith, I., Frail, D., & Murakami, T. 1998, Nature, 393, 235

Kouveliotou, C., Eichler, D., Woods, P. M., Lyubarsky, Y., Patel, S. K., Göğüş, E., van der Klis, M., Tennant, A., Wachter, S., & Hurley, K. 2003, ApJ, 596, L79

Kouveliotou, C., Fishman, G. J., Meegan, C. A., Paciesas, W. S., Wilson, R. B., van Paradijs, J., Preece, R. D., Briggs, M. S., Pendleton, G. N., & Brock, M. N. 1993, Nature, 362, 728

Kouveliotou, C., Strohmayer, T., Hurley, K., Van Paradijs, J., Finger, M. H., Dieters, S., Woods, P., Thompson, C., & Duncan, R. C. 1999, ApJ, 510, L115

Kuiper, L., Hermsen, W., & Mendez, M. 2004, ApJ, 613, 1173

Kulkarni, S. R., Kaplan, D. L., Marshall, H. L., Frail, D. A. andMurakami, T., & Yonetoku, D. 2003, ApJ, 585, 948

Lai, D. 2001, Reviews of Modern Physics, 73, 629

Lamb, R. C., Fox, D. W., Macomb, D. J., & Prince, T. A. 2002, ApJ, 574, L29

Lattimer, J. M. & Prakash, M. 2000, PhR, 333, 121

Lenters, G. T., Woods, P. M., Goupell, J. E., Kouveliotou, C., Gögüs, E., Hurley, K., Frederiks, D., Golenetskii, S., & Swank, J. 2003, ApJ, in press

Lewin, W. H. G., Van Paradijs, J., & Taam, R. E. 1995, in X-Ray Binaries, ed. W. H. G. Lewin, J. van Paradijs, & E. P. J. van den Heuvel (Cambridge: Cambridge University Press), 175–232

Lewin, W. H. G., van Paradijs, J., & van den Heuvel, E. P. J. 1997, X-ray Binaries (X-ray Binaries, ISBN 0521599342, Cambridge University Press, 1997.)

Liu, Q. Z., van Paradijs, J., & van den Heuvel, E. P. J. 2000, 147, 25

—. 2001, A&A, 368, 1021

Longair, M. S. 1994, High energy astrophysics. Vol.2: Stars, the galaxy and the interstellar medium (Cambridge: Cambridge University Press, —c1994, 2nd ed.)

Lu, E. T., Hamilton, R. J., McTiernan, J. M., & Bromund, K. R. 1993, ApJ, 412, 841

Lyne, A. G., Burgay, M., Kramer, M., Possenti, A., Manchester, R. N., Camilo, F., McLaughlin, M. A., Lorimer, D. R., D'Amico, N., Joshi, B. C., Reynolds, J. R., & Freire, P. C. C. 2004, Science, in press

Lyne, A. G. & Smith, F. G. 1990, Pulsar Astronomy (Cambridge: Cambridge University Press)

Lyubarsky, Y., Eichler, D., & Thompson, C. 2002, ApJ, 580, L69

Lyutikov, M. 2002, ApJ, 580, L65

Lyutikov, M. & Gavriil, F. P. 2005, MNRAS, submitted (astro-ph/0507557)

MacFadyen, A. I. & Woosley, S. E. 1999, ApJ, 524, 262

Manchester, R. N. & Taylor, J. H. 1977, Pulsars (San Francisco: Freeman)

Marsden, D. & White, N. E. 2001, ApJ, 551, L155

Marsden, R., Lingenfelter, R. E., Rothschild, R. E., & Higdon, J. C. 2001, ApJ, 550, 397

Mazets, E. P. & Golenetskii, S. V. 1981, Ap&SS, 75, 47

Mazets, E. P., Golenetskii, S. V., Il'inskii, V. N., Apetkar', R. L., & Gur'yan, Y. A. 1979, Nature, 282, 587

McGarry, M. B., Gaensler, B. M., Ransom, S. M., Kaspi, V. M., & Veljkovik, S. 2005, ApJ, 627, L137

McLaughlin, M. A., & Kaspi, V. M. 2005, ApJ, 618, L41

Mereghetti, S., Caraveo, P., & Bignami, G. F. 1992, A&A, 263, 172

Mereghetti, S., Cremonesi, D., Feroci, M., & Tavani, M. 2000, A&A, 361, 240

Mereghetti, S., Israel, G. L., & Stella, L. 1998, MNRAS, 296, 689

Mereghetti, S. & Stella, L. 1995, ApJ, 442, L17

Mereghetti, S., Tiengo, A., Stella, L., Israel, G. L., Rea, N., Zane, S., & Oosterbroek, T. 2004, ApJ, 608, 427

Meszaros, P. 1992, High-energy radiation from magnetized neutron stars Meszaros. (Chicago : University of Chicago Press, c1992.), 47–+

Michel, F. C. 1988, Nature, 333, 644+

Morii, M., Kawai, N., & Shibazaki, N. 2005, ApJ, 622, 544

Morii, M., Sato, R., Kataoka, J., & Kawai, N. 2003, Publications of the Astronomical Society of Japan, 55, L45

Muno, M. P. 2004, ArXiv Astrophysics e-prints

Murakami, T., Tanaka, Y., Kulkarni, S. R., Ogasaka, Y., Sonobe, T., Ogawara, Y., Aoki, T., & Yoshida, T. 1994, Nature, 368, 127

Narayan, R. & Yi, I. 1994, ApJ, 428, L13

—. 1995, ApJ, 452, 710

Nice, D. J., Splaver, E. M., Stairs, I. H. Loehmer, O., Jessner, A., Kramer, M., & Cordes, J. M. 2005, ApJ, submitted (astro-ph/0508050)

Nishenko, S. P. & Buland, R. 1987, Bull. Seism. Soc. Am., 77, 1382

Olive, J.-F., Hurley, K., Dezalay, J.-P., Atteia, J.-L., Barraud, C., Butler, N., Crew, G. B., Doty, J., Ricker, G., Vanderspek, R., Lamb, D. Q., Kawai, N., Yoshida, A., Shirasaki, Y., Sakamoto, T., Tamagawa, T., Torii, K., Matsuoka, M., Fenimore, E. E., Galassi, M., Tavenner, T., Donaghy, T. Q., & Graziani, C.2003, om AIP Conf. Proc. 662: Gamma-Ray Burst and Afterglow Astronomy 2001: First Year of the HETE Mission, 82-87

Oosterbroek, T., Parmar, A. N., Mereghetti, S., & Israel, G. L. 1998, A&A, 334, 925

Özel, F., Psaltis, D., & Kaspi, V. M. 2001, ApJ, 563, 255

Pacini, F. 1967, Nature, 216, 567

Paczyński, B. 1992, Acta Astron., 42, 145

Palmer, D. M. 1999, ApJ, 512, L113

—. 2002, Memorie della Societa Astronomica Italiana, 73, 578

Parker, E. N. 1955, ApJ, 122, 293

Patel, S. K., Kouveliotou, C., Woods, P. M., Tennant, A. F., Weisskopf, M. C., Finger, M. H., Göğüş, E., van der Klis, M., & Belloni, T. 2001, ApJ, 563, L45

Paul, B., Kawasaki, M., Dotani, T., & Nagase, F. 2000, ApJ, 537, 319

Pivovaroff, M., Kaspi, V. M., & Camilo, F. 2000, ApJ, 535, 379

Possenti, A., Cerutti, R., Colpi, M., & Mereghetti, S. 2002, A&A, 387, 993

Price, P. A., Berger, E., Reichart, D. E., Kulkarni, S. R., Yost, S. A., Subrahmanyan, R., Wark, R. M., Wieringa, M. H., Frail, D. A., Bailey, J., Boyle, B., Corbett, E., Gunn, K., Ryder, S. D., Seymour, N., Koviak, K., McCarthy, P., Phillips, M., Axelrod, T. S., Bloom, J. S., Djorgovski, S. G., Fox, D. W., Galama, T. J., Harrison, F. A., Hurley, K., Sari, R., Schmidt, B. P., Brown, M. J. I., Cline, T., Frontera, F., Guidorzi, C., & Montanari, E. 2002, ApJ, 572, L51

Rea, N., Israel, G. L., Stella, L., Oosterbroek, T., Mereghetti, S., Angelini, L., Campana, S., & Covino, S. 2003, ApJ, 586, L65

Rea, N., Testa, V., Israel, G. L., Mereghetti, S., Perna, R., Stella, L., Tiengo, A., Mangano, V., Oosterbroek, T., Mignani, R., Curto, G. L., Campana, S., & Covino, S. 2004, A&A, 425, L5

Reisenegger, A. 2003, in Proceedings of the International Workshop on Strong Magnetic Fields and Neutron Stars, La Habana, Cuba, April 7-12, 2003, submitted (astro-ph/0508050)

Revnivtsev, M. G., Sunyaev, R. A., Varshalovich, D. A., Zheleznyakov, V. V., Cherepashchuk, A. M., Lutovinov, A. A., Churazov, E. M., Grebenev, S. A., & Gilfanov, M. R. 2004, Astronomy Letters, 30, 382

Rho, J. & Petre, R. 1997, ApJ, 484, 828

Rothschild, R. E., Kulkarni, S. R., & Lingenfelter, R. E. 1994, Nature, 368, 432

Rots, A. H., Jahoda, K., Macomb, D. J., Kawai, N., Saito, Y., Kaspi, V. M., Lyne, A. G., Manchester, R. N., Backer, D. C., Somer, A. L., Marsden, D., & Rothschild, R. E. 1998, ApJ, 501, 749

Ruderman, M. 1976, ApJ, 203, 213

—. 1991, ApJ, 382, 587

Seward, F. D., Charles, P. A., & Smale, A. P. 1986, ApJ, 305, 814

Shapiro, S. L. & Teukolsky, S. A. 1983, Black Holes, White Dwarfs and Neutron Stars. The Physics of Compact Objects (New York: Wiley–Interscience)

Sigurdsson, S. & Hernquist, L. 1992, ApJ, 401, L93

Staelin, D. H. & Reifenstein, III, E. C. 1968, Science, 162, 1481

Stern, B. E., Tikhomirova, Y., Kompaneets, D., Svensson, R., & Poutanen, J. 2001, apj, 563, 80

Strohmayer, T. E. & Ibrahim, A. I. 2000, ApJ, 537, L111

Strohmayer, T. E., Zhang, W., Swank, J. H., Smale, A., Titarchuk, L., Day, C., & Lee, U. 1996, ApJ, 469, L9

Sugizaki, M., Nagase, F., Torii, K. I., Kinugasa, K., Asanuma, T., Matsuzaki, K., Koyama, K., & Yamauchi, S. 1997, PASJ, 49, L25

Tajima, T. & Shibata, K., eds. 1997, Plasma astrophysics (Reading, Mass. : Addison- Wesley, c1997.)

Tam, C. R., Kaspi, V. M., van Kerkwijk, M. H., & Durant, M. 2004, ApJ, 617, L53

Thompson, C. & Duncan, R. C. 2001, ApJ, 561, 980

Thompson, C. & Duncan, R. C. 1993, ApJ, 408, 194

Thompson, C. & Duncan, R. C. 1995, MNRAS, 275, 255

Thompson, C. & Duncan, R. C. 1996, ApJ, 473, 322

Thompson, C., Lyutikov, M., & Kulkarni, S. R. 2002, ApJ, 574, 332

Thorsett, S. E. & Chakrabarty, D. 1999, ApJ, 512, 288

Tiengo, A., Göhler, E., Staubert, R., & Mereghetti, S. 2002, A&A, 383, 182

Tiengo, A., Mereghetti, S., Turolla, R., Zane, S., Rea, N., Stella, L., & Israel, G. L., 2005, ApJ, 437, 997

Torii, K., Kinugasa, K., Katayama, K., Tsunemi, H., & Yamauchi, S. 1998, ApJ, 503, 843

van Paradijs, J., Taam, R. E., & van den Heuvel, E. P. J. 1995, A&A, 299, L41

van Riper, K. A. 1988, ApJ, 329, 339

Vasisht, G. & Gotthelf, E. V. 1997, ApJ, 486, L129

Vasisht, G., Gotthelf, E. V., Torii, K., & Gaensler, B. M. 2000, ApJ, 542, L49

Vasisht, G., Kulkarni, S. R., Frail, D. A., & Greiner, J. 1994, ApJ, 431, L35

Vrba, F. J., Henden, A. A., Luginbuhl, C. B., Guetter, H. H., Hartmann, D. H., & Klose, S. 2000, ApJ, 533, L17

Wachter, S., Patel, S. K., Kouveliotou, C., Bouchet, P., Özel, F., Tennant, A. F., Woods, P. M., Hurley, K., Becker, W., & Slane, P. 2004, ApJ, 615, 887

Wang, Z. & Chakrabarty, D. 2002, ApJ, 579, L33

Wijnands, R. & van der Klis, M. 1998, Nature, 394, 344

Wilson, C. A., Dieters, S., Finger, M. H., Scott, D. M., & van Paradijs, J. 1999, ApJ, 513, 464

Woods, P. M., Kaspi, V. M., Thompson, C., Gavriil, F. P., Marshall, H. L., Chakrabarty, D., Flanagan, K., Heyl, J., & Hernquist, L. 2004, ApJ, 605, 378

Woods, P. M., Kouveliotou, C., Göğüş, E., Finger, M. H., Swank, J., Markwardt, C. B., Hurley, K., & van der Klis, M. 2002, ApJ, 576, 381

Woods, P. M., Kouveliotou, C., Göğüş, E., Finger, M. H., Swank, J., Smith, D. A., Hurley, K., & Thompson, C. 2001, ApJ, 552, 748

Woods, P. M., Kouveliotou, C., Gavriil, F. P., Kaspi, M., V., Roberts, M. S. E., Ibrahim, A., Markwardt, C. B., Swank, J. H., & Finger, M. H. 2005, ApJ, in press (astro-ph/0505039)

Woods, P. M., Kouveliotou, C., van Paradijs, J., Finger, M. H., Thompson, C., Duncan, R. C., Hurley, K., Strohmayer, T., Swank, J., & Murakami, T. 1999, ApJ, 524, L55

Woods, P. M. & Thompson, C. 2004, in Compact Stellar X-ray Sources, ed. W. H. G. Lewin & M. van der Klis (UK: Cambridge University Press), in press (astro-ph/0406133)

Woosley, S. E. 1993, ApJ, 405, 273

Yakovlev, D. G. & Shalybkov, D. A. 1990, Soviet Astronomy Letters, 16, 86